Numerical Modelling of MHD Waves in Coronal Loops

Hendrik-Jan Van Damme

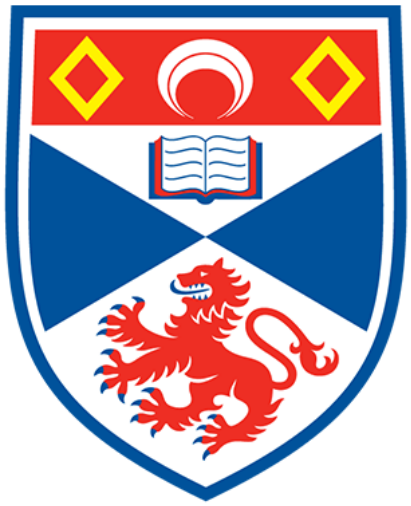

University of
St Andrews

This thesis is submitted in partial fulfilment for the degree of
Doctor of Philosophy (PhD)
at the University of St Andrews

June 2020

Abstract

Waves in the solar corona have been investigated for many years, as a potential coronal heating mechanism and in the context of coronal seismology, and they play an important role in our understanding of the solar corona. In this thesis, we present the results of numerical simulations of transverse MHD waves in coronal loops. In a first study, we consider an atmospheric model for a coronal loop where the chromosphere is included as a simple mass reservoir and the effects of gravity, thermal conduction and optically thin radiation are taken into account, and we investigate the dissipation of phase-mixed, driven Alfvén waves and the subsequent heating and evaporation from the lower atmosphere. It has been argued that this evaporation can significantly affect the transverse density profile in the boundary of the loop, thereby changing the Alfvén speed gradient and the phase mixing process. We analyse the heating from the phase-mixed Alfvén waves and the evaporation and find that in our setup, with a high-frequency driver, the effect of the evaporation on the phase mixing process is negligible as a significant amount of the wave energy in the corona is lost to the lower atmosphere.

Waves usually originate in the lower parts of the solar atmosphere, where the convective motions beneath the photosphere shuffle the magnetic field around, and they are then transmitted into the corona. However, recent observations have shown that transverse MHD waves can also be generated in-situ in the corona, by the collision of counter-propagating plasma clumps (coronal rain). When falling down, these coronal rain clumps can collide with upflows or other coronal rain clumps, and generate transverse oscillations. In order to investigate this mechanism, we develop a 2D model for the collision of counter-propagating plasma clumps based on detailed observations and statistical analysis of these events and study the generation of transverse MHD waves. We first study the relationship between various physical parameters of the clumps and the resulting oscillations and subsequently apply the model using observed coronal rain properties and investigate the likelihood of collisions and oscillations in coronal loops. In our simulations, we find that the properties of the oscillations are linked to the properties of the counter-propagating clumps, but also that coronal rain collisions and oscillations are rather unlikely in active region loops, due to the relatively large background pressure and magnetic field strength.

Candidate's declaration

I, Hendrik-Jan Van Damme, do hereby certify that this thesis, submitted for the degree of PhD, which is approximately 50,000 words in length, has been written by me, and that it is the record of work carried out by me, or principally by myself in collaboration with others as acknowledged, and that it has not been submitted in any previous application for any degree.

I was admitted as a research student at the University of St Andrews in September 2016.

I received funding from an organisation or institution and have acknowledged the funders in the full text of my thesis.

Date: 28/09/20..... Signature of candidate: .....

Supervisor's declaration

I hereby certify that the candidate has fulfilled the conditions of the Resolution and Regulations appropriate for the degree of PhD in the University of St Andrews and that the candidate is qualified to submit this thesis in application for that degree.

Date: 28/09/20..... Signature of supervisor: .....

Permission for publication

In submitting this thesis to the University of St Andrews we understand that we are giving permission for it to be made available for use in accordance with the regulations of the University Library for the time being in force, subject to any copyright vested in the work not being affected thereby. We also understand, unless exempt by an award of an embargo as requested below, that the title and the abstract will be published, and that a copy of the work may be made and supplied to any bona fide library or research worker, that this thesis will be electronically accessible for personal or research use and that the library has the right to migrate this thesis into new electronic forms as required to ensure continued access to the thesis.

I, Hendrik-Jan Van Damme, confirm that my thesis does not contain any third-party material that requires copyright clearance.

The following is an agreed request by candidate and supervisor regarding the publication of this thesis:

Printed copy

No embargo on print copy.

Electronic copy

No embargo on electronic copy.

Date: 28/09/20 Signature of candidate: .....

Date: 28/09/20 Signature of supervisor: .....

Underpinning Research Data or Digital Outputs

Candidate's declaration

I, Hendrik-Jan Van Damme, hereby certify that no requirements to deposit original research data or digital outputs apply to this thesis and that, where appropriate, secondary data used have been referenced in the full text of my thesis.

Date: 28/09/20 ..... Signature of candidate: .....

Financial Support

The research leading to the results presented within this thesis has received funding from the UK Science and Technology Facilities Council (Consolidated Grant ST/K0009 50/1), the European Union Horizon 2020 research and innovation programme (grant agreement No. 647214) and the Research Council of Norway through its Centres of Excellence scheme, project number 262622.

This work used the DiRAC@Durham facility managed by the Institute for Computational Cosmology on behalf of the STFC DiRAC HPC Facility (www.dirac.ac.uk), the Darwin Data Analytic system at the University of Cambridge, operated by the University of Cambridge High Performance Computing Service on behalf of the STFC DiRAC HPC Facility, and the University of St Andrews HPC Facility 'Kennedy'.

Publications

This thesis contains work which has been adapted from the following publications:

1. P. Pagano, H. J. Van Damme, P. Antolin & I. De Moortel. MHD simulations of the in-situ generation of kink and sausage waves in the solar corona by collision of dense plasma clumps. A&A, 626:A53, June 2019. doi: 10.1051/0004-6361/201935539.

2. H. J. Van Damme, I. De Moortel, P. Pagano & C. D. Johnston. Chromospheric evaporation and phase mixing of Alfvén waves in coronal loops. A&A, 635:A174, March 2020. doi: 10.1051/0004-6361/201937266.

Collaboration Statement

I am grateful to Dr. Patrick Antolin and Dr. Craig Johnston for their helpful discussions on coronal rain observations and code development, respectively.

Acknowledgements

I would like to thank several people for their help and support in the completion of this thesis.

Firstly, I am extremely grateful to my supervisors, Prof. Ineke De Moortel and Dr. Paolo Pagano, for their help and guidance throughout my PhD, which has been essential in the completion of this thesis.

Secondly, I would like to thank all the staff and PhD students of the Maths department for making my time so enjoyable in St Andrews. I would like to especially mention Tom, Hope, Daniel, Craig and Ben for the many badminton games, football games, board games, pub quizzes and Munro walks.

I would also like to thank my friends in Belgium. Although I lived abroad for four years, we kept in touch and even did a roadtrip together through Scotland.

Last but not least, I would like to thank my family, my parents and two sisters, for their warmth and for always supporting me. Studying and living abroad has opened a new world to me, but it has also reminded me of the wonderful family I have at home.

Contents

Chapter 1

Introduction

1.1 The solar atmosphere

The solar atmosphere is defined as the part of the Sun from which photons can escape directly into space (Priest, 2014). It is often represented as a layered structure. The lowest layer is the photosphere, which is the thin ($\sim$ 500 km) surface of the Sun, and is defined as the region where most of the visible light is emitted. The temperature of the photosphere is around 6000 K, as shown by Figure 1.1, which shows the density (blue) and the temperature (orange) as a function of height in the solar atmosphere. The density drops off exponentially with height from the base of the photosphere ($\rho_{base} \sim 10^{-4}$ kg/m^3). In the photosphere, the magnetic field emerges from the interior of the Sun, and manifests itself in different structures in the solar atmosphere. The magnetic field can be concentrated in sunspots, which are typically cooler regions in the photosphere with a strong magnetic field ($\sim 10^3$ G). Above these regions, in the corona, we usually find so called active regions, where the solar atmosphere can show a lot of magnetic activity, such as eruptions or flares.

The next layer above the photosphere is the chromosphere. The thickness of the chromosphere can vary but is roughly a few thousand kilometers. Figure 1.1 shows that the temperature decreases initially to roughly 4000 K and then increases again to 30000 K, whereas the density continues to decrease exponentially with height in the chromosphere, to $\rho \sim 10^{-10}$ kg/m^3 near the top of the chromosphere.

The temperature then increases rapidly in the narrow transition region (TR) (of the order of a few hundred km), from $\sim 10^4$ K in the chromosphere to $\sim 10^6$ K in the corona. The density decreases similarly with two orders of magnitude. The corona

hosts different magnetic structures (e.g. coronal loops and prominences) which provide efficient waveguides (see e.g. Reale 2010; Parenti 2014). We will discuss waves in the solar atmosphere in more detail in Section 1.3.3. Although represented here as a layered structure, the solar atmosphere is highly dynamical with a lot of interaction (e.g. heat, flows) between the different layers, and it is very challenging to model the full solar atmosphere in detail, due to the large range of spatial and temporal scales.

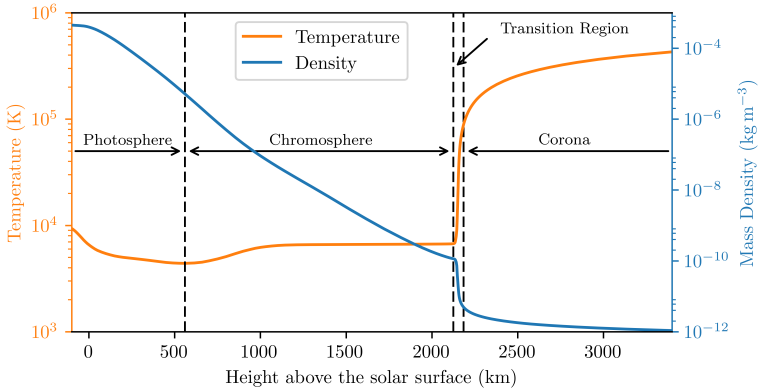

Figure 1.1: A schematic plot of the temperature (blue) and density (orange) with height in the solar atmosphere. Figure obtained from Priest (2014).

1.1.1 The coronal heating problem

The coronal heating problem is a long-standing problem in solar physics, which tries to address how the corona can be maintained at temperatures of a few million degrees. It is believed that the magnetic field provides the main energy source to heat the corona (see e.g. Klimchuk, 2006). Due to the convective motions beneath the photosphere, the surface of the photosphere is constantly in motion and the magnetic fieldlines are shuffled around. This movement stores energy in the magnetic field - if the footpoint motions are slower than the Alfvén travel time along the fieldline - or it can generate waves that propagate along the field - if the footpoint motions are faster than the local Alfvén travel time. These different mechanisms are sometimes referred to as DC and AC heating, respectively. In the case of DC heating, the magnetic energy can be released by magnetic reconnection, whereas in the case of AC heating the wave energy propagates into the solar atmosphere where it can then be dissipated. In this thesis, we will mainly focus on MHD wave propagation and dissipation in the solar atmosphere.

Observational studies have shown that MHD waves contain a significant amount of energy and are a possible candidate for coronal heating (see e.g. De Pontieu et al.

2007; McIntosh et al. 2011; Morton et al. 2012, Srivastava et al. 2017; or reviews by Arregui et al. 2012; De Moortel and Nakariakov 2012; Parnell and De Moortel 2012; Arregui 2015; De Moortel and Browning 2015). However, even with significant wave energy observed in the corona, the timescales on which the energy is dissipated are often found to be too long to counteract the coronal losses such as thermal conduction and optically thin radiation (see e.g. Parnell and De Moortel 2012; Arregui 2015; De Moortel and Browning 2015). In the corona, the values of viscosity and resistivity are generally small, and hence in order to dissipate the wave energy fast enough, large gradients in the velocity field and the magnetic field are needed. There are a few processes known to accelerate the cascade of wave energy to smaller length scales, such as resonant absorption (Ionson, 1978), phase mixing (Heyvaerts and Priest, 1983), the Kelvin-Helmholtz Instability (KHI) (see e.g. Browning and Priest, 1984) and turbulent cascade (see e.g. Hollweg, 1986). In Section 1.3.2 we provide more detail on the process of phase mixing.

1.1.2 Chromospheric evaporation and coronal rain

As heating occurs in the corona, thermal conduction spreads the heat along the field and a conductive flux is driven downwards from the corona to the lower atmosphere. This locally increases the pressure and can lead to an upward flow of mass (evaporation), locally increasing the coronal density (see e.g. Kuin and Martens, 1982). This process is called (chromospheric) evaporation. Due to the increase in density, the optically thin radiative losses (which scale with the density squared) increase and the corona will start to locally cool. This may cause a run-away effect in the temperature, as the optically thin radiative loss function increases for decreasing coronal temperatures (see e.g. Klimchuk et al., 2008), triggering the thermal instability. The local condensations can then form cool, dense plasma clumps, which, under the gravitational force, fall towards lower atmospheric heights, draining mass from the coronal loop (see e.g. Cargill, 1994; Klimchuk, 2006). These cool and dense plasma clumps are called coronal rain (see e.g. Antolin and Rouppe van der Voort, 2012; Antolin et al., 2015b). This cycle of evaporation and draining of material is sometimes also referred to as a thermal non-equilibrium (TNE) cycle (see e.g. Antiochos et al. 1999; Karpen et al. 2005; Antolin et al. 2010b; Xia et al. 2011; Froment et al. 2020). Coronal loops can undergo a series of these heating-cooling cycles (TNE cycles) (see e.g. Froment et al., 2020). Hence, observations of coronal rain can be a potential indicator for heating in coronal loops (Antolin, 2020).

Multiple observational studies have found evidence for the presence of these upflows and downflows in the TR and the lower corona (see e.g. Del Zanna 2008; Feldman et al. 2011; Dadashi et al. 2011, 2012; Tripathi et al. 2012a,b; McIntosh et al. 2012; Winebarger et al. 2013). Hansteen et al. (2010) studied the mass and energy cycle between the lower atmosphere and the corona and found that both downflows and upflows are present at locations of (strong) magnetic field braiding, leading to redshifts and blueshifts of the order of about 5 km/s (see also e.g. Zacharias et al. 2011; Guerreiro et al. 2013).

Because of improved instrumentation, coronal rain has been increasingly observed over recent years (see e.g. Schrijver 2001; De Groof et al. 2005; Antolin et al. 2010b, Antolin and Verwichte 2011, Antolin and Rouppe van der Voort 2012). We briefly summarise the most important characteristics of coronal rain, following the overview given by Antolin (2020). Coronal rain is characterised by its clumpiness and multistranded nature, i.e. it appears in different irregular clumps of plasma which have a rippled transverse structure (Antolin et al., 2015b; Antolin, 2020). The length of coronal rain clumps is typically a few hundred of kms up to tens of Mm, while the width is more constant, around 150-300 km. Because of resolution constraints of the current available instrumentation, observations are limited and it is assumed that coronal rain widths can be smaller than these values, see also Scullion et al. (2014). When the blobs fall, they fall along loop-like paths and they tend to elongate and clumps can break up into different parts (so called 'shower' events, see e.g. Antolin 2020). Observations show that the width of the blobs remains roughly constant when falling. The speed of coronal rain can vary widely, from a few km/s up to 150km/s (with most observed speeds at 70-80 km/s, see e.g. Antolin and Rouppe van der Voort 2012). Due to the nature of its formation, the temperature of coronal rain blobs is cool compared to the hot coronal environment, and varies between a few 10^3 K to 10^5 K. The coronal rain core number density varies between $10^{10} - 10^{11}$ cm^{-3}, roughly one to two orders of magnitude larger than a typical coronal density in active region loops. Several modelling studies of coronal rain formations by e.g. Fang et al. (2013, 2015); Moschou et al. (2015); Xia et al. (2017) have confirmed these complex and multi-stranded characteristics of coronal rain. Fang et al. (2013) reproduced the histograms of the lengths, widths and velocities of the coronal rain condensations from the observational study by Antolin and Rouppe van der Voort (2012), by modelling a 2D magnetic arcade where the conditions for the thermal instability mechanism were met.

1.2 The MHD equations

Because of the high temperature in the solar atmosphere, most of the plasma is ionised (consisting of electrons and ions), and the plasma can be modelled as a single fluid which is subject to forces exerted by the magnetic field. This modelling approach is also known as 'MagnetoHydroDynamics' (MHD). The MHD equations consist of Maxwell's equations of electromagnetism and the fluid equations (see e.g. Priest, 2014). Below we give a summary of the MHD equations as used in this thesis.

The MHD equations, in MKS units, are given by

$$\frac{\partial \rho}{\partial t} + \nabla \cdot (\rho \mathbf{v}) = 0, \tag{1.1}$$

$$\rho \frac{\mathrm{D}\mathbf{v}}{\mathrm{D}t} = \mathbf{j} \times \mathbf{B} - \nabla P + \rho \mathbf{g} + \mathbf{F}_\nu, \tag{1.2}$$

$$\frac{\rho^\gamma}{\gamma - 1} \frac{\mathrm{D}}{\mathrm{D}t} \left(\frac{P}{\rho^\gamma} \right) = -\nabla \cdot \mathbf{q} - L_r + \frac{j^2}{\sigma} + H_\nu + H_{bg}, \tag{1.3}$$

$$\frac{\partial \mathbf{B}}{\partial t} = \nabla \times (\mathbf{v} \times \mathbf{B}) + \eta \nabla^2 \mathbf{B}, \tag{1.4}$$

$$\nabla \times \mathbf{B} = \mu_0 \mathbf{j}, \tag{1.5}$$

$$\nabla \cdot \mathbf{B} = 0, \tag{1.6}$$

$$P = \frac{R}{\tilde{\mu}} \rho T. \tag{1.7}$$

In these equations, ρ is the mass density, t the time, $\mathbf{v}$ the velocity, $\mathbf{B}$ is the magnetic field, $\mathbf{j}$ the current density, P the gas pressure, $\mathbf{g}$ the gravitational acceleration, $\mathbf{F}_\nu$ the viscous force, $\gamma = \frac{5}{3}$ the ratio of specific heats, $\nabla \cdot \mathbf{q}$ is the thermal conduction, $L_r = n^2 \Lambda(T)$ is the net radiation, with $n = \frac{\rho}{\tilde{\mu} m_p}$ the number density, $\tilde{\mu}$ the average particle mass (in terms of the proton mass, $m_p = 1.67 \times 10^{-27}$ kg) and $\Lambda(T)$ the optically thin radiative loss function (see e.g. Klimchuk et al., 2008). σ is the electrical conductivity, H_ν is the heating by viscosity, H_{bg} is a background heating term, $\eta = \frac{1}{\mu_0 \sigma}$ is the magnetic diffusivity with $\mu_0 = 4\pi \times 10^7$ H m^{-1} the magnetic permeability of a vacuum, $R = \frac{k_B}{m_p} \approx 8.3 \times 10^3$ J K^{-1} kg^{-1} is the gas constant, where $k_B = 1.38 \times 10^{-23}$ m^2 kg s^{-2} K^{-1} is the Boltzmann constant and T is the temperature.

Equation (1.1) is the continuity equation, and describes conservation of mass for a fluid of density ρ. The second equation (Equation (1.2)), is the equation of motion, where $\frac{\mathrm{D}}{\mathrm{D}t}$ is the Lagrangian derivative (i.e. considering a reference frame moving with

the fluid),

$$\frac{\mathrm{D}}{\mathrm{D}t} = \frac{\partial}{\partial t} + \mathbf{v} \cdot \nabla.$$

The first term on the right hand side (RHS), $\mathbf{j} \times \mathbf{B}$, is the Lorentz force, the second term, $-\nabla P$ is the pressure gradient force, $\rho \mathbf{g}$ is the gravitational force and $\mathbf{F}_\nu$ is the viscous force, given by

$$\mathbf{F}_\nu = \rho\nu \left(\nabla^2 \mathbf{v} + \frac{1}{3} \nabla \left(\nabla \cdot \mathbf{v} \right) \right), \tag{1.8}$$

where ν is the kinematic viscosity (assumed uniform). The Lorentz force can be rewritten as

$$\mathbf{j} \times \mathbf{B} = \frac{1}{\mu_0} \left(\mathbf{B} \cdot \nabla \right) \mathbf{B} - \nabla \left(\frac{B^2}{2\mu_0} \right). \tag{1.9}$$

The first term on the RHS of Equation (1.9) is the magnetic tension force, and scales with the local curvature of the field. The second term is the magnetic pressure force and this force acts from regions of high magnetic field strength to regions of low magnetic field strength. The ratio of the gas pressure to the magnetic pressure is called the plasma beta and is given by

$$\beta = \frac{2\mu_0 P}{B^2}. \tag{1.10}$$

When $\beta \gg 1$, the pressure gradient force is the dominant force whereas for $\beta \ll 1$, the Lorentz force dominates.

Equation (1.3) is the energy equation, where the RHS contains all the terms through which the plasma may gain or lose energy. Here, the thermal conduction $\nabla \cdot \mathbf{q}$ can be written as (see e.g. Priest, 2014)

$$\nabla \cdot \mathbf{q} = \nabla_{||} \cdot \left(\kappa_{||} \nabla_{||} T \right) + \nabla_{\perp} \cdot \left(\kappa_{\perp} \nabla_{\perp} T \right), \tag{1.11}$$

where the subscripts $||$ and $\perp$ refer to values along and across the field. In the corona, $\kappa_{||} \gg \kappa_{\perp}$ and the conduction is primarly along the field: $\nabla \cdot \mathbf{q} \sim \nabla_{||} \cdot \left(\kappa_{||} \nabla_{||} T \right)$, with $\kappa_{||} = \kappa_0 T^{5/2}$ and $\kappa_0 \sim 10^{-11}$ W m^{-1} K^{-1}, where we also assume that the parallel and perpendicular length scales are of the same order. We remark, however, that under the circumstances in which the perpendicular length scale is much smaller than the parallel length scale, the comparison of the two terms in Equation (1.11) will need to include the ratio of the length scales.

The term $\frac{j^2}{\sigma}$ is the Ohmic heating, and the heating by viscosity, H_ν, is given by

$$H_\nu = \rho\nu \left(\frac{1}{2} e_{ij} e_{ij} - \frac{2}{3} \left(\nabla \cdot \mathbf{v} \right)^2 \right),$$

where $e_{ij} = \frac{\partial v_i}{\partial x_j} + \frac{\partial v_j}{\partial x_i}$ is the rate of strain tensor. When the RHS of Equation (1.3) is zero, the plasma is adiabatic which means that the plasma is thermally isolated from its surroundings.

Equation (1.4) is the induction equation and it describes how a magnetic field evolves in time. The terms on the RHS are the advection and diffusion terms, where diffusion is more important in regions of high η and small lengthscales. In this equation we also assumed that η is constant.

Equation (1.5) is Ampère's Law and equation (1.6) is the solenoidal constraint, which states that there are no sources or sinks in the magnetic field. Equation (1.7) is the ideal gas law, which relates the gas pressure P, density ρ and temperature T of the plasma.

The MHD equations described above are based on the following assumptions. First of all, the typical length and time scales over which the system evolves are assumed to be much larger than the microscopic ion and electron scales (the gyroradius, the mean free path length, the Debye length, the gyroperiod and the collision time), which also implies that the plasma is considered to be quasi-neutral. Secondly, the plasma is treated as a single fluid. Thirdly, the typical speeds of the plasma are taken to be much smaller than the speed of light. And lastly, the overall plasma is assumed to be in thermodynamic equilibrium, such that the particle distribution functions are close to Maxwellian.

In the solar corona the speeds of the plasma are of the order of the Alfvén speed, a few thousand km/s, which is much smaller than the speed of light. Typical lengthscales are of the order of a few Mm, larger than the mean free path length, the ion gyro-radius and the Debye length, and the timescales are larger than the gyroperiod or the collisional time. Hence, MHD theory is a suitable theory for the solar corona.

1.3 MHD waves

A plasma that is initially in stable equilibrium can be perturbed, such that the perturbation can cause oscillations (waves) about the equilibrium.

1.3.1 Uniform medium

In this section, we derive the linear MHD waves in a uniform medium. We start from a stationary plasma in equilibrium with $\mathbf{B}_0 = (0, 0, B_0)$ the magnetic field in the z direction, ρ_0 the (uniform) density and P_0 the (uniform) pressure. We consider a perturbation of the equilibrium such that $\mathbf{B} = \mathbf{B}_0 + \mathbf{B}_1$, $\rho = \rho_0 + \rho_1$, $P = P_0 + P_1$ and $\mathbf{v} = \mathbf{v}_0 + \mathbf{v}_1$, where the subscript 0 denotes the initial equilibrium state and the subscript 1 denotes the perturbation. We then linearise the ideal MHD equations and assume that the perturbations are plane-wave solutions of the form $e^{i(\mathbf{k}\cdot\mathbf{r}-\omega t)}$, where $\mathbf{k}$ is the wave vector, $\mathbf{r}$ the position vector and ω the frequency, leading to the following equation for ω (see e.g. Chapter 4 of Priest, 2014)

$$\left(\omega^4 - k^2\left(c_s^2 + v_A^2\right)\omega^2 + c_s^2 v_A^2 k^4 \cos\theta_B\right)(\mathbf{k}\cdot\mathbf{v}_1) = 0. \tag{1.12}$$

Here, $k^2 = (\mathbf{k}\cdot\mathbf{k})$, $v_A = \frac{B_0}{\sqrt{\mu_0\rho_0}}$ is the Alfvén speed, $c_s = \sqrt{\frac{\gamma P_0}{\rho_0}}$ the sound speed and θ_B the angle between $\mathbf{B}_0$ and $\mathbf{k}$. The solutions to the dispersion relation (1.12) describe relations for ω in terms of k for the different types of linear MHD waves. Solving this equation gives the following cases:

1. Incompressible solutions:

   $$\mathbf{k}\cdot\mathbf{v}_1 = 0.$$

   We then have that $\omega = kv_A\cos\theta_B$ (see e.g. Priest, 2014). This is the Alfvén wave, which is incompressible ($\mathbf{k}\cdot\mathbf{v}_1 = 0$), transverse ($\mathbf{B_0}\cdot\mathbf{v}_1 = 0$) and propagates at the phase speed $\frac{\omega}{k} = v_A\cos\theta_B$. This wave behaves like a wave on a string and the restoring force is the magnetic tension force.

2. Compressible solutions (i.e. the first bracket of Equation (1.12) is zero). This is a quadratic equation in ω^2, and has two solutions:

   $$\frac{\omega^2}{k^2} = \frac{(c_s^2 + v_A^2) \pm \sqrt{(c_s^2 + v_A^2)^2 - 4c_s^2 v_A^2\cos^2\theta_B}}{2}. \tag{1.13}$$

   The solution with the positive root is the fast magnetoacoustic wave, and the solution with the negative root the slow magnetoacoustic wave. These waves are

compressible, which means that they perturb the density and the pressure. In the corona, for propagation along the field ($\theta_B = 0$), the phase speed is v_A for fast waves and c_s for slow waves (since $v_A \gg c_s$). For propagation across the field ($\theta_B = \frac{\pi}{2}$) the fast wave propagates at the phase speed $\sqrt{c_s^2 + v_A^2}$ and the slow wave does not propagate.

1.3.2 Phase mixing of Alfvén waves

Phase mixing of Alfvén waves (Heyvaerts and Priest, 1983) is one of the mechanisms that has been proposed to address the slow dissipation of wave energy with classical transport coefficients in the solar corona. This is the process where Alfvén waves on neighbouring magnetic field lines propagate at different speeds due to a cross-field gradient in the Alfvén speed. Over time, waves on neighbouring field lines move out of phase and the wavefront tilts, which leads to the generation of large transverse gradients ("small scales") in the velocity field and the magnetic field. This, in turn, leads to enhanced Ohmic and viscous dissipation.

Phase mixing of Alfvén waves has been studied extensively as a possible coronal heating mechanism (see e.g. reviews by Parnell and De Moortel 2012; Arregui 2015). Browning and Priest (1984) and Ofman and Davila (1995) investigated the KHI for phase-mixed standing Alfvén waves in coronal loops and found that, after resonant absorption in the boundary layer of the loop (see Section 1.3.3), the KHI can be triggered, and that this can lead to turbulence and a further cascade to smaller length scales. However, Ofman and Davila (1995) found that the heating rate could decrease due to a shift in the global mode frequency because of the disruption of the density structure in the boundary layer of the loop. This was later confirmed with numerical simulations by e.g. Poedts and Goedbloed (1997). Antolin et al. (2015a), Howson et al. (2017), Karampelas et al. (2017) conducted numerical simulations of standing kink modes in coronal loops, with resonant absorption transferring the energy into the boundary layer, where the waves were then subject to phase mixing. They found that the KHI is triggered and reconfirmed the cascade to smaller length scales and a disruption of the boundary layer due to turbulent behaviour. Since Heyvaerts and Priest (1983), phase mixing has been investigated in different magnetic structures, such as a stratified atmosphere (Ruderman et al. 1999, 1998; De Moortel et al. 1999; Smith et al. 2007), an open and radially diverging stratified atmosphere (De Moortel et al. 2000; Smith et al. 2007; Ruderman and Petrukhin 2018; Petrukhin et al. 2018), coronal holes (Parker 1991;

Hood et al. 1997, 2002, 2005), 3D magnetic flux tubes (Pagano and De Moortel, 2017; Pagano et al., 2018, 2019) and 3D complex coronal magnetic fields (Howson et al., 2019, 2020). Ruderman et al. (1998, 1999), De Moortel et al. (1999, 2000) and Smith et al. (2007) showed that phase mixing is less efficient in a stratified atmosphere (due to the increase of the wavelength) compared to a uniform medium, and that in a diverging magnetic field phase mixing is enhanced (due to a decrease of the wavelength). In a gravitationally stratified, diverging atmosphere, phase mixing can have an enhancing or diminishing effect, depending on the pressure scale height (De Moortel et al., 2000; Ruderman and Petrukhin, 2018). Parker (1991) studied phase mixing in coronal holes and argued that an ignorable coordinate cannot always be assumed, and that therefore Alfvén waves do not always undergo pure phase mixing but can also couple to fast magnetoaccoustic waves. This was later also shown by Nakariakov et al. (1997, 1998) and Botha et al. (2000). Hood et al. (1997, 2002, 2005) showed that phase mixing can be a viable heating mechanism in coronal holes, for the observed frequencies of the footpoint motions (periods of the order of 5 minutes) and the background Alfvén speed (of the order of 4500 km/s). Pagano and De Moortel (2017) investigated phase mixing of continuously driven, sinusoidal, single-frequency Alfvén waves in a coronal flux tube and found that only with extreme physical parameters (i.e. large dissipative coefficients, $\eta = 10^{10}\eta_S$ with η_S the Spitzer resistivity, and high-frequency waves, $P = 6$s) can heating from phase mixing be sufficient to counter balance coronal losses such as optically thin radiation. It was previously shown analytically by Abdelatif (1987), using realistic estimates for the resistivity and viscosity, that propagating Alfvén waves (with periods of the order of 5s) which undergo phase mixing can deposit a substantial amount of heating in coronal loops, although not sufficient to balance coronal losses. In Pagano et al. (2019), the authors drive the coronal flux tube with a multi-frequency driver based on the observed power spectrum of transverse waves in the corona (Morton et al., 2016). Again the authors found that the heating from phase mixing is not sufficient to counteract the coronal losses. When multi-harmonic standing kink oscillations are considered (Pagano et al., 2018) the higher harmonics can even prevent the further generation of small length scales. From these series of papers, the authors conclude that phase mixing as a mechanism on its own is probably not sufficient to balance the coronal losses, but can play an important role in generating smaller lengthscales. Howson et al. (2019) studied phase mixing in a braided, coronal magnetic field and found that phase mixing happens throughout the whole volume, rather than only in the boundary shell for coronal flux tube models. Howson et al. (2020) studied counter-propagating, phase-mixed Alfvén waves in a similar magnetic

field configuration and found that the cascade to smaller lengthscales and the rate of the wave energy dissipation increases. However, the amount of heating is only sufficient if the driver amplitudes are significantly larger than the currently observed amplitudes.

1.3.3 Transverse oscillations in the solar atmosphere

The atmosphere of the Sun hosts different magnetic structures (e.g. coronal loops) which are efficient waveguides for MHD waves (see e.g. Reale, 2010). Recent high-cadence and high-resolution observations have established the presence of waves and oscillations throughout the solar atmosphere (see e.g. reviews by Nakariakov and Verwichte 2005, Arregui et al. 2012; De Moortel and Nakariakov 2012). Most of these perturbations have been interpreted as MHD waves and in many cases are reported to contain a substantial amount of energy, leading to a renewed interest in MHD wave dissipation as a potential coronal heating mechanism (see e.g. reviews by Parnell and De Moortel 2012; Arregui 2015). This thesis focuses on transverse MHD waves in coronal loops. Edwin and Roberts (1983) developed the linear MHD wave theory in cylindrical geometry, and we here briefly mention the definitions of a kink, sausage and torsional Alfvén mode in a cylinder. A kink mode is a compressible, transverse MHD wave that displaces the central axis of the cylinder whereas a sausage mode is a compressive, transverse mode that does not displace the central axis of the flux tube but expands and contracts symmetrically about the central axis. The incompressible Alfvén mode in a cylinder is polarized in the azimuthal direction since this is the invariant direction (i.e. the Alfvén speed does not vary in the azimuthal direction). Below we highlight a few relevant examples of the literature that discuss transverse MHD waves in coronal loops (for a more comprehensive review see e.g. Nakariakov and Verwichte 2005; Arregui et al. 2012; De Moortel and Nakariakov 2012).

Using the Transition Region and Coronal Explorer (TRACE) instrument, standing, transverse oscillations in coronal loops have been observed for the first time by e.g. Nakariakov et al. (1999); Aschwanden et al. (2002); Schrijver et al. (2002). These oscillations are often generated by a neighbouring impulsive event, such as a flare, which causes some of the nearby loops to oscillate transversely. These oscillations have been interpreted as standing kink modes (see e.g. Aschwanden et al., 1999; Nakariakov et al., 1999). Observations have shown that these standing kink modes in coronal loops damp relatively quickly, on timescales of a few periods (see e.g. Ruderman and Roberts 2002; Aschwanden et al. 2003; Ruderman and Erdélyi 2009). However, it has been ar-

gued that this rapid damping does not necessarily indicate dissipation on the same timescales, as the process of resonant absorption/mode coupling converts the energy of the global, standing kink mode in the core of the loop to torsional, azimuthal Alfvén waves in the boundary shell (see e.g. Ruderman and Roberts 2002; Aschwanden et al. 2003; Terradas et al. 2008; Goossens et al. 2011; Okamoto et al. 2015; Pascoe et al. 2016). In this process a resonance occurs in the boundary shell of the coronal loop at the location where the local Alfvén frequency matches the frequency of the global transverse kink oscillation (see e.g. Ionson, 1978). In the boundary shell, the torsional Alfvén waves can then undergo phase mixing - due to the gradient in the Alfvén speed - and dissipation, and/or they can trigger the KHI which leads to a cascade to smaller length scales, turbulent behaviour and dissipation (see e.g. Browning and Priest 1984; Ofman and Davila (1995); Antolin et al. 2015a; Howson et al. 2017; Karampelas et al. 2017).

Propagating transverse motions have been observed ubiquitously in the solar corona, and are reported to contain a significant amount of wave energy (see e.g. Verwichte et al. 2005; De Pontieu et al. 2007; Okamoto et al. 2007; Tomczyk et al. 2007; Banerjee et al. 2009; Jess et al. 2009; Lin et al. 2009; McIntosh et al. 2009; Tomczyk and McIntosh 2009; Zaqarashvili and Erdélyi 2009; McIntosh et al. 2011; Thurgood et al. 2014; Morton et al. 2016). Using the Coronal Multi-channel Polarimeter (COMP) instrument, Tomczyk et al. (2007) observed periodic Doppler shifts propagating along large, off-limb coronal loops with periods of the order of minutes, and with the power spectrum showing a peak at $\sim$ 5 minutes. The authors suggested a link with the solar interior p-modes, which was later also argued for by e.g. Morton et al. (2016) and Cally (2017). Erdélyi and Fedun (2007), Van Doorsselaere et al. (2008a,b), and Vasheghani Farahani et al. (2009) showed that these transverse propagating displacements in coronal loops can be interpreted as propagating kink modes. Similarly as in the standing kink modes in coronal loops, propagating kink modes can mode couple to torsional Alfvén waves in the boundary shell, at the location where the local Alfvén speed matches the speed of the propagating kink mode (see e.g. Verth et al., 2010). Pascoe et al. (2010, 2011) have confirmed with numerical simulations that mode coupling can indeed rapidly transport the wave energy from the propagating kink mode in the core of the loop, to the boundary shells, qualitatively matching the observed damping length and timescales of the transverse kink mode (Tomczyk et al. 2007; Tomczyk and McIntosh 2009). As they are incompressible and do not displace the loop's axis, torsional Alfvén waves cannot be detected directly by imagers (see e.g. De

Moortel and Nakariakov, 2012). Banerjee et al. (2009) and Jess et al. (2009) attributed observed non-thermal line broadening to unresolved simultaneous blue- and redshifts, which these authors interpreted as torsional Alfvén waves. Similarly, Srivastava et al. (2017) observed periodic Doppler velocities in fine structured flux tubes which they interpreted as a signature of torsional Alfvén waves.

1.4 Numerical codes

Solving the MHD equations usually requires numerical schemes. Only when simplifications are made, such as an ignorable coordinate, can the MHD equations be solved analytically (e.g. MHD equilibria or stability analysis, see e.g. Hood and Priest 1979; Hood 1992). In the context of modelling a phenomenon on the Sun, the MHD equations are usually solved numerically on a spatial domain (in 1D, 2D or 3D) where further assumptions and simplifications (e.g. which physics to be included) can be made. Although including additional physics generally makes models more realistic, a simple setup is often a useful way to investigate the effect or behaviour of a single physical process. Numerical simulations require appropriate initial conditions and boundary conditions and need to run for a sufficient amount of time to allow all relevant timescales to come into play.

Numerical schemes make use of a discrete grid, where derivatives are approximated e.g. using finite difference schemes and hence, the numerical resolution plays a role in the accuracy of the approximation (i.e. the derivatives are more accurate for higher resolution and smaller gridsizes). Due to the approximation of derivatives on a discrete grid, numerical dissipation is inherent to each numerical scheme, which can lead to non-physical dissipation and energy not being conserved. This can usually be improved by increasing the numerical resolution, but the numerical diffusion will always be non-zero. In this thesis we will use two MHD codes, the Lare code (Arber et al., 2001) and the MPI-AMRVAC code (Porth et al., 2014).

The Lare code (Arber et al., 2001) is a multidimensional code that solves the normalised MHD equations. Lare is a Lagrangian remap code, which means that each timestep has a Lagrangian step and a remap step. In the Lagrangian step, the normalised MHD equations in Lagrangian form are advanced in time and the numerical grid is advected by the plasma. In the remap step, the plasma quantities are then mapped back to their locations on the original grid. Lare makes use of a staggered

grid, where the plasma quantities are defined in different locations in a grid cell. This staggering improves the numerical stability of the code. In Chapter 2, we introduce the normalisation used in Lare and in Chapter 3, we discuss the normalised MHD equations in our model.

The MPI-AMRVAC code (Porth et al., 2014) is a multidimensional code that solves the MHD equations in conservative form. In Chapter 4, we discuss the MHD equations that we solve in our model.

1.5 Motivation, methods and aims

This thesis focuses on two aspects of MHD wave dynamics in the solar atmosphere. The first topic is the effect of chromospheric evaporation on the cross-field density gradient and the phase mixing process in coronal loops. Phase mixing of Alfvén waves has been studied intensively as a possible coronal heating mechanism (for an overview, see e.g. Parnell and De Moortel (2012) and Arregui (2015)). However, it has so far not been done in a full, non-ideal, multi-dimensional MHD model, where the effects of thermal conduction and optically thin radiation are taken into account. It has been argued that this thermodynamic feedback of the heating could substantially affect the transverse density gradient and even inhibit the phase mixing process (Cargill et al., 2016). Indeed, phase mixing typically heats the boundary layers of a coronal loop, since this is usually the location where the gradient in the Alfvén speed is present and the Alfvén waves phase mix. However, radiative losses are higher in the core of the loop, as they scale as the density squared, and since the dissipation of the phase-mixed Alfvén waves is predominantly in the boundary layers, the core is not heated which will lead to draining of mass. This draining could significantly alter the transverse density gradient, which is required for phase mixing (Cargill et al., 2016). Using the Lare2D code, we will perform 2D MHD simulations of phase mixing of Alfvén waves in a coronal loop, including optically thin radiation and thermal conduction. We will investigate the dissipation of phase-mixed Alfvén waves, and quantify the subsequent upflows and evaporation of mass from the lower atmosphere into the corona, in order to examine the effect of the evaporation on the transverse density profile and the phase mixing process in the coronal loop.

The second topic of this thesis is the generation of transverse MHD waves in coronal loops, by colliding counter-propagating plasma clumps/blobs. Observations have

shown that MHD waves predominantly originate in the lower layers of the solar atmosphere, resulting from the shuffling of the magnetic field by the photospheric footpoint motions (see e.g. Nakariakov and Verwichte 2005, Banerjee et al. 2007; Zaqarashvili and Erdélyi 2009; Matsumoto and Kitai 2010; Arregui et al. 2012; De Moortel and Nakariakov 2012; Mathioudakis et al. 2013; Arregui 2015; Jess et al. 2015; Krishna Prasad et al. 2015). However, it was shown recently that MHD waves can also be generated in-situ in the corona, by the collision of dense, counter-propagating coronal rain clumps (see e.g. Antolin et al., 2018). We will investigate the mechanism that generates transverse MHD waves in the solar corona, by colliding counter-propagating clumps. In a first study, we will investigate how the properties of the clumps affect the properties of the generated waves, by conducting a parameter study of 2D MHD simulations, using the MPI-AMRVAC code. In a second study, we will apply this model to coronal rain clumps, by basing the properties of the clumps on the extensive observational study of coronal rain by Antolin and Rouppe van der Voort (2012), in order to investigate the likelihood of collisions and oscillations.

1.6 Thesis outline

This thesis is structured as follows. The first two chapters investigate the effect of chromospheric evaporation on phase mixing of Alfvén waves in coronal loops. In Chapter 2, we introduce the 2D model for a coronal loop. In Chapter 3, we drive Alfvén waves into the system and investigate the dissipation of the phase-mixed Alfvén waves, the subsequent upflows and evaporation of mass from the lower atmosphere, and the effect of the evaporation on the transverse density profile and the phase mixing process.

Chapters 4 and 5 study the in-situ generation of transverse MHD waves in coronal loops by the collision of counter-propagating plasma clumps. In Chapter 4 we conduct an extensive theoretical parameter study to investigate the properties of the generated MHD waves, by varying the properties of the clumps. In Chapter 5 we apply the model to coronal rain clumps, by basing the properties of the clumps on a large study of coronal rain observations (Antolin and Rouppe van der Voort, 2012), and we investigate the likelihood of collisions and oscillations, and study the properties of the generated MHD waves.

In Chapter 6 we present the conclusions of this thesis and discuss possible routes for future work.

Chapter 2

Model setup

In this chapter we introduce our 2D model of a coronal loop. We start from the 1D field-aligned equations for a hydrostatic equilibrium (see e.g. Reale, 2010) of a coronal loop. These equations are solved using a fourth order Runge-Kutta (RK4) scheme. This results in a field-aligned (1D) equilibrium, which consists of a fully resolved atmosphere, including a model-chromosphere acting as a mass reservoir. Subsequently, a cross-field heating profile is imposed, leading to a central density enhancement which, after numerical relaxation, we consider to be our (2D) model coronal loop.

2.1 Introduction and motivation

When modelling the solar atmosphere, the numerical grid resolution is important in order to fully resolve the thermodynamical evolution of the plasma. Especially the narrow TR needs to be adequately resolved to accurately model the mass and energy exchange in coronal loops, see e.g. Bradshaw and Cargill (2013). These authors estimated that a grid resolution of less than 1 km (5 km) is required for a loop of length 60 Mm (180 Mm) to obtain correct physical results (coronal densities, heating and cooling cycles). However, such high resolution simulations are computationally demanding and might not be feasible in 2D or 3D.

A possible solution to decrease the computational costs is by implementing a non-uniform grid, with a finer resolution in the TR. The downside of this approach is that a non-uniform grid can cause reflections when studying wave experiments, and the TR can spatially move during heating/cooling events, which means the TR would not be resolved anymore.

Lionello et al. (2009); Mikić et al. (2013) introduced an alternative method to model the

TR by altering the optically thin radiation (OTR) and/or thermal conduction (TC) in order to artificially broaden the TR. Decreasing (increasing) the OTR (TC) for temperature ranges of the TR broadens the TR and makes it easier to numerically resolve it. Another method is to impose jump conditions across the TR (see e.g. Johnston et al., 2017a,b), which again overcomes the problem of requiring an extremely high resolution. In this chapter we will focus on broadening the TR by altering the OTR and TC, as we will drive high-frequency waves from the lower atmosphere into the corona. By broadening the TR, we have sufficient numerical resolution to resolve and model waves in the TR. Otherwise a lot of the wave energy would be lost due to the lack of resolution.

This chapter is structured as follows. In Sections 2.2 and 2.3 we discuss the 1D field-aligned, normalised MHD equations, and use a fourth order Runge-Kutta (RK4) scheme to set up a field-aligned hydrostatic equilibrium. We discuss the broadening approach for the TR proposed by Lionello et al. (2009) and Mikić et al. (2013), and the implementation of this approach in the RK4 scheme. We then extend the field-aligned (1D) hydrostatic equilibrium to a 2D model for a coronal loop, by imposing a cross-field background heating profile, and we discuss the relaxation in Lare2D (Arber et al., 2001). During the relaxation a density gradient in the cross-field direction is created (hence a gradient in the Alfvén speed), which is required for phase mixing of Alfvén waves. In Chapter 3 we drive Alfvén waves into the system and investigate the effect of the evaporation induced by the heating from the phase-mixed Alfvén waves.

2.2 Equations and normalisation

The field-aligned MHD equations (field-aligned coordinate y, time coordinate t) are given by (see e.g. Reale, 2010)

$$\frac{D\rho}{Dt} + \rho\frac{\partial v}{\partial y} = 0, \tag{2.1}$$

$$\rho\frac{Dv}{Dt} = -\frac{\partial P}{\partial y} - \rho g_{||} + \rho\nu\frac{4}{3}\frac{\partial^2 v}{\partial y^2}, \tag{2.2}$$

$$\rho\frac{D\epsilon}{Dt} = -P\frac{\partial v}{\partial y} - \frac{\partial F_c}{\partial y} + H_{bg} - n^2\Lambda(T) + \rho\nu\left(\frac{\partial v}{\partial y}\right)^2, \tag{2.3}$$

$$P = 2k_b nT. \tag{2.4}$$

In these equations, all the variables have the same meaning as in Chapter 1, section 1.2. The energy equation (equation (2.3)) has been written in terms of the specific

internal energy $\epsilon = \frac{P}{\rho(\gamma-1)}$, with $F_c = -\kappa_0 T^{5/2}\frac{\partial T}{\partial y}$ the notation for the conductive flux. The factor of $\frac{4}{3}$ in Equation (2.2) comes from the second term in Equation (1.8).

Gravity

The field aligned gravitational acceleration $g_{||}$ in Equation (2.2) is defined as

$$g_{||}(y) = g_{sun}\cos\left(\frac{\pi y}{y_{max}}\right), \quad y \in [0, y_{max}]. \tag{2.5}$$

Here, $g_{sun} = 274$ m/s^2. Remark that $g_{||}$ acts downwards in both loop legs, and switches sign at the loop apex ($y = y_{max}/2$). Figure 2.1 shows a plot of $g_{||}(y)$ with height for a loop of length $y_{max} = 120$ Mm.

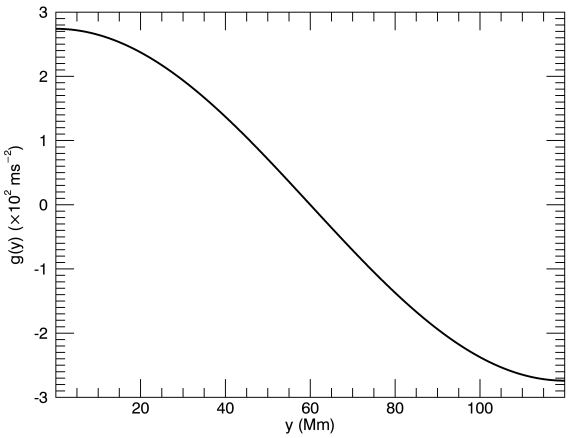

Figure 2.1: Plot of the gravitational acceleration $g_{||}(y)$ ($\times 10^2$ m/s^2), for $y \in [0, y_{max}]$.

Optically thin radiation

The optically thin radiation term in the energy equation (Equation (2.3)) is given by $n^2\Lambda(T)$, where $\Lambda(T)$ is a piecewise continuous function given by

$$\Lambda(T) = \chi T^{\alpha}.$$

Here, χ and α are constants depending on the temperature, see Table 2.1. Figure 2.2 shows a plot of $\Lambda(T)$ as a function of T. Remark that the $\Lambda(T)$ is larger for chromospheric and TR temperatures ($\sim 10^4 - 10^5$ K) than for coronal temperatures ($\sim 10^6$ K).

T (MK)	$\Lambda(T) = \chi T^{\alpha}$ (J$m^3 s^{-1}$)
$0.0100 < T \leq 0.0933$	$1.09 \times 10^{-44} T^{2}$
$0.0933 < T \leq 0.4677$	$8.87 \times 10^{-30} T^{-1}$
$0.4677 < T \leq 1.5136$	1.90×10^{-35}
$1.5136 < T \leq 3.5481$	$3.53 \times 10^{-26} T^{-3/2}$
$3.5481 < T \leq 7.9433$	$3.46 \times 10^{-38} T^{1/3}$
$7.9433 < T \leq 42.658$	$5.49 \times 10^{-29} T^{-1}$
$42.658 < T \leq 100.00$	$1.96 \times 10^{-40} T^{1/2}$

Table 2.1: Table with OTR constants χ and α, taken from Klimchuk et al. (2008).

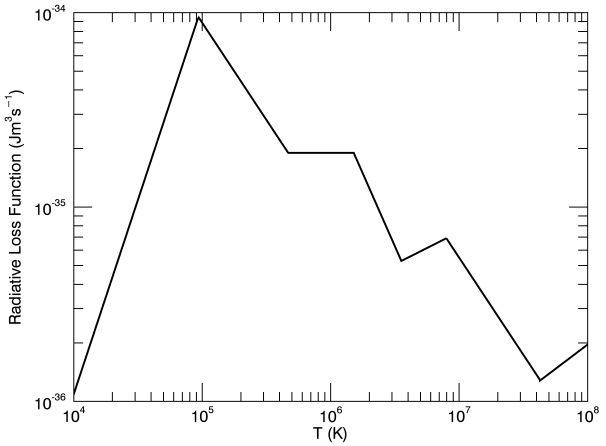

Figure 2.2: Plot of the optically thin radiative loss function $\Lambda(T) = \chi T^{\alpha}$.

2.2.1 Equilibrium and normalisation

To obtain an equilibrium we set the velocity v and time derivatives $\frac{D}{Dt}$ to zero in Equations (2.1) - (2.4). These equations then reduce to

$$\frac{dP}{dy} = -\rho g_{||} \tag{2.6}$$

$$\frac{dF_c}{dy} = n^2 \Lambda(T) - H_{bg} \tag{2.7}$$

$$P = 2 k_b n T. \tag{2.8}$$

In Equation (2.7) the conductive flux F_c has been redefined as $F_c = \kappa_0 T^{5/2} \frac{dT}{dy}$ (upward conductive flux), hence the terms on the RHS of Equation (2.7) have changed sign. We normalise these equations in the same way as the normalisation of the MHD equations in Lare. The Lare normalisation is obtained by normalising the magnetic field, density

and length:

$$\mathbf{B} = B_0\bar{\mathbf{B}}, \quad \rho = \rho_0\bar{\rho}, \quad L = L_0\bar{L},$$

We choose $B_0 = 10^{-3}$ T, $\rho_0 = 1.67 \times 10^{-12}$ kg/m^3 and $L_0 = 40$ Mm. All the other normalisation constants then follow from the choice of B_0, ρ_0 and L_0.

$$v_0 = \frac{B_0}{\sqrt{\mu_0\rho_0}}, \tag{2.9}$$

$$P_0 = \frac{B_0^2}{\mu_0}, \tag{2.10}$$

$$t_0 = \frac{L_0}{v_0}, \tag{2.11}$$

$$\epsilon_0 = v_0^2, \tag{2.12}$$

$$T_0 = \frac{\epsilon_0\bar{m}}{k_B}, \tag{2.13}$$

$$\mu_{m_0} = \bar{m}, \tag{2.14}$$

where $\bar{m} = 1.2m_p$. Normalising Equation (2.6) then gives

$$\frac{\partial\bar{P}}{\partial\bar{y}} = -\bar{\rho}\bar{g}_{||}, \tag{2.15}$$

where we used the fact that $g_0 = \frac{v_0^2}{L_0}$. Equation (2.7) is normalised as

$$\frac{\partial\bar{F}_c}{\partial\bar{y}} = C_1\bar{p}^2\bar{\chi}\bar{T}^{\alpha-2} - C_2\bar{H}_{bg}, \tag{2.16}$$

where

$$C_1 = \frac{L_0^2 p_0^2 \chi_0 T_0^{\alpha_0-2-7/2}}{4k_B^2\kappa_0},$$
$$C_2 = \frac{H_{bg,0}L_0^2}{\kappa_0 T_0^{7/2}} = \frac{\epsilon_0\rho_0 L_0^2}{t_0\kappa_0 T_0^{7/2}},$$
$$\bar{\chi} = \frac{\chi T_0^{\alpha}}{\chi_0 T_0^{\alpha_0}}.$$

Here, χ_0 and α_0 are the values in the RLF function corresponding to the normalising temperature T_0. Finally, the normalised ideal gas law is given by

$$\bar{P} = 2\bar{\rho}\bar{T}. \tag{2.17}$$

2.3 Numerical equilibrium using an ODE solver

2.3.1 Runge-Kutta scheme

The set of ordinary differential equations (ODEs) (2.15) - (2.17) can be solved using an ODE solver. We use a fourth order Runge-Kutta (RK4) scheme. The RK4 scheme (Press et al., 2007) to solve a differential equation $\frac{dy}{dx} = f(x, y)$ starts from the initial values x_0, y_0 and updates x_{n+1}, y_{n+1} at the $(n+1)$th step as

$$\begin{aligned}
k_1 &= hf\left(x_n, y_n\right), \\
k_2 &= hf\left(x_n + \frac{1}{2}h, y_n + \frac{1}{2}k_1\right), \\
k_3 &= hf\left(x_n + \frac{1}{2}h, y_n + \frac{1}{2}k_2\right), \\
k_4 &= hf\left(x_n + h, y_n + k_3\right), \\
y_{n+1} &= y_n + \frac{1}{6}\left(k_1 + 2k_2 + 2k_3 + k_4\right), \\
x_{n+1} &= x_n + h,
\end{aligned}$$

where h is the stepsize and the subscript n denotes the quantities at the nth step. In our case, we have to solve the following four (normalised) differential equations:

$$\frac{dP}{dy} = -p(y)\frac{g(y)}{2T(y)} = f_P, \tag{2.18}$$

$$\frac{dT}{dy} = \frac{F_c(y)}{T(y)^{5/2}} = f_T, \tag{2.19}$$

$$\frac{dF_c}{dy} = C_1 p(y)^2 \chi T(y)^{\alpha-2} - C_2 H_{bg} = f_F, \tag{2.20}$$

Equation (2.18) is obtained from substituting the ideal gas law (2.17) in Equation (2.15). Equation (2.19) is the definition of the conductive flux F_c, Equation (2.20) is the energy equation (2.16), where the background heating H_{bg} is constant along the field. Because we have three ODE's instead of one, the RK4 scheme extends to

$$\begin{aligned}
k_{1P} &= dy f_P\left(y, P_n, T_n\right), \\
k_{1T} &= dy f_T\left(y, F_n, T_n\right), \\
k_{1F} &= dy f_F\left(y, P_n, T_n\right), \\
k_{2P} &= dy f_P\left(y + \frac{1}{2}dy, P_n + \frac{1}{2}k_{1P}, T_n + \frac{1}{2}k_{1T}\right),
\end{aligned}$$

$$
\begin{aligned}
k_{2T} &= dy f_T \left(y + \frac{1}{2}dy, F_n + \frac{1}{2}k_{1F}, T_n + \frac{1}{2}k_{1T} \right), \\
k_{2F} &= dy f_F \left(y + \frac{1}{2}dy, P_n + \frac{1}{2}k_{1P}, T_n + \frac{1}{2}k_{1T} \right), \\
k_{3P} &= dy f_P \left(y + \frac{1}{2}dy, P_n + \frac{1}{2}k_{2P}, T_n + \frac{1}{2}k_{2T} \right), \\
k_{3T} &= dy f_T \left(y + \frac{1}{2}dy, F_n + \frac{1}{2}k_{2F}, T_n + \frac{1}{2}k_{2T} \right), \\
k_{3F} &= dy f_F \left(y + \frac{1}{2}dy, P_n + \frac{1}{2}k_{2P}, T_n + \frac{1}{2}k_{2T} \right), \\
k_{4P} &= dy f_P \left(y + dy, P_n + k_{3P}, T_n + k_{3T} \right), \\
k_{4T} &= dy f_T \left(y + dy, F_n + k_{3F}, T_n + k_{3T} \right), \\
k_{4F} &= dy f_F \left(y + dy, P_n + k_{3P}, T_n + k_{3T} \right),
\end{aligned}
$$

$$
\begin{aligned}
P_{n+1} &= P_n + \frac{1}{6}\left(k_{1P} + 2k_{2P} + 2k_{3P} + k_{4P} \right), \\
T_{n+1} &= T_n + \frac{1}{6}\left(k_{1T} + 2k_{2T} + 2k_{3T} + k_{4T} \right), \\
F_{n+1} &= F_n + \frac{1}{6}\left(k_{1F} + 2k_{2F} + 2k_{3F} + k_{4F} \right), \\
y_{n+1} &= y_n + dy,
\end{aligned}
$$

with dy the stepsize. The RK4 scheme runs in two times: (1) from the base of the transition region (y_0) to the loop apex (y_{max}) and (2) from the base of the transition region (y_0) to the base of the chromosphere ($y_{min} = 0$). To obtain a solution from one footpoint to the other footpoint, we mirror the solution for the other half of the loop about the loop apex. Because the scheme runs for the half loop, the gravity in Equation (2.18) is defined as

$$
g(y) = \frac{L_0 v_0^2}{g_{sun}} \cos\left(\frac{\pi y}{2 y_{max}} \right), \quad y \in [0, y_{max}],
$$

which is equivalent to Equation (2.5). We impose 4 initial conditions at the base of the TR ($y = y_0$).

$$
P = p_b, \tag{2.21}
$$

$$
T = T_b, \tag{2.22}
$$

$$
F_c = 0, \tag{2.23}
$$

$$
H_b = H_{guess}. \tag{2.24}
$$

A shooting method is performed on $H_b = H_{guess}$ such that the conductive flux F_c is zero at the loop apex ($F_c(y_{max}) = 0$). This works as follows: we pick two guesses $H_{guess,1}$ and $H_{guess,2}$ at $y = y_0$ for which F_c has a different sign at $y = y_{max}$. Then we know that the correct background heating H^* lies in the interval $[H_{guess,1}, H_{guess,2}]$. We then perform a bisection method that takes a new initial guess $H_{\text{mean}} = \frac{H_{guess,1}+H_{guess,2}}{2}$ for which the conductive flux F_c at the apex is closer to zero. We then repeat this procedure and eventually, this bisection method converges to a value for H_b such that $F_c \to 0$ at $y = y_{max}$.

The second iteration with the RK4 scheme to obtain the chromospheric solution is a 'backwards' RK4 scheme (from the base of the TR (y_0) to the base of the chromosphere (y_{min})). Hence, y is now updated as

$$y = y - dy.$$

In our model the chromosphere only acts as a mass reservoir and we assume that the chromosphere is isothermal and that the radiative losses are switched off. Therefore the only equation to solve is the hydrostatic equation (Equation (2.18)). The initial conditions at the base of the TR are the same as before to have a continuous solution at the base of the TR.

2.3.2 First test results

To test the RK4 solver we run the scheme with the following initial conditions representative of the base of the TR ($y = y_0$) (see e.g. Bradshaw and Mason, 2003):

$$T_b = 10^4 \text{ K}, \tag{2.25}$$

$$P_b = 2k_B n_b T_b, \text{ with } n_b = 10^{17} \text{ m}^{-3}. \tag{2.26}$$

$$F_c = 0. \tag{2.27}$$

The RK4 scheme outputs the temperature $T(y)$, the pressure $P(y)$ and the required background heating to maintain an equilibrium, $H_b = 1.43349 \times 10^{-5}$ Jm^{-3}s^{-1}.

Figure 2.3 shows the solutions of the temperature $T(y)$ and the density $\rho(y)$ for the half loop. The density decreases exponentially from the base of the chromosphere ($n \sim 10^{24}$ m^{-3}) to the base of the TR ($n \sim 10^{17}$ m^{-3}), where it steeply decreases with two orders of magnitude in the TR and is then fairly constant in the corona ($n \sim 10^{15}$ m^{-3}). The temperature is kept constant in the chromosphere ($T_{chrom} = 10^4$ K) and

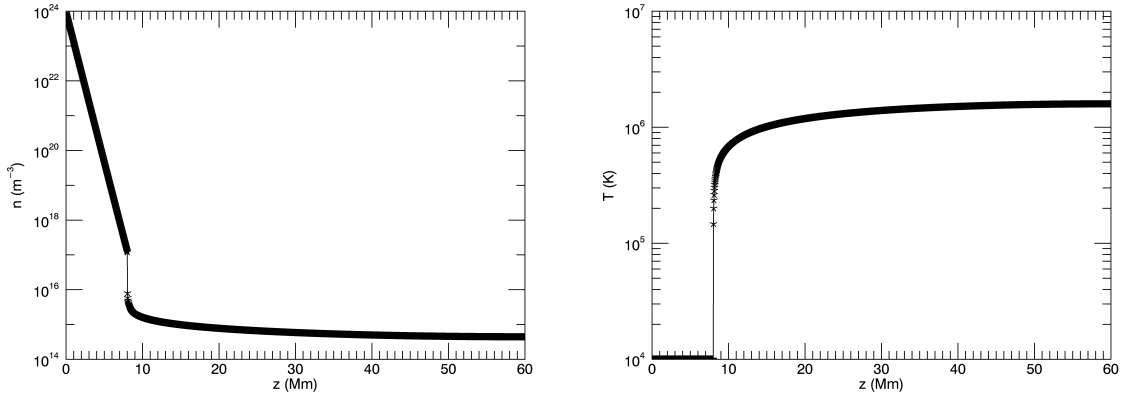

Figure 2.3: (Left) Number density n (m^{-3}) as a function of height (y) from the base of the chromosphere ($y = 0$) to the loop apex ($y = 60$ Mm). (Right) Similar plot for the temperature $T(y)$ (K). The resolution of each profile is 2048 gridpoints for the half loop, and each asterisk represents one gridpoint.

steeply increases in the TR ($T \sim 10^5$ K), up to 10^6 K in the corona. We can see that in both panels the TR is underresolved (especially in the lower TR), in the density range $n \sim 10^{16} - 10^{17}$ (m^{-3}) and temperature range $T \sim 10^4 - 10^5$ K.

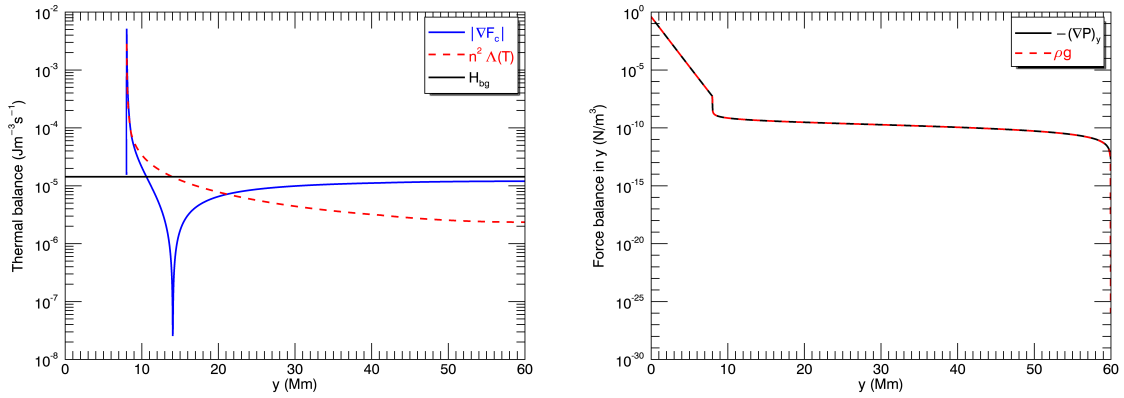

Figure 2.4: (Left) Plot of the thermal balance along the field. (Right) Plot of the field aligned force balance.

In Figure 2.4 we show the thermal balance $\frac{\partial F_c}{\partial y} = n^2\Lambda(T) - H_{bg}$ and force balance $\frac{\partial P}{\partial y} = -\rho g_{||}$ along the loop for these solutions. The plot of the thermal balance shows the absolute value of the thermal conduction $|\nabla \cdot \mathbf{F_c}| = |\frac{\partial \mathbf{F_c}}{\partial \mathbf{y}}|$ (blue), the optically thin radiation $n^2\Lambda(T)$ (red dashed line) and the background heating $H_{bg} = 1.43349 \times 10^{-5}$ Jm^{-3}s^{-1} (horizontal black line). In the corona the optically thin radiation ($\sim n^2$) is about an order of magnitude smaller than the thermal conduction, and therefore

thermal balance is predominantly between the background heating and thermal conduction. We define the location where thermal conduction changes sign ($\sim y = 14$ Mm) to be the top of the TR. At this location $\nabla \cdot \mathbf{F_c}$ goes from a loss in the corona to a gain in the TR. In the TR the optically thin radiation increases, and near the top of the TR, thermal balance is predominantly between the OTR and the background heating, whereas near the bottom of the TR, it is mainly between OTR and TC.

The right panel of Figure 2.4 shows the force balance $-\frac{\partial P}{\partial y} = \rho g_{||}$ along y, with the pressure gradient force $-\frac{\partial P}{\partial y}$ (black) and the gravitational force $\rho g_{||}$ (red dashed line). We can see that force balance is well maintained along the field.

2.3.3 Resolution in the TR

In this subsection we discuss a possible solution to resolve the TR. We define

$$L_T(y) = T(y) / \left| \frac{\partial T}{\partial y} \right|$$

the temperature length scale (m) as a function of y. Figure 2.5 shows a plot of L_T for the half loop in Figure 2.3.

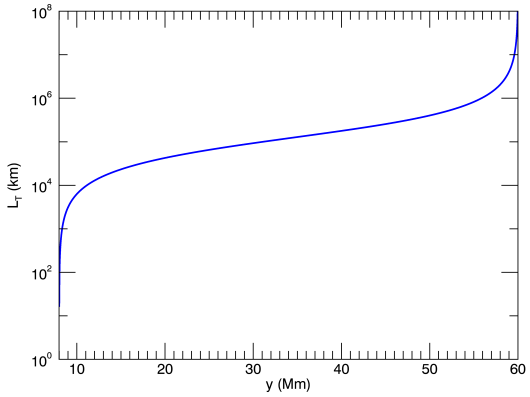

Figure 2.5: (Left) Plot of the temperature lengthscale from the base of the TR ($y = 8$ Mm) to the apex of the loop ($y = 60$ Mm).

We can see that L_T is small in the TR ($\min(L_T) = 16.8$ km near the base of the TR) because of the large temperature gradient $\frac{\partial T}{\partial y}$. This means that we would need a numerical grid resolution of at most 16.8 km to resolve the TR. The temperature lengthscale increases in the corona and is of the order of 10^8 km near the apex of the loop (because of the small $\frac{\partial T}{\partial y}$). We have the following relationship for L_T in terms of

the thermal conduction and optically thin radiation:

$$L_T \sim \sqrt{\frac{\kappa_{||}(T)T}{n^2\Lambda(T)}}. \tag{2.28}$$

This relationship can be derived from the energy equation (Equation (2.16)), by performing a dimensional analysis and assuming that the energy balance is between thermal conduction and optically thin radiation:

$$\begin{aligned} \frac{\partial}{\partial y}\left(\kappa_{||}(T)\frac{\partial T}{\partial y}\right) &\sim n^2\Lambda(T), \\ \implies \frac{1}{L_T}\left(\kappa_0\frac{T^{7/2}}{L_T}\right) &\sim n^2\Lambda(T), \\ \iff \frac{1}{L_T^2} &\sim \frac{n^2\Lambda(T)}{\kappa_0 T^{7/2}}, \\ \iff L_T &\sim \sqrt{\frac{\kappa_0 T^{7/2}}{n^2\Lambda(T)}}. \end{aligned}$$

The radiation function $\Lambda(T)$ is larger for the temperature range in the TR than the corona (i.e. $10^4 < T < 10^5$ K, see Figure 2.2). Moreover n^2 is about four orders of magnitude larger for the TR than the corona, and the temperature T is two orders of magnitude smaller in the TR than in the corona, so L_T is a lot smaller in the TR than in the corona. This results in a larger temperature gradient $\frac{\partial T}{\partial y}$ in the TR than in the corona. From Equation (2.28) we see that if we want to broaden the TR (i.e increasing L_T), we can increase the thermal conduction and decrease the optically thin radiation (below a cutoff temperature T_c) as suggested by Lionello et al. (2009) and Mikić et al. (2013).

2.4 Broadening the TR

In this section we present the method to broaden the TR introduced by Lionello et al. (2009) and Mikić et al. (2013). These authors define a cut off temperature T_c below which $\kappa_{||}(T)$ increases and $\Lambda(T)$ decreases as

$$\kappa_{||}(T) = \begin{cases} \kappa_0 T^{5/2} & T \geq T_c \\ \kappa_0 T_c^{5/2} & T < T_c. \end{cases} \tag{2.29}$$

$$\Lambda(T) = \begin{cases} \Lambda(T) & T \geq T_c \\ \Lambda(T) \left(\frac{T}{T_c}\right)^{5/2} & T < T_c. \end{cases} \tag{2.30}$$

If $T < T_c$, the parallel thermal conductivity $\kappa_{||}(T)$ is replaced by $\kappa_{||}(T_c)$ and $\Lambda(T)$ is decreased with a factor $\left(\frac{T}{T_c}\right)^{5/2}$. This ensures that L_T increases by a factor of $\left(\frac{T_c}{T}\right)^{5/2}$ when $T < T_c$ (Equation (2.28)), hence broadening the TR. The modification to the thermal conduction and optically thin radiation is defined in such a way to preserve $\kappa_{||}(T)\Lambda(T)$. It was shown in Lionello et al. (2009) and Mikić et al. (2013) that this broadening technique does not change the coronal density and temperature profiles, because of the preservation of $\kappa_{||}(T)\Lambda(T)$, and that it also preserves the energetics of the TR (e.g. evaporation and draining). This was also pointed out in Johnston et al. (2020). In the latter paper, the authors demonstrated that the conditions enforced on the parallel thermal conductivity and radiative loss rate conserve the total amount of energy that is delivered to the chromosphere, and that, while there can be small differences with the flows in the modified region (where $T < T_c$), the mass flux out of the modified region is preserved. Hence this modification does not have an impact on the evaporative upflows into the corona.

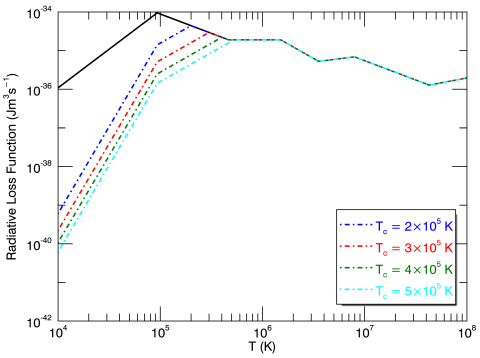

Figure 2.6: Plot of $\Lambda(T)$ for different values of T_c (coloured dotted-dashed lines), the unmodified radiation (solid line, see Klimchuk et al. (2008)).

Figure 2.6 shows a plot of $\Lambda(T) = \chi T^{\alpha}$ for different cut off temperatures T_c (coloured dotted-dashed lines) and the unmodified radiation (solid line). We can see that in some cases $\Lambda(T)$ can decrease up to four orders of magnitude when $T < T_c$, compared to the normal radiation (see e.g. Klimchuk et al., 2008).

2.4.1 Partial implementation of the Mikić approach in the RK4 solver

The Mikić approach broadens the TR beyond its original extent and hence the location of the base of the TR changes. Because the Runge-Kutta scheme fixes the length over which it iterates, it cannot adjust the base of the TR and it will not converge to the correct solution when the full Mikić approach is included. Indeed, because the RK4 scheme cannot adjust the length over which it iterates, the calculated background heating rate will be smaller and the coronal density and temperature solutions will be lower as well.

We prefer however to obtain a coronal profile for the density and the temperature that already has some broadening of the TR as initial conditions for the Lare2D code, because the relaxation time in Lare2D will be shorter. We therefore only implement the modification to the radiation (see Equation (2.30)) in the RK4 scheme. Hence, the output of the RK4 scheme will only be an approximate equilibrium, which is followed by a further relaxation in Lare2D, in which the full Mikić approach has been implemented. During this relaxation we also impose a transverse background heating function, to create the transverse density gradient. This process sets up an atmosphere in approximate hydrostatic equilibrium with a broadened TR, in which we can drive waves.

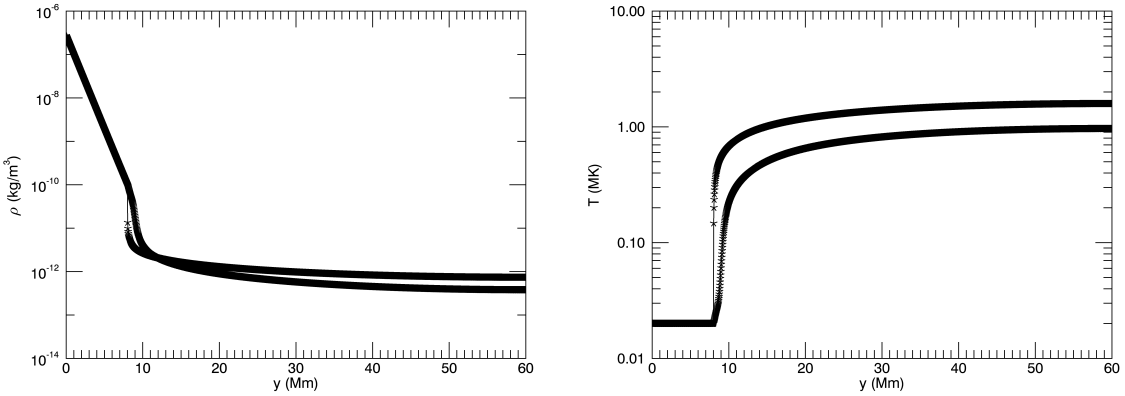

Figure 2.7: Plot of the density ρ (kg/m^3) (left) and temperature T (MK) (right) from the base of the chromosphere to the apex ($0 < y < 60$ Mm), with and without the Mikić radiation. The symbols represent the gridpoint resolution.

Figure 2.7 shows the density and the temperature solution of the RK4 scheme with and without the Mikić radiation. The initial conditions at the base of the TR in the

RK4 scheme are

$$T_b = 2 \times 10^4 K, \tag{2.31}$$

$$P_b = 2k_B n_b T_b, \text{ with } n_b = 5 \times 10^{16} \text{ m}^{-3}, \tag{2.32}$$

$$F_c = 0. \tag{2.33}$$

These conditions give a loop apex temperature of 1 MK when the Mikić radiation is included. We can see that the TR already shows some broadening compared to the solution with the unmodified radiation. We remark that the coronal density in the solution with the Mikić radiation is lower, because the background heating calculated by the RK4 scheme is lower.

2.5 Extending the setup to 2D hot loop

In this section we modify the field-aligned approximate equilibrium to a 2D hot loop model with a cross-field gradient in the density, and hence also in the Alfvén speed. This is achieved by imposing a transverse profile (in x) in the background heating function of the form

$$H_{bg}(x) = \frac{H_1 + H_2}{2} + \frac{H_2 - H_1}{2} \tanh(a(-|x| + 1)). \tag{2.34}$$

Here, $-2 < x < 2$ Mm, $H_1 = 3.24 \times 10^{-6}$ Jm^{-3}s^{-1} is the background heating calculated by the RK4 solver for the initial conditions (2.31) - (2.33) with the Mikić radiation, $H_2 = 4H_1$, and $a = 5$ Mm^{-1} is a parameter which determines the steepness of the tanh-profile.

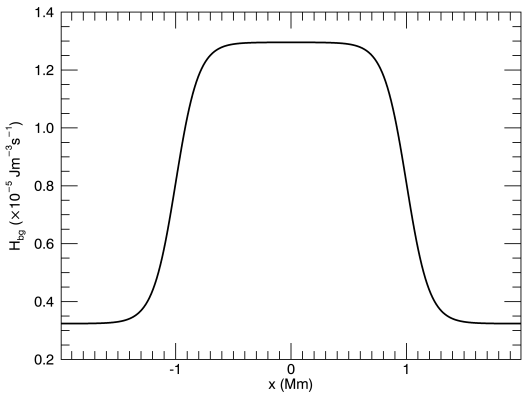

Figure 2.8: Plot of the background heating $H_{bg}(x)$.

Figure 2.8 shows a plot of $H_{bg}(x)$. The background heating H_{bg} is maximal for $-0.5 < x < 0.5$ Mm (H_2) and minimal for $|x| > 1.3$ Mm (H_1). In between these regions the background heating varies smoothly. The aforementioned regions will respectively be refered to as the interior of the loop, the exterior and the boundary shells. We remark that along each fieldline the background heating is constant. The relation between the imposed background heating and the resulting apex density can be estimated from the RTV scaling laws (Rosner et al., 1978), which describe the relation between fundamental parameters at the loop apex of a coronal loop in hydrostatic equilibrium:

$$T = c_T (pL)^{1/3}, \tag{2.35}$$

$$H = c_H p^{7/6} L^{-5/6}. \tag{2.36}$$

Here, $c_T = 1.4$ and $c_H = 3$ are constants, T and p are the loop apex temperature and pressure, L is the length of the loop and H the heating rate per unit volume (Reale, 2010, p. 30). From these equations we can estimate how the density $\rho_{new,apex}$ and the pressure $P_{new,apex}$ at the apex would change when imposing H_2 as a background heating. From Eqn. (2.36) we know that (for a constant loop length)

$$H_1 \sim P_{old,apex}^{7/6}/L^{5/6} \Leftrightarrow 4H_1 \sim \left(4^{6/7} P_{old,apex}\right)^{7/6}/L^{5/6} \Leftrightarrow H_2 \sim P_{new,apex}^{7/6}/L^{5/6},$$

hence the pressure at the apex is expected to increase with a factor of $4^{6/7} \approx 3.3$. From Eqn. (2.35) we then have

$$T_{new,apex} \sim (P_{new,apex} L)^{1/3} = \left(4^{6/7} P_{old,apex} L\right)^{1/3} \sim 4^{2/7} T_{old,apex},$$

so the apex temperature is expected to increase by a factor of $4^{2/7} \approx 1.5$. From the ideal gas law, we know that

$$\rho_{new,apex} \sim \frac{P_{new,apex}}{T_{new,apex}} \sim \frac{4^{6/7} P_{old,apex}}{4^{2/7} T_{old,apex}} \sim 4^{4/7} \rho_{old,apex},$$

so the density at the apex is expected to increase with a factor of $4^{4/7} \approx 2.2$. The scaling laws used in the calculations above are based on the assumption that H_1 is the background heating rate to maintain an equilibrium. However, because of the partial implementation of the Mikić approach in the RK4 solver (section 2.4.1), H_1 is a smaller background heating for an approximate equilibrium, and we expect the real increase to be lower than the estimated increase.

Numerical relaxation

The numerical relaxation performed in Lare2D allows the atmosphere to adjust both to the full Mikić approach (including the modifications to both the optically thin radiation and the thermal conduction below T_c) and to the imposed transverse heating profile. The relaxation is performed with viscosity and resistivity set to zero, but with the shock viscosities switched on, to allow the forces to fully equilibrate. We stop the relaxation once the field-aligned velocities are significantly less than the local Alfvén speed and sound speed (less than 0.1%) and the forces are in equilibrium.

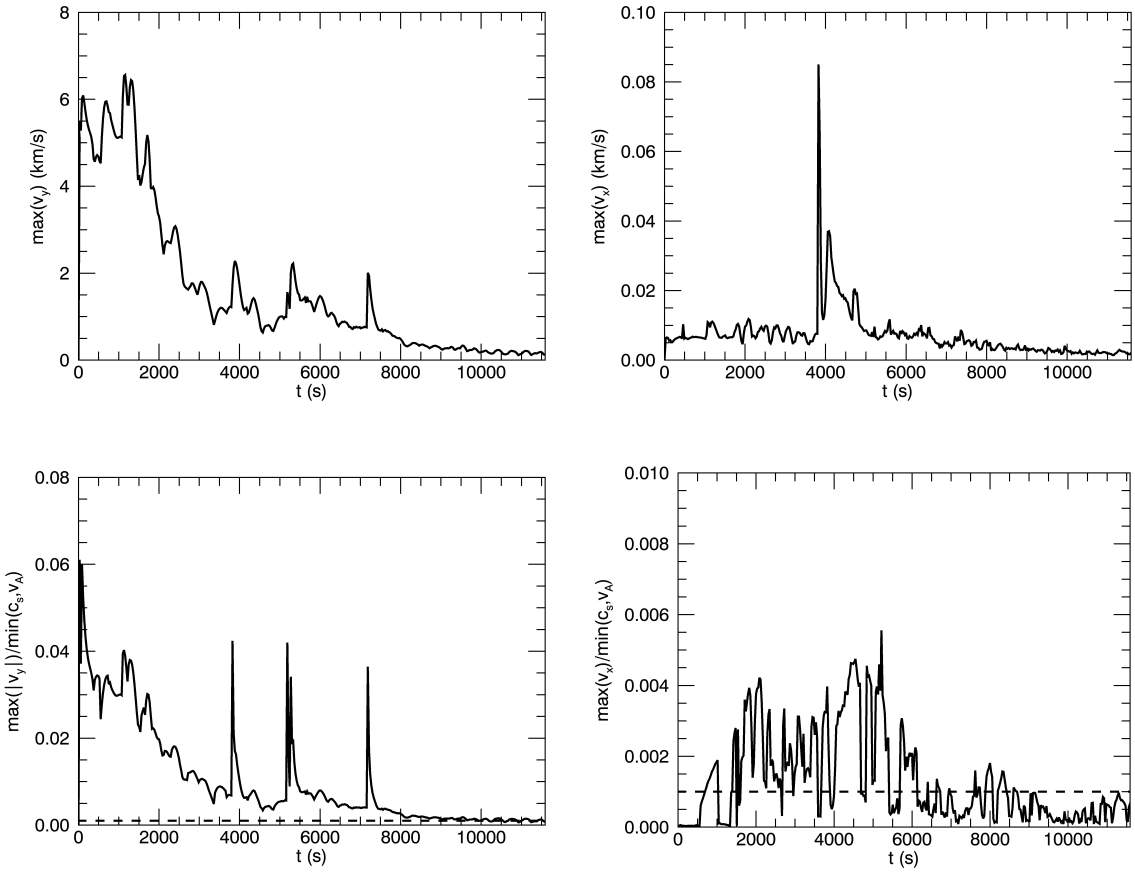

Figure 2.9: (Top) Plots of $\max(v_y)$ (km/s) and $\max(v_x)$ (km/s) in the domain with time. (Bottom) Plots of $\max(v_y)/\min(v_A, c_s)$ and $\max(v_x)/\min(v_A, c_s)$ in the domain with time. The dashed lines are at 0.1%.

Figure 2.9 shows plots of the maximal velocities in the domain with time, during the relaxation ($t \sim 11000$s). The maximal field-aligned velocity, $\max(v_y)$ (top left panel), is of the order of 5 km/s in the first 2000s of the simulation, but decreases to less than 1km/s after approximately 4000s. This is on average less than 1% than the local Alfvén speed v_A and sound speed c_s, as shown by the plot of the (relative) maximal

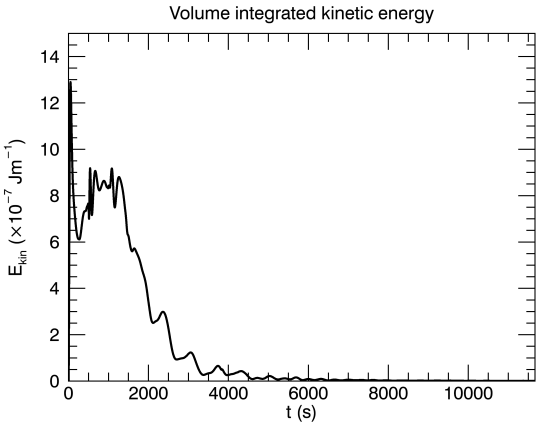

Figure 2.10: Plot of the volume integrated kinetic energy in the domain with time.

field-aligned velocity (bottom left panel). The maximal transverse velocity, $\max(v_x)$ (top right panel in Figure 2.9), is always less than 0.1 km/s, which is significantly less than the local Alfvén speed and sound speed in the domain (bottom right panel of Figure 2.9). This means that the transverse adjustment of the loop is minimal during the relaxation. Near the end of the relaxation, the maximal field-aligned and transverse velocities are less than 0.1% of the local Alfvén speed and sound speed, as shown by the dashed lines in the bottom panels of Figure 2.9. Figure 2.10 shows the evolution of the volume integrated kinetic energy in the domain, confirming a significant decrease in the kinetic energy during the relaxation.

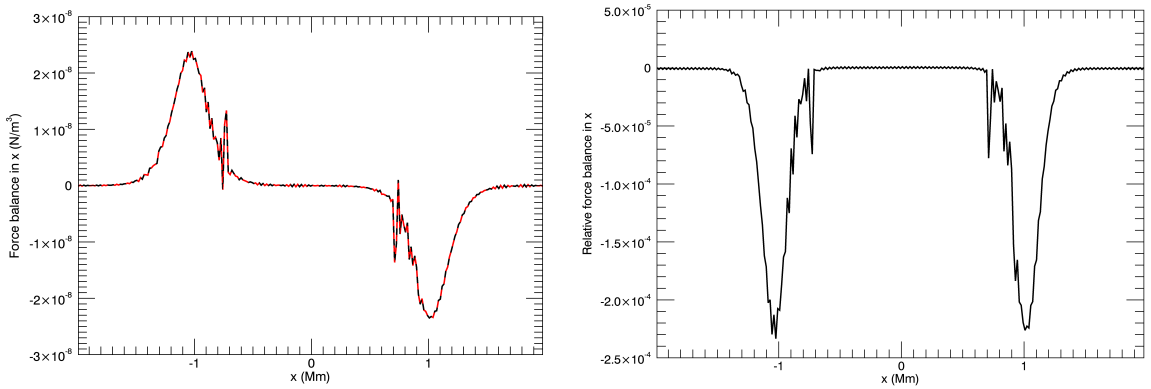

Figure 2.11: Plot of the horizontal force balance $\frac{dp}{dx} = (\mathbf{j} \times \mathbf{B})_x$ (left panel) and relative force balance $(\frac{dp}{dx} - (j \times \mathbf{B})_x)/\max(\frac{dp}{dx})$ (right panel) in x at the loop apex ($y = 60$ Mm). The solid black line in the left panel is $\frac{dp}{dx}$ and the red dashed line is $(\mathbf{j} \times \mathbf{B})_x$.

Figures 2.11 and 2.12 show the force balance in the x direction at the apex ($y = 60$ Mm) and in the y direction in the middle of the domain ($x = 0$ Mm) respectively, after relaxation ($t \sim 11000$s). In the x direction $(\nabla P)_x$ and $(\mathbf{j} \times \mathbf{B})_x$ equilibrate better than

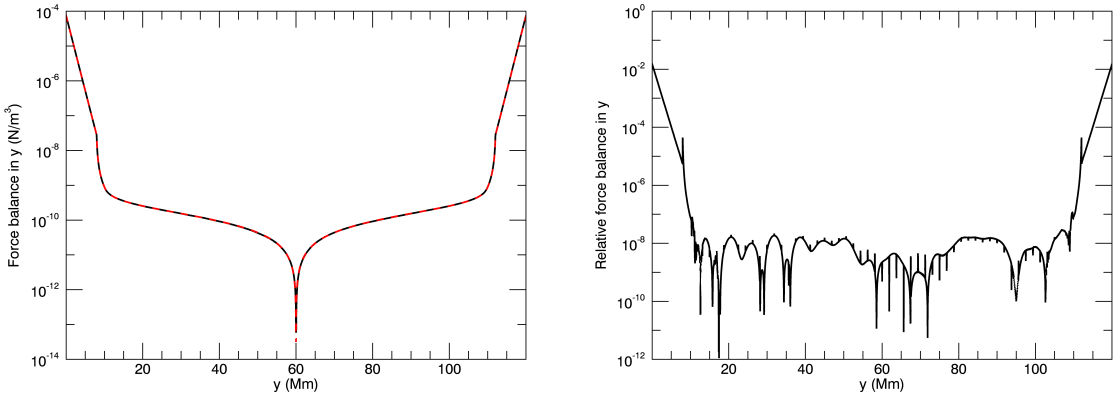

Figure 2.12: Plot of the vertical force balance $\frac{dp}{dy} = -\rho g$ (left panel) and relative force balance $(\frac{dp}{dy} + \rho g)/\max(\frac{dp}{dy})$ (right panel) as a function of y in the middle of the loop ($x = 0$ Mm). The solid black line in the left panel is $\left|\frac{dp}{dy}\right|$ and the red dashed line is $|-\rho g|$.

0.1%, as shown by the relative plot of the force balance in the right panel of Figure 2.11. In the y direction the $(\nabla P)_y$ and $-\rho g$ equilibrate better than 1% on the line $x = 0$ Mm after relaxation (right panel of Figure 2.12). In both cases the forces equilibriate better than 1%, which shows that an approximate force equilibrium is attained on these two lines. This analysis shows that the loop is approximately in equilibrium at the end of the relaxation. We remark however that there are still field-aligned flows present in the domain (as can be seen from e.g. Figure 2.9), which we will need to take into account when analysing the driven system in Chapter 3.

Temperature and density evolution

During the relaxation, the plasma adjusts to the imposed background heating profile and to the (full) Mikić approach in the modified region ($T < T_c$). Figure 2.13 shows the final temperature and the density in the core of the loop ($x = 0$ Mm, green lines) and the shell region ($x = -1$ Mm, blue lines), together with the initial temperature and density (black lines). The temperature increases in both the middle of the domain and the shell region as a result of the increased background heating. The vertical dashed line at $T = 5 \times 10^5$ K is the cut-off temperature below which the Mikić approach is implemented and the TR is broadened. The right panel of Figure 2.13 shows a similar plot for the density. We can see that the density increases in the core and the shell region of the loop.

Figure 2.14 shows the evolution of the temperature and the density at the apex

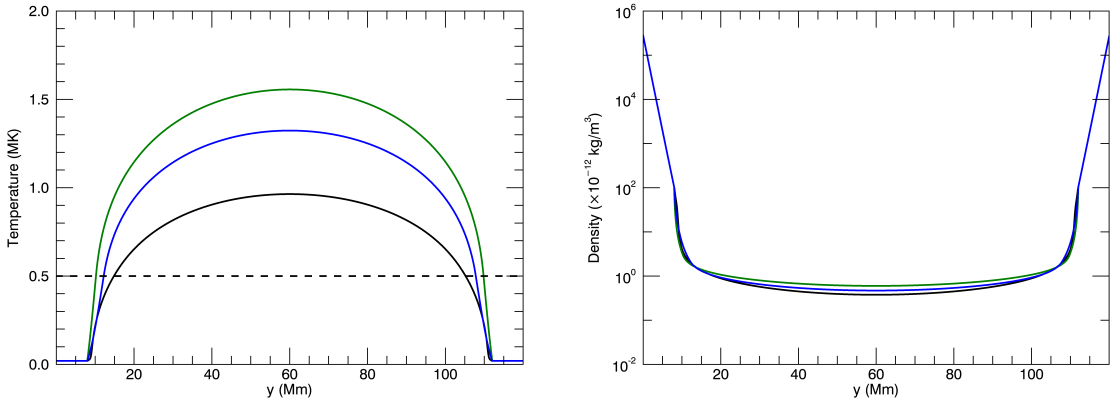

Figure 2.13: (Left) Plot of the temperature before relaxation (black) and after relaxation ($t = 11590$s), at $x = 0$ Mm (green) and $x = -1$ Mm (blue). (Right) Similar plot for the density.

during the relaxation, in the middle of the loop ($x = 0$ Mm) and in the shell region ($x = -1$ Mm). The black horizontal line on each plot is the average taken over the last 2000s. Compared to the initial 1D equilibrium, the temperature and the density at the apex increase in the shell region (37% and 25%, respectively) and in the core of the loop (61% and 59%, respectively). This increase is lower than the estimated increase from the scaling laws, because of the smaller background heating H_1 as mentioned earlier. We can see that on top of the increase in the temperature and the density, there are small oscillations with a period of $\sim 500 - 600$s (related to slow waves during the relaxation). Near the end of the relaxation the amplitudes of these oscillations decrease as the system further relaxes and slow waves are damped by thermal conduction (see e.g. De Moortel and Hood, 2003). In Chapter 3 we provide more details on the 2D equilibrium.

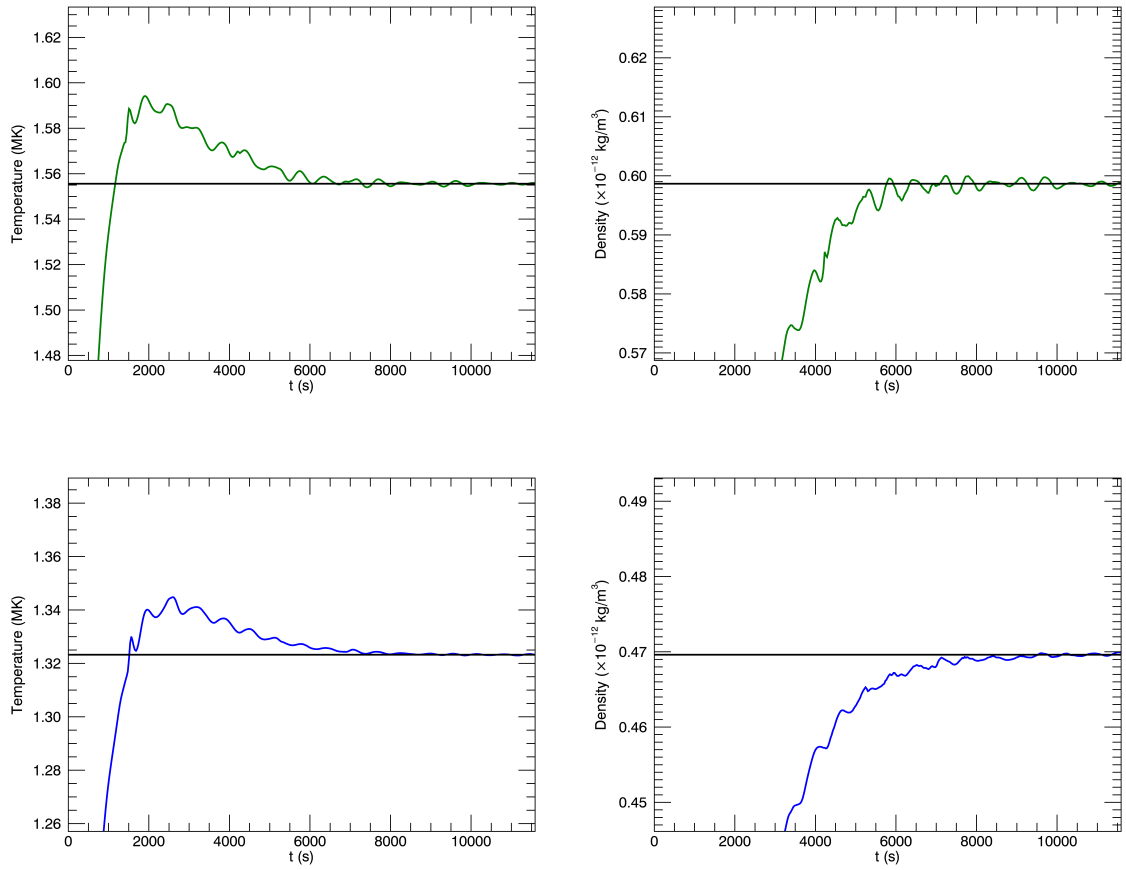

Figure 2.14: (Top) Plots of the evolution of the apex temperature (left) and density (right) during the relaxation, in the middle of the loop ($x = 0$ Mm). The horizontal black line on each plot represents the average value over the last 2000s. (Bottom) Similar plots for the shell region ($x = -1$ Mm).

2.6 Conclusions

In this chapter we introduced the model setup for the driven simulations in Chapter 3. We constructed a 1D field-aligned hydrostatic equilibrium for a coronal strand using a fourth order Runge-Kutta scheme and a broadening approach for the TR. We then extended the field-aligned model to 2D by imposing a transverse background heating profile.

Chapter 3

Chromospheric evaporation due to phase mixing of Alfvén waves

In this chapter we present 2.5D numerical simulations of phase mixing of Alfvén waves in a coronal loop. We introduce a full atmospheric model for a coronal loop, including gravitational stratification, optically thin radiation, thermal conduction and a background heating. We aim to quantify the heating from the dissipation of the phase-mixed Alfvén waves and study the effect of the subsequent evaporation from the lower atmosphere into the corona on the transverse density profile. The results of this chapter have been published in Van Damme et al. (2020).

3.1 Introduction

Phase mixing of Alfvén waves (Heyvaerts and Priest, 1983) is the process where Alfvén waves on neighbouring magnetic field lines propagate at different speeds due to a cross-field gradient in the Alfvén speed. Over time these waves become out of phase and large transverse gradients ("small scales") in the velocity and the magnetic field perturbations are generated, which can lead to an enhanced (Ohmic and/or viscous) dissipation (heating). Hence, since its discovery it has been intensively studied in the literature as a possible coronal heating mechanism (for a review, see e.g. Parnell and De Moortel 2012; Arregui 2015). We mention a few papers that highlight the difficulties related to phase mixing of Alfvén waves as a coronal heating mechanism. Pagano and De Moortel (2017) studied the contribution of phase-mixed, footpoint driven, propagating Alfvén waves in a coronal loop to coronal heating. These authors found that the heating from phase mixing can be sufficient to balance coronal losses only when using extreme physical parameters (e.g. large dissipative coefficients, high-frequency waves,

large physical amplitudes). Pagano et al. (2019) modify the model from Pagano and De Moortel (2017), by imposing a footpoint driver based on the power spectrum of transverse oscillations in the corona (see e.g. Morton et al., 2016). They find that the heating by phase mixing of Alfvén waves is not sufficient to counteract the coronal losses, but conclude that transverse waves could still play a role in coronal heating as they enhance the process of developing small scales.

Numerical simulations of phase mixing of Alfvén waves often assume a cross-field density gradient, providing the gradient in the Alfvén speed. However, the effect of the subsequent evaporation, following a heating event in the corona, on the local density structure - and hence the phase mixing process - is usually not taken into account. Ofman et al. (1998) studied this feedback mechanism for resonant absorption and found that, using thermodynamic equilibrium scaling laws, the evaporation caused the heating layers to drift (although it was later shown by Cargill et al. (2016) that this result from the scaling laws is likely overestimated). For the process of phase mixing, Cargill et al. (2016) calculated that, even in the case of sufficient wave heating by phase mixing, it cannot sustain the required density gradient, because it would lead to draining of the coronal loop due to optically thin radiation and thermal conduction acting on much faster timescales than the heating by phase mixing of Alfvén waves. Indeed, because the heating due to phase mixing of Alfvén waves is located in the shell regions of the loop, the core of the loop is not heated and the radiation (which scales with the density squared) cools the core of the loop, which can lead to draining and hence reducing (or even eliminating) the initially assumed density gradient. Hence, the assumption of a cross-field density gradient in coronal loop models cannot be self-consistently maintained by phase mixing.

In this chapter, we present 2.5D numerical simulations of phase mixing of Alfvén waves in a coronal loop and study the effect of chromospheric evaporation on the density gradient following heating from the dissipation of phase-mixed Alfvén waves. This chapter is structured as follows. In Section 3.2 we introduce the model setup for the numerical simulations. We present a full atmospheric model for a coronal loop and (after numerical relaxation) drive propagating Alfvén waves into the system. In Section 3.3 we discuss the results of the simulations, in particular we aim to quantify the dissipation from the phase-mixed Alfvén waves and the effect of the evaporation on the local coronal density. In Section 3.4 we end the chapter with a discussion and a conclusion.

3.2 Model setup

We use the numerical code Lare2D (Arber et al., 2001) to solve the following (normalised) MHD equations:

$$\frac{\partial \rho}{\partial t} = -\nabla \cdot (\rho \mathbf{v}), \tag{3.1}$$

$$\rho \frac{D\mathbf{v}}{Dt} = -\nabla P + \rho \mathbf{g} + \mathbf{j} \times \mathbf{B} + \rho \nu \left(\nabla^2 \mathbf{v}\right), \tag{3.2}$$

$$\rho \frac{D\epsilon}{Dt} = -P \nabla \cdot \mathbf{v} - \nabla \cdot \mathbf{F_c} - \rho^2 \Lambda(T) + H_{bg}(x) + \frac{j^2}{\sigma} + Q_{visc}, \tag{3.3}$$

$$P = 2\rho T, \tag{3.4}$$

$$\frac{\partial \mathbf{B}}{\partial t} = \nabla \times (\mathbf{v} \times \mathbf{B}) - \nabla \times (\eta \nabla \times \mathbf{B}) \tag{3.5}$$

$$\mathbf{j} = \nabla \times \mathbf{B}. \tag{3.6}$$

Here, all the variables have the same meaning as in Chapter 1, Section 1.2. The field-aligned gravitational acceleration $\mathbf{g} = -g_{||}\hat{\mathbf{y}}$ in equation (3.2), and the optically thin radiation $\rho^2\Lambda(T)$ and the background heating function $H_{bg}(x)$ in equation (3.3) are as in Chapter 2.

The numerical domain is 4 Mm $\times$ 120 Mm and consists of 256 gridpoints in x (cross-field direction) and 4096 gridpoints in y (field-aligned direction). The boundary conditions are periodic in x and zero gradient in y with the velocity set to zero. The plasma is considered to be fully ionised everywhere in the numerical domain. We remark that this is unrealistic for the chromosphere, however in our model the chromosphere only acts as a mass reservoir. We also do not take into account the thermodynamic evolution of the chromosphere, by imposing a cut-off temperature of $T_{chrom} = 2 \times 10^4$ K, below which the radiative losses are switched off. In order to fully resolve the TR, we use the same approach as in Lionello et al. (2009) and Mikić et al. (2013), with a cut-off temperature of $T_c = 5 \times 10^5$ K. The details of this approach have been described in Section 2.4.

To determine if the TR is resolved, we compare the temperature length scale $L_T = \frac{T}{\partial T/\partial y}$ with the field-aligned grid resolution dy. Figure 3.1 shows a logarithmic plot of the initial (after relaxation) temperature T (MK) at $x = 0$ Mm (left panel) and the temperature length scale L_T (km) (right panel) in the first transition region ($y = 8 - 13$ Mm), with (blue) and without (red) the full Mikić approach. The profile of the temperature without the Mikić approach is the initial condition obtained from the RK4

scheme, see Chapter 2, Figure 2.7. The profile with the full Mikić approach is obtained after relaxation in Lare2D in the middle of the loop (at $x = 0$ Mm). The dashed horizontal line represents the field-aligned grid resolution ($dy = 29.3$ km). We can see that without the Mikić approach the temperature is underresolved in the lower TR, with $\min(L_T) \approx 19$ km in this region, which is smaller than the field-aligned grid resolution. The Mikić approach clearly broadens the lower TR, and increases the minimal L_T upto $\min(L_T) = 125$ km.

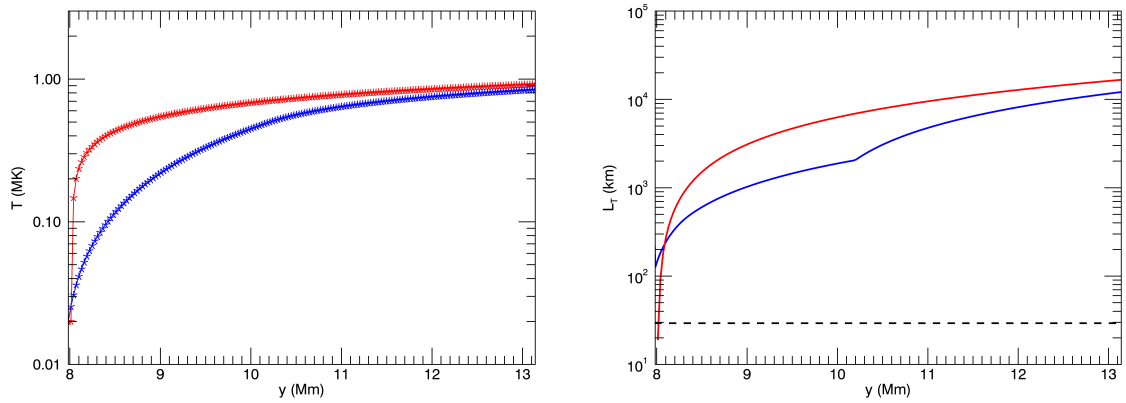

Figure 3.1: (Left) Logarithmic plot of the initial temperature T (MK) in the first TR ($y = 8 - 13$ Mm) in the middle of the loop ($x = 0$ Mm), with (blue) and without (red) the Mikić approach. The symbols represent the field-aligned grid resolution. (Right) Similar logarithmic plot of the temperature lengthscale L_T (km), with the dashed line representing the field-aligned grid resolution ($dy = 29.3$ km).

Figure 3.2 shows contour plots of the temperature, the density and the plasma beta which are obtained after the numerical relaxation discussed in Chapter 2. In the coronal part of the loop, there is a clear cross-field gradient in the temperature and the density. The coronal temperature ranges between $1.0 - 1.6$ MK and the coronal density varies between $\rho = 2.5 - 6 \times 10^{-13}$ kg/m^3, with a density ratio of $\rho_i/\rho_e = 2.4$ at the apex. A plot of the cross-field density and temperature at the apex can be found in Figure 3.3. This density ratio provides a gradient in the Alfvén speed, which is required for phase mixing. The black lines overplotted on these contour plots are the (initial) locations of the chromosphere-TR and TR-corona boundaries. The top of the TR is defined as the location where thermal conduction $\nabla \cdot F_c$ changes sign (i.e. from a loss in the corona to a gain in the TR). The chromospheric boundary is defined as the location where the temperature has decreased to $T = 2 \times 10^4$ K. The locations of these boundaries are determined in the initial setup and are then assumed fixed in all subsequent calculations. For the particular setup studied in this paper, this assumption

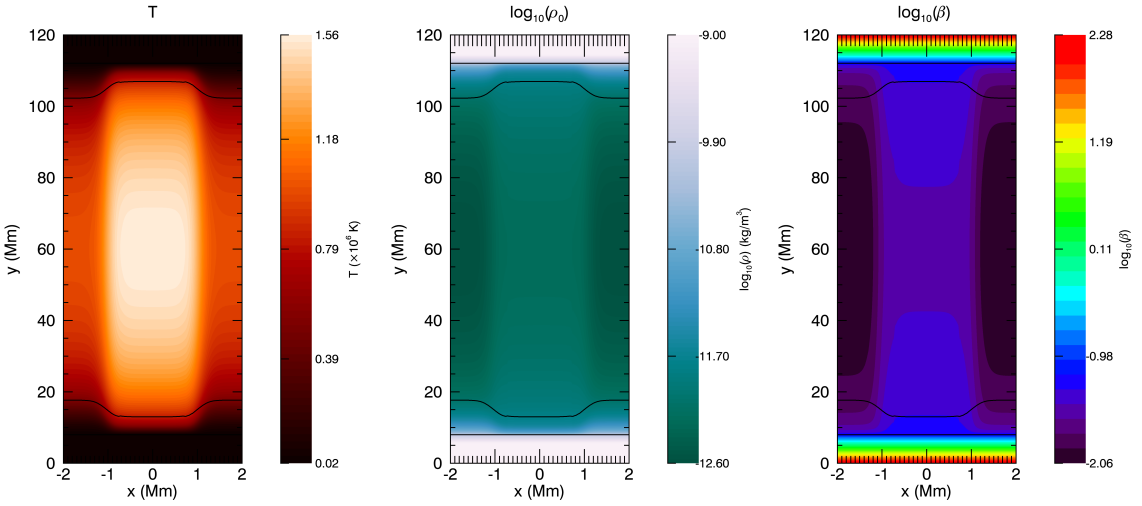

Figure 3.2: Contour plots of the temperature T (MK), the density ρ ($\times 10^{-12}$ kg/m^3) and the plasma beta β after relaxation ($t = 11600$ s).

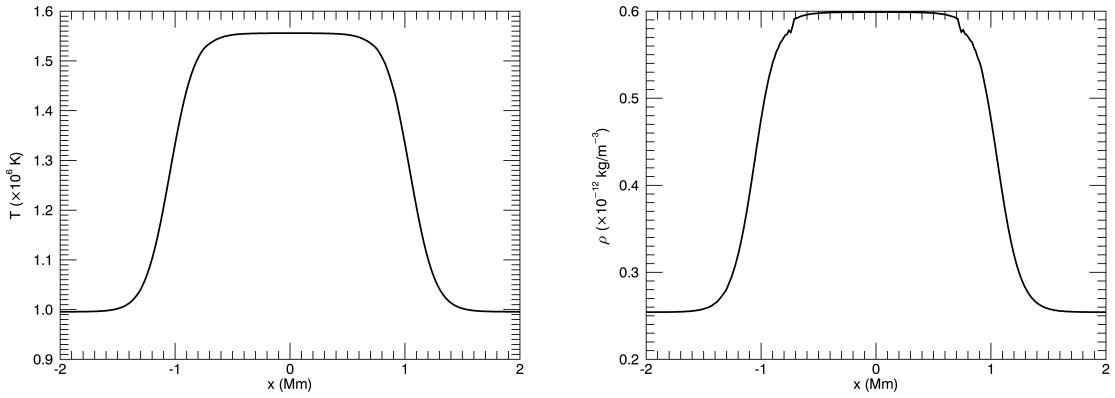

Figure 3.3: Plot of the cross-field temperature T (MK) and density ρ ($\times 10^{-12}$ kg/m^3) at the apex ($y = 60$ Mm) after relaxation ($t = 11600$ s).

is reasonable as the modest additional heating due to phase mixing occurring in the corona does not affect the location of the TR and the chromospheric boundaries. The plasma beta is of the order of $10^{-2} - 10^{-1}$ in the corona.

Figure 3.4 shows a (field-aligned) cross-section of the temperature and density at $x = -2$ Mm (exterior, black lines), $x = -1$ Mm (shell, blue lines) and $x = 0$ Mm (middle of the loop, green lines). Inserted panels on these plots show a zoomed version of the profiles in the first transition regions, with the symbols representing the numerical grid resolution. It is clear that the temperature and density are well resolved in the TR. We note that the temperature at the top of the TRs remains between $0.51 - 0.83$ MK (hence the cutoff temperature $T_c = 0.5$ MK is always located in the TR).

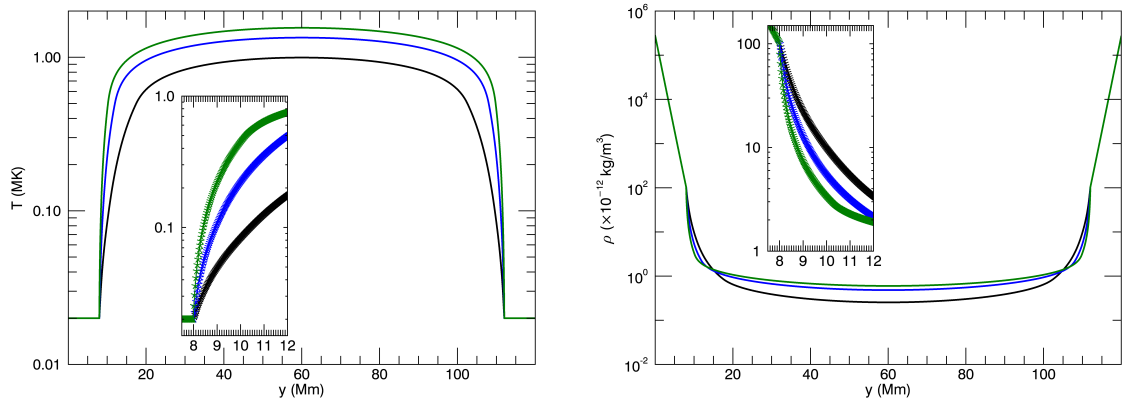

Figure 3.4: Plot of the field-aligned temperature (left) and density (right) at $x = -2$ Mm (black), $x = -1$ Mm (blue) and $x = 0$ Mm (green). The small panel inserted on the plot of the temperature and the density shows a zoomed version in the TR (between $y = 7.5$ Mm and $y = 12$ Mm). The symbols represent the numerical gridpoints.

Figure 3.5 shows contours of the magnetic field components B_x and B_y as well as the Alfvén speed v_A. Before relaxation, the background field is uniform and straight, with $B_y = 10$ G. After the (numerical) relaxation, there is a small cross-field gradient in B_y as well as a slight expansion of the field in the TR (reflected in the B_x contour). The Alfvén speed shows a similar pattern as the contour of the density (Fig. 3.2), varying between $1000 - 1800$ km/s in the corona, with the highest Alfvén speed attained in the exterior coronal part of the loop. In the TR the Alfvén speed is larger in the interior of the loop than the exterior (because the TR is shallower for the interior of the loop), and this profile then reverses in the corona. This means that Alfvén waves will initially propagate faster inside than outside the loop, and that the phase mixing gradients from the TR will be reduced before they increase again in the corona (see Section 3.3.1).

3.2.1 Driver

We implement a continuous, sinusoidal, high-frequency driver into the system, near the top of the first chromosphere (CHROM1) at $y = 7.8$ Mm, through an additional force in the momentum equation in the invariant z direction.

$$\rho \frac{dv_z}{dt} = -\rho v_0 \omega \cos(\omega t), \tag{3.7}$$

with $v_0 = 0.7$ km/s (1% of the local Alfvén speed), and $\omega = \frac{2\pi}{P}$ the angular frequency, where $P = 12$ s is the period of the driver. We remark that the driver frequency is sig-

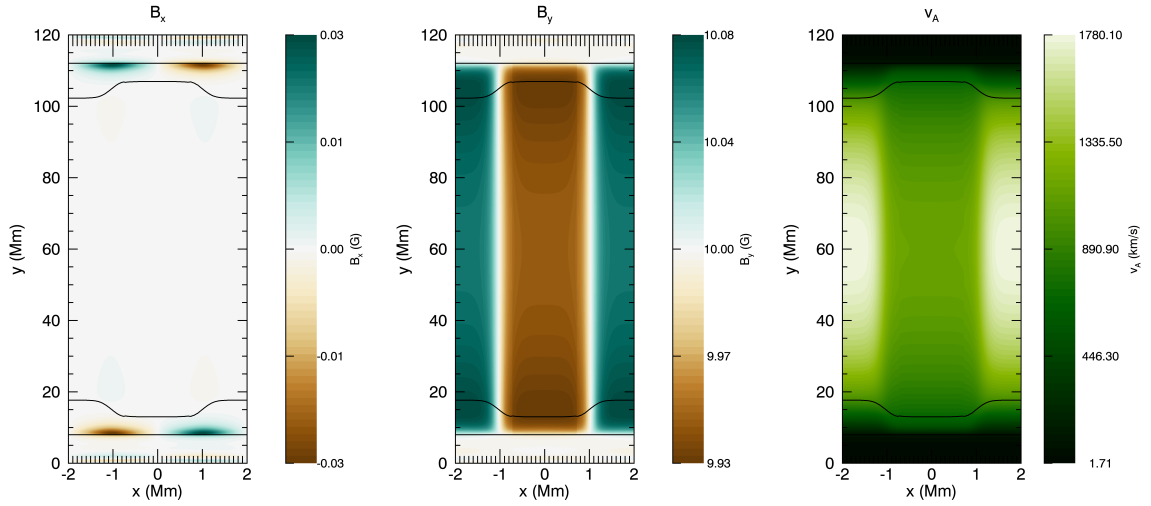

Figure 3.5: Contour plots of the magnetic field components B_x (G) (left) and B_y (G) (middle) and the Alfvén speed v_A (km/s) (right) after the numerical relaxation.

nificantly higher than many observed frequencies in the corona, where most oscillations have periods of the order of a few minutes (see e.g. De Moortel and Nakariakov, 2012). We use a high-frequency driver in order to have a sufficient amount of wavelengths in the corona and to have significant phase mixing. With $\max(v_{A,cor}) = 1150$ km/s and $L_{cor} = 94$ Mm (at $x = 0$ Mm), we can roughly fit 7 wavelengths in the coronal part of the loop for a driver with a period of 12 seconds. The additional force is applied on a strip of 10 gridpoints, symmetrically distributed about $y = 7.8$ Mm. This driver generates (upwards and downwards) propagating Alfvén waves along the field (in the y direction). The driver is implemented near the top of CHROM1 because of computational efficiency, i.e. to ensure that the resolution results in at least 5 gridpoints over a wavelength ($\lambda(y) > 5\Delta y$). Indeed, if we were to implement the driver at the bottom boundary of the domain, we would need a higher field-aligned resolution to resolve the smaller wavelength in the chromosphere (because of the low Alfvén speed).

3.3 Results and analysis

We run an ideal and a viscous simulation for ~ 6000 s ($500t_P$, with $t_P = 12$ s, i.e. the period of the driver), long enough to see the effects of thermal conduction and optically thin radiation. These are of the order of $1000 - 5000$ seconds in the domain (see Appendix A). The dynamic viscosity we use is $\rho\nu = 5 \times 10^{-4}$ kg m^{-1}s^{-1}, which is two orders of magnitude smaller than the dynamic viscosity in the corona, assuming a temperature of $T \sim 10^6$ K (see e.g. Priest, 2014, p. 81). This viscosity is chosen to

maximise the effect of phase mixing. For larger viscosities, the waves already undergo substantial damping before phase mixing can develop significant cross-field gradients (near the far end of the coronal part of the loop). We do not include resistivity to prevent the diffusion of the background field and the Alfvén speed profile. We also run a continued relaxation simulation for the same amount of time to separate the effects of the implementation of the driver on the field-aligned flows.

3.3.1 Propagation of the Alfvén waves

Figure 3.6 shows a contour of the velocity v_z (km/s) for the ideal simulation at $t = 92.7$ s ($8t_P$) and at $t = 982.8$ s ($86t_P$). At $t = 92.7$s the (upward) right-propagating Alfvén waves have travelled into the corona and the wavefront is in the upper leg of the loop near the top of TR2 ($y \sim 100$ Mm). Due to the Alfvén speed profile (Figure 3.5), the wavefront travels initially faster in the interior of the loop ($-1 < x < 1$ Mm) than the exterior when it enters the corona. The exterior wavefront then catches up with the interior wavefront ($y \approx 40$ Mm), and it is ahead of the interior wavefront for the upper part of the corona ($y > 60$ Mm). Hence the transverse gradients associated with the phase mixing are first "undone" in the lower leg of the loop, and the strongest gradients are found in the upper leg of the loop near the top of TR2.

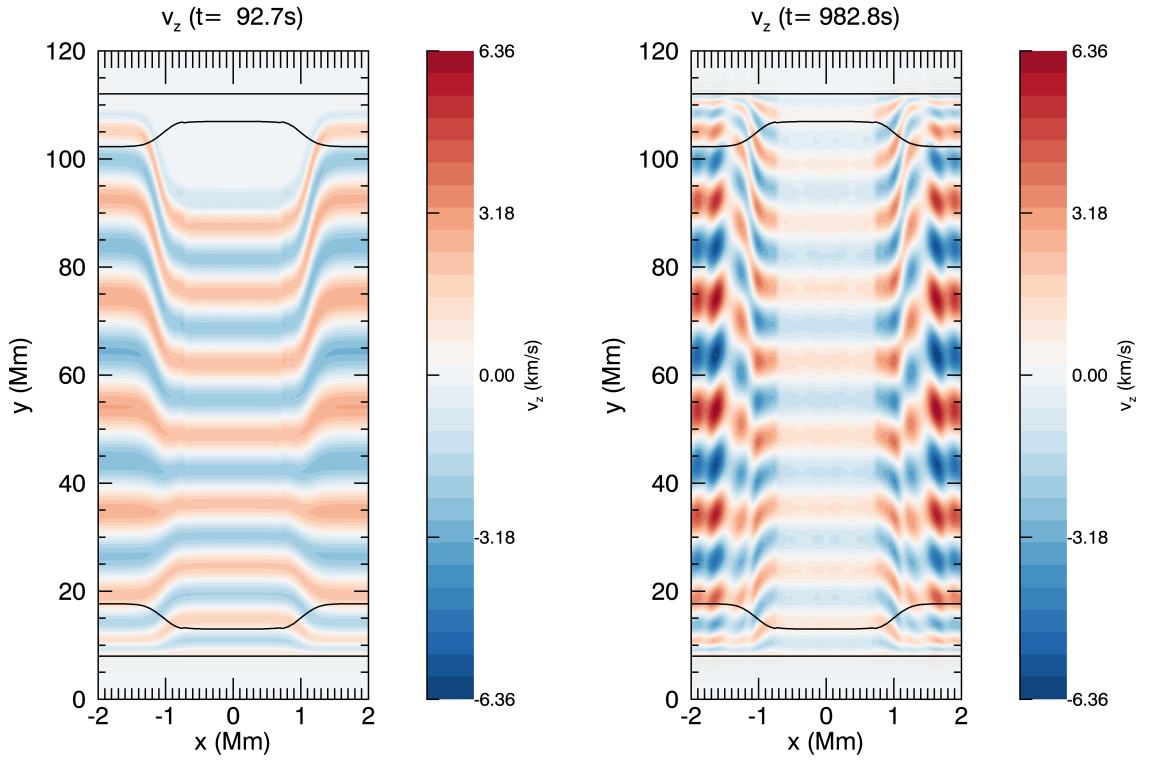

Figure 3.6: Contours of v_z (km/s) at $t = 92.7$ s and $t = 982.8$ s.

The right panel of Figure 3.6 shows a contour of v_z (km/s) at $t = 982.8s$. At this stage in the simulation we see a finer scale pattern in v_z in the exterior region and the shell region of the loop (which could lead to additional heating in the viscous simulation), associated with the fact that reflections of the Alfvén waves of the second TR-chromosphere boundary interfere with incoming driven waves, see Section 3.3.1. Due to this interference, the maximal amplitude of v_z in the corona has increased to 7 km/s (compared to 2-3 km/s at earlier times).

Partial reflection of the Alfvén waves

Due to the high frequency driver, most of the wave energy does not reflect near the second TR, because the wavelength of the driven waves is smaller than the width of the transition region. Indeed, most of the wave energy propagates down into the second chromosphere, with only a small fraction ($\sim$ 15%) reflected back into the corona. Figure 3.7 shows a plot of v_z (km/s) along $x = 0$ Mm at $t = 178.5$ s (green), $t = 183.1$ s (black) and $t = 187.7$ s (blue), and displays the constructive and destructive interference of these reflections with incoming waves from the driver. At this stage in the simulation ($t \sim 180$ s) the wavefront of the reflections has propagated back into the corona and is located at $y \approx 55$ Mm. The interference of these reflections with incoming (upwards propagating) waves changes the maximal amplitude of v_z by about 15%. This interference is also shown in the right panel of Figure 3.7 which shows $\max(v_z)$ (km/s) in the middle of the domain ($x = 0$ Mm) for the first 500 s. The maximal amplitude initially increases up to ~ 2.3 km/s when the Alfvén waves propagate into the corona, and it remains constant up to $t \approx 150$ s. Afterwards, $\max(v_z)$ oscillates between $\sim 2 - 2.7$ km/s because of the interference with the reflections (relative change of $\sim$ 15%). The vertical blue line at $t = 182$ s is the time when the front of the first reflected Alfvén wave reaches the apex of the loop again ($y = 60$ Mm).

Standing wave regime

The interference of the incoming waves with the reflections sets up an approximate standing regime in the domain after $t \sim 1000$ s. This can be seen in Figure 3.8, which shows a space time contour of v_z in the middle of the loop ($x = 0$ Mm). In the first $t \sim 1000$ s the propagation of the waves in the corona matches the black diagonal line, which shows that the Alfvén waves are propagating at the Alfvén speed. After about 1000 s we see a change from a propagating regime to a standing regime as there now are locations along y where the amplitude of v_z becomes a node/antinode. During the time

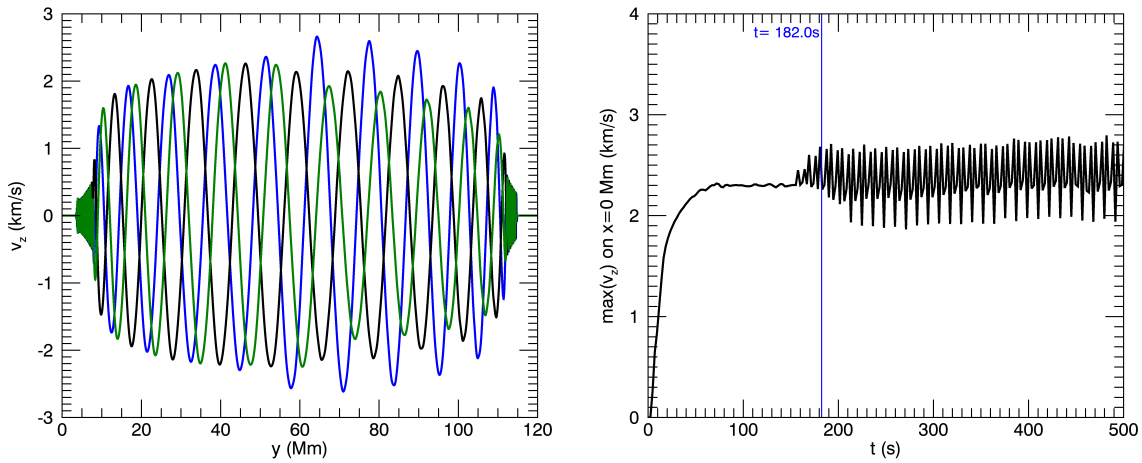

Figure 3.7: (Left) Plot of v_z (km/s) at $x = 0$ Mm at $t = 178.5$ s (green), $t = 183.1$ s (black) and $t = 187.7$ s (blue). (Right) Plot of max(v_z) along $x = 0$ Mm with time.

when the waves are propagating ($t < 1000$ s), max(v_z) ranges between $2 - 2.5$ km/s in the corona, but after $t > 1000$ s, max(v_z) increases to 1-6 km/s. The wavelength of the standing wave in the corona ($t > 1000$ s) is similar to the wavelength of the propagating Alfvén waves in $0 < t < 1000$ s.

Figure 3.9 shows the envelopes of v_z (max(v_z) and min(v_z), taken over each period of the wave) with time, at a node ($y = 60$ Mm) and an antinode ($y = 63.5$ Mm) of v_z. These two locations are marked by the dashed vertical lines in Figure 3.8. In both panels the envelope is roughly constant (~ 2 km/s) for the first 1000 s, but afterwards the envelope decreases (~ 1 km/s) at $y = 60$ Mm and increases (~ 6 km/s) at $y = 63.5$ Mm. There also seems to be a longer period present in the envelopes of the order ~ 650 s, which is related to the relaxation of the background plasma (see Section 3.3.2). After $t \sim 3000$ s the envelopes at both locations seem to reach a steady state.

When viscosity is present or when phase mixing takes place, the standing regime is only partially established because less wave energy is reflected. In this case the initially propagating regime eventually evolves to a steady-state which is a combination of standing and propagating waves. This can be seen in Figure 3.10 which shows a space time contour of v_z (km/s) in the middle of the shell region ($x = -1.18$ Mm) for the viscous simulation. We can see that most of the wave energy is dissipated by the phase mixing in the upper part of the corona ($y > 60$ Mm), before reflection takes place near the second TR.

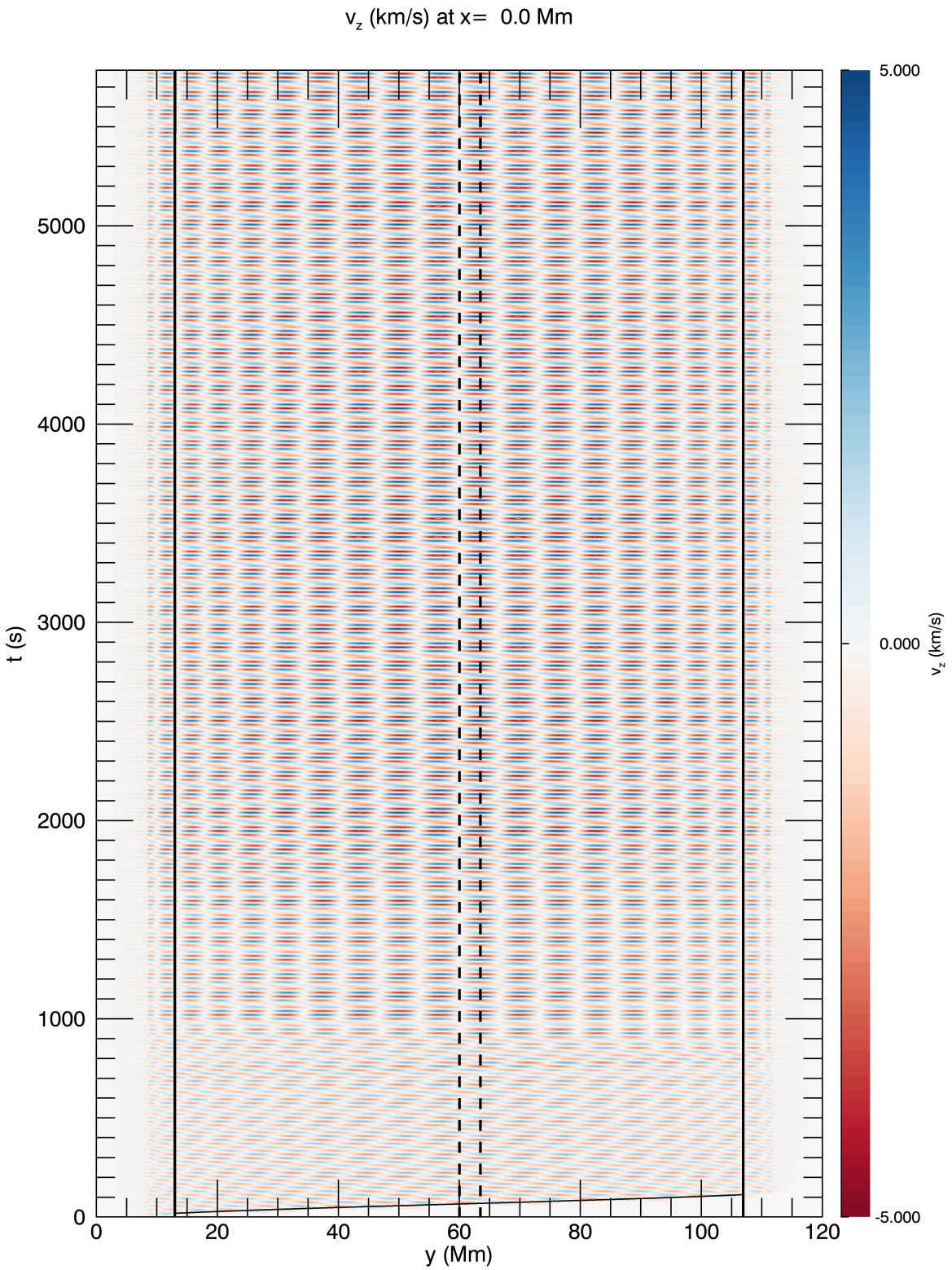

Figure 3.8: Contour of v_z (km/s) at $x = 0$ Mm with time. After $t \sim 1000$ s the interference of right propagating Aflvén waves and the reflected waves leads to a standing regime in v_z. The diagonal line in the corona is the path of an Alfvén wave propagating at the Alfvén speed in the corona.

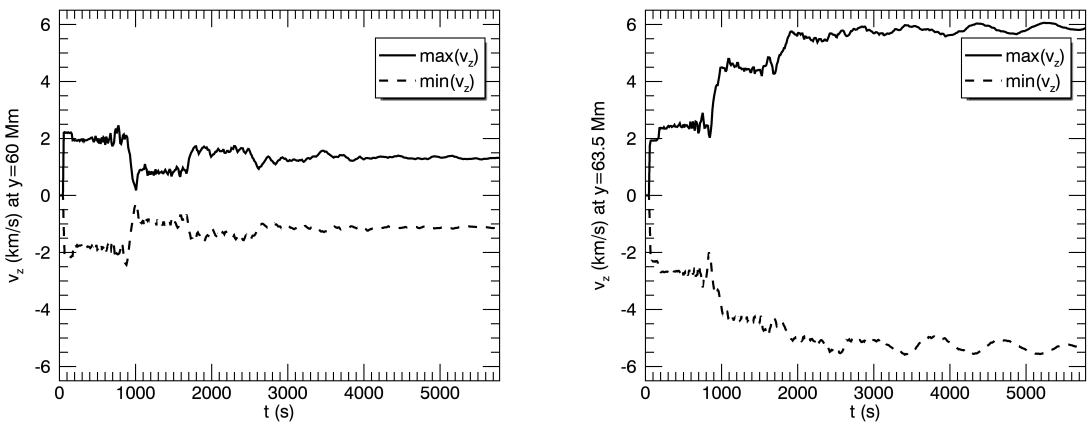

Figure 3.9: (Left) Plot of the maximal and minimal amplitude of v_z (km/s) at the apex ($y = 60$ Mm) with time. (Right) Similar plot at $y = 63.5$ Mm.

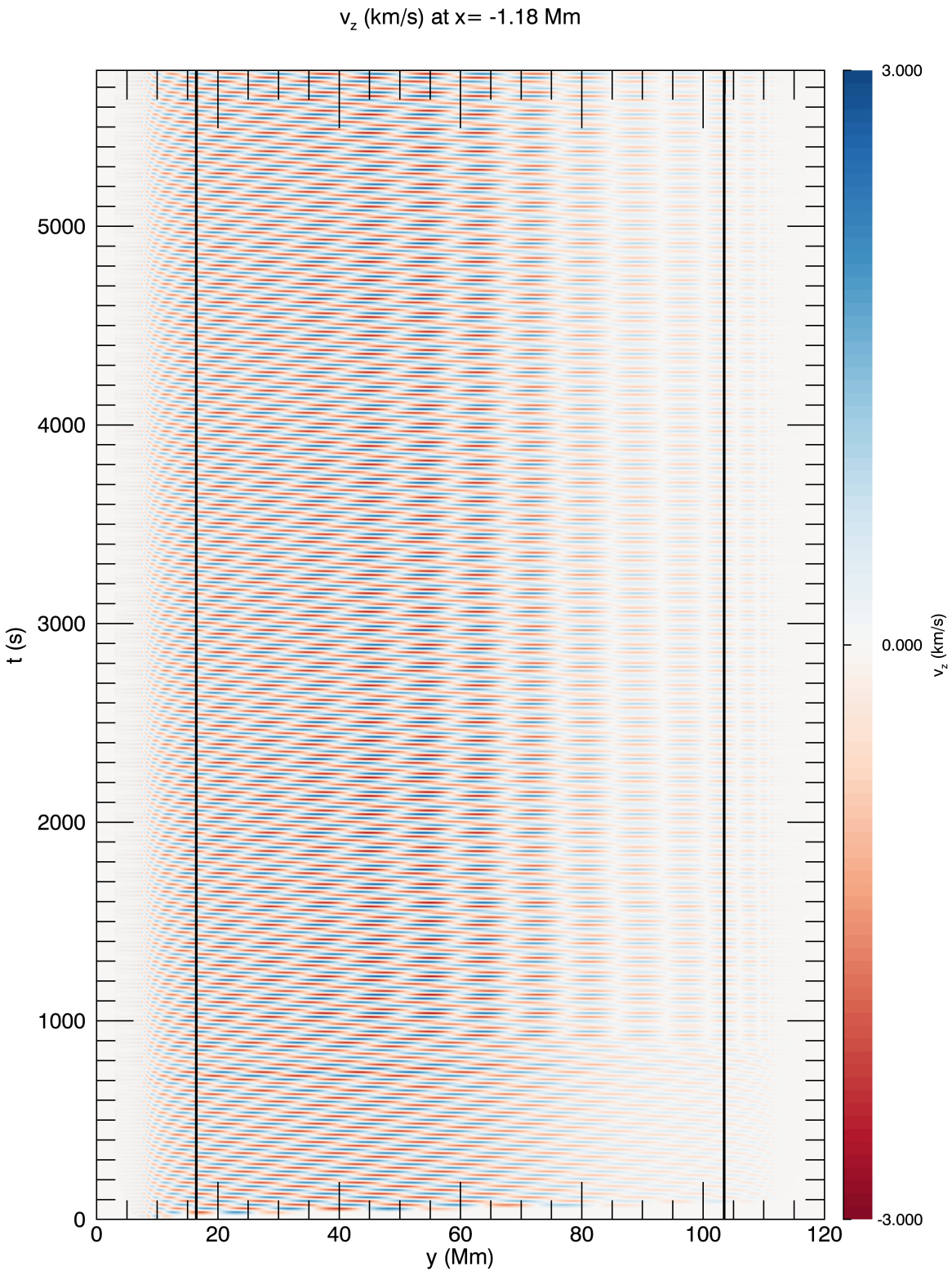

Figure 3.10: Contour of v_z (km/s) at $x = -1.18$ Mm with time, for the viscous simulation.

3.3.2 Field-aligned flows and relaxation of the plasma

The goal of this chapter is to study the evaporation of TR and chromospheric plasma into the corona, caused by the (viscous) dissipation of the phase-mixed Alfvén waves. However, other field-aligned flows are also present in the domain. In order to be able to distinguish these flows from the evaporation, we make a detailed comparison between the ideal simulation, the viscous simulation, and the continued (ideal) relaxation simulation.

Figure 3.11 shows the averaged field-aligned velocity v_y (km/s) at the TR-corona boundaries for the interior part of the loop ($-1 < x < 1$ Mm), for the continued relaxation simulation (dotted line), the ideal simulation (dashed line) and the viscous simulation (solid line). The top panel represents the TR1-corona boundary ($y \sim 13$ Mm) and the bottom panel the TR2-corona boundary ($y \sim 107$ Mm), hence a positive (negative) v_y in the top (bottom) panel is an upflow from the TR1 (TR2) into the corona. We can see that the field-aligned flows are generally small, $|v_y| \sim 0.1$ km/s (less than 0.1% compared to the local Alfvén and sound speed, $v_A \sim 640$ km/s and $c_s \sim 130$ km/s), but for the ideal driving simulation the upflows into the corona are larger. This can especially be seen from the larger local maxima and minima of the field-aligned flows. The reason why the implementation of a driver in the domain creates larger upflows into the corona is due to the ponderomotive force effect, and is explained in Appendix B. In the viscous simulation the upflows are slightly smaller than in the ideal driving simulation, because of the effect of the viscosity. We remark that the upflows caused by the ponderomotive force might be exaggerated in our model, as the ponderomotive force from Alfvén waves does not act on neutrals and the chromosphere in our model is treated as a fully ionised plasma (see e.g. Laming, 2017). However we note that these upflows are of less interest in this study, as the evaporative upflows are obtained by comparing the upflows in the non-ideal and ideal simulations (and we essentially subtract the ponderomotive upflows). The field-aligned flows in Figure 3.11 show a periodicity of ~ 650 s in all the simulations, which is related to the relaxation of the background plasma to the imposed background heating profile. This movement of plasma along the field (due to the relaxation) propagates at the slow speed. Indeed, the time for a slow wave to travel from the top of CHROM1 ($y = 8$ Mm) to the top of CHROM2 ($y = 112$ Mm) is 652s for the interior region, which corresponds to the period of the field-aligned flows.

The extra upflows from the TRs into the corona induced by the driver increase the mass in the corona. Figure 3.12 shows the mass change $\int(\rho - \rho_0)dV$ (kg/m) with time

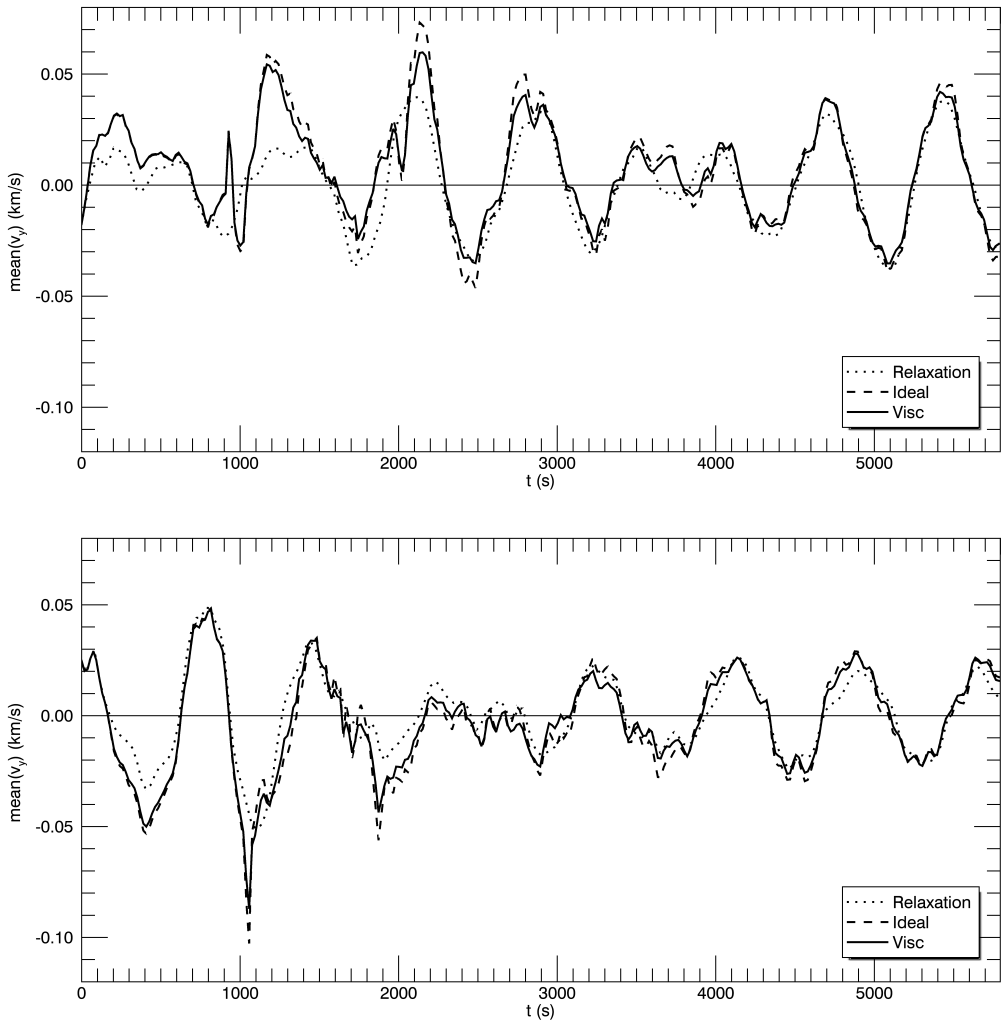

Figure 3.11: Plots of the mean(v_y) (km/s) with time on the TR-corona boundary for the interior of the loop ($-1 < x < 1$ Mm) for the continued relaxation simulation (dotted line), the ideal simulation (dashed line) and the viscous simulation (solid line). The top panel represents the TR1-corona boundary ($y = 13$ Mm) and the bottom panel the TR2-corona boundary ($y = 107$ Mm). A positive (negative) v_y in the top panel (bottom panel) is an upflow in the corona.

in the corona (black), the TRs (red) and the chromospheres (blue) for the continued relaxation simulation (left panel) and the ideal simulation (right panel). Here, ρ_0 is the initial density at $t = 0$ s. The green line is the sum of the blue and the red line and represents the combined mass change of the TRs and chromospheres. The continued relaxation simulation shows no significant change in the mass of the corona, while the mass in the corona in the ideal driving simulation increases due to the ponderomotive force effect associated with the Alfvén waves. We see a corresponding decrease in mass in the lower atmosphere (green line), as well as a mass flow from the chromosphere

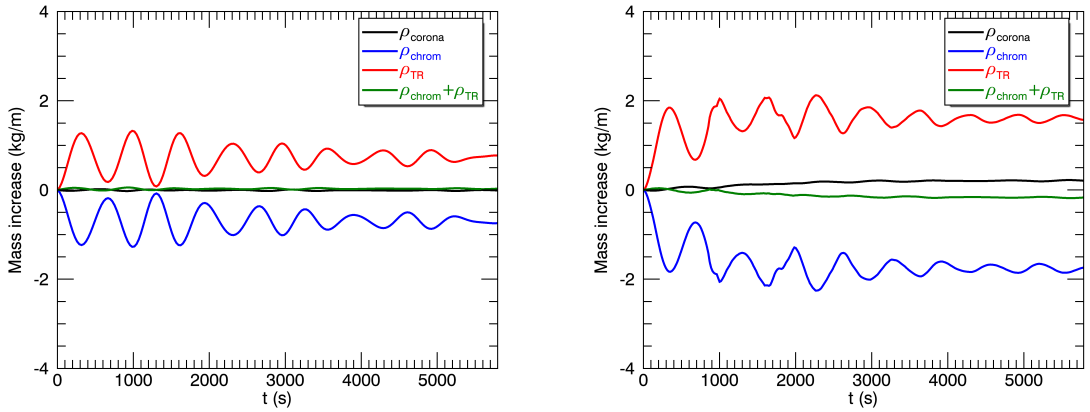

Figure 3.12: Plot of the mass change (kg/m) in the corona (black), TRs (red) and chromospheres (blue) for the continued relaxation simulation (left) and ideal simulation (right). The green line is the sum of the red and blue line and represents the mass change in the chromospheres and TRs.

into the TR.

Before we discuss the heating by the (viscous) dissipation from the phase-mixed Alfvén waves, we first discuss the plasma changes (heating, mass increase) present in the continued relaxation simulation. Figure 3.13 shows the space time contours of the absolute temperature change $T - T_{mean}$ ($\times 10^4$ K) and the relative density change $(\rho - \rho_{mean})/\rho_{mean}$ in the middle of the shell region ($x = -1.18$ Mm) for the continued relaxation simulation. Here, the average that is subtracted is taken over the course of the continued relaxation simulation ($\sim$ 5800 s), for every y. We see a periodic, adiabatic heating and cooling ($\sim$ 650 s) near the corona-TRs boundaries and at the loop apex, related to the relaxation of the loop. The same periodicity is seen in the contour of the relative density change. The size of the heating and cooling events is of the order $\sim$ 300 K (0.02%) for the first 3000 s, and this gets smaller near the end of the simulation as the relaxation is ongoing. The space time contour of the relative density change shows a similar decrease and increase in the density at the loop apex and near the corona-TRs boundaries (of the order of $\sim 0.3\%$).

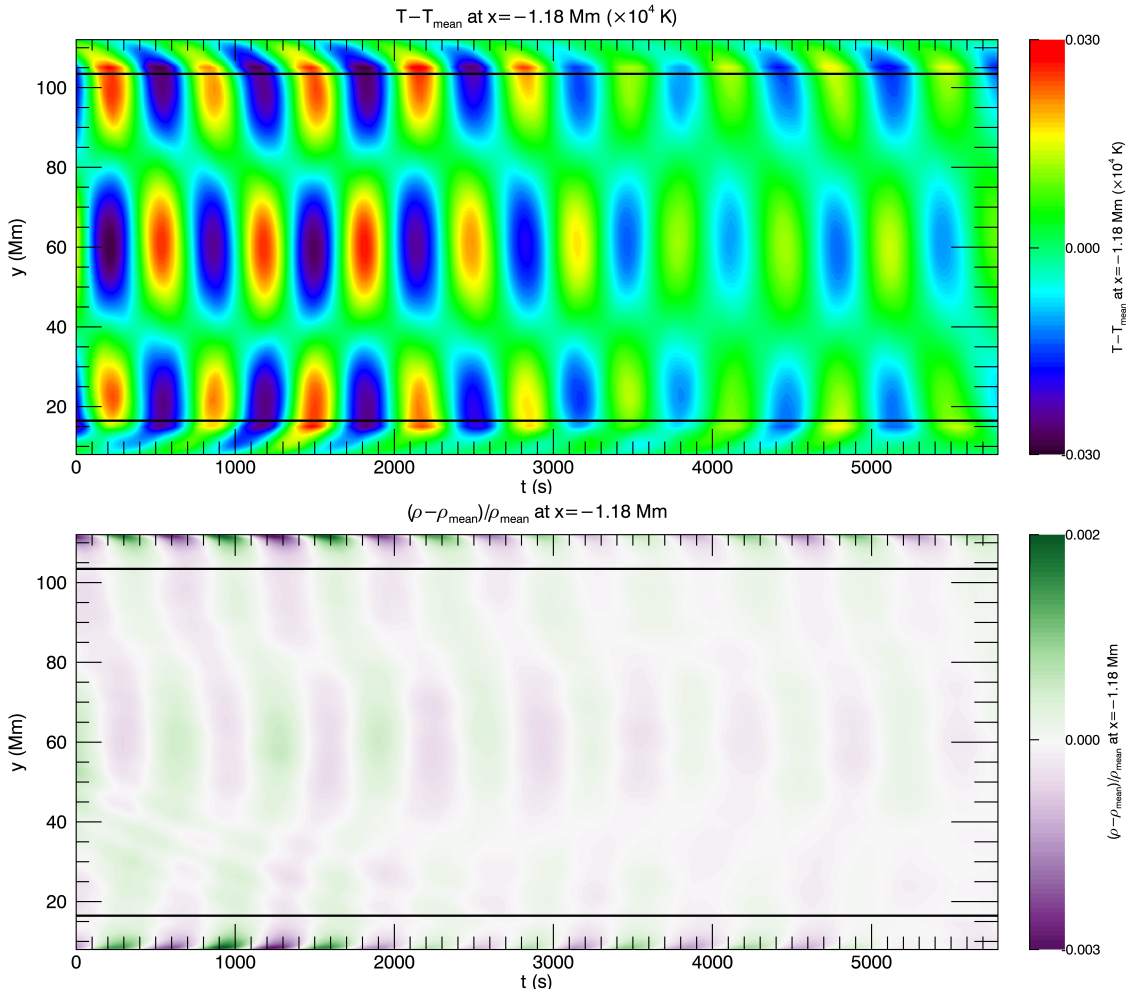

Figure 3.13: Time space contours of $T - T_{mean}$ ($\times 10^4$ K) and $(\rho - \rho_{mean})/\rho_{mean}$ for the continued relaxation simulation in the shell of the loop ($x = -1.18$ Mm). The average that is subtracted is taken over the course of the continued relaxation simulation (~ 5800 s) for every y.

3.3.3 Plasma changes in the ideal and the viscous simulation

Energies and Poynting flux

Figure 3.14 shows the volume integrated kinetic (blue), magnetic (green) and internal (red) energy change (Jm^{-1}) in the domain for the ideal (left panel) and the viscous simulation (right panel). The curves are plotted every 34s to cancel out the period of the driver (12s) and make the plot clearer. We can see that the magnetic and kinetic energies increase from the start as the driver injects wave energy into the system. The magnetic and kinetic energy oscillate out of phase as soon as the partial standing regime is established in the domain ($\sim$ 600 s) and after $t \sim 2000$ s they reach a steady state and oscillate about an equilibrium. This steady state was also discussed

in Figure 3.9. The steady state in the viscous simulation is 25% lower than in the ideal simulation, which is consistent with the fact that more dissipation is present in the viscous simulation. The internal energy increases in the ideal simulation due to the work done on the system by the driver, which injects energy into the domain. The top panels of Figure 3.15 show the volume integrated wave energy, $\int \left(\frac{\rho v_z^2}{2} + \frac{B_z^2}{2\mu_0} \right) dV$, in the corona (left) and in the left shell (right) for the ideal simulation (dashed line) and the viscous simulation (solid line). We can see that the wave energy in the corona for the viscous simulation is 18% smaller in the first 1000 s and 25% smaller near the end of the simulation (compared to the ideal simulation). In the left shell, 45% of the wave energy has been damped in the viscous simulation compared to the ideal simulation. This leads to a larger increase in the internal energy in the viscous simulation, about five times larger in the left shell for the viscous case than the ideal case (bottom panels of Figure 3.15).

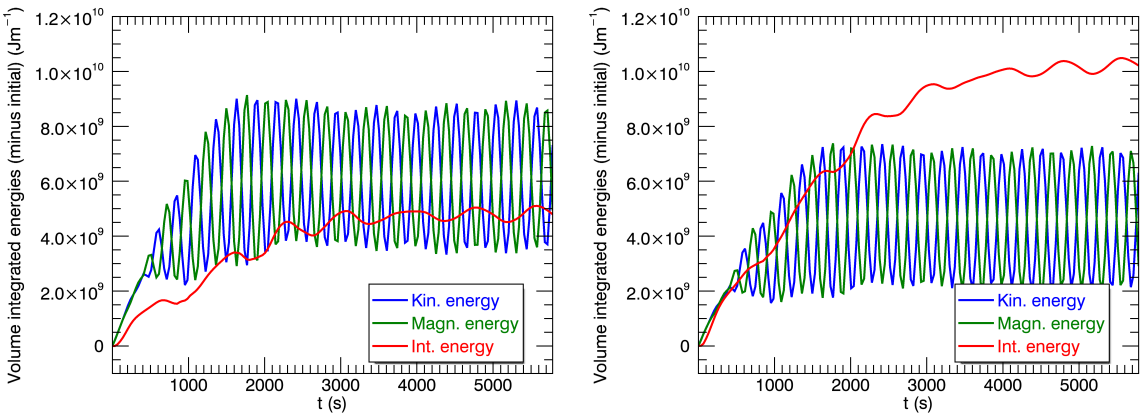

Figure 3.14: Plots of the volume integrated kinetic (blue), magnetic (green) and internal energies (red) components minus their initial value in the whole domain for the ideal simulation (left panel) and the viscous simulation (right panel). These curves are sampled every 34s rather than every timestep to make the graph clearer.

The left panel of Figure 3.16 shows the averaged vertical component of the Poynting flux $\langle (E \times B)_y \rangle$, on the boundaries of the (left) shell of the loop, for the ideal simulation (dashed lines) and the viscous simulation (solid lines). The green lines represent the lower corona-TR boundary (inflow), and the red line the upper corona-TR boundary (outflow). The inflow of Poynting flux on the lower corona-TR boundary is of the order of ~ 2 Jm^{-2}s^{-1} in the ideal and the viscous simulation. Although the outflow of energy is of the same order in the ideal simulation, in the viscous case this is about an order of magnitude smaller (~ 0.2 Jm^{-2}s^{-1}). This means that the shells are powered by ~ 1.8 Jm^{-2}s^{-1} (the difference between the inflow and outflow), which

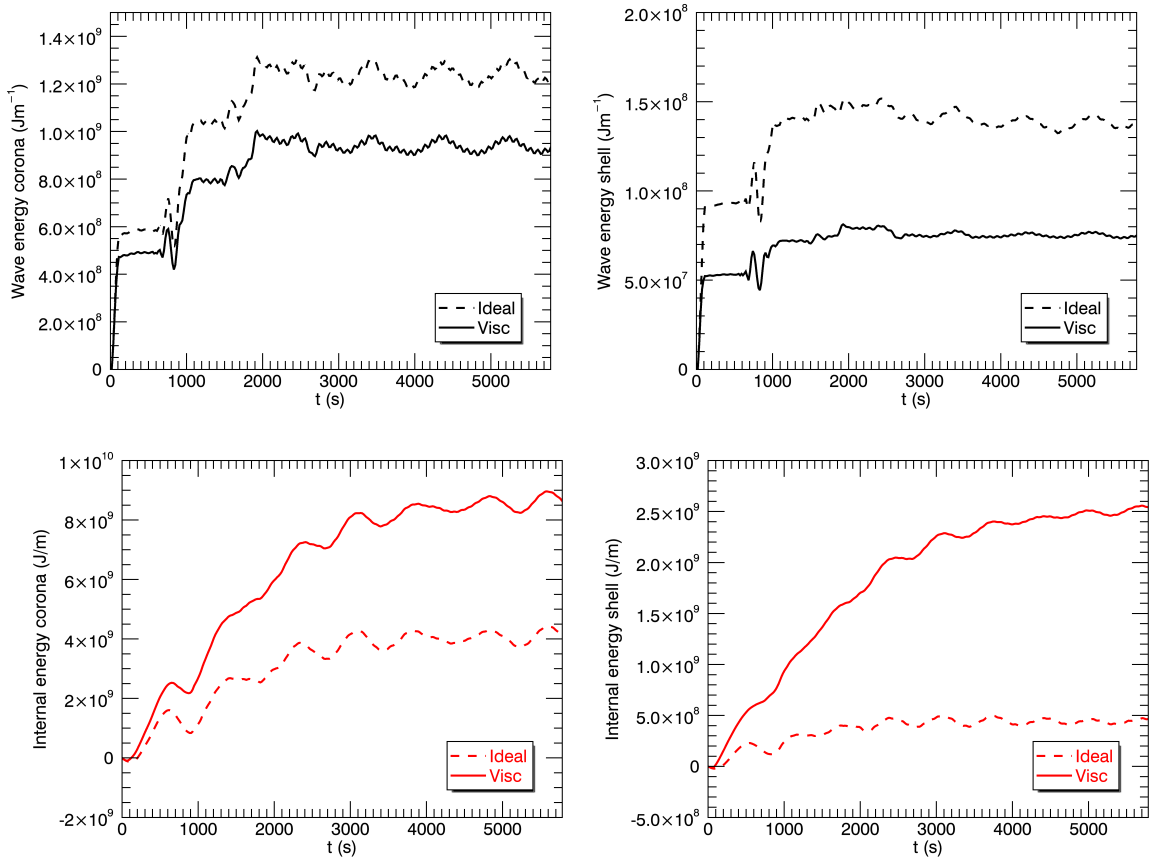

Figure 3.15: The top panels show the integrated wave energy (J/m) in the corona (left) and the left shell (right), for the ideal (dashed line) and the viscous simulation (solid line). The bottom panel shows a similar plot of the integrated internal energy (J/m) in the corona (left) and the left shell (right). In all panels the initial volume integrated energy has been subtracted.

is four orders of magnitude too low to heat active region loops in the corona ($\sim 10^4$ Jm^{-2}s^{-1}), and two orders too low to heat the quiet corona ($\sim 3 \times 10^2$ Jm^{-2}s^{-1}), see e.g. Withbroe and Noyes (1977). The right panel of Figure 3.16 shows the time and volume integrated vertical component of the Poynting flux $\int_0^t \int (E \times B)_y \, dS d\tilde{t}$ (J/m), over the boundaries of the left shell. The coloured lines represent the same boundaries as in the left panel. Again, the inflow and outflow of energy is similar for the ideal simulation, but in the viscous simulation the difference between the green and the red solid line is of the same order as the internal energy increase ($\sim 10^9$ J/m) (see Figure 3.15). This means that most of the wave energy has been dissipated in the shell regions in the viscous simulation, which contributes to an increase in the internal energy. In the ideal simulation the internal energy increase in the shell regions is five times smaller than the viscous simulation near the end of the simulation. The right panel of Figure

3.16 also shows that the standing regime ($t > 1000$ s) decreases the inflow (mostly in the ideal simulation (green dashed line), but also in the viscous simulation (green solid line)), because the standing regime creates a node in v_z which decreases the Poynting flux (see e.g. Prokopyszyn et al., 2019). In the viscous simulation the standing regime is less prominent in the shell regions because the waves are predominantly damped before they reach TR2.

The main reason why the injected Poynting flux is so low (~ 2 Jm^{-2}s^{-1}) is because of the small amplitude driver and the small background field (~ 10 G). Increasing the driver amplitude with an order of magnitude (factor of 10) increases the Poynting flux by a factor 10^2, which would be similar to the energy requirements of the quiet Sun (Withbroe and Noyes, 1977). Indeed, using Ohm's law ($\mathbf{E} = -\mathbf{v} \times \mathbf{B}$) we can rewrite the vertical component of the Poynting flux as

$$\begin{aligned}(E \times B)_y &= v_y(B_z^2 + B_x^2) - B_y(v_x B_x + v_z B_z), \\ &\approx v_y B_z^2 - B_y v_z B_z,\end{aligned}$$

where we have neglected the (cross-field) x component because this is negligible compared to the y and z component. Increasing the driver amplitude v_z by an order of magnitude also increases B_z by an order of magnitude, hence the Poynting flux would be a factor of 100 larger and the energy requirements for the quiet Sun would be obtained. Increasing the background field B_y would further increase the injected Poynting flux, but the Alfvén speed would then be higher in the corona, which would lead to fewer wavelengths in the corona and smaller phase mixing gradients (and consequently less heating). We remark that although the energy input would be higher, the question about dissipating the energy into heat on the relevant timescales remains to be investigated.

Heating in the shell regions

In Figure 3.17 we show contours of the relative temperature increase $(T - T_0)/T_0$ at $t = 5340$ s for the ideal (left panel) and the viscous simulation (right panel). The viscous dissipation of the phase-mixed Alfvén waves in the shell regions of the loop leads to a temperature increase. The temperature increase starts in the far leg of the loop ($y \sim 60$ Mm), as this is where the strongest phase mixing gradients occur (see Figure 3.6). At later times, when a steady state is established (Figure 3.14), a small increase in the relative temperature (3600 K, 0.5% relative increase) all along the shell

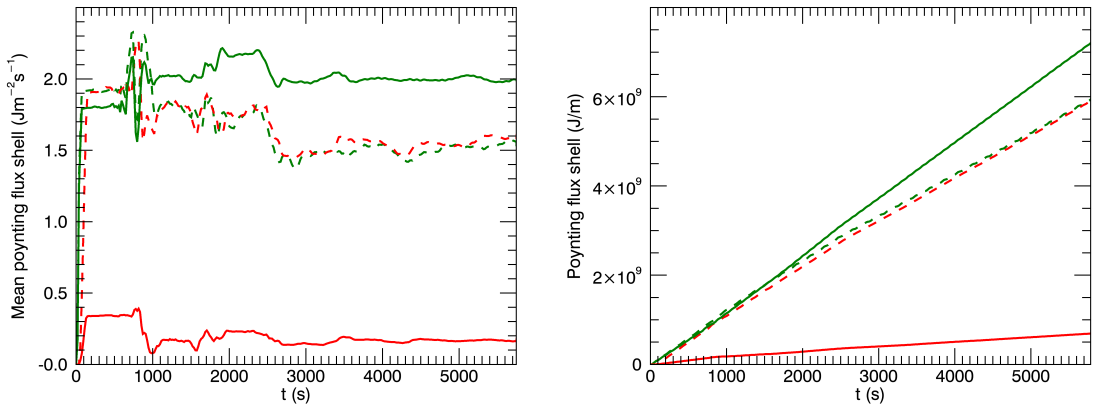

Figure 3.16: (Left) Plot of the averaged Poynting flux $\langle (E \times B)_y \rangle$ (Jm^{-2}s^{-1}) on the boundaries of the left shell, for the ideal simulation (dashed lines) and the viscous simulation (solid lines). The green lines represent the lower boundary and the red line the upper boundary. (Right) Similar plot of the time integrated Poynting flux.

regions can be observed, however the increase remains slightly higher in the far leg of the loop. The temperature increase spreads along the full length of the shell region because phase mixing happens in different locations (due to the Alfvén speed profile, see right panel of Figure 3.5) and because thermal conduction spreads the heat along the field. In the interior and the exterior of the loop the Alfvén waves are not phase mixing and there is no noticable temperature increase. In the ideal simulation, we do not see any increase in the temperature in the shell regions.

Figure 3.18 shows a space time contour of $T - T_{mean}$ ($\times 10^4$ K) of the ideal (top panel) and the viscous simulation (bottom panel) in the middle of the left shell ($x = -1.18$ Mm), indicated by the dashed vertical line in Figure 3.17. The average temperature T_{mean} that is subtracted is taken over the last 5800 s in the continued relaxation simulation, for every y. In the ideal simulation we see again periodic heating and cooling events (of the order of 500 K, with a period of $\sim$ 650 s), respectively near the TRs and at the apex of the loop, which were also seen in the space time contour of $T - T_{mean}$ for the continued relaxation simulation (Figure 3.13). In the viscous simulation stronger heating events (of the order of 4000 K) are present due to the dissipation of the phase-mixed Alfvén waves. In Figure 3.18 we see a first heating event around $t \sim 300$ s in the upper leg of the loop (at $y \approx 70$ Mm). Comparing with the contour plots of v_z (Figure 3.6), it is clear that this heating event is a result of the viscous dissipation of the phase-mixed Alfvén waves. Following this heating event, a thermal conduction front can be seen in the form of a downward propagating increase in temperature (i.e. towards higher values of y). Stronger heating events

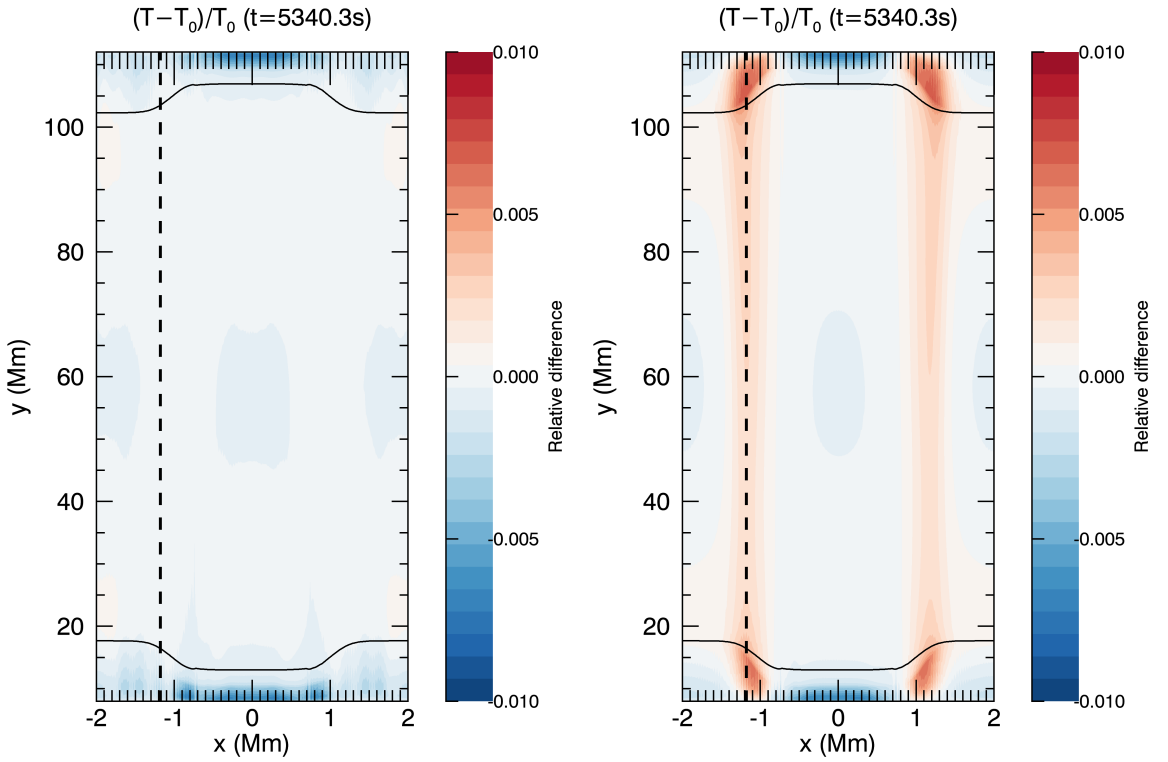

Figure 3.17: Contour of $(T - T_0)/T_0$ for the ideal (left panel) and viscous simulation (right panel) at $t = 5340$ s. The dashed line at $x = -1.18$ Mm denotes the location in the shell where the maximal $T - T_0$ increase is observed.

occur at later times at $y \approx 70$ Mm, and eventually there is heating all along y, as phase mixing happens in different locations due to the Alfvén speed profile (Figure 3.5) and thermal conduction spreads the heat along the field. We remark that the heating is less strong towards the end of the simulation ($t > 4000$ s), as the system reaches a steady state (see e.g. Figure 3.14) and the radiation starts to become more significant ($\tau_{rad} \sim 3000 - 4000$ s in the corona, see Appendix A). In the contour of the viscous simulation, there also seems to be a 650 s periodicity present in the heating events. This could mean that viscosity also affects the slow waves (present from the relaxation and/or associated with the driver), since these slow waves also phase mix in the shells, as there is a gradient in the sound speed present in the shells of the loop because of the temperature gradient (see e.g. Figure 3.2). We therefore run a fourth simulation with viscosity on but without a driver, in order to investigate the effect of viscosity on the slow waves present from the relaxation. This is the dominant source of slow waves in the simulations, as can be seen from e.g. Figure 3.11, which shows that the field-aligned flows are dominated by a $\sim$ 650 s period and have a similar amplitude for all the simulations. In Figure 3.19 we show the equivalent of Figure 3.18

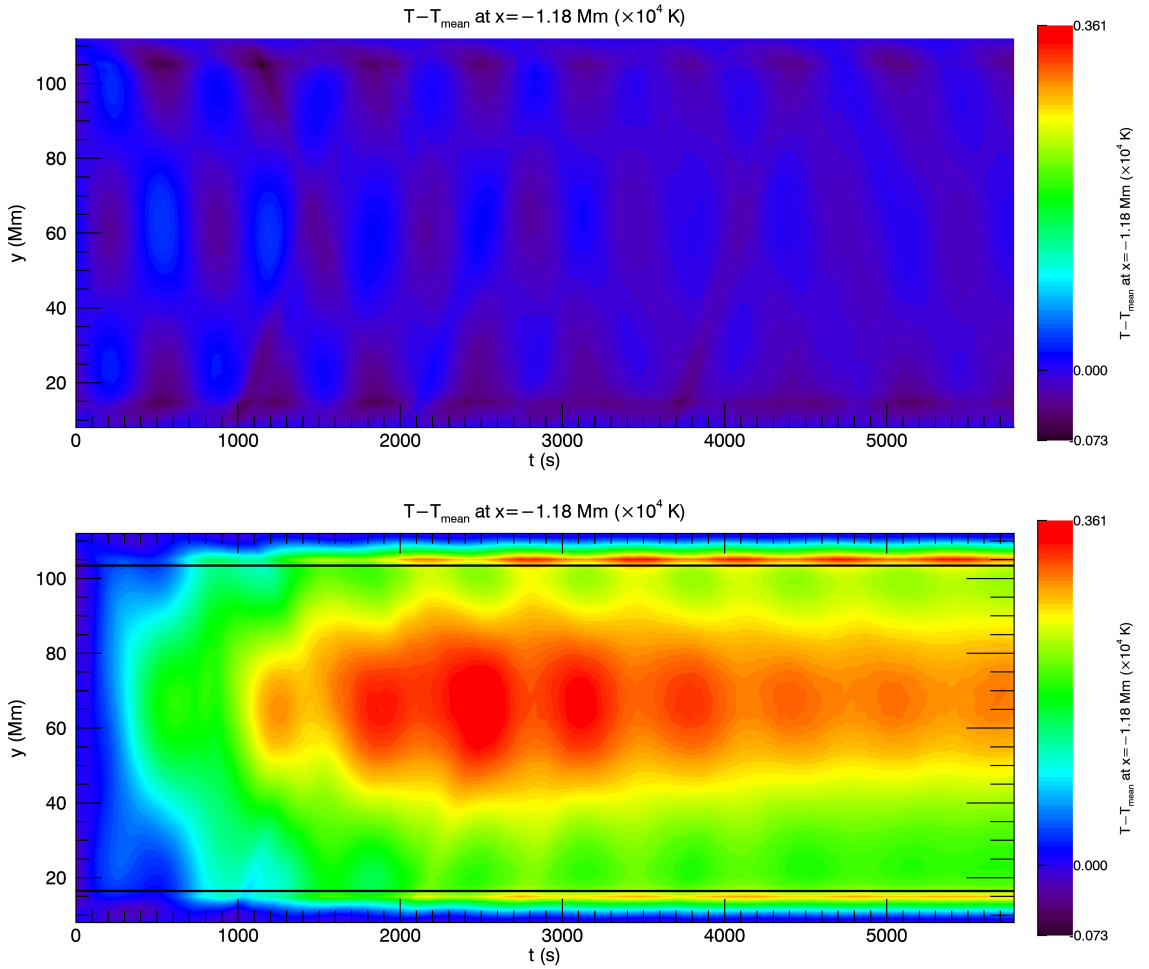

Figure 3.18: Space time contour of $T - T_{mean}$ ($\times 10^4$ K) for the ideal (top panel) and the viscous simulation (bottom panel) in the shell of the loop ($x = -1.18$ Mm). The T_{mean} is taken over the last 5800 s in the continued relaxation simulation, for every y.

for this fourth simulation. We can see that there is essentially no heating present in the shell regions in this simulation, which means that the effect of the viscosity on the slow waves phase mixing is minimal. Hence the heating events in Figure 3.19 can be predominantly attributed to the phase mixing of Alfvén waves.

The top panel of Figure 3.20 shows a space time contour of $T - T_{mean}$ ($\times 10^4$ K) for the viscous simulation with paths of the thermal conduction fronts overplotted. These paths are based on the local conduction speed $v_{cond,local}$,

$$v_{cond,local} \sim \frac{(\gamma - 1)\kappa_0 T^{5/2} \frac{dT}{dy}}{P}, \tag{3.8}$$

which is an estimate for the local propagation speed of a heat front, derived from the energy equation (Equation (3.3)). The bottom panel of Figure 3.20 shows a plot of

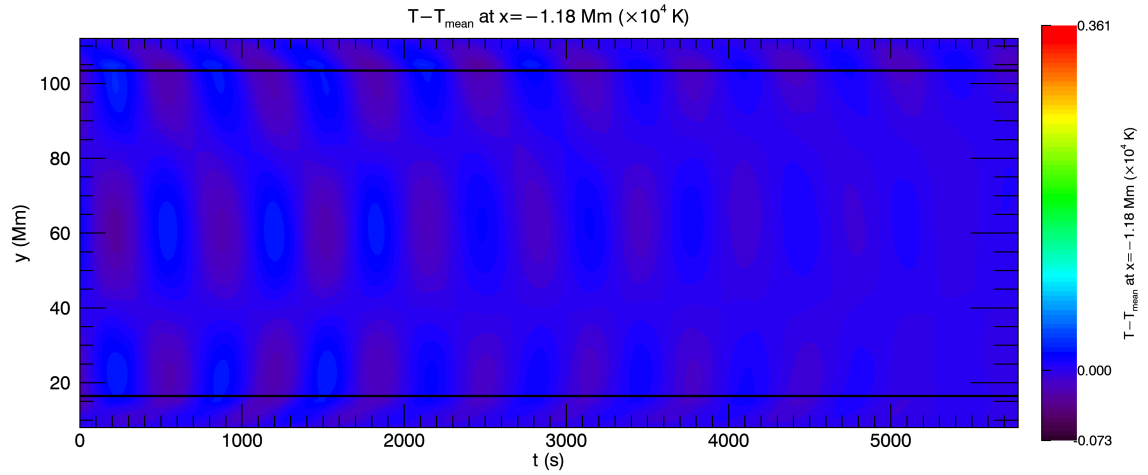

Figure 3.19: Space time contour of $T - T_{mean}$ ($\times 10^4$ K) for the viscous simulation without a driver, in the shell of the loop ($x = -1.18$ Mm). The T_{mean} is taken over the last 5800 s in the continued relaxation simulation, for every y.

$v_{cond,local}$ (km/s) in the shell region, at $x = -1.18$ Mm, as a function of y from the apex ($y = 60$ Mm) to the top of the second chromosphere ($y = 120$ Mm). We can see that $v_{cond,local}$ is slow at locations where the temperature gradient $\frac{dT}{dy}$ is small (near the apex and the chromosphere), and that it accelerates from the apex towards the TR. The conduction paths in the top panel of Figure 3.20 are (t (s),y (Mm)) curves, and are based on the local conduction speed $v_{cond,local}$. We fix a start point (t_0, y_0) and an end point (t_{end}, y_{end}) by eye, to match where the heating starts in the corona ($y \approx 67$ Mm) and ends in the TR ($y \approx 105$ Mm; the location where $T = T_c$). We then obtain the next point through an iteration such that $(t_{k+1}, y_{k+1}) = (t_k + dy/v_{cond,local}, y_k + dy)$, and at the end of the iteration (when $y_{final} = y_{end}$) we rescale t_{final} to t_{end}. Hence these paths only show the acceleration of the conduction towards the lower TR. We can see that, although these paths are based on an estimate of the speed of the conduction front, there is some similarity between the spread of the heating and the paths.

Evaporative upflows and coronal mass increase

The heating events in the viscous simulation discussed in the previous section lead to evaporative upflows from the lower atmosphere into the corona. Figure 3.21 shows a plot of the average upflows $\langle v_y \rangle$ on the (left) shell corona-TR boundaries, for the ideal (dashed lines) and the viscous simulation (solid lines). Again, we see that the upflows are dominated by a period of the order ~ 650 s, associated with the relaxation of the loop, which was also present in the average upflows on the coronal boundaries of the interior of the loop (Figure 3.11). The upflows are of the order of $|v_y| \sim 20 - 30$ m/s,

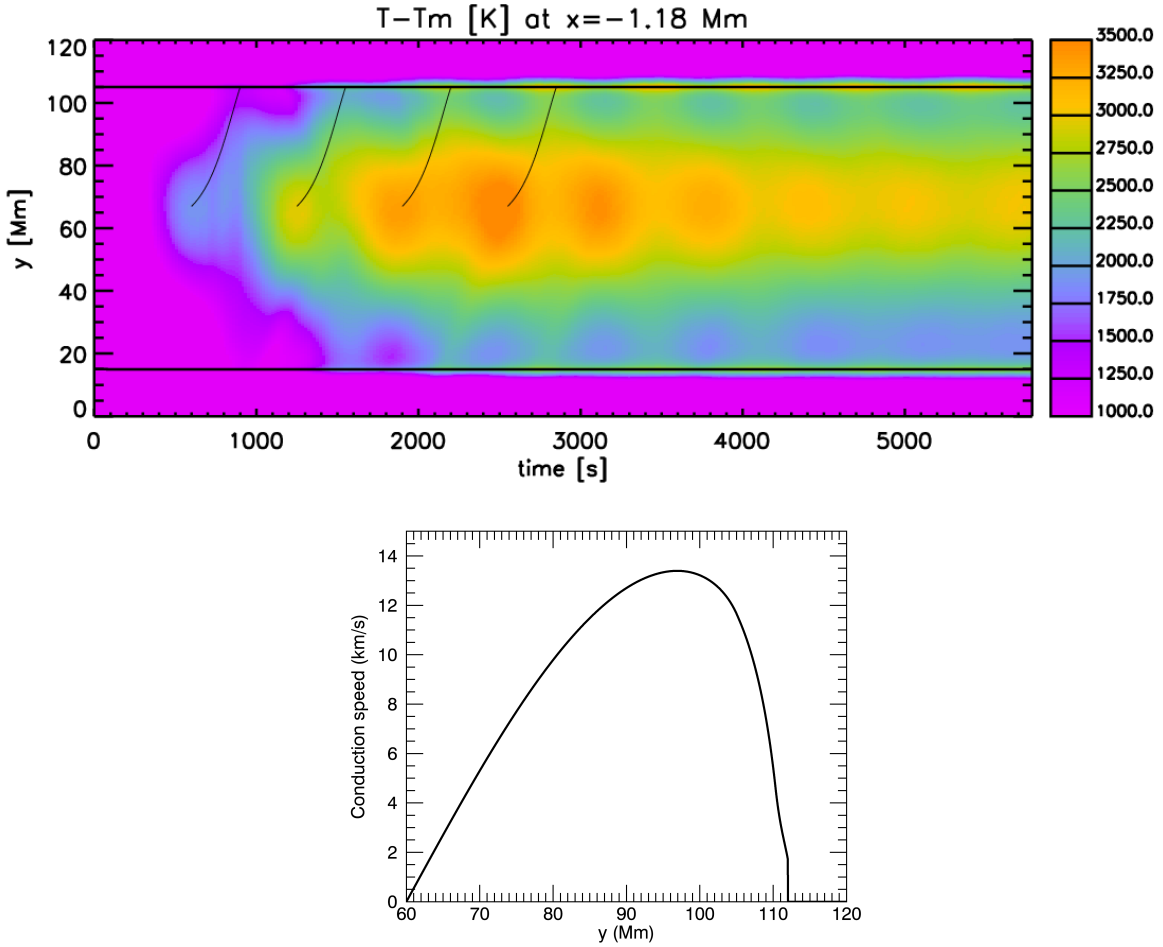

Figure 3.20: (Top) Space time contour of $T - T_{mean}$ ($\times 10^4$ K) for the viscous simulation in the shell of the loop ($x = -1.18$ Mm), with the paths of several conduction fronts overplotted. The T_{mean} subtracted is taken over the last 5800 s in the continued relaxation simulation, for every y. (Bottom) Plot of the conduction speed $v_{cond,local}$ (km/s), at $x = -1.18$ Mm as a function of y.

which is smaller than the average upflows on the coronal boundaries of the interior of the loop. For the first 1000 s the upflows are very similar for the ideal and the viscous simulation, as the largest heating events in the shell regions happen when $t > 1000$ s (Figure 3.18). Indeed, after $t \sim 1500$ s larger upflows from the TRs into the corona are present on both boundaries in the viscous simulation. The difference between the ideal and the viscous upflows - i.e. the evaporation - is largest on the upper coronal boundary, as the strongest heating events happen in the upper leg of the loop (Figure 3.18). This evaporation is of the order 5-10 m/s. Remark that the viscosity also acts on the ponderomotive upflows and the evaporation in the viscous simulation, hence the difference between the ideal and the viscous simulation is a lower limit for the evaporative upflows. Near the end of the simulation ($t > 4000$ s) the upflows in the

ideal and the viscous simulation are smaller because a steady state has been reached and the heating events are smaller (Figure 3.14 and Figure 3.18). The continued relaxation of the system also leads to smaller field-aligned flows (e.g. Figure 3.13).

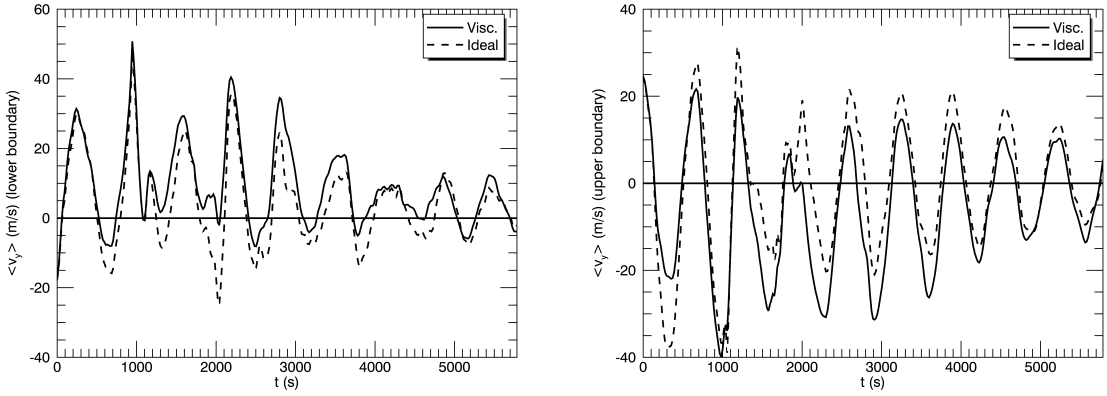

Figure 3.21: Plot of the mean upflow $\langle v_y \rangle$ (km/s) on the two corona-TR boundaries of the (left) shell (-1.35 Mm $< x < -0.75$ Mm), for the viscous simulation (solid line) and the ideal simulation (dashed line). A negative upflow on the upper boundary (right panel) is an upflow from TR2 into the corona.

We remark that the broadening technique of the TR (Lionello et al., 2009; Mikić et al., 2013) used in the simulations does not affect the induced evaporation. Indeed, Johnston et al. (2020) demonstrate that this technique conserves the total amount of energy that is delivered to the chromosphere. It was also shown that, while there can be small differences with the flows in the modified region (where $T < T_c$), the mass flux into the corona is preserved and the induced flows converge above T_c. Hence, the evaporative upflows are not affected by the broadening technique in our simulations. However, we remark that the artificial broadening of the TR likely increases the transmission of Alfvén waves to the lower atmosphere, hence reducing the amount of wave energy available for dissipation (heating) in the corona and the subsequent evaporation.

These evaporative upflows in the viscous simulation move mass from the TRs and the chromospheres into the corona. Figure 3.22 shows a contour of the relative density $(\rho - \rho_0)/\rho_0$ for the ideal (left panel) and the viscous simulation (right panel) at $t = 5340$ s. We can see a mass increase in the coronal part of the shell regions in the viscous simulation of the order of $\sim 1\%$, with a corresponding decrease in the TRs. This mass increase is not present in the ideal simulation. Both contours show a slight increase in the interior region in the corona due to the ponderomotive force effect by the driver (see Appendix B).

In order to quantify the mass increase in the shell regions, Figure 3.23 shows time-

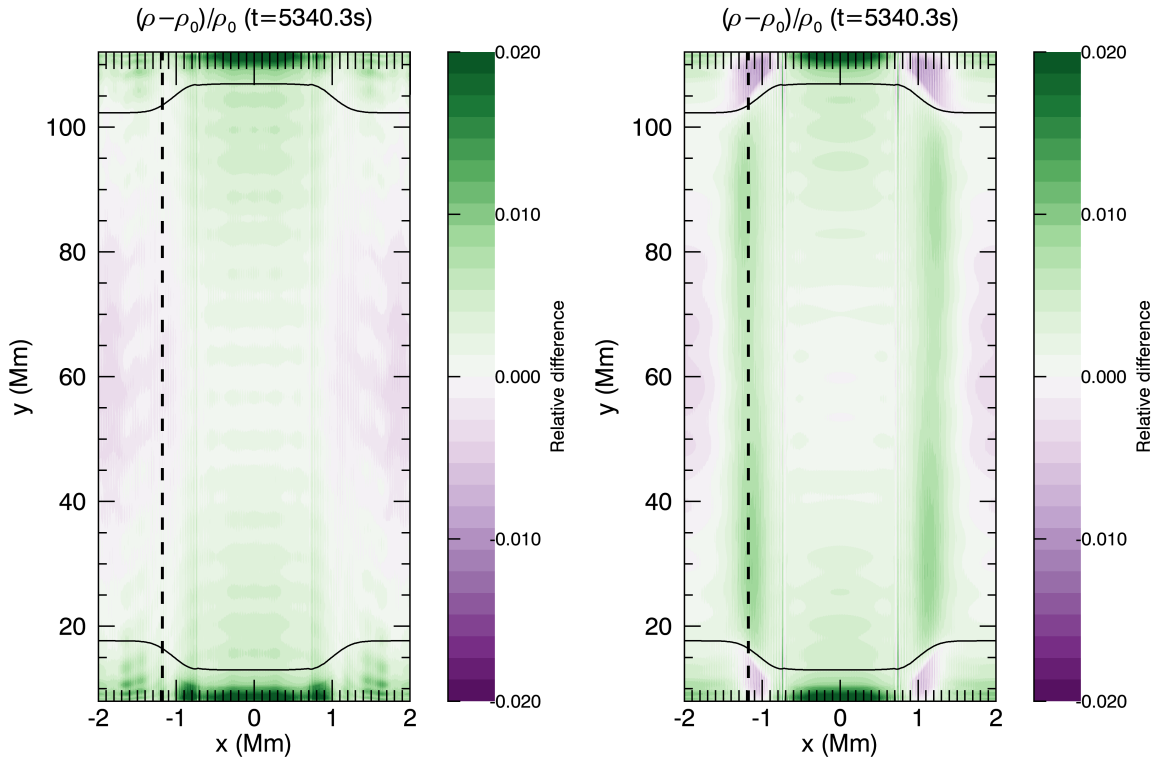

Figure 3.22: Contour of the relative density $(\rho - \rho_0)/\rho_0$ for the ideal (left panel) and the viscous simulation (right panel) at $t = 5340$ s.

distance contours of the relative density change $(\rho - \rho_0)/\rho_0$ along $x = -1.18$ Mm for the viscous (bottom panel) and the ideal simulation (top panel). In both contours the periodicity of the density changes is associated with the background long-period oscillations (~ 650 s) as discussed before. In the ideal simulation only the ponderomotive mass increase is present, visible as the green diagonal bands (at e.g. 900 s,1600 s) from the TRs into the corona which show a mass flow from the lower atmosphere into the corona (dotted lines). Similar diagonal features can also be seen in the contour of $T - T_{mean}$ in the shell region in the ideal simulation (Figure 3.18). In the viscous simulation a larger mass increase is present. For $t < 1000$ s the two panels do not differ much, but after $t \sim 1500$ s the evaporation is stronger which corresponds with the largest evaporative upflows (Figure 3.21) and the largest heating events by the dissipation of the phase-mixed Alfvén waves (Figure 3.18). The mass evaporation is present from both TRs into the corona, and both TRs show a decrease in the density when the evaporation starts.

Figure 3.24 shows a plot of the mass increase $\int(\rho - \rho_0)dV$ (kg/m) for the lower layers of the atmosphere (chromospheres and transition regions; green lines) and the corona (black lines), for the ideal (dashed line), viscous (solid line) and the continued

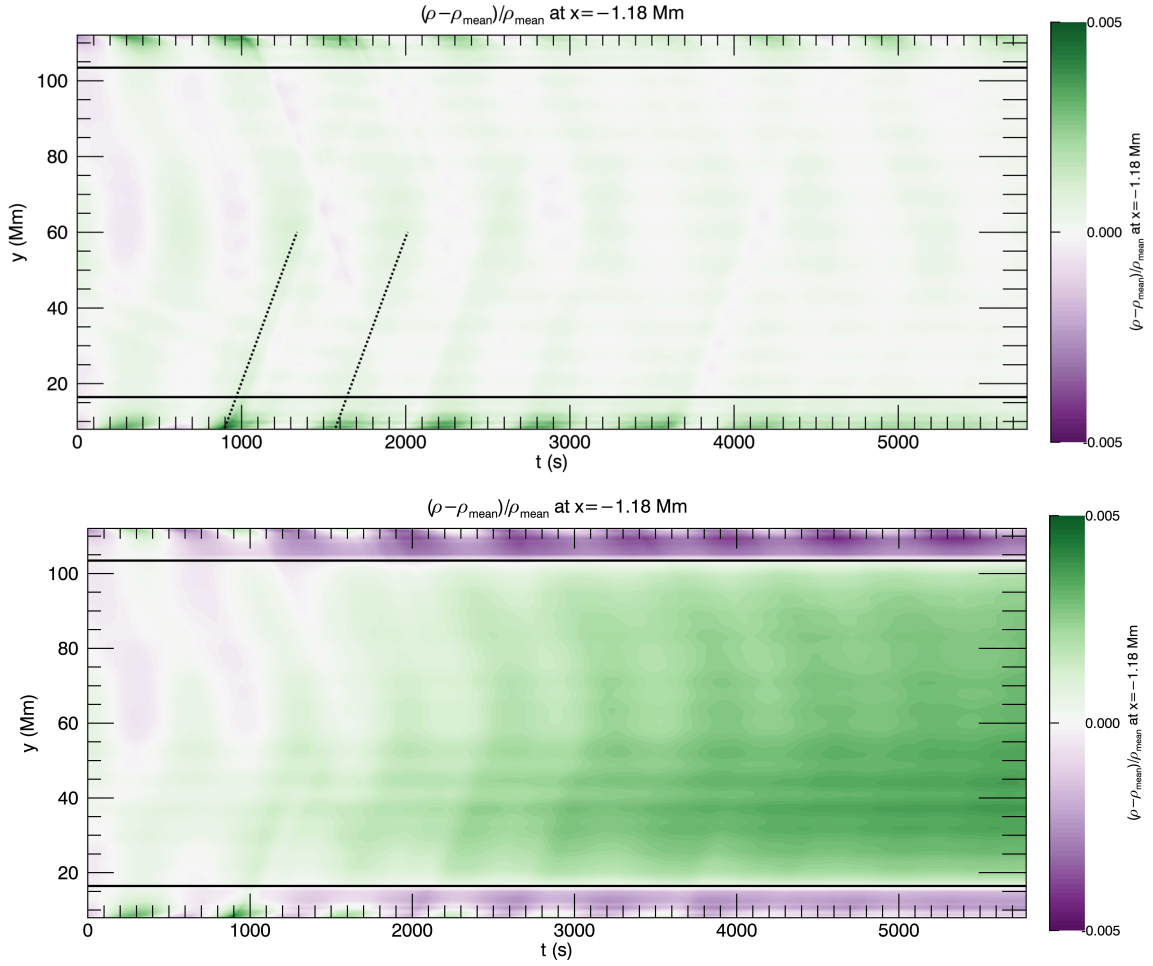

Figure 3.23: Time distance maps of $(\rho - \rho_{mean})/\rho_{mean}$ for the ideal (top panel) and the viscous simulation (bottom panel) in the shell of the loop ($x = -1.18$ Mm). The ρ_{mean} subtracted is taken over the last 5800 s in the continued relaxation simulation, for every y.

relaxation simulation (dotted line). This figure repeats the findings we found earlier. In the continued relaxation simulation there is no significant mass increase in the corona given that the upflows due to the background evolution are oscillatory (Figure 3.11). The ideal and the viscous simulation both show a mass increase in the corona, and a corresponding mass decrease in the TRs and the chromospheres. In the ideal simulation this is due to the implementation of the driver and the ponderomotive effect associated with the Alfvén waves, and in the viscous simulation there is the extra effect of the evaporation due to the (viscous) dissipation of the phase-mixed Alfvén waves. At the end of the simulation, the coronal mass increase (i.e. integrated over the entire coronal region of the numerical domain) in the viscous simulation is about 35% larger than the ideal simulation.

The right panel of Figure 3.24 shows the mass increase in the coronal part of the

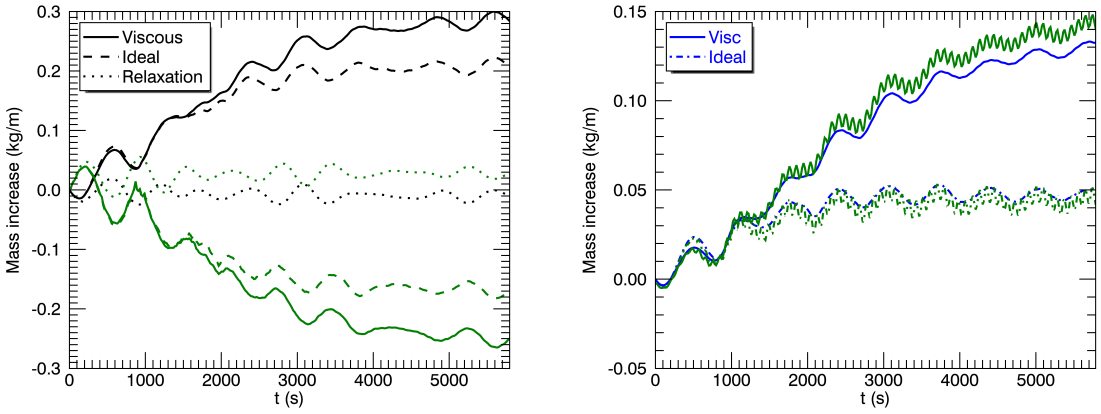

Figure 3.24: (Left) Plot of the mass change $\int (\rho - \rho_0)\, dV$ (kg/m) for the corona (black lines) and the CHROMs and TRs (green lines) for the ideal simulation (dashed lines), the viscous simulation (solid lines) and the continued relaxation simulation (dotted lines). (Right) Plot of the mass change $\int (\rho - \rho_0)\, dV$ (kg/m) for the shells of the loop (blue lines) for the viscous (solid line) and the ideal simulation (dotted-dashed line). The green lines are the time integrated average mass flux coming through the boundaries of the shells.

shells of the loop (blue) for the viscous (solid line) and the ideal simulation (dotted-dashed line). The green lines represent the time integrated averaged mass flux through the corona-TR boundaries of the shell, $\int_0^t \langle\rho\rangle(\langle\mathbf{v}\rangle \cdot \langle\mathbf{n}\rangle) L d\tilde{t}$, with L the length of the shell boundary and $\langle\mathbf{n}\rangle$ the average normal vector to each respective shell boundary. The mass increase in the shell region is about 2.5 times larger near the end of the simulation in the viscous case, due to the net evaporation from the dissipation of the phase-mixed Alfvén waves. The green lines confirm that the mass increase is due to a mass flux coming through the boundaries (hence an evaporation from the lower atmospheres).

We can estimate the evaporation that is required for the larger mass increase in the shells in the viscous simulation (right panel of Figure 3.24), using the continuity equation (Equation (3.1))

$$\frac{\partial \rho}{\partial t} = -\nabla \cdot (\rho \mathbf{v})\,.$$

Integrating both sides over the coronal volume of the shells (V) and over time from 0 to t gives

$$\int_V (\rho(t) - \rho(t=0))\, dV = -\int_0^t \int_S (\rho \mathbf{v}) \cdot \mathbf{n} dS d\tilde{t}. \tag{3.9}$$

where we have used the divergence theorem to rewrite the integral on the RHS. The inner integral on the RHS can be approximated by $\langle\rho\rangle\langle v_y\rangle 4L$, with L the width of

the shell, if we assume that most of the mass change is due to an evaporative upflow. This was already shown by the green curves in the right panel of Figure 3.24. Hence Equation 3.9 can be rewritten as

$$\frac{d}{dt}\left(\int_V (\rho(t) - \rho(t=0))\, dV\right) \approx \langle\rho\rangle\langle v_y\rangle 4L, \tag{3.10}$$

so the average upflow $\langle v_y\rangle$ through the shell boundaries can be approximated by

$$\langle v_y\rangle \approx \frac{1}{\langle\rho\rangle 4L}\frac{d}{dt}\left(\int_V (\rho(t) - \rho(t=0))\, dV\right). \tag{3.11}$$

By taking the difference in the mass increase in the coronal part of the shells between the viscous and the ideal simulation (the blue lines in the right panel of Figure 3.24), we get an approximation for the average evaporation $\langle v_{evap}\rangle$ through the shell boundaries.

$$\langle v_{evap}\rangle = \langle v_{y,visc}\rangle - \langle v_{y,ideal}\rangle \approx \frac{1}{\langle\rho_{ideal}\rangle 4L}\frac{d}{dt}\left(\int_V (\rho_{visc}(t) - \rho_{ideal}(t))\, dV\right), \tag{3.12}$$

where we have also used the fact that $\langle\rho_{visc}\rangle \approx \langle\rho_{ideal}\rangle$ on the shell boundary. Equation (3.12) is shown in the right panel of Figure 3.25. Initially $\langle v_{evap}\rangle$ is negative because the mass increase in the shells is initially larger for the ideal simulation (right panel of Figure 3.24). After $t > 1000$ s when the mass increase is larger for the viscous simulation, the evaporation is of the order of 10m/s, with a peak of 20m/s around $t \sim 2000$ s. This profile of the estimated evaporation is very similar to the actual difference (between the viscous and the ideal simulation) in the average upflows on the boundaries of the shell, as shown by the left panel of Figure 3.25, which was obtained from Figure 3.21.

Effect on the Alfvén speed gradient and the phase mixing

Figure 3.26 shows a plot of the relative temperature $\frac{T-T_0}{T_0}$, density $\frac{\rho-\rho_0}{\rho_0}$ and Alfvén speed $\frac{v_A-v_{A0}}{v_{A0}}$ in the upper half of the corona ($y = 88$ Mm) at the end of the simulation ($t = 5800$ s), for the ideal simulation (left panel) and the viscous simulation (right panel). At this location the strongest heating events (Figure 3.18) and the largest mass increase (Figure 3.23) were present. In the ideal simulation there is a small increase ($\sim 0.1\%$) in the density in the interior part of the loop, due to the ponderomotive effect of the driver. The viscous simulation shows a relative change in the temperature and the density of the order 0.3% in the shells of the loop, which leads to a decrease in the local Alfvén speed of $\sim 0.2\%$ (a similar change is not present in the ideal simulation).

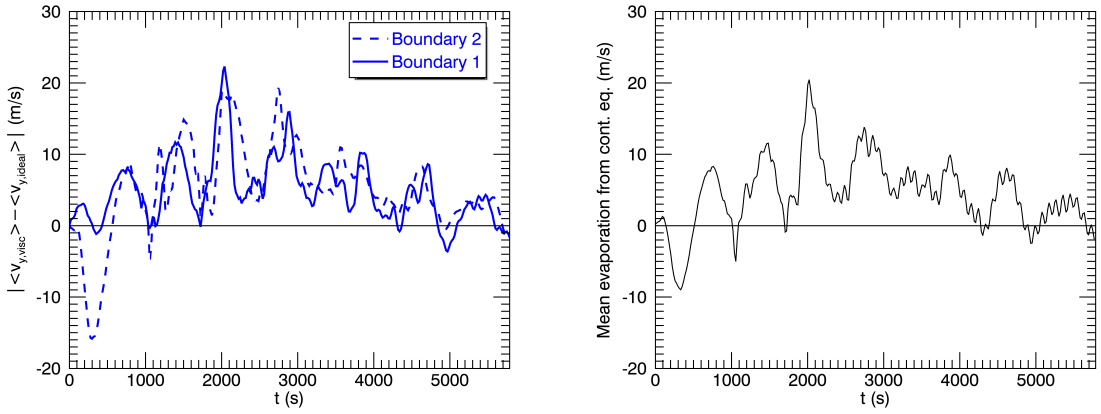

Figure 3.25: (Left) Plot of the difference in mean upflows $\langle v_{y,visc} \rangle - \langle v_{y,ideal} \rangle$ on the lower boundary (solid line) and the upper boundary (dashed line) of the left shell. (Right) Plot of the mean evaporation $\langle v_{evap} \rangle$ through the shell boundary, estimated from the continuity equation.

This is however insignificant compared to the Alfvén speed gradient ($\frac{v_{Ae}}{v_{Ai}} \sim 2$ at the apex) and hence, the effects are too small to significantly change the phase mixing process.

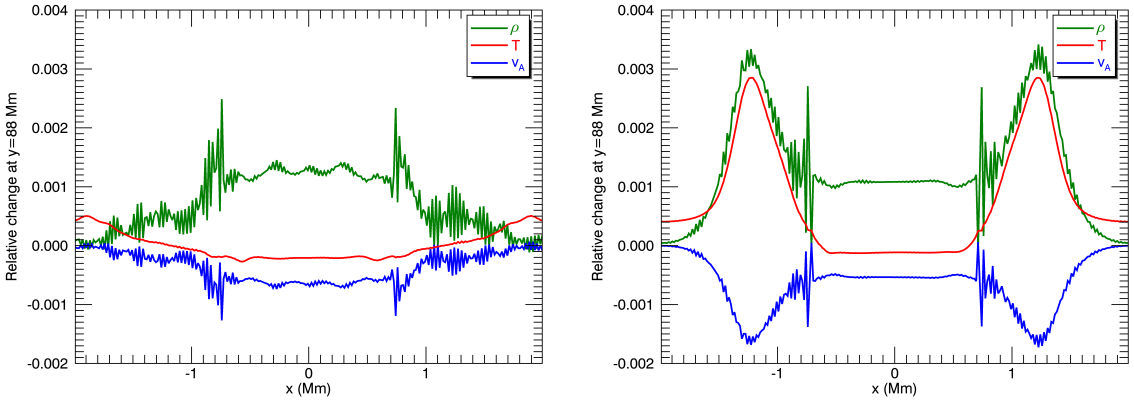

Figure 3.26: Plot of the relative change in T, ρ, v_A at $y = 88$ Mm, at the end of the simulation ($t = 5800$ s), for the ideal simulation (left) and the viscous simulation (right).

3.4 Discussion and conclusion

In this chapter, we have investigated whether a pre-existing density profile is modified by evaporative upflows following (viscous) heating from phase mixing of Alfvén waves.

Throughout the simulations (running for a total time of $\sim$ 6000 s), a complex combination of Alfvén waves (v_z) and longitudinal (field-aligned) flows (v_y) is present in the domain. The longitudinal flows are caused by (1) long-period oscillations ($\sim$ 650 s) resulting from the ongoing relaxation due to the imposed cross-field background heating profile, (2) the ponderomotive effects associated with the driven Alfvén waves and (3) the evaporative upflows resulting from (viscous) heating of the phase-mixed Alfvén waves in the coronal part of the shell regions of the loop. By comparing with the ideal simulation, we are able to distinguish the evaporative upflows present in the viscous simulation from the other (ideal) field-aligned perturbations. This allows us to identify the change in mass in the coronal part of the shell regions caused by the (viscous) heating from the phase-mixed Alfvén waves. For the particular setup studied in this chapter, we find that the amount of heating through viscous dissipation of the phase-mixed Alfvén waves in the corona is very small (maximal relative temperature increase of 1% in the shell regions). The evaporative upflows associated with this heating are insignificant and hence, in this study, the effect of the heating-evaporation cycle on the transverse density profile (or the Alfvén speed profile) is negligible.

One of the reasons for the small effects of the (viscous) heating from the phase-mixed Alfvén waves is the choice of our driver. The high-frequency driver (P $\sim$ 12 s) allows on the one hand the rapid development of phase mixing in the shell regions but on the other hand, a substantial amount of the Poynting flux (about 10-15%) is transmitted down to the far TR and chromosphere (see e.g. Hollweg 1984a,b; Berghmans and de Bruyne 1995; De Pontieu et al. 2001). We estimated that increasing the amplitude of the driven Alfvén waves by an order of magnitude would increase the Poynting flux by two orders of magnitude, which could account for the heating requirements of the Quiet Sun (see e.g. Withbroe and Noyes, 1977). However, given that 10-15% of the Poynting flux in the coronal shell regions is lost to the lower atmosphere, it remains to be investigated if this could have a substantial effect. Increasing the background field with an order of magnitude would also increase the Poyting flux further, although this would increase the coronal Alfvén speed and would lead to fewer wavelengths in the corona, smaller phase mixing gradients and less viscous dissipation from the phase-mixed Alfvén waves. In the interior of the loop, almost all energy (of the order of 85%) is transmitted to the far TR and chromosphere. The viscosity used in this study is a uniform viscosity and is two orders of magnitude smaller than the (parallel) viscosity in the corona (see e.g. Priest, 2014). However, the perpendicular (cross-field) viscosity is ten orders of magnitude smaller than the parallel viscosity (see e.g. Braginskii,

1965), hence it is likely that we have overestimated the effect of the viscosity on the (cross-field) phase mixing gradients (and the viscous dissipation) in this study.

Chapter 4

Transverse MHD waves generated by colliding clumps

In this chapter, we investigate the generation of transverse MHD waves in the solar corona by the collision of counter-propagating clumps. In particular, we describe the results of several parameter studies of the collision of two counter-propagating clumps. The results of these parameter studies have been published in Pagano et al. (2019). The parameter study builds on a 2D MHD model from Antolin et al. (2018) who analyse observations of collisions of clumps along a coronal rain complex at the limb of the Sun. Using the 2D MHD model, Antolin et al. (2018) interpret the generated oscillations as transverse MHD waves. In this chapter we conduct a parameter study to investigate how changing the properties of the clumps affects the wave generation.

4.1 Introduction

Over recent decades, MHD waves have been increasingly observed in the Sun's atmosphere (e.g. Tomczyk et al. (2007), De Moortel and Nakariakov (2012), Arregui (2015)). Observations have shown that these waves can have a photospheric/chromospheric origin, i.e. they are generated by photospheric footpoint motions driven by convective cells beneath the photosphere (e.g. Suzuki and Inutsuka (2005), Matsumoto and Kitai (2010)). However, waves that are generated in the lower layers of the atmosphere, can undergo strong reflection when propagating into the corona (e.g. Soler et al. (2017)).

Besides being generated in the lower layers of the Sun's atmosphere, MHD waves can also be excited in-situ in the corona. A series of studies (Kohutova and Verwichte (2017), Kohutova and Verwichte (2018a), Verwichte and Kohutova (2017) and Verwichte et al. (2018)) showed that transverse MHD waves can be excited in coronal rain

systems. Coronal rain systems typically consist of a coronal loop which is subject to the thermal instability and undergoes a cycle of condensations (e.g. Antiochos et al. (1999) and Antolin et al. (2010a)). During these cycles the loop cools drastically and dense blobs of plasma form in the interior of the loop. These blobs, coronal rain, then fall along the loop towards lower heights under the force of gravity. The formation of coronal rain can perturb the magnetic field and excite transverse oscillations, as reported by Kohutova and Verwichte (2017), Kohutova and Verwichte (2018a), Verwichte and Kohutova (2017) and Verwichte et al. (2018). Another way that coronal rain can generate transverse oscillations is by collisions with other plasma material. Falling coronal rain can collide with hotter material propagating upwards in the loop (e.g. from evaporation of chromospheric material). These counter-propagating clumps of plasma can collide and perturb the magnetic field, leading to transverse oscillations of the coronal strands. Antolin et al. (2018) observed collisions of counter-propagating clumps along a coronal rain complex, and analysed the oscillations produced by these collisions. They modelled the colliding clumps using 2D MHD simulations and interpreted these transverse oscillations as transverse kink and sausage modes. They conclude that the mechanism of colliding clumps can be a source of transverse MHD waves in the corona.

The parameters of the simulation in the MHD model introduced in Antolin et al. (2018) were chosen to match one particular observation of transverse oscillations by colliding clumps. However, there remains open questions about the mechanism of generating transverse oscillations by colliding flows/clumps, such as the evolution of the forces during the collision and the influence of different parameters of the flows on the generation of the oscillations. In this chapter, we analyse the mechanism and the evolution of the forces during the collision in more detail. We also present a parameter study to investigate how different parameters of the clumps affect the nature of the generated transverse MHD waves. The parameter studies we consider are varying (1) the density and the velocity of the clumps, (2) the speeds of the clumps, (3) the distribution of the mass of the clumps, (4) the angle of the colliding interface of the clumps, (5) the offset between rectangular clumps, (6) the length of the clumps and (7) the width of the clumps. Studies (1), (2) and (3) are related to the momentum and kinetic energy of the clumps, studies (4), (5) are related to the asymmetry of the system and studies (6) and (7) to the dimensions of the clumps. In future studies, we would like to investigate if these collisions of counter-propagating clumps are common in the corona, and if they can contribute to the energy budget of the corona

(coronal heating). These collisions could also be an interesting tool for helioseismology.

This chapter is outlined as follows. In Section 4.2 we introduce the numerical MHD model used for the parameter studies and describe in detail a 'reference simulation'. This reference simulation is a scenario where two clumps of plasma collide and transverse MHD waves are generated. We analyse the evolution of the forces and introduce a method for measuring the amplitudes of the generated modes. Next, we discuss the 7 parameter studies outlined in the previous paragraph. These are separated in three sections: in Section 4.3 we discuss the parameter studies related to the momentum and the kinetic energy of the clumps, by changing the density and the velocity of the clumps. In Section 4.4 we discuss the effect of asymmetry in the system on the generated modes, by considering a change in the inclined colliding interface and an offset between the clumps. In Section 4.5 we discuss how the dimensions of the clumps - changing the length and the width of the clumps - can change the generated modes. We end the chapter with a discussion and a conclusion in Section 5.6.

4.2 Model setup and reference simulation

Using the numerical MHD code MPI-AMRVAC (Porth et al., 2014), we implement a 2D model for counter-streaming plasma clumps. This code solves the ideal MHD equations given by

$$\frac{\partial \rho}{\partial t} + \boldsymbol{\nabla} \cdot (\rho \mathbf{v}) = 0, \tag{4.1}$$

$$\frac{\partial (\rho \mathbf{v})}{\partial t} + \boldsymbol{\nabla} \cdot (\rho \mathbf{v}\mathbf{v}) = -\boldsymbol{\nabla} P + \frac{1}{c}\mathbf{j} \times \mathbf{B}, \tag{4.2}$$

$$\frac{\partial \mathbf{B}}{\partial t} = \boldsymbol{\nabla} \times (\mathbf{v} \times \mathbf{B}), \tag{4.3}$$

$$\frac{\partial e}{\partial t} = -\boldsymbol{\nabla} \cdot \left[\left(e + P + \frac{B^2}{8\pi} \right) \mathbf{v} - (\mathbf{B} \cdot \mathbf{v}) \mathbf{B} \right]. \tag{4.4}$$

Remark that the MHD equations stated here are in *cgs* units, with c the speed of light, $\mathbf{j} = \frac{c}{4\pi} \boldsymbol{\nabla} \times \mathbf{B}$ the current density and $e = \frac{P}{\gamma - 1} + \frac{1}{2}\rho v^2 + \frac{B^2}{8\pi}$ the total energy. We assume that the plasma is fully ionised. Although coronal rain is only partially ionised (Antolin and Rouppe van der Voort, 2012), Oliver et al. (2016) showed that in the case of partially ionised plasmas the neutrals are still coupled to the ions (even in the case of 50% ionisation the coupling is strong). Hence in this study the particles are still coupled to each other and can be treated as a single MHD fluid. A contour of the

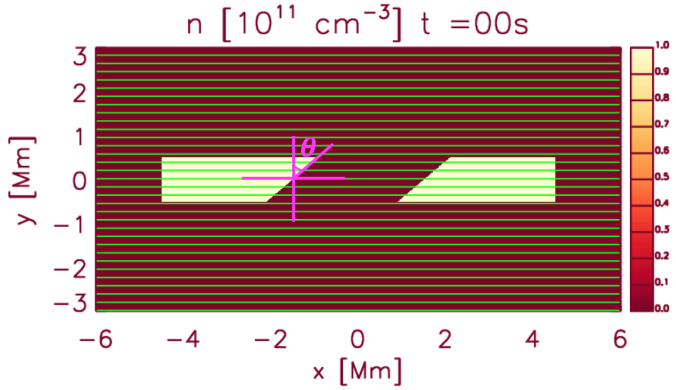

Figure 4.1: Contour of the number density n at $t = 0$ s, with magnetic fieldlines (green) overplotted (traced from the $x = -6$ Mm boundary). The angle θ of the interface of the clumps is denoted in pink.

number density n at $t = 0$ s of the reference simulation is shown in Figure 4.1.

The numerical domain is a 2D, cartesian domain and has dimensions 12 Mm (x-direction) by 6 Mm (y-direction). Two trapezoidal clumps of plasma, both 1 Mm wide (in y) and 3 Mm long (in x, measured along $y = 0$), are placed opposite one another in the x-direction at a distance of 3 Mm. The angle of the interface of the clumps is $\theta = 50$ degrees with the positive y axis (see Figure 4.1). The magnetic field is uniform and in the x-direction, $B_x = 6.5$ G. The clumps are 100 times denser than the coronal background number density, $n_{ext} = 1.2 \times 10^9$ cm^{-3} ($n_{clump} = 100 n_{ext}$). The background temperature is 1 MK, and the temperature of the clumps is 100 times cooler to maintain pressure equilibrium ($T_{clump} = 10^4$ K). The plasma beta is $\beta \sim 0.1$. The clumps travel towards each other at an initial velocity of ± 70 km/s, which is chosen to match the observations presented in Antolin et al. (2018). The external Alfvén speed is $v_{A,ext} = 580$ km/s and the external sound speed is $c_{s,ext} = 165$ km/s. This results in an external Alfvén Mach number of $M_{A,ext} = \frac{v}{v_{A,ext}} = 0.12$ and an external Mach number of $M_{S,ext} = \frac{v}{c_{s,ext}} = 0.42$, so we do not expect the formation of shocks when the clumps are propagating. The internal Alfvén speed ($v_{A,int} = 58$ km/s) and internal sound speed ($c_{s,int} = 16.5$ km/s) are however 10 times smaller and hence the internal Mach number ($M_{S,int} = 4.2$) and Alfvén Mach number ($M_{A,int} = 1.2$) are 10 times larger than their external counterpart. Since the Mach numbers are larger than 1, information cannot be transmitted upstream inside the clumps when they are propagating, which will lead to a more violent collision. The ram pressure ρv^2 of the clumps is 0.5 J/m^3 and this is 30 times larger than the thermal pressure and 3 times larger than the magnetic pressure. Note that these ratios are proportional to the square of the Mach number and the square of the Alfvén Mach number respectively.

The boundary conditions in the simulation are continuous in x and y (i.e. the values in the outmost cell in the domain are copied in the ghost cells), which allows plasma to leave the domain. The simulation runs for 300 s, which is sufficient for the system to reach a new equilibrium after the collision. Hereafter we refer to this simulation as "the reference simulation", as we will take this simulation as a benchmark to compare with.

4.2.1 Collision

Figure 4.2 shows contours of the density, pressure and temperature at $t = 25, 66, 78$ s (1st, 2nd and 3rd column respectively). These times are chosen to represent the different phases of the simulation. In a first phase of the simulation ($t < 66$ s) the clumps are propagating towards each other and are colliding, and their kinetic energy is used to deform the magnetic field. We refer to this phase as the 'collision phase'. At $t = 66$ s the magnetic field deformation reaches a maximum, and for $t > 66$ s the system responds to the collision and produces oscillations as it evolves towards a new equilibrium. The generated waves propagate in the domain, and we will refer to this phase as the 'propagation phase'.

In the early stage of the collision phase, the two clumps of plasma approach each other and compress the plasma in front of the clumps. This leads to an increase of the gas pressure and the temperature in the region between the two clumps as can be seen in the contour of the pressure and the temperature at $t = 25$ s. The contour of the temperature shows an increase up to 3 MK in the region between the clumps, which is the maximal temperature over the whole simulation. This temperature is only attained for a few seconds, after which it decreases because of mixing with cooler plasma. This increase of pressure in the middle of the domain leads to strong gradients causing a pressure gradient force ($\boldsymbol{\nabla} P$) pointing outwards of the middle of the domain. The x component $(\boldsymbol{\nabla} P)_x$ slows the clumps down and the y component $(\boldsymbol{\nabla} P)_y$ creates a v_y and causes a distortion of the magnetic field. This can be seen in the contour of v_y at $t = 25$ s in Figure 4.5. The contour of the density at $t = 25$ s shows the expansion of the magnetic field in the y direction in the middle of the domain. The magnetic field is mostly deformed on the interface where the clumps initially touch. Because the interface of the clumps is at an angle, the deformation is also tilted and asymmetric.

At $t = 66$ s the magnetic fieldlines show a significant deformation. The internal magnetic field (the magnetic field inside the clumps ($-0.5 < y < 0.5$ Mm)) shows an

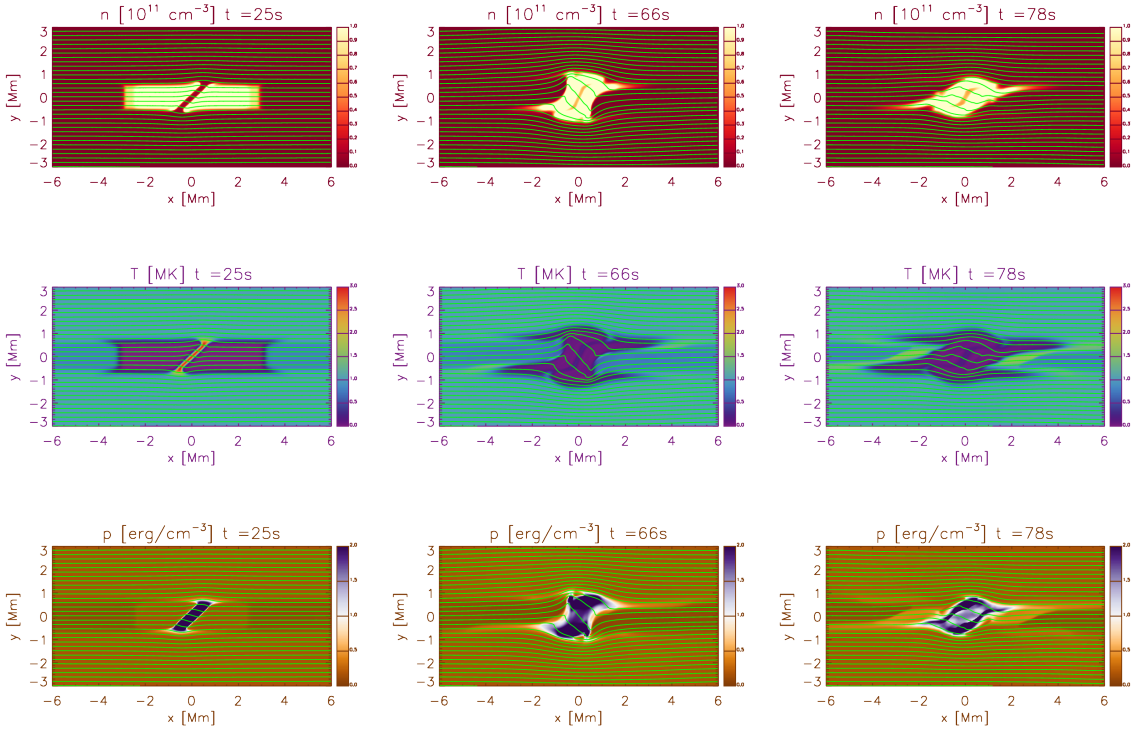

Figure 4.2: Contours of the density, temperature and pressure at $t = 25, 66, 78$ s for the reference simulation.

asymmetric deformation because of the inclined interface of the clumps. The external field has expanded due to the higher gas pressure caused by the collision. After the collision phase ($t > 66$ s) the system responds to the collision and generates several oscillations. In Subsection 4.2.3 we will discuss the generated modes in greater detail.

Energies and forces

We now discuss the evolution of the different volume integrated energies and forces in the simulation to understand the collision and the response of the system. Figure 4.3 shows a plot of the volume integrated kinetic, magnetic and internal energy in the domain with time (minus their initial value). We look at the kinetic energy in the x direction and the y direction separately. Similarly the magnetic energy is split up in an x component and a y component.

The vertical dashed line at $t = 66$ s divides the simulation into the 'collision phase' ($t < 66$ s) and the 'propagation phase' ($t > 66$ s). In the first phase, the clumps of plasma travel towards each other and slow down due to the increase of gas pressure (pressure gradient force $(\boldsymbol{\nabla} P)_x$) in the middle of the domain. This leads to a decrease in v_x and a decrease in the x component of the kinetic energy ($\int \frac{\rho v_x^2}{2} \mathrm{dV}$; blue solid

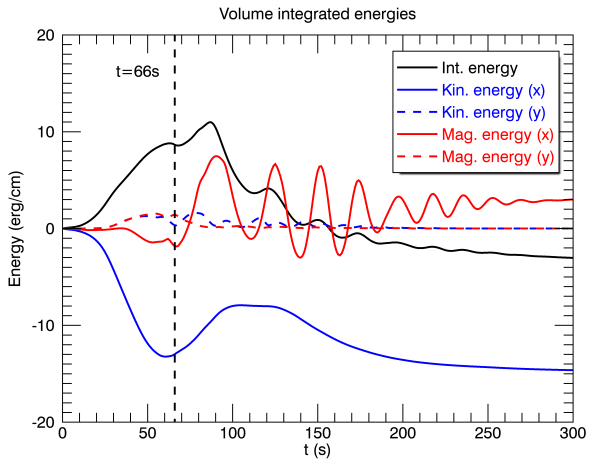

Figure 4.3: Plot of the volume integrated energies (minus their initial value) with time for the reference simulation. The dashed line at $t = 66$ s marks the two phases in the simulation: a 'collision phase' ($t < 66$ s) and a 'propagation phase' ($t > 66$ s).

line). The y component of the kinetic energy ($\int \frac{\rho v_y^2}{2} \mathrm{dV}$; blue dashed line) increases slightly as the pressure gradient force $(\boldsymbol{\nabla} P)_y$ generates a v_y. The internal energy ($\int \frac{p}{\gamma - 1} \mathrm{dV}$; black line), increases as the plasma between the clumps is compressed and is adiabatically heated. The x component of the magnetic energy ($\int \frac{B_x^2}{2\mu_0} \mathrm{dV}$; solid red line) decreases because the internal magnetic field is kinked by the collision, decreasing B_x and increasing B_y. Hence we see an increase in the y component of the magnetic energy ($\int \frac{B_y^2}{2\mu_0} \mathrm{dV}$; dashed red line).

In Figure 4.4 we show vector plots of the pressure gradient force $\boldsymbol{\nabla} P$ and the Lorentz force $\mathbf{j} \times \mathbf{B}$ at $t = 25, 66, 78$ s. The vector plots at $t = 25$ s show that the pressure gradient force $\boldsymbol{\nabla} P$ is mainly perpendicular to the interface of the clumps ($\theta = 50$ degrees), opposing the direction of propagation of the clumps. The x component slows the clumps down and the y component accelerates the plasma in the y direction, leading to a distortion of the magnetic field. The vector plot of the Lorentz force $\mathbf{j} \times \mathbf{B}$ at $t = 25$ s shows that the Lorentz force acts as a restoring force, since it is mainly pointing in the y direction towards the centre of the domain. This is due to a magnetic tension force and magnetic pressure gradient force caused by the expansion of the external magnetic field as a result of the collision. In Figure 4.6 we show the forces in the y direction and the speed v_x and v_y averaged over the rectangular box shown in the top panel. The vertical dashed lines at $t = 25, 66, 78$ s are the same times as the contours shown in Figures 4.4 and 4.5. During the collision phase we again see an increase in the pressure gradient force $(\boldsymbol{\nabla} P)_y$ and a build up of the restoring Lorentz force $(\mathbf{j} \times \mathbf{B})_y$ as the magnetic field expands. The pressure gradient force is larger in the first 40 s

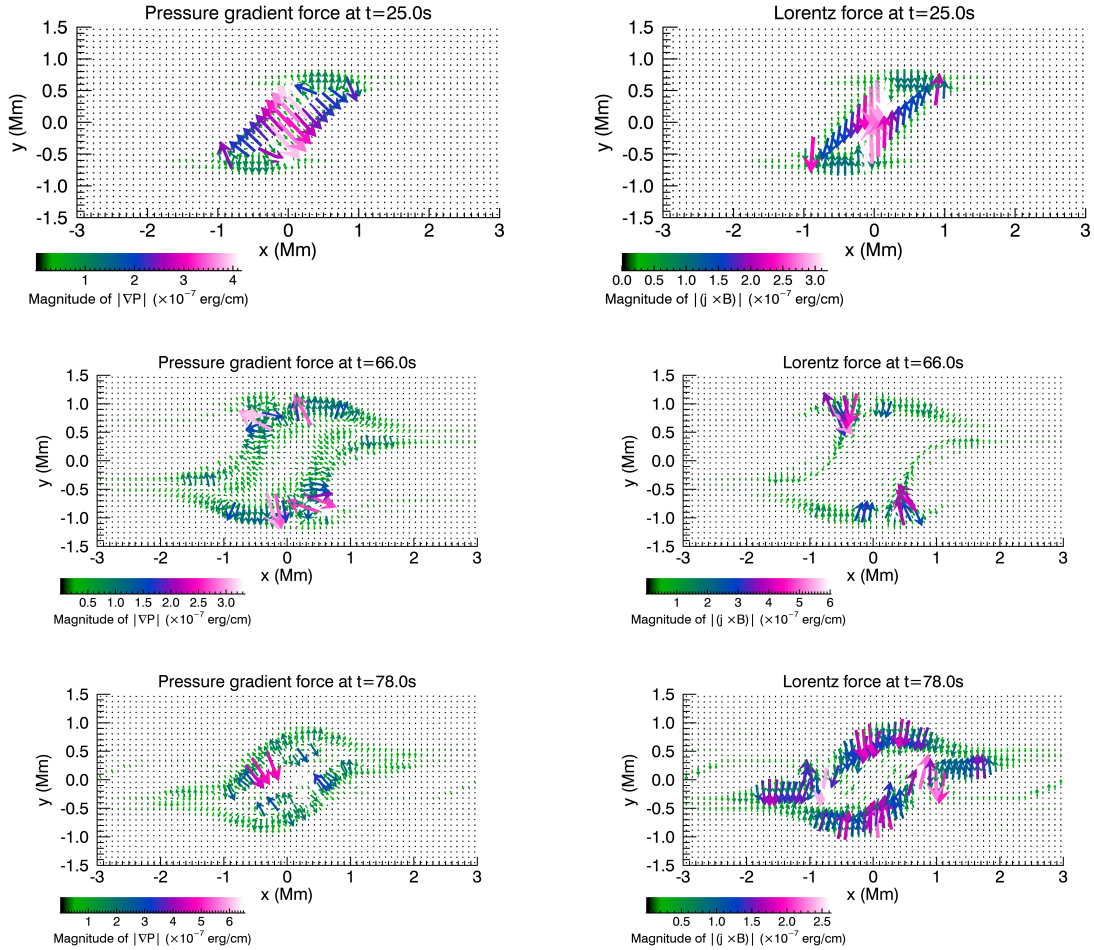

Figure 4.4: Vector plots of the pressure gradient force $\boldsymbol{\nabla} P$ (left column) and the Lorentz force $\mathbf{j} \times \mathbf{B}$ (right column) at $t = 25, 66, 78$ s.

of the simulation, which explains the increase in v_y in this period. After $t = 40$ s, the restoring Lorentz force becomes larger and the overall force is pointing inwards. We see a stagnation in v_y because the collision continues at this stage and plasma is still coming into the centre of the domain. Only at $t = 60$ s does v_y start to decrease and 4s later, v_x starts to decrease as well, reversing the motion of the plasma. At $t = 66$ s, the restoring Lorentz force reaches its maximum. At this time the magnetic field has been deformed maximally by the collision. The Lorentz force then drives the oscillatory behaviour seen in the propagation phase. The contour of $\mathbf{j} \times \mathbf{B}$ at $t = 66$ s (Figure 4.4) shows that the Lorentz force is directed inwards and is larger than the opposing pressure gradient force. The contour of v_y at $t = 66$ s shows the reversement of the plasma motion.

In the propagation phase ($t > 66$ s), the system responds to the collision and undergoes a series of oscillations as it tries to reach a new equilibrium. This oscillatory

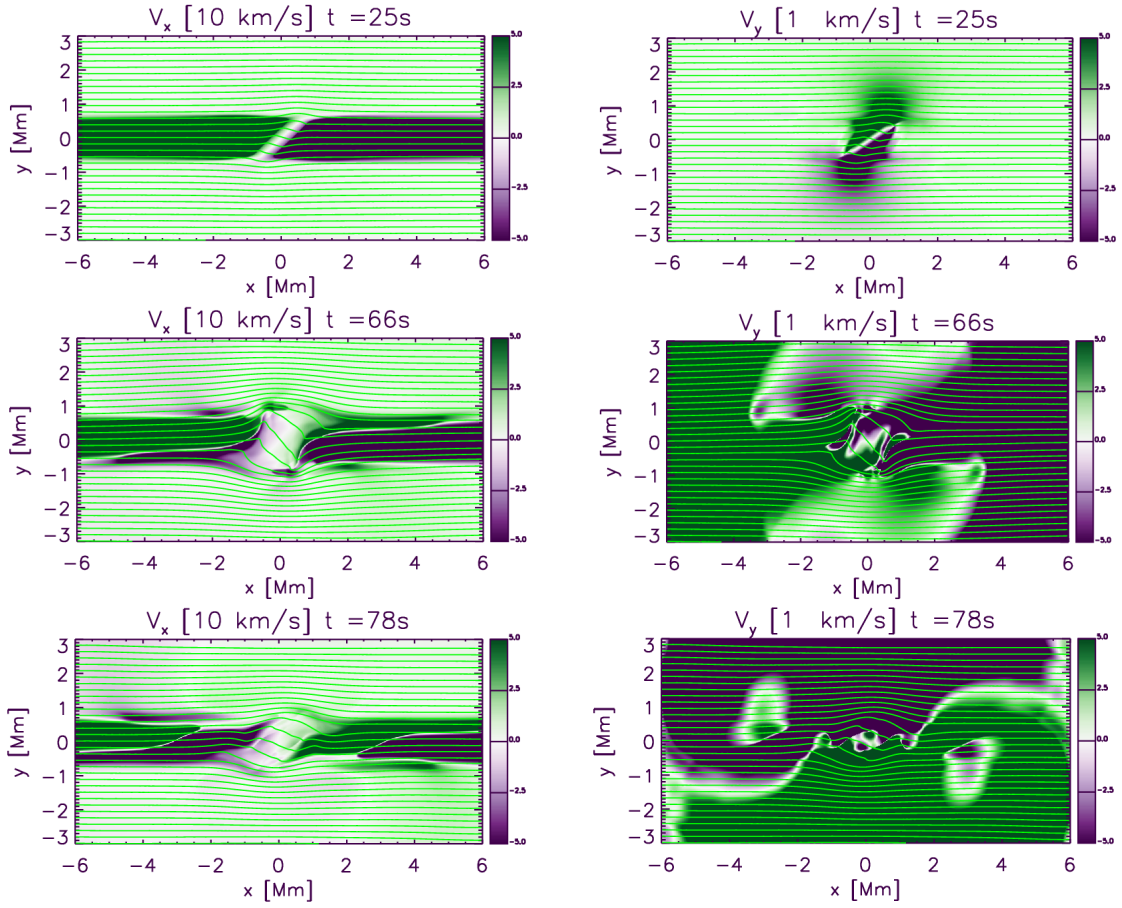

Figure 4.5: Contours of the velocity components v_x (left column) and v_y (right column) at $t = 25, 66, 78$ s.

behaviour can be seen in $\int \frac{p}{(\gamma-1)}\mathrm{dV}$, $\int \frac{\rho v_y^2}{2}\mathrm{dV}$ and $\int \frac{B_x^2}{2\mu_0}\mathrm{dV}$ (Figure 4.3). The local maxima and minima in the internal energy correspond to compressions followed by rarefractions of the plasma. The internal energy overall is decreasing as the plasma evolves to a new equilibrium after the collision. Note that after $t = 150$ s the internal energy is below its initial value, because at this time plasma starts to leave the domain. Hence the total energy of the system is not conserved. The oscillations in $\int \frac{\rho v_y^2}{2}\mathrm{dV}$ represent the compressions and expansions of the system as a response to the collision. We see that $\int \frac{B_x^2}{2\mu_0}\mathrm{dV}$ also oscillates as magnetic field is leaving and entering through the y boundaries ($y = \pm 3$ Mm) as a response to the oscillations. The x component of the kinetic energy starts to increase again as the plasma motion is inverted and the flows travel now outwards from the centre of the domain. This can be seen in the contour of v_x at $t = 78$ s in Figure 4.5. After $t = 150$ s the x component of the kinetic energy starts to decrease as plasma is leaving the domain. The contours of the forces and velocities at $t = 78$ s show the system during one of its oscillations. The restoring

Lorentz force points inwards to the centre of the domain and v_y is directed towards the centre of the domain, which means the system is compressing at $t = 78$ s. In Figure 4.6 the propagation phase is characterised by a strong oscillatory $(\mathbf{j} \times \mathbf{B})_y$ and v_y. v_x becomes negative as the motion of the plasma has reverted and plasma flows away from the centre of the domain. It takes about 6-7 oscillations to damp v_y and $(\mathbf{j} \times \mathbf{B})_y$.

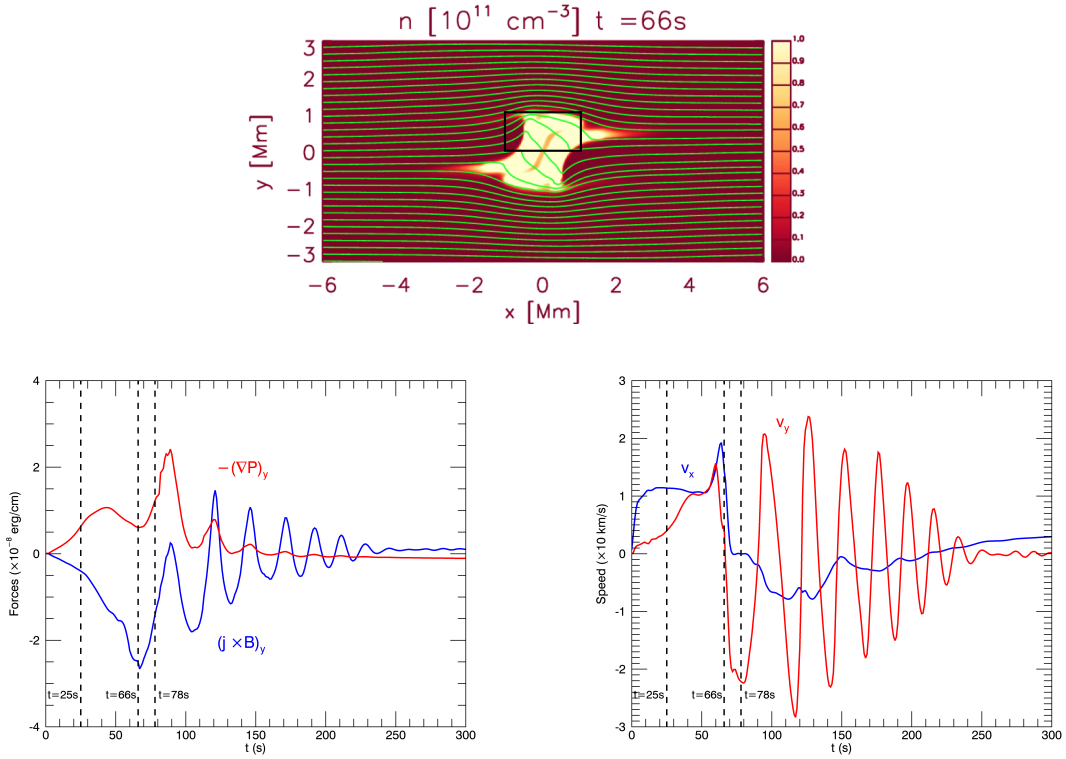

Figure 4.6: Plots of the average forces (left) and speed (right) with time in the rectangular box shown in the top panel. The rectangular box ranges from $-1 < x < 1$ Mm and $0 < y < 1$ Mm.

4.2.2 Measurement of the amplitudes

In this subsection we explain how the amplitudes of the generated modes are measured. Figure 4.7 illustrates with a 2D example how the amplitudes are measured. Suppose we have an initial straight waveguide with boundaries given by the horizontal magnetic fieldlines L_1, L_2 (dashed black lines). At a later time, the waveguide has been deformed and the boundaries L_1 and L_2 are now given by the black solid lines. The deformation consists of a displacement of the central axis of the waveguide ("a kink-like perturbation") and a compression/expansion about the central axis ("a sausage-like perturbation"). The central axis of the waveguide at $t = 0$ s is the line $y = 0$.

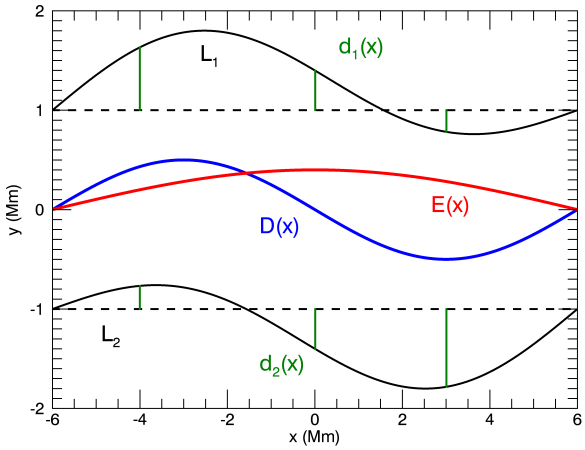

Figure 4.7: Illustration of how the kink and sausage amplitudes are measured. The black lines L_1 and L_2 are magnetic fieldlines placed symmetrically about the central axis ($y = 0$) of a waveguide, that undergoes a kink and sausage-like perturbation. The function $D(x)$ represents the displacement of the central axis, the function $E(x)$ an expansion/compression about the central axis.

We define $d_1(x)$ ($d_2(x)$) as the displacement of the fieldline L_1 (L_2) compared to its initial position. This is shown by the green vertical lines for some x in Figure 4.7. Remark that $d_1(x)$ ($d_2(x)$) is positive when $L_1(x) > 1$ Mm ($L_2(x) > -1$ Mm) and negative otherwise. The displacement of the central axis of the waveguide at each x is then given by

$$D(x) = \frac{d_1(x) + d_2(x)}{2}.$$

The expansion/compression about the central axis of the waveguide at each x is given by

$$E(x) = \frac{d_1(x) - d_2(x)}{2}.$$

These two quantities are illustrated by the blue and red line, respectively. We can use $D(x)$ ($E(x)$) for the definition of the kink-like (sausage-like) amplitude of the generated perturbations in our simulation. For each time t we define a kink amplitude $K(t)$ as the total displacement of the central axis of the waveguide,

$$K(t) = \max(D(x)) - \min(D(x)).$$

The sausage amplitude $S(t)$ is defined as the total expansion/compression about the central axis,

$$S(t) = \max(E(x)) - \min(E(x)).$$

Because the collision of two clumps of plasma is a highly dynamical and complex sys-

tem, the system is not an ideal waveguide, and the generated perturbations are highly non-linear. We do not claim that $K(t)$ and $S(t)$ are the amplitudes of the kink mode and the sausage mode, but they give an indication of the total energy of these modes.

To apply this method to the simulation, we identify a pair of internal and external fieldlines. Figure 4.8 shows the pair of internal (dark blue lines) and external fieldlines (pink lines) for $t = 0$ s and $t = 63$ s, together with a contour of the density and the magnetic fieldlines overplotted in green. The magnetic fieldlines are traced from the left hand boundary ($x = -6$ Mm) throughout the simulation. The internal fieldlines are at $y = \pm 0.1$ Mm initially. The external fieldlines are determined from a density threshold (i.e. the density of the clumps) such that this pair of fieldlines initially encloses the two clumps. The location of this pair of fieldlines is initially at $y = \pm 0.5$ Mm. We apply the method described previously in Figure 4.7 to these two pairs of fieldlines. Figure 4.9 shows the evolution of $K(t)$ and $S(t)$ for these two pairs of fieldlines. We denote by $K_{int}(t)$ and $S_{int}(t)$ ($K_{ext}(t)$ and $S_{ext}(t)$) the evolution of $K(t)$ and $S(t)$ for the internal (external) fieldlines. Except for the initial phase of the simulation ($t < 40$ s), we can see that K_{int} is always larger than K_{ext}, and similarly that S_{ext} is larger than S_{int}. This happens because the internal fieldlines are closer to the central axis and they show the displacement/kinking of the central axis more clearly. The external fieldlines show more expansion than the internal fieldlines as they are outside the collision region and they respond stronger to the expansion caused by the collision. In the analysis that follows we will use the internal fieldlines to measure "the kink amplitude" $K(t)$ and the external fieldlines are used to measure "the sausage amplitude" $S(t)$.

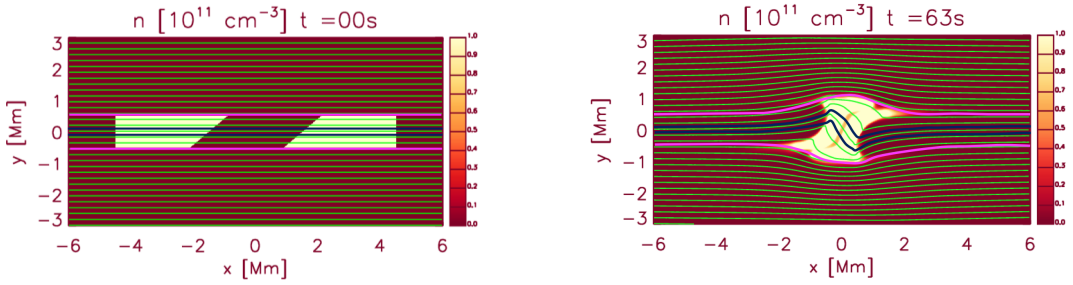

Figure 4.8: Contours of the density for $t = 0$ s and $t = 63$ s, with magnetic fieldlines (green) overplotted. The black fieldlines are internal fieldlines used for the measurement of $K(t)$, the pink fieldlines are external fieldlines used to measure $S(t)$.

In Figure 4.10 we show how the measurement of the kink amplitude $K(t)$ (i.e. $K_{int}(t)$) and sausage amplitude $S(t)$ (i.e. $S_{ext}(t)$) is applied in the simulation at $t = 63$ s. The left panel shows the internal fieldlines (black lines) together with the displacement

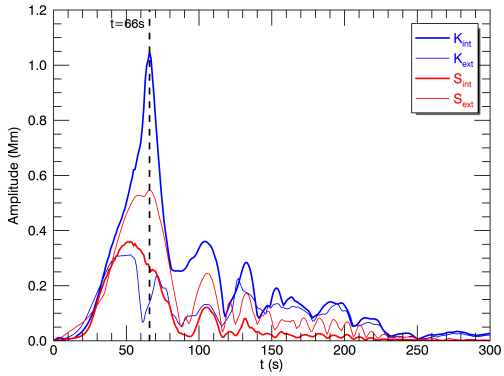

Figure 4.9: Plot of the evolution of $K_{int}(t), K_{ext}(t)$ in blue and $S_{int}(t)$ and $S_{ext}(t)$ in red. The thicker (thinner) lines represent the amplitudes for the internal (external) fieldlines.

$D(x)$ (blue line) of the central axis and the resulting kink amplitude $K(t = 63\text{ s}) \approx 0.95$ Mm. Similarly, the right panel shows the external fieldlines (black lines) together with the expansion $E(x)$ (red line) of the waveguide about the central axis and the resulting sausage amplitude $S(t = 63\text{ s}) \approx 0.45$ Mm.

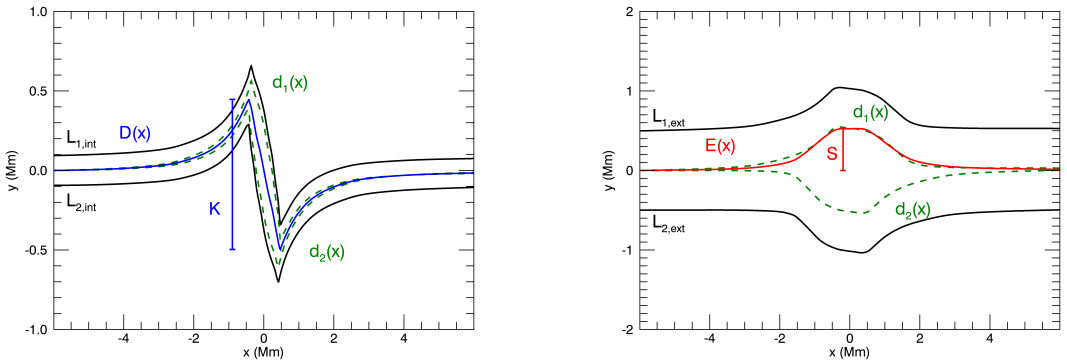

Figure 4.10: Measurement of the kink amplitude $K(t)$ (left panel) and sausage amplitude $S(t)$ (right panel) for the reference simulation at $t = 63$ s.

4.2.3 Analysis of the amplitudes of the generated modes

In Figure 4.11 (left panel) we show the kink amplitude $K(t)$ (blue line) and sausage amplitude $S(t)$ (red line) for the reference simulation with time. The kink amplitude $K(t)$ increases during the collision phase ($t < 66$ s) as the internal magnetic fieldlines are continuously deformed by the collision of the clumps. The asymmetric setup of the clumps (the interface of the clumps is inclined at an angle of $\theta = 50°$) is crucial in the kinking of the internal fieldlines and is investigated in detail in Section 4.4.1. Both the

maximal amplitudes $\max(K(t))$ and $\max(S(t))$ are attained at $t = 66$ s. After $t = 66$ s, the kink amplitude decays and shows an oscillatory behaviour as the system responds to the collision. The sausage amplitude $S(t)$ shows a similar behaviour. It increases initially as the external magnetic field expands from the collision and then decays in a similar manner as the kink amplitude.

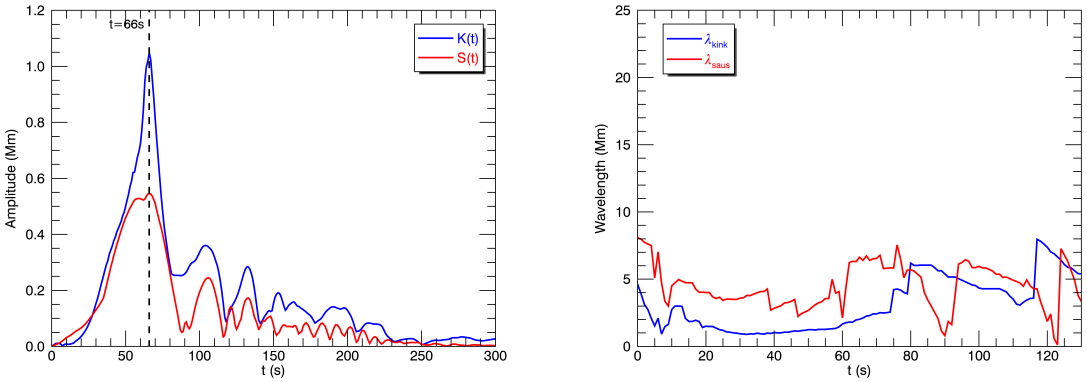

Figure 4.11: (Left) Plot of the kink amplitude $K(t)$ (blue line) and sausage amplitude $S(t)$ (red line) with time for the reference simulation. (Right) Plot of the kink wavelength λ_{kink} and the sausage wavelength λ_{saus} with time.

Maxima	P_{kink}	P_{saus}
1st & 2nd	76 s	80 s
2nd & 3rd	56 s	30 s
3rd & 4th	42 s	24 s

Table 4.1: Table with the period of the kink oscillation P_{kink} and the period of the sausage oscillation P_{saus}, determined from the time difference of the local maxima of the oscillations in Figure 4.11.

From the oscillations in the kink amplitude $K(t)$ and sausage amplitude $S(t)$ in Figure 4.11 we can deduce an estimate for the period of the generated modes using the time difference in the local maxima of the oscillations. This is half the period because a consecutive maximum is reached when $K(t)$ reverses its profile. Table 4.1 shows the period P_{kink} for the kink mode and P_{saus} for the sausage mode determined from the first four local maxima ($t = 66, 104, 132, 153$ s for $K(t)$ and $t = 66, 106, 121, 133$ s for $S(t)$). The period P_{kink} is initially 76 s but decreases to 42 s later in the simulation. The period P_{saus} similarly decreases from 80 s to 24 s. Near the end of the simulation the sausage period P_{saus} is of the order of ~ 20 s which is consistent with the transverse Alfvén travel time in the clumps. The right panel of Figure 4.11 shows the wavelength

λ_{kink} of the kink mode (blue) and λ_{saus} of the sausage mode (red) with time. The kink wavelength λ_{kink} is defined as

$$\lambda_{kink} = 2|x_1 - x_2|,$$

where x_1 (x_2) is the x-coordinate of the maximum (minimum) of $D(x)$. The method for determining the kink wavelength is not possible for the sausage modes because the minimum of $E(x)$ is always at the left boundary of the domain ($x = -6$ Mm) where we start tracing the external pair of fieldlines. Instead we define the sausage wavelength λ_{saus} as

$$\lambda_{saus} = 2|x_1^* - x_2^*|,$$

with x_1^* (x_2^*) the location where $\frac{d^2E}{dx^2}$ is maximal (i.e. x_1^* and x_2^* are the locations where the first derivative $dE(x)/dx$ changes most, hence these are the locations where the "bump" in $E(x)$ starts and ends, see e.g. the right panel of Figure 4.10). Figure 4.11 shows the wavelengths for the first 130 s of the simulation. After $t = 130$ s the method for calculating λ_{kink} gives unphysical results (due to unphysical changes in the location of x_1 and x_2 because the kink and sausage oscillations are damped significantly). Initially when the clumps are not yet colliding ($t < 25$ s) λ_{kink} and λ_{saus} do not represent anything physical. Once the clumps start colliding, they distort the magnetic field ($t > 25$ s) and λ_{kink} increases because $\max(D(x))$ and $\min(D(x))$ propagate away from $x = 0$ at the local Alfvén speed. The maximal distortion is at $x = 0$ when the clumps start colliding, but because of the inclined interface the maximal distortion moves further away from $x = 0$ until the collision is over. Hence λ_{kink} is proportional to the collision time. λ_{saus} similarly increases in the collision phase ($t < 66$ s) as the width of the "bump" in $E(x)$ increases due to the larger expansion of the external field. After $t = 66$ s the λ_{kink} and λ_{saus} show a more oscillatory behaviour. The maxima in λ_{kink} at $t = 80$ s and $t = 119$ s correspond with the local minima in $K(t)$ in the left panel of Figure 4.11 when the oscillation reverses. λ_{saus} decreases after $t > 66$ s because the restoring Lorentz force reduces the expansion of the external field. The minima at $t = 90$ s and $t = 123$ s are the times when the oscillation reverses and the magnetic field is less expanded. These times coincide with the local minima of $S(t)$.

One way to check if the method for calculating the wavelength gives good results is to fit a cosine to $D(x)$ and $E(x)$, based on λ_{kink} and λ_{saus} respectively. In Figure 4.12 we plot the kink and sausage measurements at $t = 66$ s together with a cosine fit that matches $D(x)$ and $E(x)$ empirically. The left panel shows the displacement $D(x)$

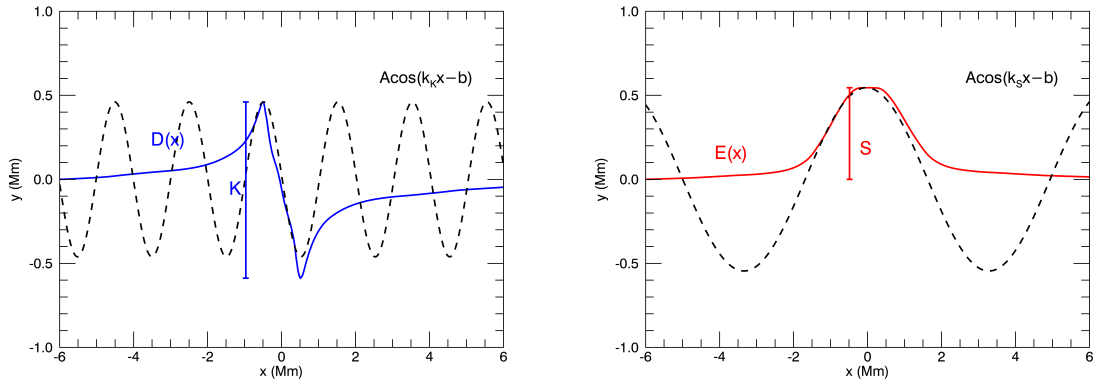

Figure 4.12: (Left) Plot of $D(x)$ (blue) and the kink amplitude K at $t = 66$ s, together with a cosine fit (black dashed line). (Right) Similar plot for the sausage perturbation at $t = 66$ s.

(blue), the kink amplitude K and a cosine fit (dashed line), given by

$$y = A_K \cos(k_K x - b_K).$$

The cosine fit has wavelength λ_{kink} ($k_K = \frac{2\pi}{\lambda_{kink}}$) and amplitude $A_K = \max(D(x))$ of the kink perturbation at $t = 66$ s. The parameter b_K is a phase parameter, which is chosen by eye to align the cosine fit with $D(x)$. The right panel of Figure 4.12 shows a similar plot for the sausage mode at $t = 66$ s, with $E(x)$ the expansion of the central axis (red) and S the sausage amplitude. In this case, the cosine fit is given by,

$$y = A_S \cos(k_S x - b_S),$$

where $k_S = \frac{2\pi}{\lambda_{saus}}$, $A_S = \max(E(x))$ and b_S the (empirical) phase parameter for the sausage mode. In both cases the cosine fit is a good fit for $D(x)$ and $E(x)$ which shows that the method for calculating λ_{kink} and λ_{saus} is satisfactory.

We can estimate the propagation speed of the kink and sausage perturbations, by using the fact that $v_{ph} = \frac{\lambda}{P}$, where v_{ph} is the phase speed, λ the wavelength and P the period. The wavelength λ_{kink} is 4.3 Mm at $t = 104$ s (corresponding to the second local maximum in $K(t)$) and the period at that time is $P = 56$ s. This gives a speed of

$$v_{ph,K} = \frac{\lambda_{kink}}{P} = \frac{4.3 \times 10^6 \text{ m}}{56 \text{ s}} = 76.8 \text{ km/s},$$

which corresponds to the internal Alfvén speed at this time calculated from the average

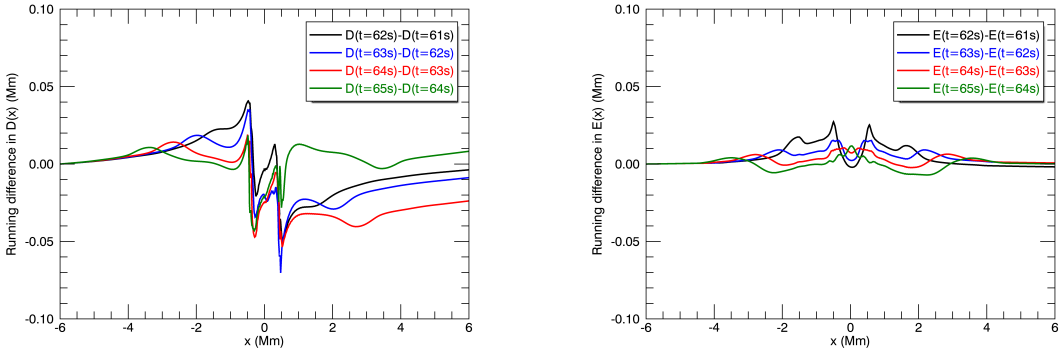

Figure 4.13: Plot of the running difference in $D(t = i + 1) - D(t = i)$ (left panel) and $E(t = i + 1) - E(t = i)$ for $i = 60, 61, 62, 63, 64$. We can see the front of the fast wave travelling outwards from the centre of the domain.

magnetic field and density inside the collision ($|B| \sim 6$ G and $\rho \sim 5 \times 10^{-11}$ kg/m^3, giving $v_{A,int} = 75.7$ km/s). The phase speed of the sausage mode at $t = 106$ s is given by

$$v_{ph,S} = \frac{\lambda_{saus}}{P} = \frac{5.4 \times 10^6 \text{ m}}{80 \text{ s}} = 67.5 \text{ km/s}.$$

This is again similar to the internal Alfvén speed ($v_{A,int} = 75.7$ km/s) of the clumps.

During the collision fast waves are also produced. This can be seen in Figure 4.13 where we plot the running difference of $D(x)$ and $E(x)$ between $t = 60 - 65$ s, at the end of the collision phase. A clear front can be seen propagating towards negative x from the centre of the domain, travelling at a speed of 680 km/s. This is similar to the external Alfvén speed, $v_{A,ext} = 580$ km/s. In this study the fast waves are of less interest, and we will not go into further detail.

4.3 Parameter studies related to the mass and the speed of the clumps

In this section we present three parameter studies that are related to the mass and speed of the clumps. We are interested how the mass and speed of the colliding clumps affect the amplitudes of the generated modes. Antolin et al. (2018) remarked that the plasma β has an effect on the wave amplitude; indeed, a lower plasma β results in a larger magnetic tension force and will lead to smaller amplitudes. In these parameter studies we will keep the plasma β constant and the same as in the reference simulation, $\beta \sim 0.1$. In the first parameter study (PS1) we vary the density contrast ρ_c and the

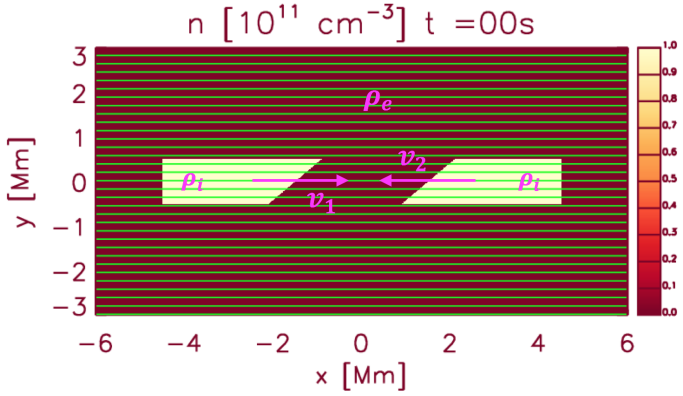

Figure 4.14: Contour of the number density n (10^{11} cm^{-3}) at $t = 0$ with magnetic fieldlines overplotted in green.

velocity v of both clumps. The density contrast and velocity are varied in such a way to keep the momentum and the kinetic energy of the clumps the same for some cases. In the second parameter study (PS2) we vary the individual velocities v_1 and v_2 of the clumps, while keeping ρ_c constant. In the last parameter study (PS3) we vary the individual density contrasts $\rho_{c,1}$ and $\rho_{c,2}$ of the clumps and keep the velocity v constant.

4.3.1 PS1: Varying the density contrast ρ_c and the velocity v of the colliding flows

In the first parameter study we vary the speed v and the density contrast ρ_c of the flows, and we investigate how the size and nature of the amplitudes $K(t)$ and $S(t)$ change accordingly. We run 25 cases, by considering 5 different speeds $v = [70/2, 70/\sqrt{2}, 70, 70 \times \sqrt{2}, 70 \times 2] = [35, 49.5, 70, 99, 140]$ km/s and 5 different density constrasts $\rho_c = \frac{\rho_i}{\rho_e} = [100/2, 100/\sqrt{2}, 100, 100 \times \sqrt{2}, 100 \times 2] = [50, 70.7, 100, 141.1, 200]$. Recall that the reference simulation has $v = 70$ km/s and $\rho_c = 100$. Figure 4.14 explains the setup of PS1.

Figure 4.15 shows a 5×5 table of all 25 simulations. The speed v and density contrast ρ_c are chosen in such a way that on each diagonal of the table (blue dots) all simulations have constant momentum ($\sim \rho_c v$) and on each "L-pattern" (red dots) the kinetic energy $\left(\sim \frac{1}{2}\rho_c v^2\right)$ is constant. The reference simulation is located in the middle of the table ($\rho_c = 100, v = 70$km/s).

In Table 4.2 we show the internal Alfvén Mach number $M_A = v/v_{A,int}$ (top table) and the internal Mach number $M_S = v/c_{s,int}$ (bottom table) of the clumps for each simulation of PS1. We can see that the clumps in all simulations are supersonic and that for the majority of the simulations the clumps are super-Alfvénic. For these

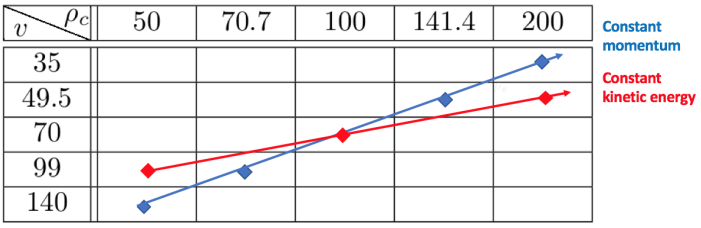

Figure 4.15: Table with the 25 cases we consider in PS1. On each diagonal (blue dots) the momentum is fixed, on each L-shape pattern (red dots) the kinetic energy of the system is constant.

simulations we expect the collisions to be more violent than for simulations where the clumps are sub-Alfvénic. Note that simulations with the same initial kinetic energy have the same Mach numbers, and that the Mach numbers increase with increasing v and increasing ρ_c.

$v \setminus \rho_c$	50	70.7	100	141.4	200
35	0.43	0.51	0.6	0.72	0.85
49.5	0.6	0.72	0.85	1.01	1.2
70	0.85	1.01	1.2	1.43	1.71
99	1.2	1.43	1.71	2.03	2.41
140	1.71	2.03	2.41	2.87	3.41

$v \setminus \rho_c$	50	70.7	100	141.4	200
35	1.49	1.77	2.11	2.51	2.98
49.5	2.11	2.51	2.98	3.54	4.21
70	2.98	3.54	4.21	5.01	5.96
99	4.21	5.01	5.96	7.09	8.44
140	5.96	7.09	8.44	10.03	11.93

Table 4.2: Tables of the internal Alfvén Mach number $M_A = v/v_{A,int}$ (top) and the internal Mach number $M_S = v/c_{s,int}$ of the clumps for each case in PS1.

Kink amplitude $K(t)$

In Figure 4.16 we show the evolution of the kink amplitude $K(t)$ with time for 5 simulations with constant momentum (left panel) and 3 cases with constant kinetic energy (right panel). These cases are given by the blue and red dots in Figure 4.15.

For both panels the maximal kink amplitude $\max(K(t))$ is attained at different times because clumps with a larger initial speed lead to an earlier collision of the clumps. The scaling is not linear in the sense that the maximal amplitude occurs later

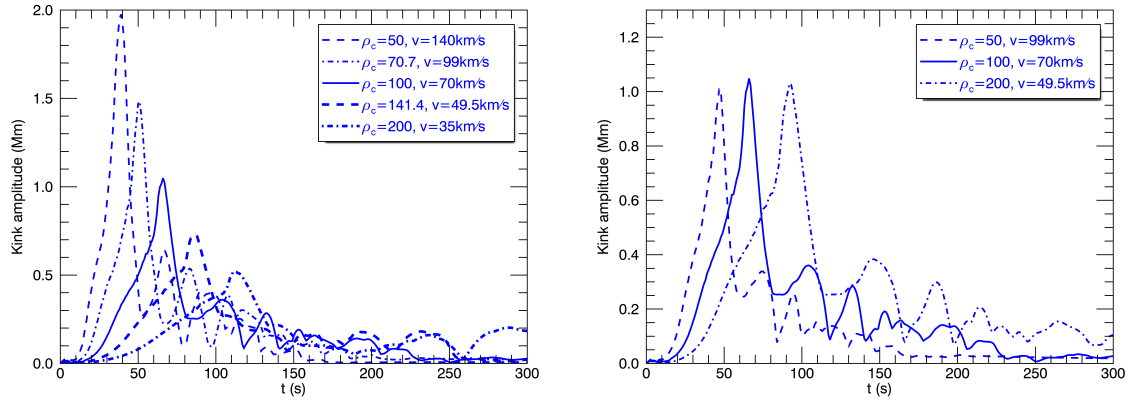

Figure 4.16: (Left) Plot of the kink amplitude $K(t)$ (Mm) with time for 5 simulations with constant momentum. (Right) Plot of $K(t)$ (Mm) with time for 3 simulations with constant kinetic energy.

when the clumps have more kinetic energy (e.g. faster travelling clumps in the left panel), because it takes longer for the restoring magnetic forces to invert the plasma motion. Max($K(t)$) for the 5 cases with constant momentum is larger for simulations where the clumps have a larger initial speed v, and hence also a larger kinetic energy (max($K(t)$) $\sim \rho_c v^2$). The right panel of Figure 4.16 shows that the max($K(t)$) is constant for simulations with constant kinetic energy. This implies that the kinetic energy of the system is the key parameter that determines the maximal amplitude of the generated mode. The evolution of $K(t)$ after the collision is also very similar for these three cases. For cases where the clumps have a lower density contrast ρ_c, the evolution of $K(t)$ shows shorter period oscillations after max($K(t)$). In general the period of the oscillations is dependent on the density constrast of the clumps, because this decreases the internal Alfvén speed and the propagation speed of the modes.

Table 4.0 shows the max($K(t)$) obtained in each case and confirms that max($K(t)$) scales with the kinetic energy, as boxes with the same color have the same initial kinetic energy. Simulations that have the same momentum (on the diagonals of the table) do not have a similar maximal amplitude. The cases where we do not report a maximal amplitude are too extreme (too large v and ρ_c in 5 cases), because the magnetic field is too distorted from the collision. In some of these cases the magnetic fieldlines show cusps and the field does not act as a waveguide anymore and our method of determining the amplitudes fails. An example of such a case can be found in Figure 4.17.

The lower half of Table 4.0 shows the wavelength λ_{kink} at the time of max($K(t)$) for each case. We see that the wavelength is shorter for cases where the clumps have a

v \ ρ_c	50	70.7	100	141.4	200
35	0.062	0.103	0.183	0.32	0.522
49.5	0.174	0.307	0.504	0.727	1.03
70	0.49	0.707	1.049	1.434	1.785
99	1.014	1.483	1.91	/	/
140	1.975	2.485	/	/	/

v \ ρ_c	50	70.7	100	141.4	200
35	3.914	5.086	4.477	3.727	3.094
49.5	4.594	3.961	3.258	2.602	1.898
70	3.398	2.719	2.016	1.547	1.406
99	2.297	1.781	1.359	/	/
140	1.453	1.57	/	/	/

Table 4.0: (Top) Table with the maximal kink amplitude $\max(K(t))$ (Mm) for each case. Boxes with the same color have the same initial kinetic energy. We do not report on 5 cases because the collision is too extreme and the magnetic field is too distorted. (Bottom) Table with the kink wavelength λ_{kink} (Mm) of the kink mode at the time of $\max(K(t))$ for each case.

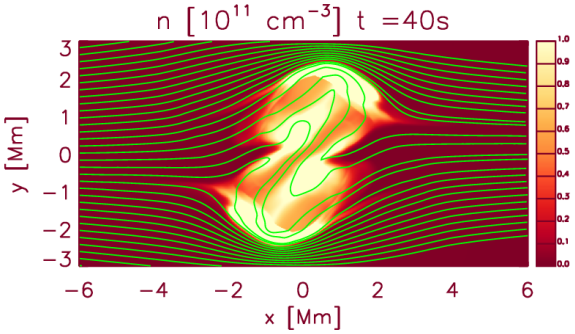

Figure 4.17: Contour of the number density at $t = 40$ s for the simulation with $v = 140$ km/s and $\rho_c = 200$. The magnetic fieldlines are overplotted in green.

higher velocity and the collision time is shorter. For cases that have the same velocity but a different ρ_c (rows of Table 4.0), the wavelength is larger when ρ_c is smaller because the Alfvén speed increases and $\max(D(x))$ and $\min(D(x))$ are further apart. Cases with the same kinetic energy have similar wavelengths but the wavelength is in general larger when ρ_c is smaller. The wavelength for the case $\rho_c = 50$ and $v = 35$ km/s is smaller than expected because the collision in this case is too weak to cause a significant distortion of the magnetic field.

Sausage amplitude $S(t)$

In Figure 4.18 we plot the evolution of the sausage amplitude $S(t)$ for the same cases as in Figure 4.16.

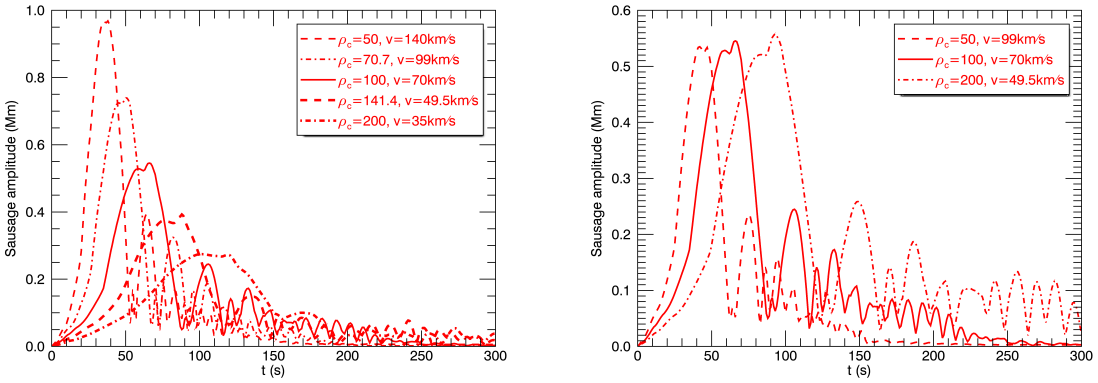

Figure 4.18: (Left) Plot of the sausage amplitude $S(t)$ (Mm) with time for 5 simulations with constant momentum. (Right) Plot of $S(t)$ (Mm) with time for 3 simulations with constant kinetic energy.

Similar conclusions as for $K(t)$ can also be drawn for $S(t)$. The maximal amplitude $\max(S(t))$ scales with the kinetic energy of the system, i.e. cases with the same initial kinetic energy produce a similar $\max(S(t))$. The evolution of $S(t)$ after the $\max(S(t))$ again shows shorter period oscillations for clumps with smaller ρ_c, as the Alfvén speed inside the collision has increased.

$v \setminus \rho_c$	50	70.7	100	141.4	200
35	0.094	0.124	0.161	0.21	0.275
49.5	0.163	0.212	0.278	0.393	0.558
70	0.282	0.379	0.545	0.75	0.971
99	0.535	0.74	0.972	/	/
140	0.968	1.242	/	/	/

Table 4.3: Table with the maximal sausage amplitude $\max(S(t))$ (Mm) for each case.

Table 4.3 shows the maximal sausage amplitude $\max(S(t))$ obtained in each case. As for the kink amplitude $K(t)$, the maximal sausage amplitude $\max(S(t))$ is similar for simulations with the same initial kinetic energy. Table 4.4 shows the sausage wavelength λ_{saus} for each case. We can see that λ_{saus} is similar for cases with the same kinetic energy, as the distortion and the expansion of the field is similar in these cases. For example, the first row shows that when ρ_c increases, the sausage wavelength decreases as the collision has more kinetic energy and the magnetic field has more expanded in the y direction, which decreases the width of the bump in $E(x)$. This is shown in Figure 4.19 which shows the expansion $E(x)$ for the cases with $v = 35$ km/s and $\rho_c = 50, 100, 140$ at the time of $\max(S(t))$. However, the sausage wavelength

does not always decrease when the kinetic energy increases. For some cases with larger kinetic energy (towards the bottom right corner of the table), the expansion of the external field is also in the x direction, which increases λ_{saus}. This is shown in the right panel of Figure 4.19 which shows the expansion $E(x)$ for the cases with $\rho_c = 70.7$ and $v = 70, 99, 140$ km/s at the time of $\max(S(t))$.

$v \setminus \rho_c$	50	70.7	100	141.4	200
35	7.898	7.664	6.82	6.07	4.852
49.5	7.055	6.773	5.086	6.305	6.539
70	5.367	4.477	6.727	6.586	7.102
99	6.07	6.773	7.055	/	/
140	7.43	7.523	/	/	/

Table 4.4: Table with the sausage wavelength λ_{saus} at the time when $S(t)$ reaches its maximum for each case.

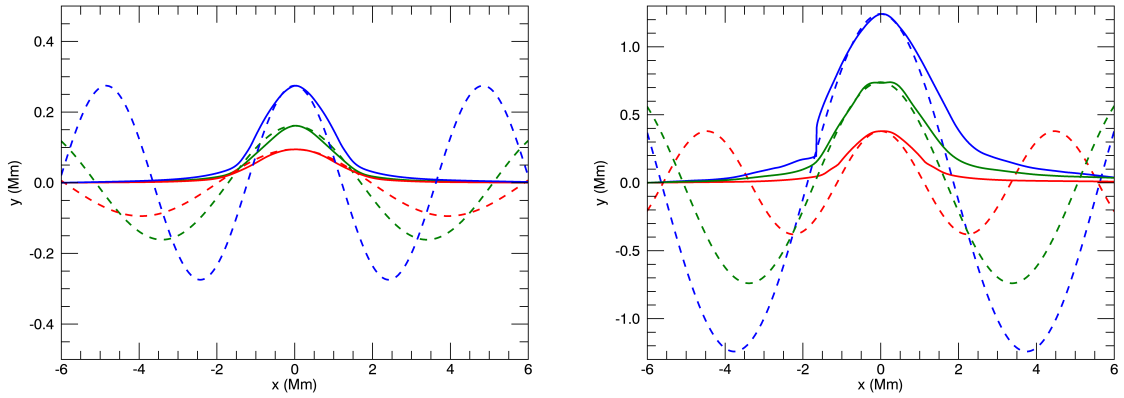

Figure 4.19: (Left) Plot of the expansion $E(x)$ at the time of $\max(S(t))$ for the cases with $v = 35$ km/s and $\rho_c = 50$ (red), $\rho_c = 100$ (green), $\rho_c = 140$ (blue), together with the cosine fit (dashed lines), determined by the wavelength λ_{saus}. (Right) Similar plot for the cases with $\rho_c = 70.7$ and $v = 70, 99, 140$ km/s.

4.3.2 PS2: Varying the speeds v_1, v_2 of the colliding flows

In PS2 we vary the speeds of the flows v_1, v_2, where v_1 denotes the speed of the left clump ($x < 0$ initially) and v_2 the speed of the right clump ($x > 0$ initially). The density contrast $\rho_c = 100$ is held constant.

We consider 5 cases: $v_1/v_2 = [70/70, 80/60, 90/50, 100/40, 110/30]$ km/s. The speeds are varied in such a way that the relative speed between the clumps stays

constant (140 km/s), and the kinetic energy of the system (with respect to the centre of mass) of each case is the same. The kinetic energy with respect to the centre of mass is defined as

$$E_{kin,CM} = \frac{1}{2}\rho\left(\mathbf{v} - \mathbf{V_{CM}}\right)^2,$$

where $\mathbf{V_{CM}}$ is the velocity of the centre of mass,

$$\mathbf{V_{CM}} = \frac{\int \rho \mathbf{v} \mathrm{dV}}{\int \rho \mathrm{dV}}.$$

Remark that when the two clumps have the same density, we have that $\mathbf{V_{CM}} = 0.5(\mathbf{v_1} + \mathbf{v_2})$ where $\mathbf{v_1}$ and $\mathbf{v_2}$ are the velocities of the left and right clump respectively. In the previous parameter study (PS1) $\mathbf{V_{CM}} = 0$ for all cases because both clumps have the same density and $\mathbf{v_1} = -\mathbf{v_2}$. In this parameter study, the centre of mass travels at a velocity $V_{CM} = [0, 10, 20, 30, 40]$ km/s for each case respectively, which gives for each clump an initial kinetic energy of

$$E_{K,clump} = \frac{\rho_{clump}\left(\mathbf{v} - \mathbf{V_{CM}}\right)^2}{2} = \frac{\rho_{clump} 70^2}{2},$$

so the total initial kinetic energy of the system for each case is $\rho_{clump} 70^2$. Because the kinetic energy is the same for all cases, we expect the maximal amplitudes to be similar in each case.

Table 4.5 shows the internal Alfvén Mach numbers M_A and the internal Mach numbers M_S for each case in PS2, for the first blob (top table) and the second blob (bottom table). The first blob is always supersonic and super-Alfvénic, while the second blob is supersonic but only super-Alfvénic when $v_2 \geq 60$ km/s.

v_1/v_2	70/70	80/60	90/50	100/40	110/30
$M_A = v/v_{A,int}$	1.2	1.38	1.55	1.72	1.89
$M_S = v/c_{s,int}$	4.21	4.82	5.42	6.03	6.62

v_1/v_2	70/70	80/60	90/50	100/40	110/30
$M_A = v/v_{A,int}$	1.2	1.03	0.86	0.69	0.52
$M_S = v/c_{s,int}$	4.21	3.62	3.01	2.41	1.81

Table 4.5: Tables of the internal Alfvén Mach number $M_A = v/v_{A,int}$ and the internal Mach number $M_S = v/c_{s,int}$ of the first blob (top) and the second blob (bottom) for each case in PS2.

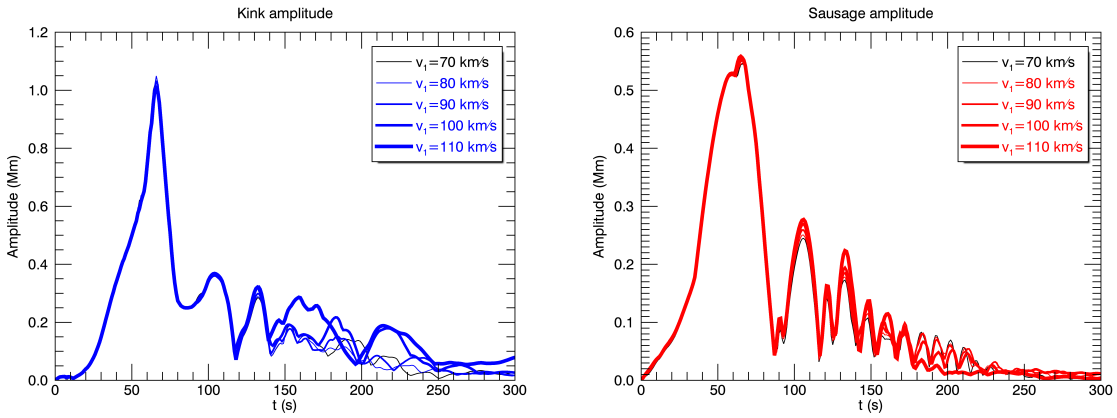

Figure 4.20: (Left) Plot of the kink amplitudes $K(t)$ with time for each case ($v_1/v_2 = [70/70, 80/60, 90/50, 100/40, 110/30]$ km/s). (Right) Similar plot for the sausage amplitudes $S(t)$.

Figure 4.20 shows the evolution of the kink amplitude $K(t)$ (left panel) and sausage amplitude $S(t)$ (right panel) for each case with time. The maximal kink amplitude $\max(K(t))$ is indeed very similar for each case and the evolution of $K(t)$ in the propagation phase ($t > 66$ s) also shows a very similar behaviour. Because the relative speed between the clumps is the same for each case, the time when $\max(K(t))$ is attained is also the same. $\text{Max}(S(t))$ and the evolution of $S(t)$ are similar for each case as well (the right panel of Figure 4.20). This shows again that the kinetic energy with respect to the centre of mass is the key parameter that determines the size of the maximal amplitudes of the generated modes.

4.3.3 PS3: Varying the density contrasts $\rho_{c,1}, \rho_{c,2}$ of the colliding flows

In PS3 we vary the density contrast ρ_c of the clumps and keep the speed $v = 70$ km/s constant. We consider the cases $\rho_{c,1}/\rho_{c,2} = 100/100, 200/100, 400/100, 800/100, 1000/100$. The reference simulation has $\rho_{c,1}/\rho_{c,2} = 100/100$. We also ran a test case where the clumps had a significantly lower density ($\rho_{c,1}/\rho_{c,2} = 3/3$), which we have omitted here because the clumps come to a halt before they collide (due to the increase of the gas pressure in the centre of the domain). In Table 4.6 we give the initial kinetic energy with respect to the centre of mass for each case. When $\rho_{c,1}$ is different from $\rho_{c,2}$ the centre of mass shifts towards the heavier clump. The velocity of the centre of mass v_{CM} is always in the range $0 - 70$ km/s, where $v_{CM} = 0$ when $\rho_{c,1} = \rho_{c,2}$ and $v_{CM} = 70$km/s when $\rho_{c,2} = 1$ (i.e. $\rho_2 = \rho_{ext}$ and there is essentially no second clump). The latter

extreme case is not considered in this parameter study.

$\rho_{c,1}$	$\rho_{c,2}$	v_{CM} (km/s)	Total kin. energy $\rho(v - v_{CM})^2/2$ (erg)	Rel. kin. energy
100	100	0	1.08×10^5	1
200	100	21.75	1.46×10^5	1.34
400	100	40.24	1.77×10^5	1.64
800	100	53.16	1.99×10^5	1.84
1000	100	56.16	2.05×10^5	1.88

Table 4.6: The total initial kinetic energy (w.r.t. the centre of mass) and relative total kinetic energy (w.r.t. the reference simulation) for each case in PS3.

Table 4.7 shows the internal Alfvén Mach numbers M_A and the internal Mach numbers M_S for each case in PS3. As the density of the first blob is increased, the internal Alfvén Mach number and internal Mach number increase. The second blob has $M_A = 1.21$ and $M_S = 4.21$ in each case, as the density is unchanged ($\rho_{c,2} = 100$). Both blobs are always supersonic and super-Alfvénic.

$\rho_{c,1}/\rho_{c,2}$	100/100	200/100	400/100	800/100	1000/100
$M_A = v/v_{A,int}$	1.2	1.71	2.41	3.41	3.81
$M_S = v/c_{s,int}$	4.22	5.96	8.43	11.93	13.33

Table 4.7: Table of the internal Alfvén Mach number $M_A = v/v_{A,int}$ and the internal Mach number $M_S = v/c_{s,int}$ of the first blob for each case in PS3.

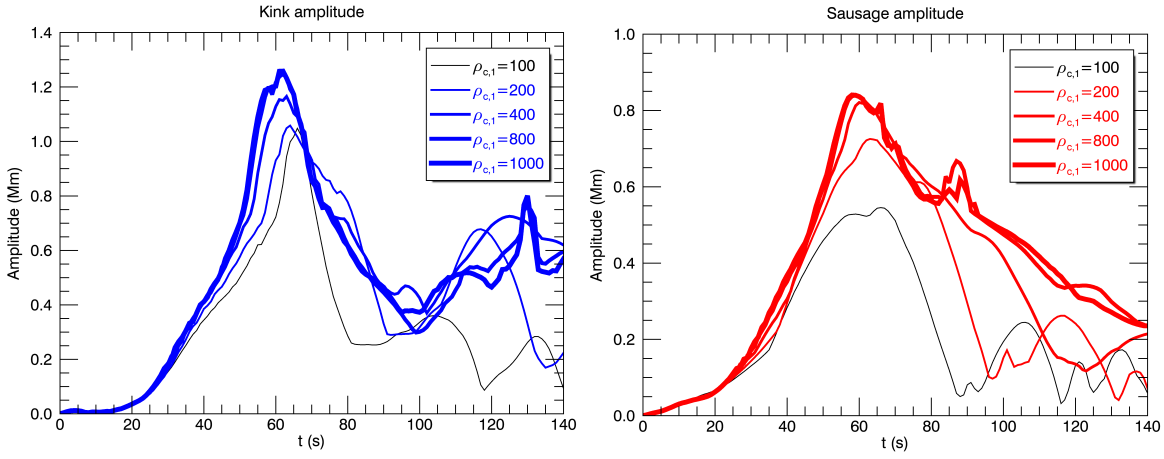

Figure 4.21: (Left) Plot of the evolution of the kink amplitude $K(t)$ for each case with time. (Right) Similar plot for the sausage amplitude $S(t)$.

Figure 4.21 shows the evolution of the kink amplitude $K(t)$ and sausage amplitude $S(t)$ with time for each case. We restrict the time axis to $t = 140$ s, because after

this time in some cases the clumps propagate out of the domain through the $x = 6$ Mm boundary. This happens for the cases with $\rho_{c,1} = 800$ and $\rho_{c,1} = 1000$. Note that the maximal amplitudes are still reached at a similar time as in the reference simulation ($t \sim 65$s), because we have not changed the speed of the clumps. For the cases with $\rho_{c,1} \geq 200$, $\max(K(t))$ and $\max(S(t))$ increase as the kinetic energy of the system increases, however the maximal amplitudes seem to saturate, and they do not scale anymore with the kinetic energy of the system. When the density contrast $\rho_{c,1}$ differs too much from $\rho_{c,2}$, the collision becomes less efficient because the clump with the smaller ρ_c is compressed and pushed backwards and downwards in the direction of negative y due to the inclination of the interface of the clumps. This leads to less kinking and expansion of the field. This is shown by Figure 4.22, which shows a contour of the density for the case $\rho_{c,1} = 1000$ at $t = 62$ s (the time of $\max(K(t))$). This case is representative for all the other cases where $\rho_{c,1} \neq \rho_{c,2}$. The saturation effect of the maximal amplitudes is also shown in Figure 4.23 where we show the maximal amplitudes for each case.

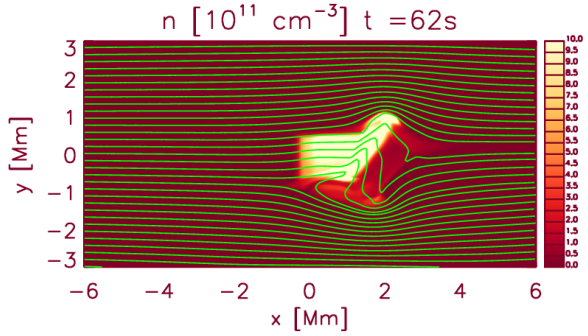

Figure 4.22: Contour of the density for the case $\rho_{c,1} = 1000$ at $t = 62$ s.

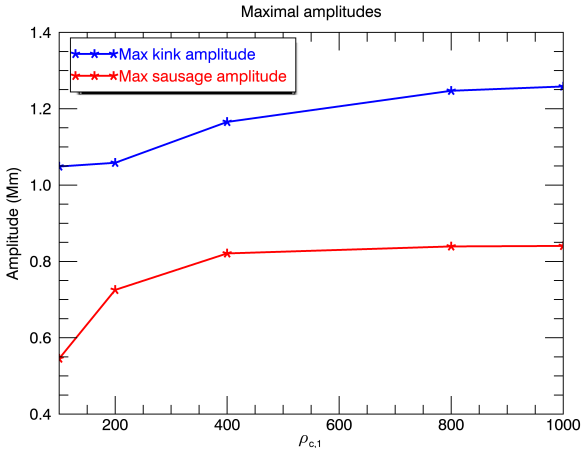

Figure 4.23: Plot of the $\max(K(t))$ (blue) and $\max(S(t))$ (red) for each case.

4.4 Parameter studies related to the asymmetry of the setup

In this section we investigate how the asymmetry of the system affects the relative size of the amplitudes of the generated kink and sausage perturbations by varying the angle of the interface of the clumps (PS4) and the offset of rectangular clumps with respect to the $y = 0$ axis (PS5).

4.4.1 PS4: Varying the angle θ of the colliding clumps

In this parameter study we vary the angle θ of the interface of the colliding clumps (see Figure 4.1 for the definition of θ). All other quantities (ρ_c and v) are unchanged and as in the reference simulation ($\rho_c = 100$, $v = 70$km/s). We consider the cases $\theta = 0, 20, 40, 50, 60, 80$ degrees. The angle of the interface of the reference simulation is $\theta = 50$ degrees. Figure 4.24 shows contours of the number density at $t = 0$ for the 6 cases we consider in PS4. Each case has the same initial kinetic energy, because the angle θ is varied in such a way that the area of the clumps - and therefore the total mass of the clumps - does not change. The internal Alfvén Mach number ($M_A = 1.21$) and the internal Mach number ($M_S = 4.22$) are unchanged from the reference simulation, as the speed ($v = 70$ km/s) and the density ($\rho_c = 100$) of the clumps are the same for each case.

Figure 4.25 shows the evolution of the kink amplitude $K(t)$ (left panel) and sausage amplitude $S(t)$ (right panel) for each case. For the case $\theta = 0$ no kink amplitude is generated due to the symmetric setup of the clumps. Only a sausage amplitude is generated in this case ($\max(S(t)) = 0.52$ Mm). When the angle θ increases, the asymmetry of the system increases and a larger $\max(K(t))$ is generated, due to a larger force imbalance in the y direction (see Figure 4.26 and paragraph below). The maximal $K(t)$ of 1.05 Mm is attained for the case with $\theta = 50$ degrees. For $\theta > 60$ degrees the asymmetry is too large and the collision of the clumps is less efficient, which leads to smaller $\max(K(t))$.

The $\max(S(t))$ does not seem to be affected by the asymmetry of the system, as for the cases with $\theta \leq 60$ degrees the $\max(S(t))$ is ~ 0.6 Mm. This seems to be in accordance with the fact that the initial kinetic energy of all the simulations is the same. When $\theta = 80$ degrees, the asymmetry is too large and the $\max(S(t))$ is smaller. The evolution of $K(t)$ and $S(t)$ after the collision does not seem to depend on the angle

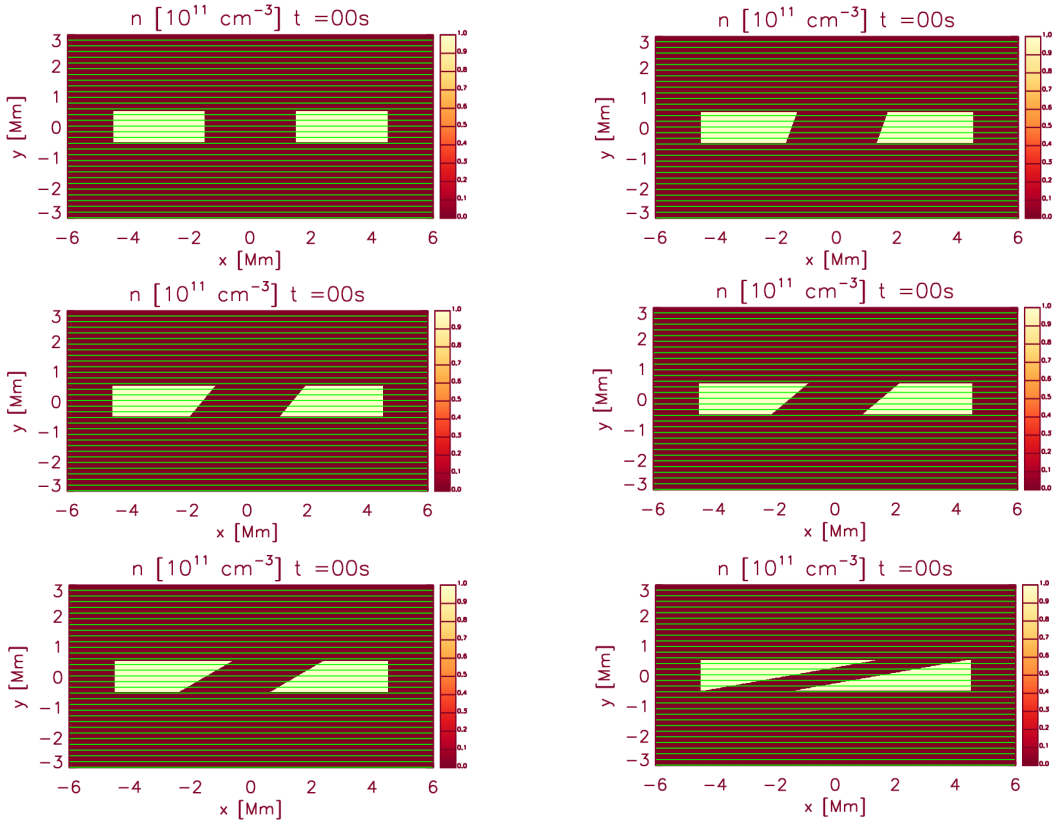

Figure 4.24: Contours of the number density at $t = 0$ (with magnetic fieldlines overplotted in green) for the different cases considered in PS4. From top left to bottom right are the cases with $\theta = 0, 20, 40, 50, 60, 80$ degrees.

θ. This shows that the period of the oscillations (i.e. the time differences between local maxima) is determined by the local properties of the clumps ($\rho_c, v_{A,int}$) rather than the asymmetry of the system.

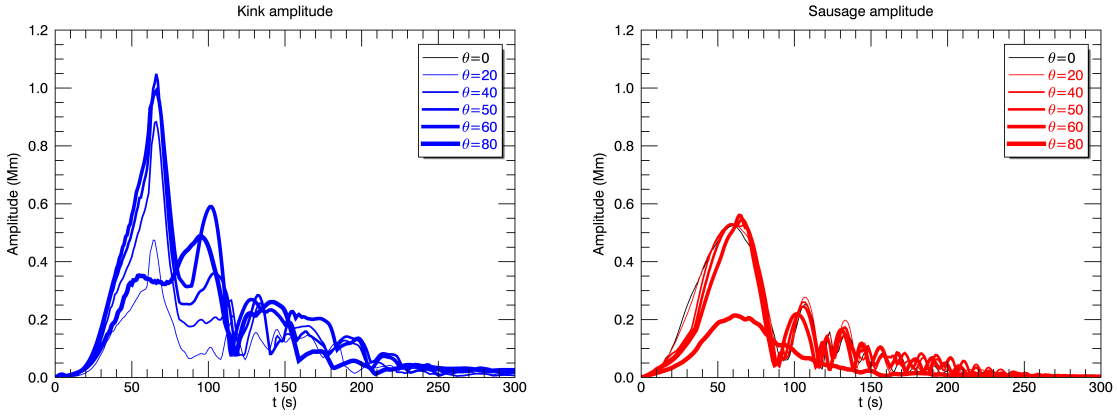

Figure 4.25: (Left) Plot of the kink amplitudes for each angle θ with time. (Right) Similar plot for the sausage amplitudes.

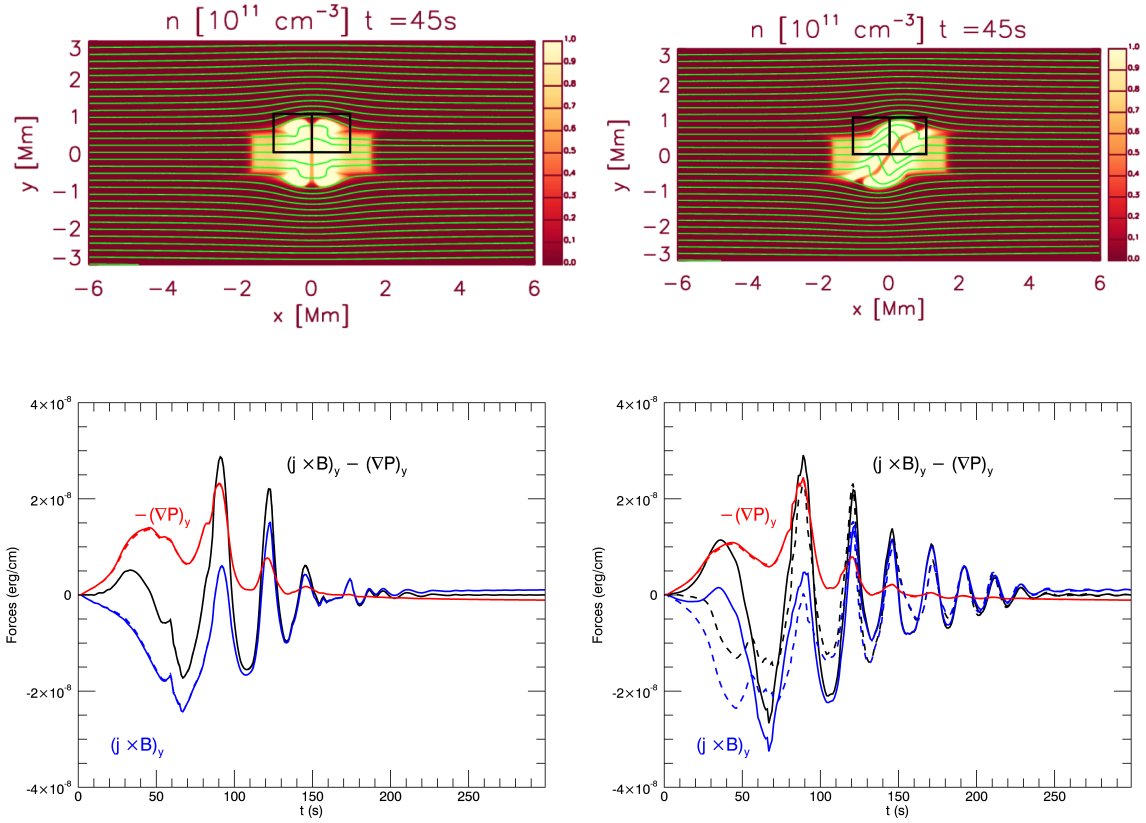

Figure 4.26: (Top) Contours of the density at $t = 45$ s for the case $\theta = 0$ (left) and $\theta = 50$ degrees (right). (Bottom) Plot of the average Lorentz force $(\mathbf{j} \times \mathbf{B})_y$ (blue) and pressure gradient force $-(\boldsymbol{\nabla} P)_y$ (red) in the two black squares in the top panels. The solid (dashed) lines correspond to the average forces taken in the square where $x < 0$ Mm ($x > 0$ Mm).

To investigate how the asymmetry of the clumps leads to a different distortion of the magnetic field (more or less kinking), we look at the forces in the vertical direction (y) inside the collision. In Figure 4.26 we show the average forces in the y direction for two regions in $x < 0$ Mm and $x > 0$ Mm, for the case $\theta = 0$ degrees and $\theta = 50$ degrees. We average the Lorentz force $(\mathbf{j} \times \mathbf{B})_y$ (blue lines) and pressure gradient force $-(\boldsymbol{\nabla} P)_y$ (red lines) in the two black squares shown in the top panels of Figure 4.26. The solid (dashed) lines represent the forces in the square with $x < 0$ Mm ($x > 0$ Mm). In the case where $\theta = 0$ the dashed and solid lines are almost identical for all averaged forces, because the system is perfectly symmetric. This results in the generation of a sausage mode only. For the case $\theta = 50$ degrees, the averaged $-(\boldsymbol{\nabla} P)_y$ is very similar for $x > 0$ Mm and $x < 0$ Mm in the collision phase ($t < 50$ s), however $(\mathbf{j} \times \mathbf{B})_y$ is now larger for $x > 0$ Mm and smaller for $x < 0$ Mm. This results in a negative net force for $x > 0$ Mm (black dashed line) and a positive net force for $x < 0$ Mm (black solid line).

This asymmetry in the Lorentz force (caused by the angle θ of the interface) leads to a kinking of the internal fieldlines and the generation of a kink perturbation.

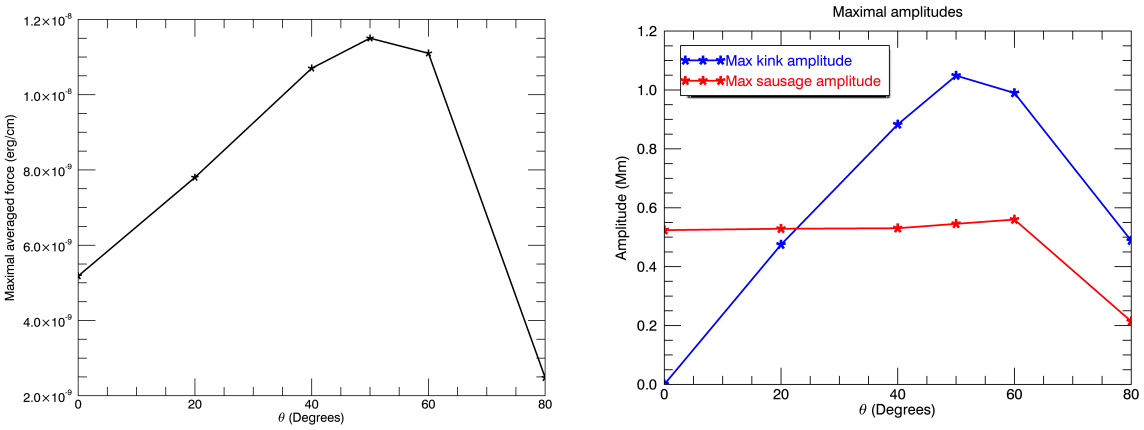

Figure 4.27: (Left) Plot of the maximal averaged net force in the left square shown in Figure 4.26 for each case and $0 < t < 60$ s. (Right) Plot of the $\max(K(t))$ (blue) and the $\max(S(t))$ (red) for each case.

In the left panel of Figure 4.27 we show the maximal averaged net force $(\mathbf{j} \times \mathbf{B})_y - (\boldsymbol{\nabla} P)_y$ in the left square ($x < 0$ Mm) for all cases and $t < 60$ s. We can see that this corresponds with the $\max(K(t))$ for each case shown by the right panel of Figure 4.27. The maximal averaged net force is reached for the case $\theta = 50$ degrees which agrees with $\max(K(t))$. The collision of the clumps becomes less efficient when the interface is strongly inclined ($\theta = 80$ degrees), which leads to a smaller averaged net force inside the collision and smaller maximal amplitudes.

In Table 4.8 we show the initial angular momentum w.r.t. the origin of the Cartesian frame of reference ($x = 0, y = 0$) for each case in PS4, normalised to the reference simulation ($\theta = 50$ degrees). The origin ($x = 0, y = 0$) is also the initial location of centre of mass of the system. The initial angular momentum is expected to partially govern the kink distortion of the magnetic field, as absorbing angular momentum requires a torque from magnetic tension. The angular momentum L is calculated as

$$|L| = \int_V |\mathbf{r} \times (\rho \mathbf{v})| \mathrm{dV} = \int_V |r| \rho |v_x| \sin(\alpha) \mathrm{dV},$$

where $\mathbf{r}$ is the positional vector from the origin, and α the angle between $\mathbf{r}$ and $\mathbf{v}$. We see from Table 4.8 that the initial angular momentum increases when the angle θ of the interface of the clumps increases, because the asymmetry of the setup increases with

larger θ. The initial angular momentum is zero when $\theta = 0$, as the setup is symmetric about $y = 0$. Note that a larger angular momentum does not necessarily mean that the maximal kink amplitude will be larger, as for extreme cases (e.g. $\theta = 80$ degrees) the collision is less efficient.

Angle (degrees)	$\theta = 0$	$\theta = 20$	$\theta = 40$	$\theta = 50$	$\theta = 60$	$\theta = 80$
$\|L\|$	0	0.16	0.64	1	1.55	3.91

Table 4.8: Table of the initial angular momentum $|L| = \int_V |\mathbf{r} \times (\rho \mathbf{v})| \mathrm{dV}$ for each case in PS4, normalised against the reference simulation ($\theta = 50$ degrees).

4.4.2 PS5: Varying the offset of rectangular clumps

In PS5 we investigate the asymmetry of the system by varying the offset of rectangular clumps ($\theta = 0$) about the $y = 0$ axis. We use rectagular clumps in this parameter study rather than trapezoidal clumps for simplicity reasons (otherwise there is another degree of complexity). This parameter study could be useful to relate with observations of colliding clumps where the clumps only partially collide or shear past each other.

Figure 4.28 shows the initial setup for each case in this parameter study. We consider the following 9 cases: $y_{cent,i} = [\pm 0, \pm 0.05, \pm 0.1, \pm 0.125, \pm 0.166, \pm 0.2, \pm 0.3, \pm 0.4, \pm 0.5]$ Mm, where $y_{cent,i}$ represents the y coordinate of the central axis of clump i. The left clump ('clump 1') is offset towards positive y and the right clump ('clump 2') towards negative y. Due to the offset of the clumps the width of the interface of the clumps that is colliding is $2 \times (0.5 - |y_{cent,i}|)$ Mm. In terms of a percentage of the width of the clumps that is colliding, we have the cases: 100%(offset = ± 0), 90%(offset = ± 0.05), 80%(offset = ± 0.1), 75%(offset = ± 0.125), 67%(offset = ± 0.166), 60%(offset = ± 0.2), 40%(offset = ± 0.3), 20%(offset = ± 0.4), 0%(offset = ± 0.5). The density contrast ($\rho_c = 100$) and speed ($v = 70$ km/s) of the clumps are as in the reference simulation, hence the internal Alfvén Mach number ($M_A = 1.21$) and the internal Mach number ($M_S = 4.22$) of the clumps are the same as in the reference simulation for each case.

Before analysing the evolution of the amplitudes it is worth noting that the chosen pair of external fieldlines to measure the sausage amplitude $S(t)$ changes when the offset changes. The external fieldlines are chosen from the density threshold of the clumps and are hence at the location where they enclose the clumps. Because of the offset the external fieldlines now enclose a larger region. The external fieldlines are for

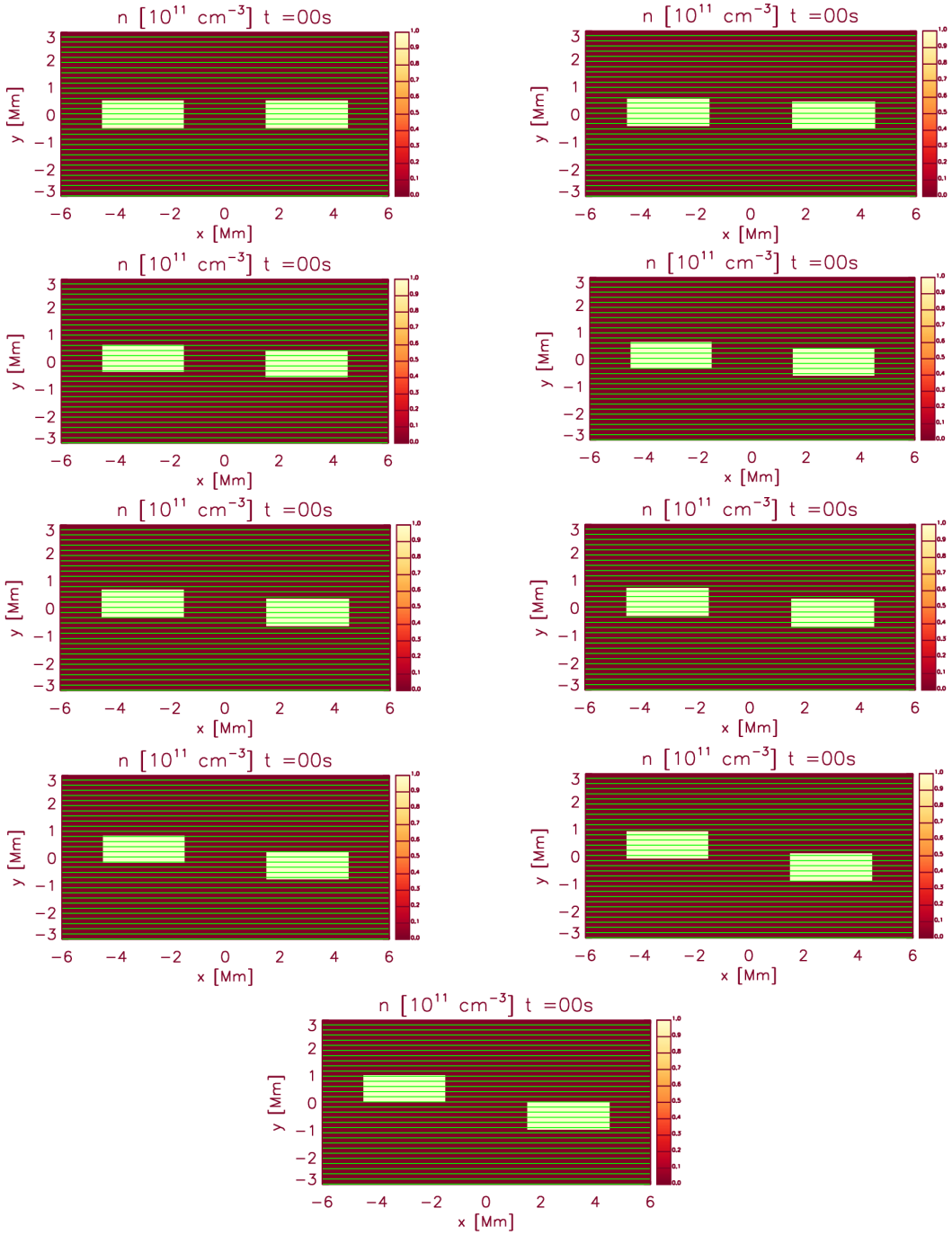

Figure 4.28: Contour of the number density for the simulations in PS5 with varying offset. From top left to bottom are the simulations with offsets: $y_{cent,i} = 0, \pm 0.05, \pm 0.1, \pm 0.125, \pm 0.166, \pm 0.2, \pm 0.3, \pm 0.4, \pm 0.5$ (in Mm). Here $y_{cent,i}$ represents the y coordinate of the central axis of clump i.

each case initially at $y = (\pm 0.5 + y_{cent,i})$ Mm. The pair of internal fieldlines to measure $K(t)$ is still the same as before (chosen to be at $y = \pm 0.1$ Mm). These fieldlines are always internal and symmetrical w.r.t the part of the interface that is colliding, except for the cases when the offset is $y_{cent,i} = \pm 0.4$ Mm and $y_{cent,i} = \pm 0.5$ Mm. In the former

case the internal fieldlines enclose the part of the interface that is colliding, while in the latter case the clumps do not collide but travel past each other. In Figure 4.29 we show the internal and external pair of fieldlines for the case $y_{cent,i} = \pm 0.2$ Mm at $t = 0$ s.

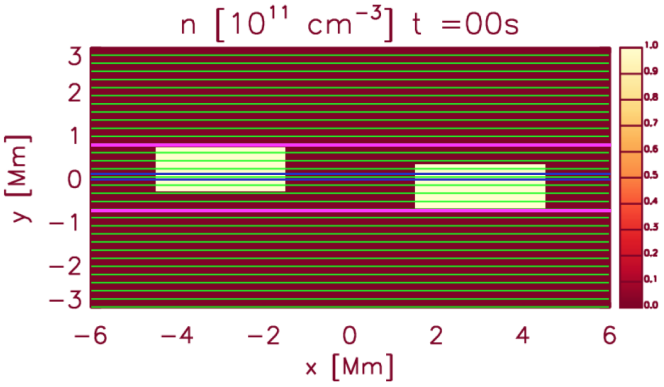

Figure 4.29: Contour of the density at $t = 0$ s for the case $y_{cent,i} = \pm 0.2$ Mm with magnetic fieldlines overplotted (green). The pink fieldlines are the external fieldlines used to measure the sausage amplitude $S(t)$. The dark blue fieldlines are internal fieldlines used for the measurement of the kink amplitude $K(t)$.

To illustrate a typical collision, we show in Figure 4.30 contours of the density for the case with $y_{cent,i} = \pm 0.2$ Mm at $t = 35, 64, 103$ s together with plots of the measurement of the amplitudes at these times. At $t = 35$ s the collision is ongoing (the clumps start to touch at $t = 30$ s). The top 40% of clump 1 and the bottom 40% of clump 2 do not collide and keep propagating in the x direction. As the interface of the clumps is straight ($\theta = 0$), the internal fieldlines are not kinked and $K(t)$ is small at this stage. The middle row shows a contour of the density at the end of the collision phase ($t = 64$ s) when $K(t)$ reaches a local maximum ($K(t = 64s) = 0.28$ Mm). The collision has also caused an expansion of the magnetic field which results in a sausage amplitude of $S(t = 64s) = 0.4$ Mm. Max($S(t)$) is reached a little bit later at $t = 69$s ($S(t = 69s) = 0.45$ Mm). The bottom two panels of Figure 4.30 show the simulation at $t = 103$ s when max($K(t)$) is reached, $K(t = 103s) = 0.6$ Mm. It is only after the collision (when the system produces oscillations to reach a new equilibrium) that the internal fieldlines are more kinked and max($K(t)$) is attained.

In Figure 4.31 we plot the evolution of the kink amplitude $K(t)$ and sausage amplitude $S(t)$ for each case. We can see that max($K(t)$) increases when the clumps are more offset (up to an offset of $y_{cent,i} = \pm 0.3$ Mm), and that the maximum is attained for the offset $y_{cent,i} = \pm 0.3$ Mm (40% collision). For the cases with offsets $y_{cent,i} = [\pm 0.4, \pm 0.5]$ Mm the clumps mostly travel past each other and the collision is less efficient, which

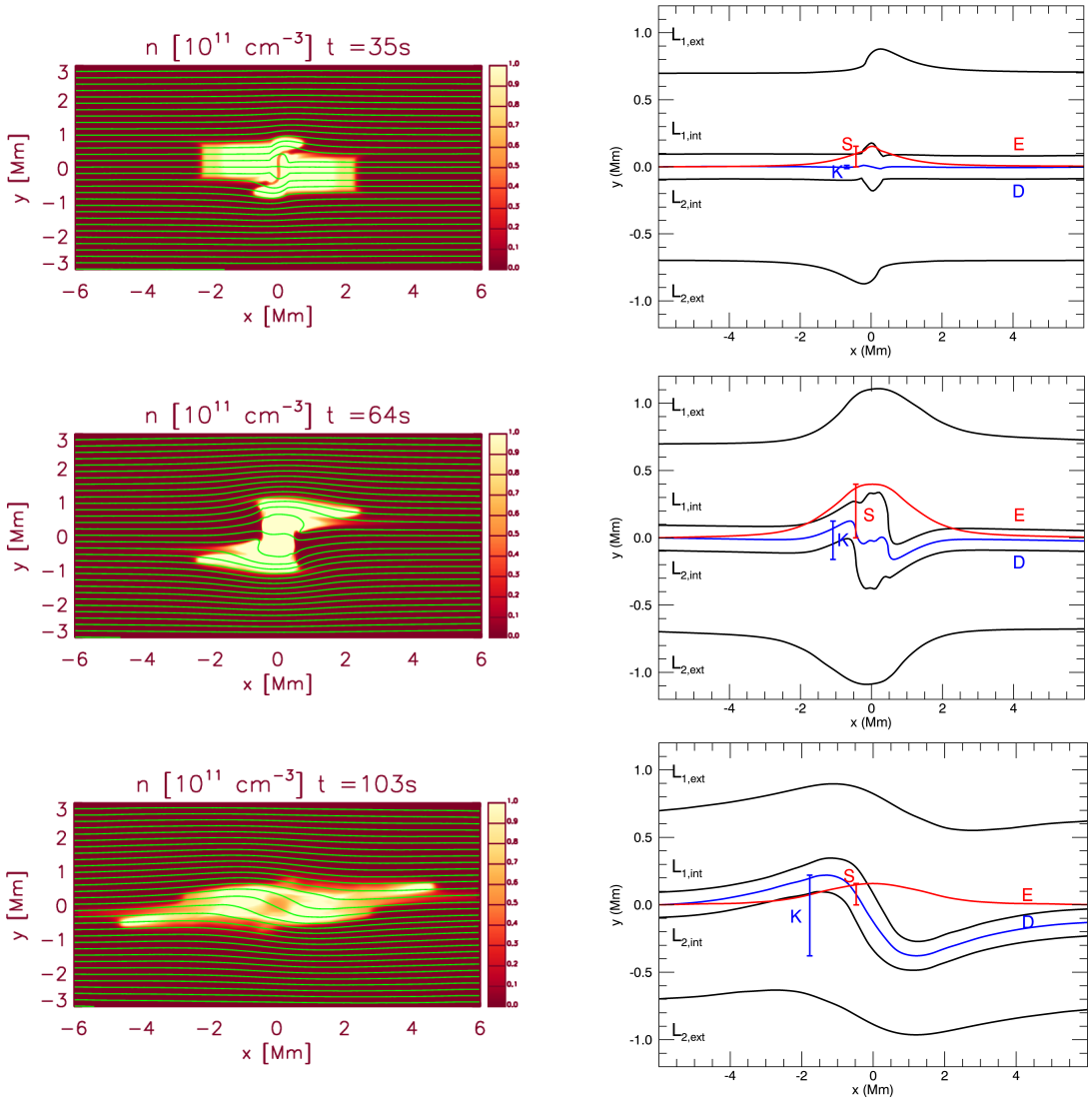

Figure 4.30: (Left) Contours of the density (with magnetic fieldlines overplotted in green) of the case $y_{cent,i} = \pm 0.2$ Mm at $t = 35, 64, 103$ s. (Right) Plots of the corresponding measurements of the kink amplitude $K(t)$ (blue) and sausage amplitude $S(t)$ (red) at these times.

leads to smaller maximal amplitudes. The maximal amplitudes obtained in this parameter study are smaller than the maximal amplitudes in PS4, because the clumps only partly collide. The evolution of $K(t)$ shows a different behaviour than in the previous parameter studies. $K(t)$ only slightly increases in the collision phase ($t < 66$ s) and $\max(K(t))$ is obtained at a later time, around $t \sim 100$ s instead of at the end of the collision phase ($t \sim 66s$). This is because the internal fieldlines are initially not significantly kinked because the angle θ of the colliding interface of the clumps is at zero degrees. The maxima of $K(t)$ after the collision phase are also a lot larger and do not seem to undergo the same damping as in the previous parameter studies. This is

because the width of the collision region is larger when the clumps are offset. A similar result is obtained in Section 4.5 when the width of the clumps is varied (PS7). For the cases $y_{cent,i} = [\pm 0.4, \pm 0.5]$ Mm, $K(t)$ remains rather large after $t \sim 200$ s. This is an artificial effect because the clumps have left the numerical domain by this time and the fieldlines are not perfectly horizontal, which results in an (artificial) displacement of the central axis and a non-zero $K(t)$. As before, the sausage amplitude $S(t)$ (right panel of Figure 4.31) increases during the collision phase and reaches a maximum at $t \approx 65$ s. The $\max(S(t))$ is largest when there is no offset and decreases when the offset increases, because the collision becomes less efficient and produces smaller forces. The evolution of $S(t)$ after the collision phase is similar as in PS4 (except for the cases with an offset of $y_{cent,i} = [\pm 0.4, \pm 0.5]$ as described earlier).

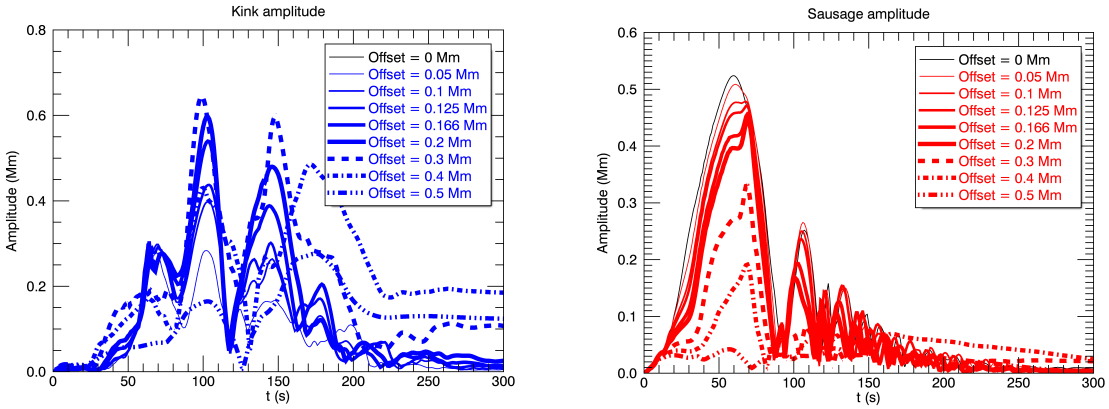

Figure 4.31: Plot of $K(t)$ (left) and $S(t)$ (right) for each case with time.

In Figure 4.32 we show $\max(K(t))$ (blue) and $\max(S(t))$ (red) for each case. This Figure summarises the results above and is similar to Figure 4.27 in the sense that $\max(K(t))$ increases when the offset (asymmetry) increases, and a maximum is reached for an offset of 0.3 Mm. When the offset is too large (0.4 Mm or 0.5 Mm), $\max(K(t))$ decreases as the collision is less efficient because the clumps mostly travel past each other. For $\max(S(t))$, the maximum is reached when there is no offset, and it decreases when the offset increases because the collision produces smaller forces.

In Table 4.9 we again show the initial angular momentum $|L| = \int_V |\mathbf{r} \times (\rho \mathbf{v})| \mathrm{dV}$ w.r.t. the origin $(x = 0, y = 0)$ for each case in PS5, normalised to the simulation where the largest kink amplitude is obtained (offset of 0.3 Mm). We can see that the initial angular momentum increases for increasing offset, because the asymmetry of the setup increases. Again, we note that a larger angular momentum does not result in a larger maximal kink amplitude, as for extreme cases the collision is less efficient and the clumps only partially collide.

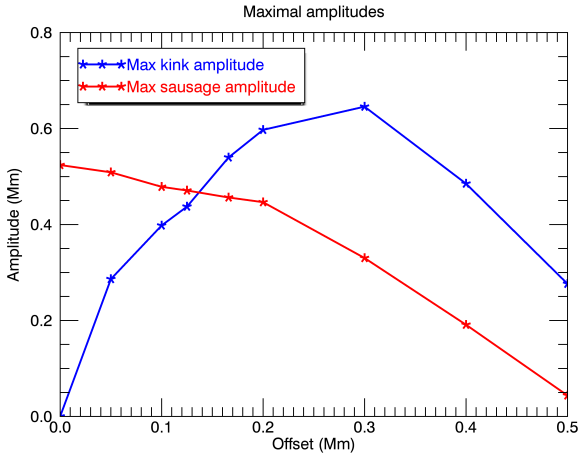

Figure 4.32: Plot of max($K(t)$) (blue) and max($S(t)$) (red) for each case.

Offset (Mm)	0	0.05	0.1	0.125	0.166	0.2	0.3	0.4	0.5
$\|L\|$	0	0.16	0.32	0.4	0.56	0.67	1	1.36	1.68

Table 4.9: Table of the initial angular momentum $|L| = \int_V |\mathbf{r} \times (\rho \mathbf{v})| dV$ for each case in PS5, normalised against the simulation with an offset of 0.3 Mm.

4.5 Parameter studies related to the size of the clumps

In this section we investigate the influence of the shape of the clumps on the generated modes by varying the length (PS6) and the width of the clumps (PS7).

4.5.1 PS6: Varying the length L_{clump} of the colliding clumps

Figure 4.33 shows the 6 cases we consider in PS6: $L_{clump} = 1.5, 2.4, 3, 3.6, 3.9, 4.2$ Mm. The length of the clumps in the reference simulation is $L_{clump} = 3$ Mm. We also consider a case where we have infinitely long clumps by having the clumps initially touch the x-boundaries of the domain. Due to the boundary conditions this is equivalent to having infinitely long clumps. Observations of coronal rain where the clumps have a significant length (in some cases of the order of several tens of Mm) are reported in e.g. Antolin et al. (2015b).

The density contrast $\rho_c = \rho_i/\rho_e = 100$ and the speed $v = 70$ km/s are the same as in the reference simulation, hence the internal Alfvén Mach number ($M_A = 1.21$) and the internal Mach number ($M_S = 4.22$) of the clumps are the same as in the reference simulation for each case. By varying the length of the clumps, their area changes and

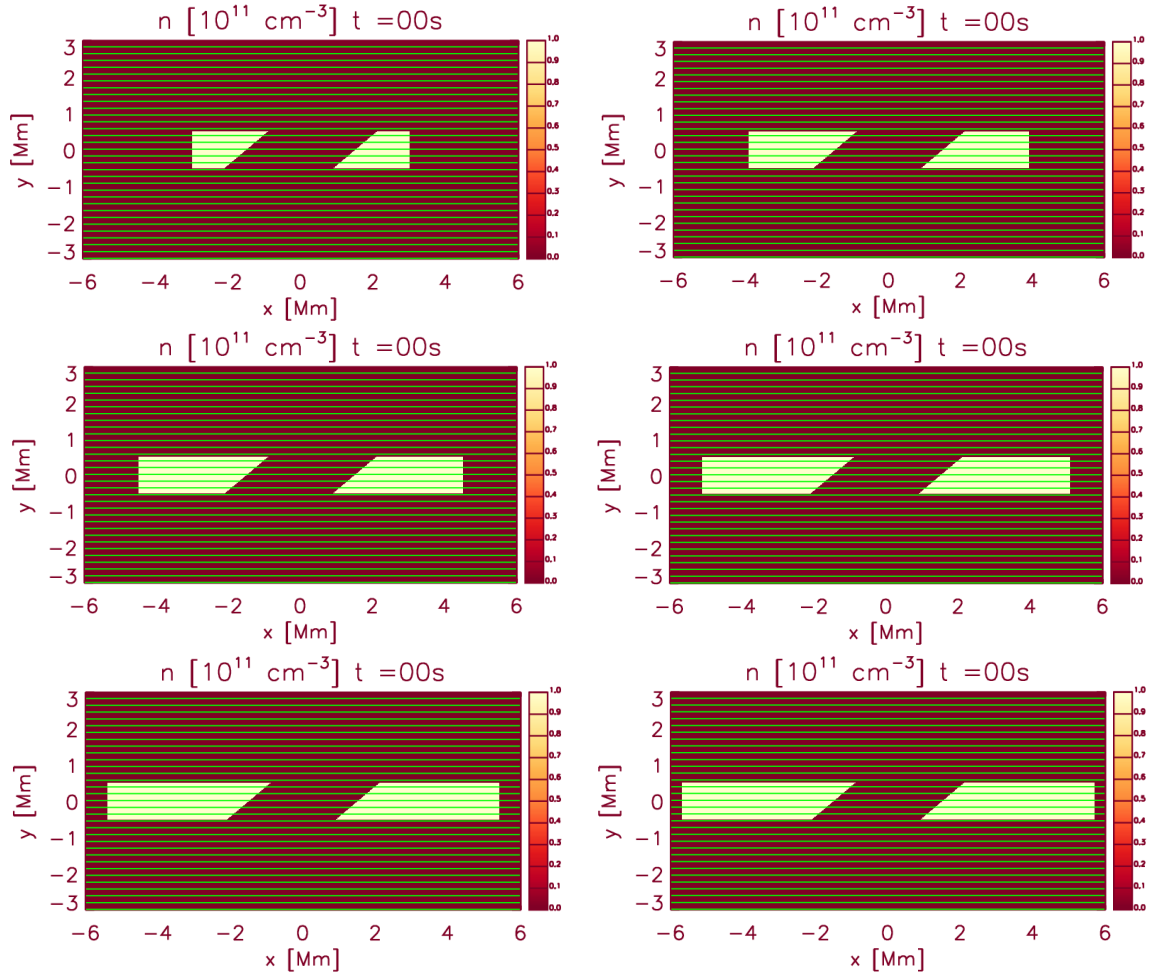

Figure 4.33: Initial conditions for the simulations with varying L_{clump}. From top left to bottom are the simulations with $L_{clump} = 1.5, 2.4, 3, 3.6, 3.9, 4.2$Mm.

hence the kinetic energy is different in each case. This is shown in Table 4.10. If we scale the length with a factor m the kinetic energy also scales with m.

L_{clump} (Mm)	Total kin. energy $\rho_c v^2/2$ (erg)	Relative tot. kin. energy
1.5	5.41×10^4	0.5
2.4	8.67×10^4	0.801
3	1.08×10^5	1
3.6	1.3×10^5	1.199
3.9	1.41×10^5	1.301
4.2	1.51×10^5	1.398

Table 4.10: The total initial kinetic energy and relative total kinetic energy for each case in PS6.

Figure 4.34 shows the evolution of the kink amplitude $K(t)$ (left panel) and sausage amplitude $S(t)$ (right panel) with time for each case. Max$(K(t))$ increases when the

length of the clumps increases, because the kinetic energy of the system is larger. The scaling is initially linear, but there seems to be a saturation effect for the cases with $L_{clump} > 3.6$ Mm ($\max(S(t))$ shows a similar saturation effect). This saturation happens because the restoring Lorentz force of the external field becomes strong enough at a certain point such that it prevents any further growth of the internal magnetic field distortion. This is also seen in the case with infinite clump length. We also remark that the maximal amplitudes are reached at a later time when the clumps are longer, because the time of the collision is longer and the field gets more distorted. The evolution of $K(t)$ and $S(t)$ after the collision do not show significant differences between the cases.

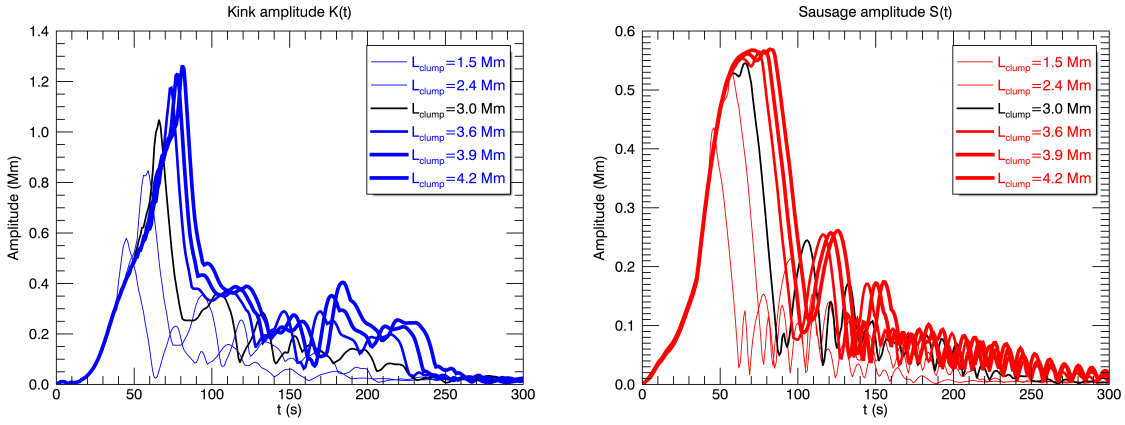

Figure 4.34: (Left) Plot of the evolution of the kink amplitude $K(t)$ for each length L_{clump}. (Right) Similar plot for the sausage amplitude $S(t)$.

In Figure 4.35 we show the evolution of $K(t)$ and $S(t)$ for the case with infinite clump length. Again we notice a saturation effect in $K(t)$ and $S(t)$, which can be explained in terms of the forces. The right panel of Figure 4.35 shows the average forces for the case $L_{clump} = 3$ Mm and $L_{clump} = \infty$ (averaged over the left square in Figure 4.26). The forces for the case $L_{clump} = 3$ Mm are representative for the cases with finite clump length, and these forces follow a similar behaviour as the one discussed in Section 4.4.1. The average forces for the case $L_{clump} = \infty$ do not show any oscillations as the clumps are continuously colliding, due to the fact that mass is constantly flowing through the x boundaries. The pressure gradient force $-(\boldsymbol{\nabla} P)_y$ (red dashed line) and the Lorentz force $(\mathbf{j} \times \mathbf{B})_y$ (blue dashed line) keep growing up to $t \approx 150s$. At this stage part of the clumps are leaving the x boundaries on the other side and the system is evolving into two counter-propagating streams of plasma (see Figure 4.36). The distortion of the magnetic field can no longer grow and $K(t)$ and

$S(t)$ remain constant. The increase in $K(t)$ and $S(t)$ near the end of the simulation ($t \approx 250$ s) is an artificial effect and happens because the plasma streams diverge in the y direction (due to a significantly distorted magnetic field, see e.g. Figure 18 in Pagano et al. (2019)). It is also worth looking at the wavelength of the generated modes when L_{clump} is varied.

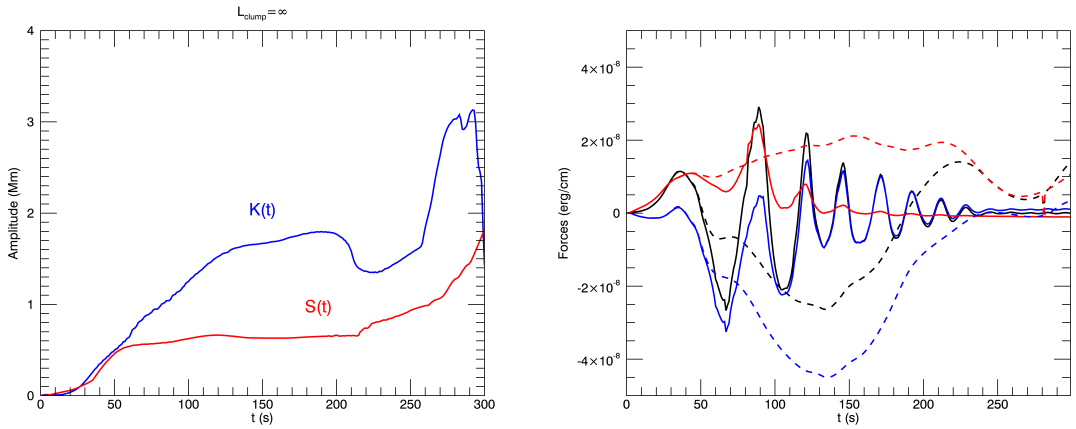

Figure 4.35: (Left) Plot of the evolution of $K(t)$ and $S(t)$ for the case $L_{clump} = \infty$. (Right) Plot of the average forces $-(\boldsymbol{\nabla} P)_y$ (red), $(\mathbf{j} \times \mathbf{B})_y$ (blue) and $(\mathbf{j} \times \mathbf{B})_y - (\boldsymbol{\nabla} P)_y$ (black) in the square with $x < 0$ Mm (see e.g. Figure 4.26), for the case $L_{clump} = 3$ Mm (solid lines) and $L_{clump} = \infty$ (dashed lines).

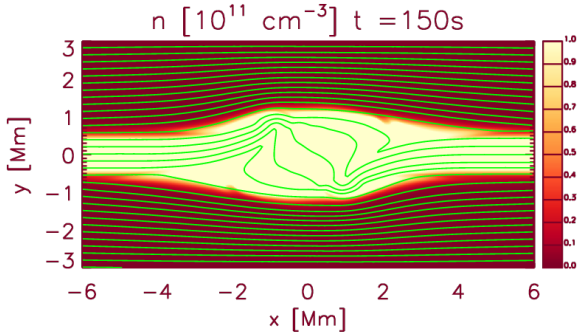

Figure 4.36: Contour of the number density n ($\times 10^{11}$ cm^{-3}) at $t = 0$ with magnetic fieldlines overplotted in green, at $t = 150$s for the simulation where the clumps have infinite length.

The left panel of Figure 4.37 shows the displacement $D(x)$ for the case $L_{clump} = 1.5$ and $L_{clump} = 4.2$ Mm at the time of $\max(K(t))$ ($t = 45$ s and $t = 81$ s respectively). The kink amplitude $K(t) = \max(D(x)) - \min(D(x))$ is larger for clumps with longer length, but also $\max(D(x))$ and $\min(D(x))$ are further apart (and hence the wavelength λ_{kink} is larger). This is shown by the dashed vertical lines for each case. For cases with longer

L_{clump}, λ_{kink} is larger because the collision lasts longer and max($D(x)$) and min($D(x)$) propagate away from $x = 0$ at the local Alfvén speed (which is the same for all cases) as soon as the collision starts. This is also confirmed by the right panel of Figure 4.37 where we plot the wavelength λ_{kink} for each case at the time of max($K(t)$). The wavelength increases approximately linearly when L_{clump} increases. We find similar results for the sausage wavelength λ_{saus} (bottom panels of Figure 4.37).

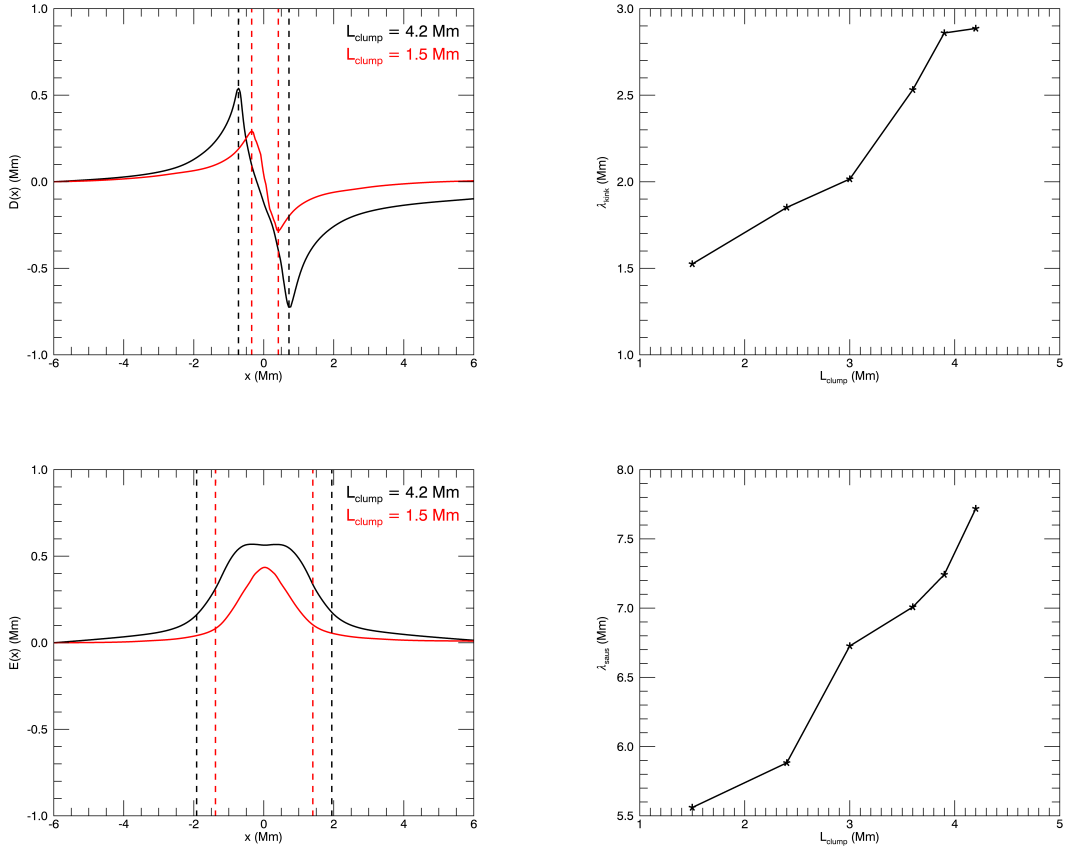

Figure 4.37: (Top left) Plot of the displacement $D(x)$ at the time of max($K(t)$) for the cases $L_{clump} = 1.5, 4.2$ Mm. The dashed lines mark the locations of max($D(x)$) and min($D(x)$). The distance between the dashed lines is an estimate for half the wavelength. (Top right) Plot of wavelength λ_{kink} for all cases with finite clump length, at the time of max($K(t)$). (Bottom) Similar panels for the sausage wavelength λ_{saus}.

4.5.2 PS7: Varying the width W_{clump} of the colliding clumps

Figure 4.38 shows the 3 cases we consider in this parameter study: $W_{clump} = 1, 2, 3$ Mm. The width of the clumps in the reference simulation is $W_{clump} = 1$ Mm. All other quantities are as in the reference simulation. By increasing the width of the clumps the area increases and hence the kinetic energy for each case is different. This is shown in Table 4.11.

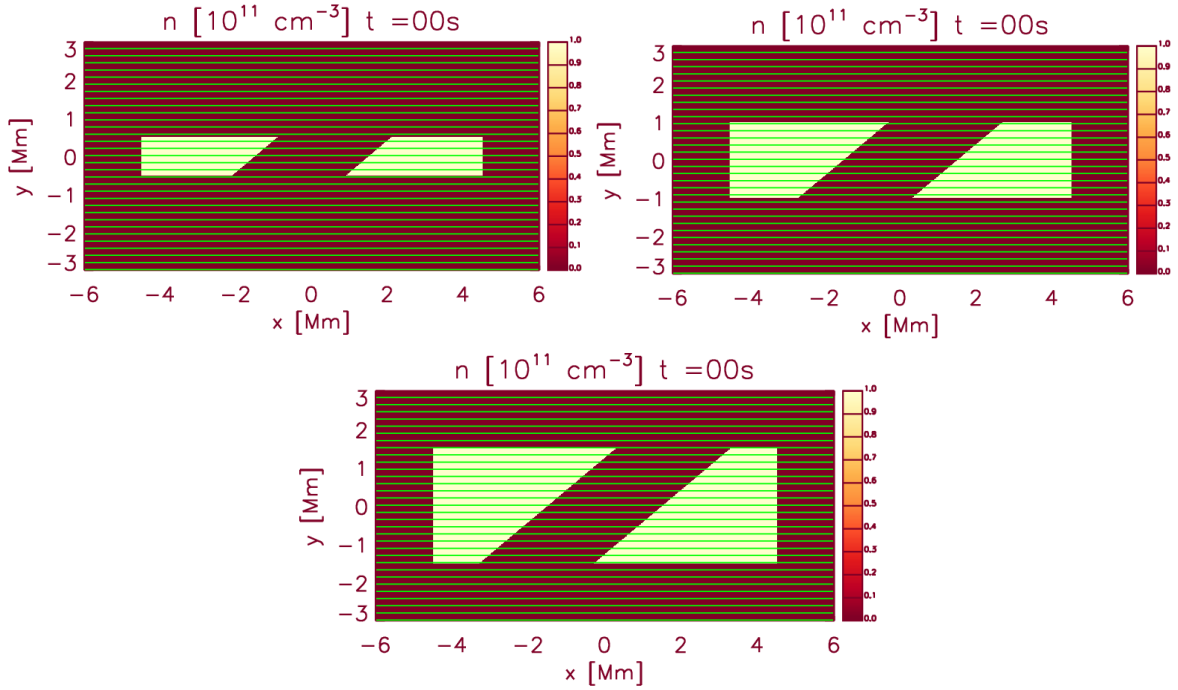

Figure 4.38: Setup of the three cases in PS7 ($W_{clump} = 1, 2, 3$ Mm).

Width (Mm)	Total kin. energy $\rho_c v^2$ (erg)	Relative tot. kin. energy
1	1.08×10^5	1
2	2.14×10^5	1.98
3	3.22×10^5	2.98

Table 4.11: The total initial kinetic energy and relative total kinetic energy for each case in PS7.

Figure 4.39 shows the evolution of $K(t)$ and $S(t)$ for each case. Max($K(t)$) is attained at $t \approx 65$s for all cases, but again shows a saturation. This is because for wider clumps the distortion of the magnetic field is less efficient as the width of the interface that is colliding is larger. The kinetic energy that is available now has to distort more internal magnetic fieldlines, but it does not increase the maximal distortion (max($K(t)$)). This is also shown by Figure 4.40 which shows contours of the density

(left panels) together with the measurement of the amplitudes (right panels) for the three cases at $t = 66$ s. We can see that more fieldlines are distorted for wider clumps, but the maximal distortion is essentially the same in all three cases. The evolution of $K(t)$ after the collision is different for wider clumps, in the sense that the oscillations in $K(t)$ seem to be decay less. This is because the wave guide is larger in the y direction, and the damping time is proportional to the travel time across the clumps. A similar result was found in PS5 when the offset of rectangular clumps was investigated. The evolution of $S(t)$ shows that $\max(S(t))$ is larger for wider clumps, but again $\max(S(t))$ seems to saturate. The evolution of $S(t)$ after the collision does not show a difference in the damping of the oscillations between the cases. The width of the clumps does not have an effect on the wavelength of the oscillations, because the length of the clumps is the same for all three cases.

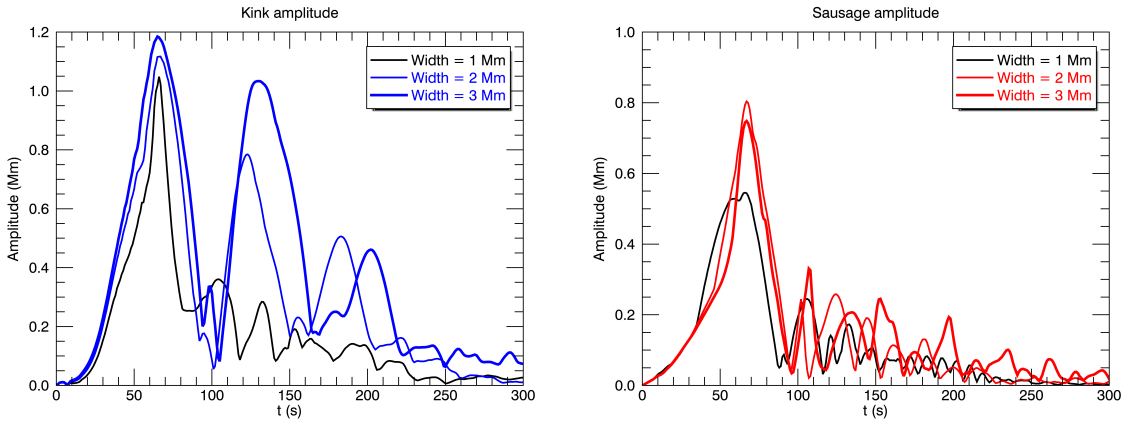

Figure 4.39: (Left) Plot of the evolution of the kink amplitude $K(t)$ for each case. (Right) Similar plot for the sausage amplitude $S(t)$.

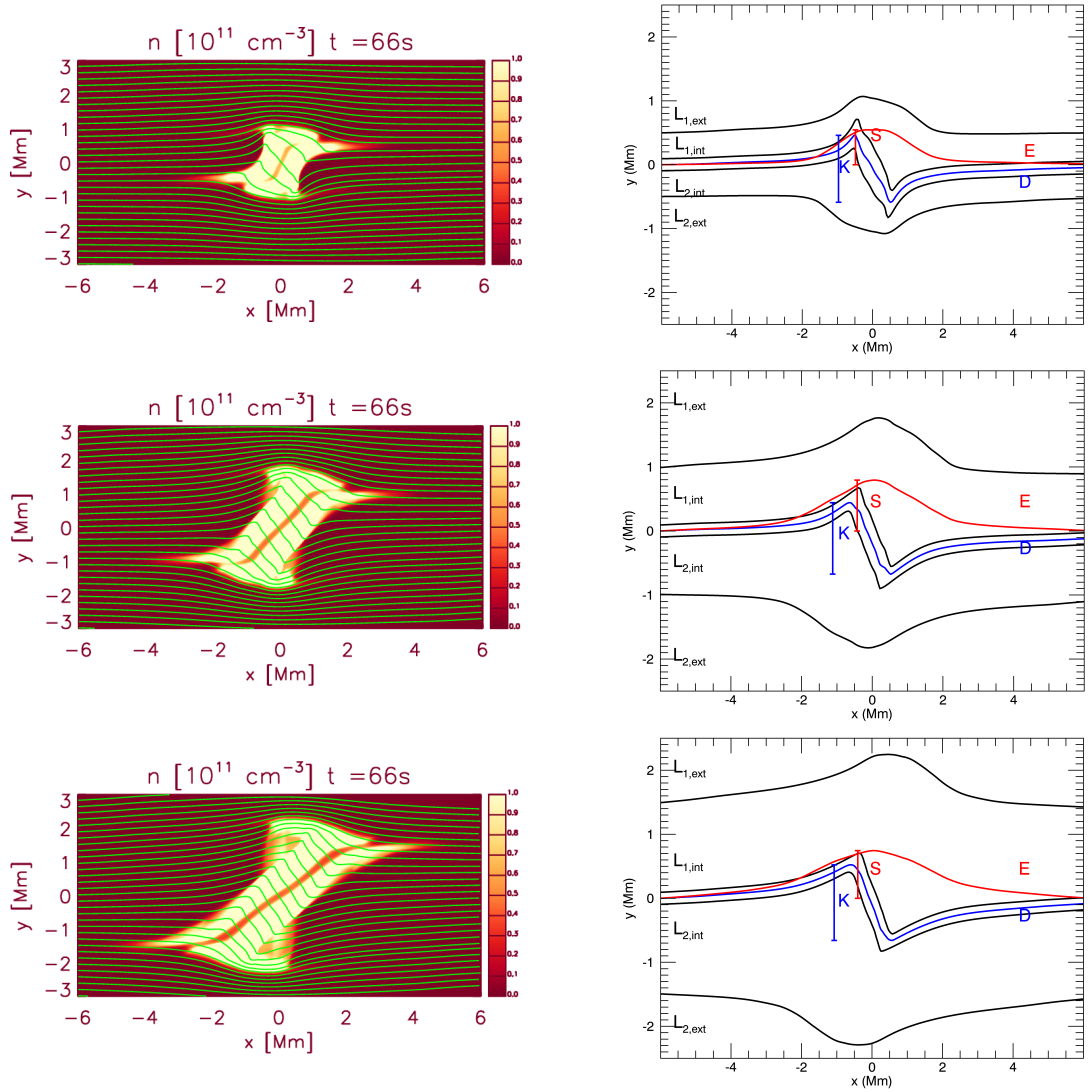

Figure 4.40: Contours of the number density (with magnetic fieldlines overplotted in green) of the cases $W_{clump} = 1, 2, 3$ Mm at $t = 66$ s, together with plots of the measurement of $K(t)$ and $S(t)$ at $t = 66$ s. Max($K(t)$) (Max($S(t)$)) for $W_{clump} = 1, 2, 3$ Mm is attained at $t = 66, 67, 65$ s ($t = 66, 67, 67$ s) respectively.

4.6 Discussion and conclusion

In this chapter we have analysed the collision between clumps of plasma and the subsequent in-situ generation of transverse MHD waves. These collisions have been observed in, for example, coronal rain complexes and could be a source of transverse MHD waves in the corona.

In Section 4.2 we introduced a 2D MHD model for colliding flows (based on the model from Antolin et al. (2018)) and analysed the reference simulation of two colliding,

trapezoidal clumps in a coronal environment. We have seen that the collisions between the clumps is characterised by two phases, a 'collision phase' where the clumps collide and the kinetic energy of the clumps is used to distort the magnetic field. In the second phase, the 'propagation phase', the restoring magnetic forces produce oscillations that propagate in the domain. We developed a way of measuring the amplitudes of the generated modes: we associated a kink mode with a displacement of the central axis of the wave guide, and a sausage mode with a symmetric expansion/compression about the central axis.

In Sections 4.3, 4.4 and 4.5 we conducted an extensive parameter study to investigate the size and nature of the generated perturbations. In the first section (Section 4.3) we varied the density and the speed of the clumps and found that the amplitude of the generated modes scales with the kinetic energy of the system (PS1). When the speed is varied in an asymmetric manner (PS2), we found that the maximal amplitudes still scale with the kinetic energy of the system (with respect to the centre of mass). An asymmetry in the speed of the clumps does not change the maximal amplitudes, as long as the kinetic energy is maintained. We have seen that varying the density asymmetrically (PS3) leads to less efficient collisions and a saturation in the maximal amplitude of the generated modes. It can even distort the magnetic field in such a way that it no longer behaves as a waveguide (i.e. the magnetic field is too distorted). This could potentially lead to small reconnection events and the formation of plasmoids if non-ideal MHD effects were to be included, although it should be noted that the timescales of this process might be longer than the time of the collision.

In Section 4.4 we investigated the asymmetry of the setup by varing the angle of the colliding interface (PS4) and the offset between rectangular clumps (PS5). We found that an asymmetric setup of the clumps preferentially generates kink modes (due to kinking of the internal fieldlines) and that sausage modes are more apparent in a symmetric setup. However, we also found that the generation of sausage modes is less dependent on the angle. An angle of 50 degrees (or an offset of 0.3 Mm) seems to be the angle (offset) which generates the largest kink amplitude. Too much asymmetry (an extreme angle or offset) leads to less efficient collisions and smaller maximal amplitudes.

In the final section (Section 4.5) we investigated how the size of the clumps determines the generated perturbations. We varied the length (PS6) and width (PS7) of the clumps. We found that longer clumps lead to longer collision times and this in-

creases the wavelength of the generated modes. Increasing the length too much however leads to saturation effects of the maximal sausage and kink amplitudes as the restoring magnetic forces limit the growth of the distortion of the magnetic field. Increasing the width of the clumps has a similar saturation effect on the size of the amplitude, as the kinetic energy of the collision is now distributed over a larger area. The width of the clumps does not have a significant effect on the wavelength of the generated modes. We also found that wider clumps seem to undergo less damping as the waveguide is larger in the transverse direction.

Chapter 5

Coronal rain collisions and oscillations in coronal loops

5.1 Introduction

In Chapter 4, we conducted a parameter study of colliding plasma clumps, and investigated in detail the generation of the transverse MHD waves. In this chapter, we extend the investigation of the colliding clumps/blobs by basing the parameters of the clumps in the model on the observational study of coronal rain presented in Antolin and Rouppe van der Voort (2012). We will run a large set of simulations of colliding clumps using the techniques from Chapter 4 to analyse the transverse MHD waves resulting from the collisions. In Section 5.2 we discuss the observational study of Antolin and Rouppe van der Voort (2012), and in section 5.3 we obtain distributions for the parameters of the blobs in our simulations. In Section 5.4 and 5.5 we present the results and the analysis of the simulations. We end the chapter with a discussion and conclusion section (Section 5.6).

5.2 Observational study of coronal rain

Antolin and Rouppe van der Voort (2012) (Antolin2012 from now on) observe coronal rain in Active Region (AR) 11017, a plage region at the east solar limb on 2009 May 10, with the CRISP instrument of the Solar Swedish Telescope (SST). The observations are in Hα and run from 8:50 to 10:15 UT with a cadence of 6.36s. The dataset consists of 2552 coronal rain blobs falling along 242 loop-like paths at the east limb of the Sun, with a smaller subset of blobs falling along loop-like paths on the disk. We will present

the histograms for both subsets of the dataset, but when determining the parameters for the simulations we will only use the observations of the blobs on the limb, since this is the larger dataset.

Velocity

The velocity of the blobs is determined by measuring the projected velocity on the plane of sky (POS), v_{proj}, and the Doppler velocity, v_{Dop}. The total velocity of the blobs is then obtained from $v_{tot} = \sqrt{v_{proj}^2 + v_{Dop}^2}$.

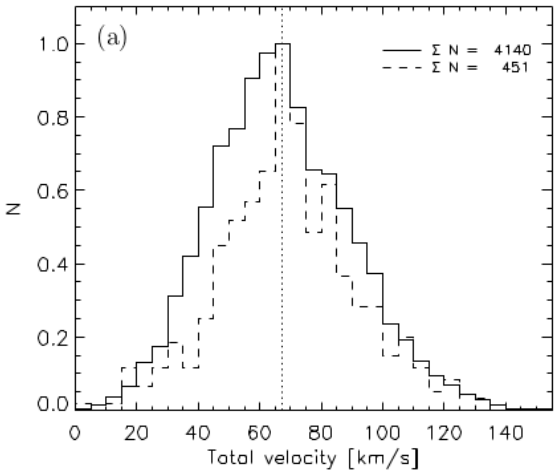

Figure 5.1: Normalised histogram of the total velocity v_{tot} of the coronal rain blobs (km/s). The solid histogram indicates the dataset on the limb of the Sun and the dashed histogram the dataset on the disk. The dotted vertical line marks the average velocity, 70 km/s. Figure obtained from Antolin2012, Figure 4.

Figure 5.1 shows the normalised histogram of the total velocity v_{tot} (km/s) for all observations. The speed of the falling blobs ranges widely from $v = 3 - 150$ km/s with an average of 70 km/s, shown by the dotted line. The standard deviation of the total velocity is of the order of 5 km/s, which is also the binwidth of the histogram. The speed of the blobs is smaller than their expected free-fall speed (i.e. the speed they would obtain falling under the force of gravity from the location where they are formed), with the average acceleration of the blobs of the order of 0.08 km/s^2 compared to the estimated effective gravity of $0.13 - 0.21$ km/s^2. These smaller velocities and accelerations have also been mentioned by e.g. Schrijver 2001; De Groof et al. 2005; Antolin and Rouppe van der Voort 2012; Ahn et al. 2014; Kohutova and Verwichte 2016; Verwichte et al. 2017. Recent numerical simulations have shown that the pressure gradient along the loop is the major agent that slows the blobs down (see e.g. Oliver et al. 2016; Kohutova and Verwichte 2018b; Martínez-Gómez et al. 2020).

Length and width

Blobs can change their shape when falling down. In general blobs tend to elongate when falling, but they can even break up into smaller clumps, leading to so called "shower" events (see Antolin2012). Figure 5.2 shows a normalised histogram of the lengths (left panel) and the widths (right panel) of the observed blobs in Antolin2012. The length of the blobs varies between $L = 0.2 - 2.5$ Mm with an average of 0.71 Mm, and with a peak at 0.5 Mm. Observations shows that the width of the blobs remains more constant when falling and only for extremely wide blobs (larger than 0.7 Mm) does the width seem to decrease due to shearing with the environment. The width of the blobs ranges from $0.15 - 0.8$ Mm with an average of 0.3 Mm. However, the authors note that the width histogram is likely an upper estimate, as smaller widths are harder to observe due to the resolution of the instrument (the lower threshold of the instrument is 150 km, see Antolin2012). This was also mentioned by Scullion et al. (2014).

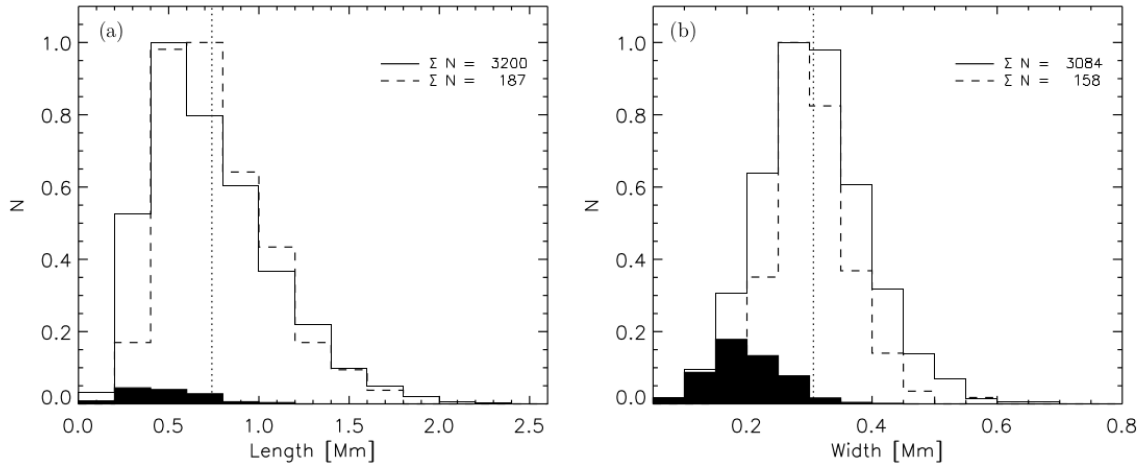

Figure 5.2: Normalised histograms for the lengths and the widths of the blobs. The black histograms denote the measurements for which the 1σ errors are above 10% of the measured values (See Antolin2012, section 3.2 for more details). Figures obtained from Antolin2012, Figure 10.

Temperature

Figure 5.3 shows the normalised histogram of the temperature of the blobs. Due to the nature of its formation (thermal instability), coronal rain is characterised by cool, chromospheric temperatures of the order of $\sim 10^3 - 10^4$ K. The distribution shows a peak around ~ 7000 K and the average temperature of the blobs is 10^4 K.

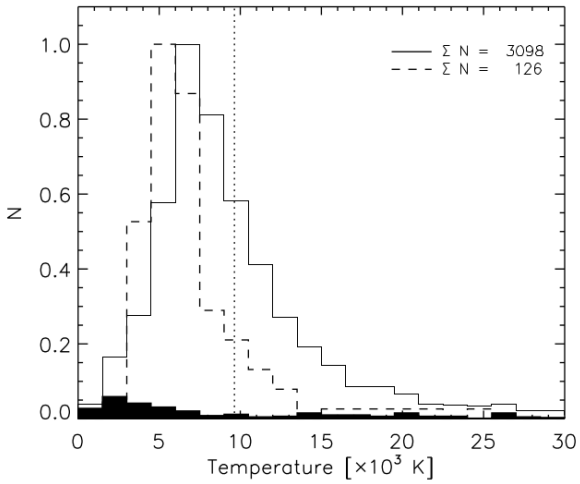

Figure 5.3: Normalised histogram of the temperature of the blobs. Figure obtained from Antolin2012, Figure 15.

5.3 Parameter study

In order to study the oscillations generated by collisions of coronal rain blobs in active regions, we use the 2D model from Chapter 4 and devise a large set of representative simulations (201) for which we base the properties of the blobs in our model on the study by Antolin2012. The number of simulations is large enough such that statistical conclusions can be made, but it keeps computational costs reasonable.

We will use a "bullet-like" shape for the blobs, as shown in Figure 5.4. This shape is more natural than the trapezoidal shape which we used in Chapter 4, which was used to initiate a kink-like deformation of the field. Because in our model we will include an offset between the blobs, this will provide an asymmetry to get a kink-like deformation of the field. It was also shown by Antolin et al. (2018) that bullet-shaped blobs with an offset give similar deformations of the field and oscillations compared to trapezoidal-shaped blobs.

The following parameters need to be determined in each simulation: the velocity of the blobs, v_1, v_2, the density ρ_1, ρ_2, the lengths L_1, L_2, the widths W_1, W_2 and the offset O. In our model we will assume that $v_1 = v_2 = v$ and that the mass $M = \rho_1 \text{Area}_1 = \rho_2 \text{Area}_2$ (kg/m) is the same for both blobs, in order for the collision and the early evolution after the collision to take place in the centre of the domain.

Our model can represent the collision between a downwards propagating coronal rain blob and an upward propagating blob or flow (e.g. an evaporation), as observed in

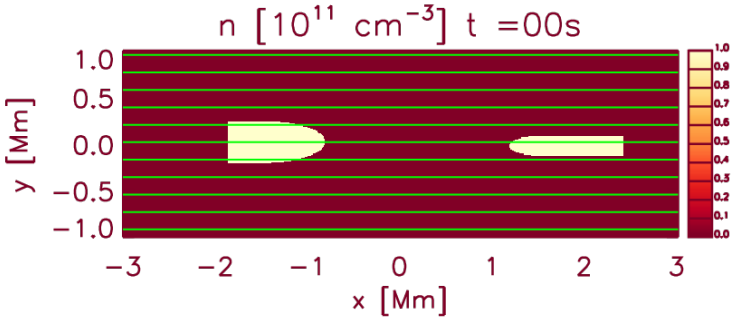

Figure 5.4: Contour of the number density of two bullet-shape blobs.

Antolin et al. (2018). In our setup, this would be the left and right blob, respectively. In Chapter 4 (section 4.3.2) we showed that the relative velocity of the blobs determines the collision. Hence, our model could also represent collisions between coronal rain blobs which are falling down at different speeds.

5.3.1 Blob parameters

Velocity v

Figure 5.5 shows the histogram of the $n = 201$ velocities in our parameter study. We obtain this histogram by rescaling the normalised histogram of the total velocity of the observed coronal rain blobs (Figure 5.1) to n observations and then drawing (at random) k_i velocities in bin i, where k_i is the number of observations in bin i (hence $\sum_i k_i = n$). The velocity ranges between $12.5 - 132.2$ km/s, with the average velocity $\langle v \rangle = 67.6$ km/s (vertical dashed line) and the standard deviation $\sigma(v) = 22.4$ km/s. This is in agreement with the observed histogram in Figure 5.1.

Widths W_1, W_2

Figure 5.6 shows the histograms of the widths W_1 (green) and W_2 (orange) of the blobs in our parameter study. These were obtained by applying the same procedure as before, and drawing twice n points from the rescaled histogram of the observed coronal rain widths in Figure 5.2. The dashed lines represent the average width, $\langle W_1 \rangle = \langle W_2 \rangle = 0.31$ Mm and $\sigma(W_1) = \sigma(W_2) = 0.09$ Mm, which is consistent with the observed histogram in Figure 5.2.

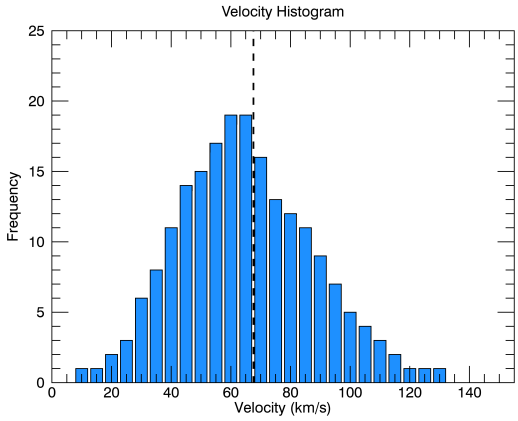

Figure 5.5: Histogram of the n velocities of the blobs for our simulations, based on the normalised histogram in Figure 5.1. The dashed vertical line is the average velocity, $\langle v \rangle = 67.6$ km/s.

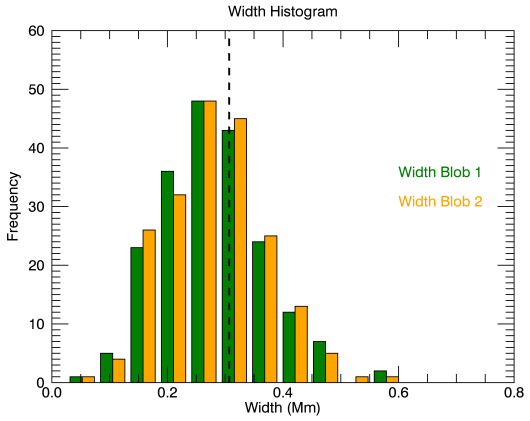

Figure 5.6: Histogram of the n widths W_1 (green) and W_2 (orange) in Mm, based on the normalised histogram in Figure 5.2. The dashed vertical line is the average width, $\langle W_1 \rangle = \langle W_2 \rangle = 0.31$ Mm.

Lengths L_1, L_2

Antolin2012 states that blobs tend to get longer and accelerate when falling (although they experience a less than free-fall acceleration). We therefore link the length of the blobs with the velocity in our model, by re-ordering the lengths array for the first blobs, such that longer blobs travel faster and shorter blobs travel slower.

Figure 5.7 shows the histogram of the n lengths L_1 in Mm, based on the (rescaled) normalised histogram of the observed lengths of the coronal rain blobs in Figure 5.2. This was again obtained by applying the same procedure as before. The dashed vertical line

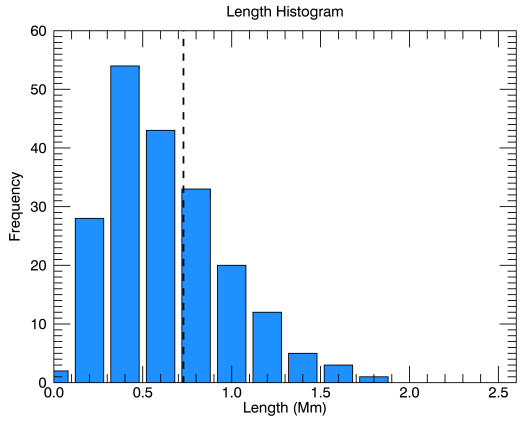

Figure 5.7: Histogram of the n lengths L_1 (Mm), based on the normalised histogram in Figure 5.2. The dashed vertical line is the average length of L_1, $\langle L_1 \rangle = 0.73$ Mm.

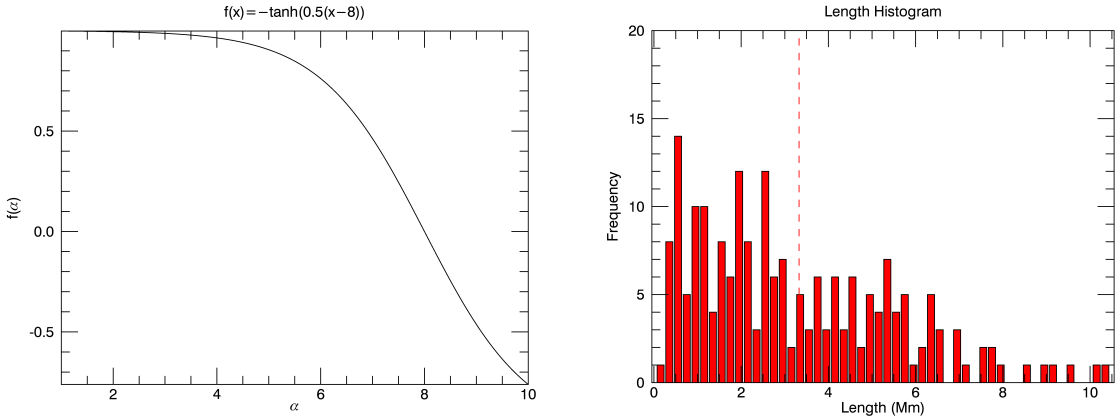

Figure 5.8: (Left) Plot of the distribution $f(\alpha) = -\tanh(0.5(\alpha - 8))$ for $1 < \alpha < 10$. (Right) Histogram of the n lengths L_2 (red) in Mm. The red dashed line is the average L_2, $\langle L_2 \rangle = 3.3$ Mm.

represents the average, $\langle L_1 \rangle = 0.73$ Mm and the standard deviation is $\sigma(L_1) = 0.35$ Mm, which is in agreement with the observed histogram in Figure 5.2.

In this parameter study, we will assume that the right blob is always longer or equal in length than the left blob in a simulation. If we assume the right blob would be travelling upward along a coronal loop, this setup allows us to model the collision of a short, dense (falling) blob with an (evaporative) upflow (modelled as an elongated blob travelling upwards) within our parameter study. We therefore have that $\alpha := \frac{L_2}{L_1} \geq 1$, and we assume that α is distributed according to some function such that it is more likely that $L_2 \approx L_1$ and less likely that L_2 is much longer than L_1. The left panel of

Figure 5.8 shows the function $f(\alpha) = -\tanh(0.5(\alpha - 8))$ with $1 < \alpha < 10$. The upper value of $\alpha = 10$ was chosen arbitrarily. Using a Monte Carlo method, we create a probability distribution from $f(\alpha)$. We draw points (α_i, y_i) at random in the rectangle defined by $[1, 10] \times [\min(f), \max(f)]$ and discard a point if $y_i > f(\alpha_i)$. We repeat this procedure until we have n points α_i. The length L_2 of the second blob is then determined from $L_2 = \alpha L_1$, where $\alpha = [\alpha_1, \alpha_2, ..., \alpha_n]$. The right panel of Figure 5.8 shows the histogram for the length L_2 (red) in Mm. The average length of the second blob, $\langle L_2 \rangle = 3.3$ Mm (red dashed line), is larger than $\langle L_1 \rangle = 0.73$ Mm, and the standard deviation $\sigma(L_2) = 2.3$ Mm is also larger.

Densities ρ_1, ρ_2

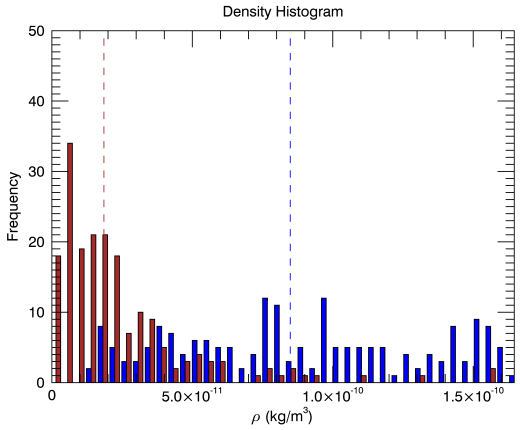

Figure 5.9: Histogram of the n densities ρ_1 (blue) and ρ_2 (brown) in kg/m^3. The dashed lines on Figure 5.9 are the median of ρ_1 and ρ_2, 8.5×10^{-11} kg/m^3 and 1.9×10^{-11} kg/m^3 respectively.

Figure 5.9 shows the histogram of the n densities ρ_1 (blue) and ρ_2 (brown) of the blobs. The density ρ_1 is drawn uniformly from the interval for coronal rain core densities, $[1.67 \times 10^{-11}, 1.67 \times 10^{-10}]$ kg/m^3 (Antolin, 2020). The density ρ_2 of the second blob is then calculated from the assumption that both blobs have the same mass. Hence

$$\rho_2 = \frac{M}{\text{Area}_2} = \frac{\rho_1 \text{Area}_1}{\text{Area}_2},$$

where Area_i is the area of blob i. The area of a (bullet-shape) blob consists of a rectangle and a half ellipse, as sketched in Figure 5.10. The rectangle has length $L' = L - \frac{3W}{2}$ and width W, and the ellipse has short axis $W/2$ and long axis $\frac{3W}{2}$, such that the total length of the blob is L. As we determine L and W independently for each blob, it can happen that $\frac{3W}{2} > L$ ($L' < 0$). When this happens (very wide and

short blobs), the blobs only have a bullethead (ellipse) with short axis $W/2$ and long axis L (right panel of Figure 5.10). In this way the blobs always have length L and width W as required. The area of the blobs is then $L'W + \frac{3\pi W^2}{8}$ when $L' > 0$ and $\frac{\pi LW}{4}$ when $L' < 0$.

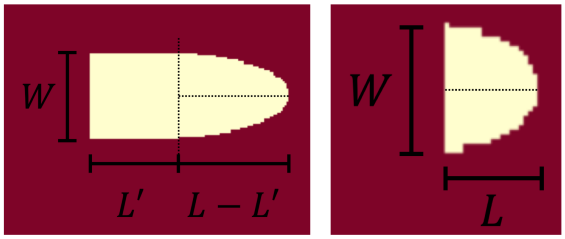

Figure 5.10: (Left) Schematic plot of a bullet-shaped blob, when $L' > 0$. The blob consists of a rectangle and a half ellipse, separated by the dotted vertical line in the plot. (Right) Similar plot when $L' < 0$, with the blob now only consisting of a half ellipse.

The dashed lines on Figure 5.9 are the median of ρ_1 and ρ_2, 8.5×10^{-11} kg/m^3 and 1.9×10^{-11} kg/m^3 respectively. Because the second blob in general has larger dimensions ($L_2 \geq L_1$), the density ρ_2 is on average smaller than ρ_1, as can be seen in the histogram. We remark that in 107 simulations we still have a density ρ_2 in the interval of the observed coronal rain densities in Antolin (2020) ($[1.67 \times 10^{-11}, 1.67 \times 10^{-10}]$ kg/m^3). The standard deviations are $\sigma(\rho_1) = 4.3 \times 10^{-11}$ kg/m^3, and $\sigma(\rho_2) = 3.3 \times 10^{-11}$ kg/m^3.

Offset

A last parameter in our model is the offset of the blobs, which determines whether the blobs partially or fully collide.

Because coronal rain blobs are tied to magnetic strands, we assume that the possible offset between the centres of two blobs is $[-R_{strand}, R_{strand}]$, with R_{strand} the average radius of a strand. The average area of a strand is $A_{strand} = \frac{A_{loop}}{N_{strands}} \approx 0.1$ Mm^2, where $A_{loop} \approx 8.8 \times 10^2$ Mm and $N_{strands} \approx 9000$ are estimated in Antolin2012. Hence $R_{strand} = \sqrt{\frac{A_{strand}}{\pi}} = 0.18$ Mm. The y coordinates of the centre of the blobs will be in $[-R_{strand}, R_{strand}] = [-0.18, 0.18]$ Mm, therefore we draw n coordinates uniformly at random from this interval for the first and the second blob.

The offset O is then given by the difference in the y coordinates of the centres of the blobs (see Figure 5.11). In the simulations, we place the clumps symmetrically about the $y = 0$ line in the domain, i.e. the central axis of the left blob at $y = O/2$ and the central axis of the right blob at $y = -O/2$.

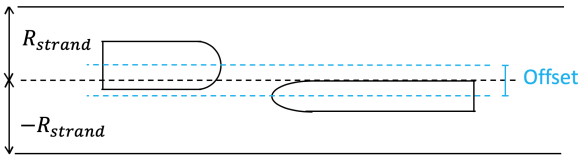

Figure 5.11: Sketch of the offset between the clumps. The solid black lines mark the boundary of the strand, and the dashed line is the central axis of the strand ($y = 0$). The dashed blue lines are the symmetry lines of the clumps.

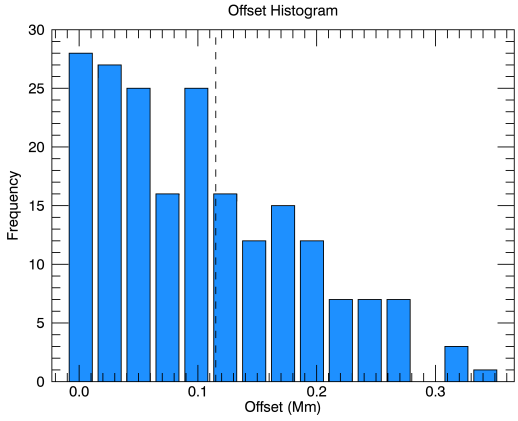

Figure 5.12: Histogram of the n offsets O (Mm) in our parameter study. The dashed vertical line represents the average offset, $\langle O \rangle = 0.115$ Mm.

Figure 5.12 shows the histogram of the n offsets O, with the dashed line representing the average offset (0.115 Mm), and the standard deviation is 0.08 Mm. The offset between the blobs is sometimes too large to lead to a collision. We find 10 simulations where the blobs do not collide, which we exclude from the parameter study (bringing the total number of simulations down to 191).

5.3.2 Background parameters: active region loops

So far, we have focused on establishing the parameters of the blobs but the external parameters in the simulations are still to be determined. To begin, we set the exterior density to be the minimal blob density, $\rho_e = \min(\rho_i) = 1.44 \times 10^{-12}$ kg/m^3. This is a typical coronal density for an active region loop (see e.g. Brooks et al., 2012) and it ensures that the blobs are denser than the exterior, apart from one simulation where one blob has the density of the environment. Figure 5.13 shows the histograms of the density contrasts for the blobs, $\frac{\rho_1}{\rho_e}$ and $\frac{\rho_2}{\rho_e}$. We can see that the contrast ranges from $1-150$, which is consistent with observations (Antolin, 2020). The dashed lines on the histograms represent the median, 59 for $\frac{\rho_1}{\rho_e}$ and 13 for $\frac{\rho_2}{\rho_e}$.

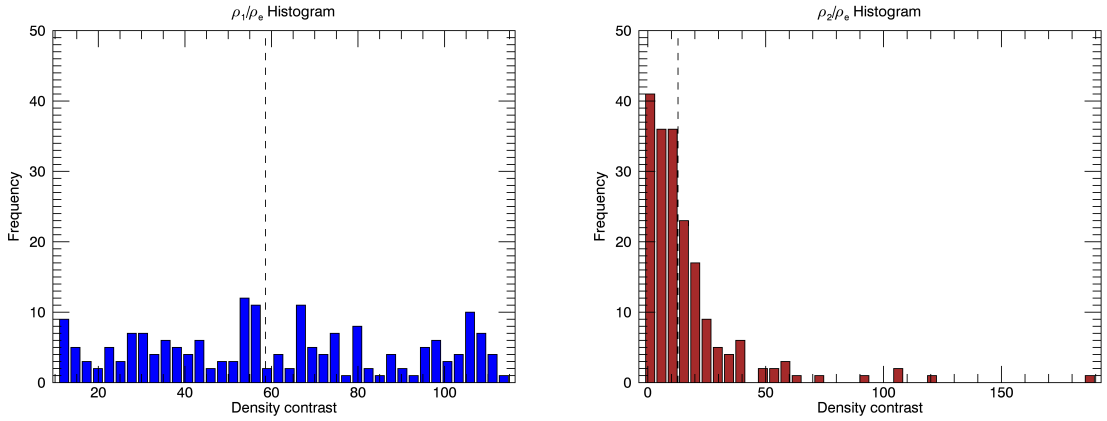

Figure 5.13: Histograms of the density contrast $\frac{\rho_1}{\rho_e}$ (left) and $\frac{\rho_2}{\rho_e}$ (right). The dashed vertical lines represent the median, 59 for $\frac{\rho_1}{\rho_e}$ and 13 for $\frac{\rho_2}{\rho_e}$.

The background temperature is uniform and set to a typical coronal value of 1 MK. The temperatures of the blobs is then determined from the fact that the blobs are in pressure equilibrium with the environment (i.e. the gas pressure is uniform in the domain). Hence,

$$T_i = \frac{\rho_e T_e}{\rho_i}.$$

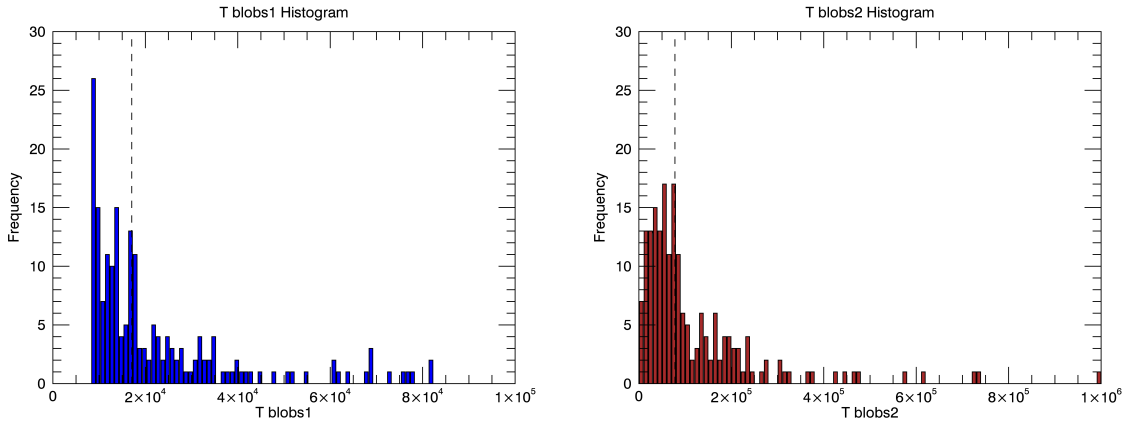

Figure 5.14: Histograms of the temperature of the blobs. The dashed vertical lines represent the median temperature, $\mathrm{Med}(T_1) = 1.7 \times 10^4$ K and $\mathrm{Med}(T_2) = 7.8 \times 10^4$ K. The binsize in the histogram on the left is 10^3 K, in the histogram on the right 10^4 K.

Figure 5.14 shows the histograms of the temperatures of the blobs for the first blob (blue) and the second blob (red). We can see that the temperature of the first (left) blob ranges between 8000 K and 8×10^4 K, with the peak of the distribution towards lower temperatures. This is consistent with the histogram of the temperatures in

Antolin2012 (Figure 5.3). The median is given by the dashed line, Med(T_1) = 1.7×10^4 K. The right panel of Figure 5.14 shows the histogram of the temperatures of the second blob. This distribution is flatter and ranges between 5000 K and 10^6 K, and the median is Med(T_2) = 7.8×10^4 K. The plasma beta is chosen to be 0.01 such that the resulting magnetic field is 25 G, which corresponds to a typical magnetic field in active region loops, see e.g. Froment et al. (2017). These parameters result in an exterior Alfvén speed of $v_{A,ext} = 1858$ km/s and an external sound speed of $c_{s,ext} = 166$ km/s, which means that all simulations are sub-Alfvénic and subsonic with respect to the environment.

5.3.3 Mach number regimes

Figure 5.15 shows a histogram of the internal Mach numbers $M_S = v/c_{s,int}$ (left) and the internal Alfvén Mach numbers $M_A = v/v_{A,int}$ (right) of the first (top row) and second blob (bottom row) in all 191 simulations. We can see that the majority of the blobs are supersonic (Med($M_{S,1}$) = 3.04 and Med($M_{S,2}$) = 1.45), and that all blobs are sub-Alfvénic (Med($M_{A,1}$) = 0.27 and Med($M_{A,2}$) = 0.13). This means that, as the Alfvén speed is the more important one in a low beta regime, information will be able to transmit upstream in the blobs and the collisions will likely be less violent.

5.3.4 Model setup and numerical code

We use the numerical MHD code MPI-AMRVAC (Porth et al., 2014) to run the 191 simulations. For more details on this code and the equations we refer to Chapter 4, section 4.2. The numerical domain is a 2D, cartesian domain and has dimensions 18 Mm (x-direction) by 6 Mm (y-direction), with 1536 gridpoints in the x-direction and 512 gridpoints in the y-direction. The grid resolution is then $dx = dy = 11.7$ km. The boundary conditions in the simulation are continuous in the ghost cells in x and y (i.e. the values in the outmost cell in the domain are copied in the ghost cells), which allows plasma to leave the domain. The simulations run for 200s, which is sufficient to investigate the oscillations resulting from the collision. We do not include gravity, non-ideal effects or thermal conduction, optically thin radiation or a background heating, as these do not affect the generation of the waves and/or act on a longer timescale.

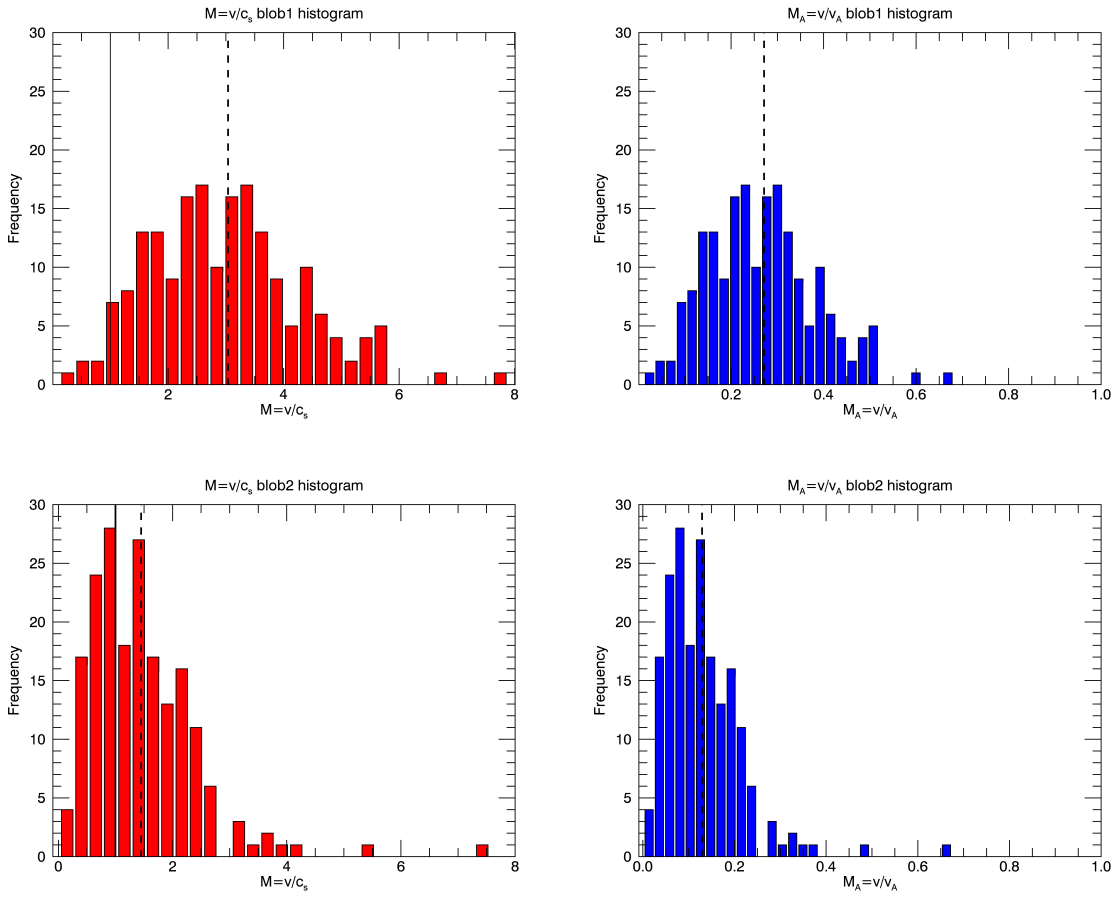

Figure 5.15: Histograms of the internal Mach numbers M_S (left) and the internal Alfvén Mach numbers M_A (right), for the first blob (top row) and the second blob (bottom row) in the simulations. The dashed vertical lines represent the median in each histogram, $\text{Med}(M_{S,1}) = 3.04$, $\text{Med}(M_{A,1}) = 0.27$, $\text{Med}(M_{S,2}) = 1.45$, $\text{Med}(M_{A,2}) = 0.13$. The vertical line at $M_S = 1$ in the left histograms marks the separation between subsonic and supersonic blobs.

5.4 Results: Active region loops

5.4.1 Measured amplitudes

We first analyse the amplitudes of the oscillations that are generated by the collision of the blobs in each simulation. These amplitudes are measured in the same way as in Chapter 4, with an external pair of fieldlines enclosing the two blobs measuring the sausage amplitude, and an internal pair of fieldlines symmetrically placed at a distance of 1 gridpoint along the symmetry line of collision, to measure the kink amplitude. An example of these pairs of fieldlines is shown in Figure 5.16.

Figure 5.17 shows a histogram of the maximal kink and maximal sausage amplitudes

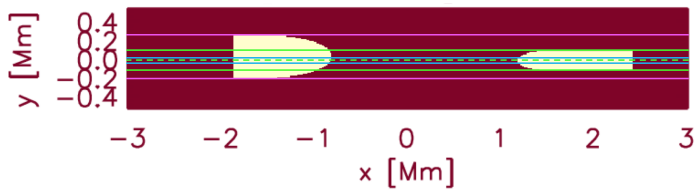

Figure 5.16: Contour of the number density of two blobs. The pink lines are the external pair of fieldlines used for the measurement of the sausage amplitude, the light blue pair of fieldlines is the internal pair of fieldlines used to measure the kink amplitude. The green solid lines mark the overlapping region of the colliding blobs and the green dashed line is the symmetry line of collision.

for all 191 simulations. The median maximal amplitudes are given by the blue (kink) and the red (sausage) dashed lines, and are 1.7 km and 3.1 km, respectively. The dotted vertical line marks the gridsize in the simulations (11.7 km). The maximal amplitudes are extremely small and the majority are smaller than the gridsize. Although we are able to obtain sub-grid measurements for these amplitudes by interpolating the magnetic field components and field line coordinates between grid points, we will not consider these amplitudes as reliable. Even the largest of the maximal amplitudes (~ 33 km) is too small to be observable with the resolution of current instruments (the resolution of Hinode SOT, used for the observations in Antolin et al. (2018), is ~ 80 km.). Future instruments, such as DKIST VBI blue ($393-486$ nm) (see e.g. Tritschler et al., 2016), will have a resolution of 16 km and could be able to observe some of these amplitudes.

5.4.2 Collisions

We investigate the collisions in three different simulations in more detail, to understand why the maximal ampitudes are a lot smaller than the observations presented in Antolin et al. (2018). We choose the simulation which generates the largest maximal amplitudes (simulation 158), and two simulations where the maximal amplitudes are within 10% of the median maximal amplitudes (simulations 137 and 165). Table 5.1 gives an overview of the different parameters in these simulations.

Figure 5.18 shows contours of the number density for these three simulations at $t = 0$s (left panels) and at the time of the maximal kink amplitude (right panels). The first two rows are the average simulations (simulations 137 and 165) and the bottom row is the maximal simulation (simulation 158). We can see that in the average simulations the blobs do not collide at the time of the maximal kink distortion. There is barely

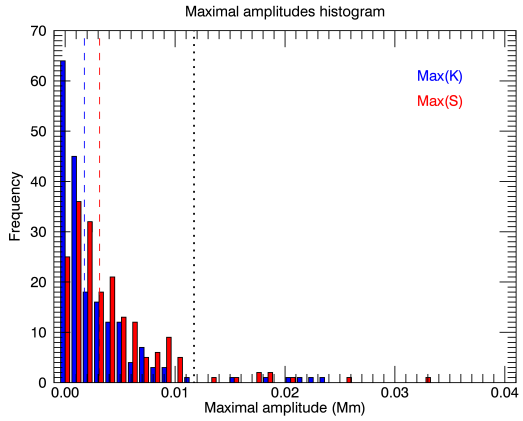

Figure 5.17: Histogram of the maximal kink amplitudes (blue) and the maximal sausage amplitudes (red) in Mm for the 191 simulations. The dashed blue and red lines at 0.0017 Mm and 0.0031 Mm represent the median of the maximal kink and maximal sausage amplitudes. The dotted vertical line is the gridsize in the simulations (0.0117 Mm).

Simulation	137	158	165
v	78.7 km/s	89.7 km/s	95 km/s
ρ_1	2.8×10^{-11} kg/m^3	1.6×10^{-10} kg/m^3	9.8×10^{-11} kg/m^3
ρ_2	8.7×10^{-12} kg/m^3	2.7×10^{-10} kg/m^3	5.2×10^{-12} kg/m^3
L_1	0.87 Mm	1.04 Mm	1.14 Mm
L_2	1.97 Mm	1.22 Mm	10.23 Mm
W_1	0.32 Mm	0.45 Mm	0.12 Mm
W_2	0.41 Mm	0.2 Mm	0.26 Mm
Offset	0.11 Mm	0.04 Mm	0.12 Mm

Table 5.1: Table of the different parameters for simulations 137, 158 and 165.

any distortion visible in the magnetic field, as was already clear from the histogram of the maximal amplitudes (Figure 5.17). This happens for two reasons. Firstly, in the majority of the simulations there is a lack of collisions as the increase of the thermal pressure between the blobs slows the blobs down and eventually brings them to a halt before they can collide. Secondly, the field distortion is very small because of the relatively large restoring Lorentz force (due to the relatively large magnetic field strength, $B = 25$ G), which prevents a significant distortion of the field, and prevents the onset of oscillations. The maximal simulation (bottom row) is one of the few simulations where the clumps do collide, but the resulting distortion in the field is extremely small. Hence in this case 'kink amplitude' does not imply the presence of a true kink wave, but rather refers to the presence of a kink-like distortion of the field.

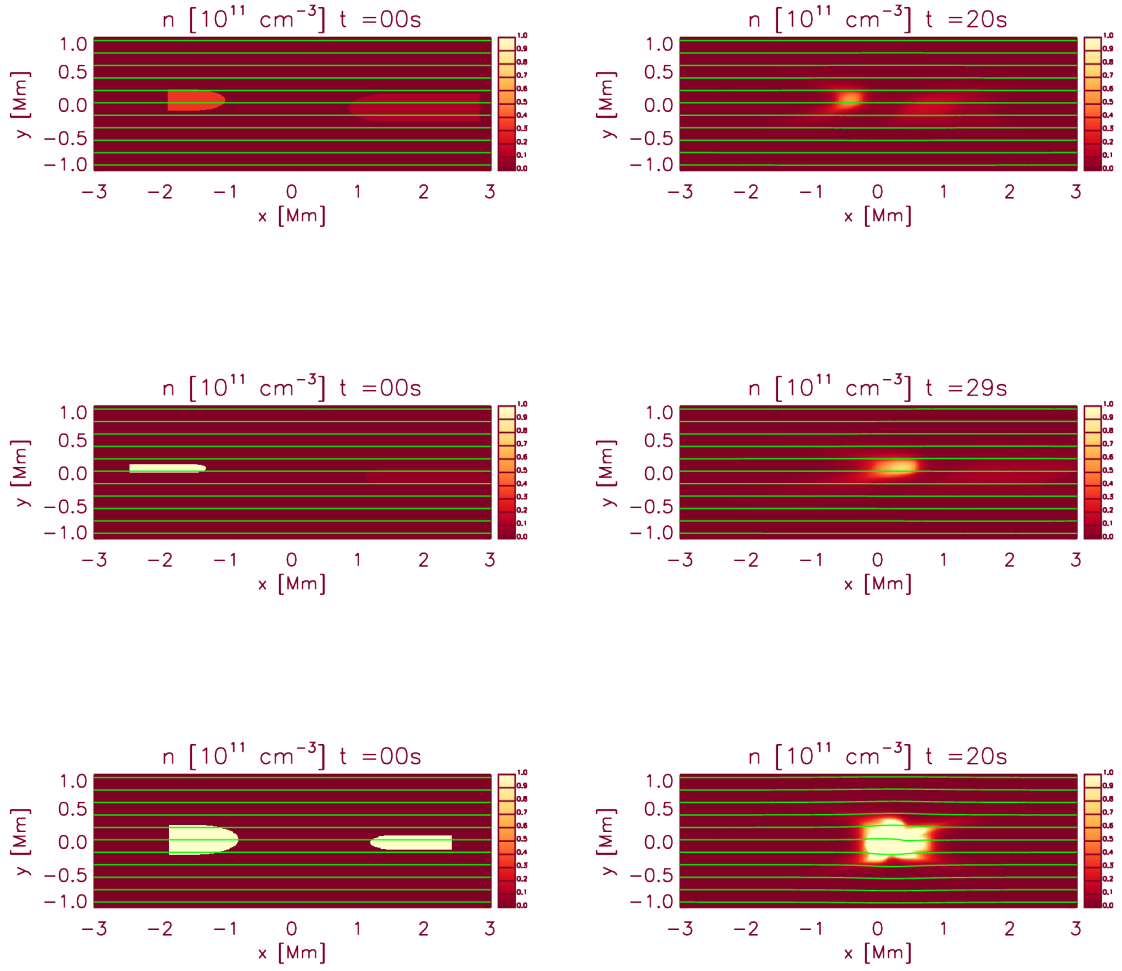

Figure 5.18: Contours of the number density at $t = 0$s (left panels) and at the time of the maximal kink amplitude (right panel) for three simulations. The top two rows are two average simulations (simulation 137 and simulation 165), the bottom row is the simulation where the largest amplitudes are obtained (simulation 158).

Figure 5.19 shows the pair of internal and external fieldlines used to measure the amplitudes at the time of the maximal kink amplitude ($t = 20$s) for the simulations 137 (left) and 158 (right). In simulation 158, we see a sausage-like expansion of the external pair of fieldlines and a kink-like displacement in the internal pair of fieldlines ($\max(K) = 0.024$ Mm and $\max(S) = 0.033$ Mm). In simulation 137, there is barely a sausage-like expansion and a kink-like displacement visible in the external and internal pair of fieldlines ($\max(K) = 0.0019$ Mm and $\max(S) = 0.003$ Mm).

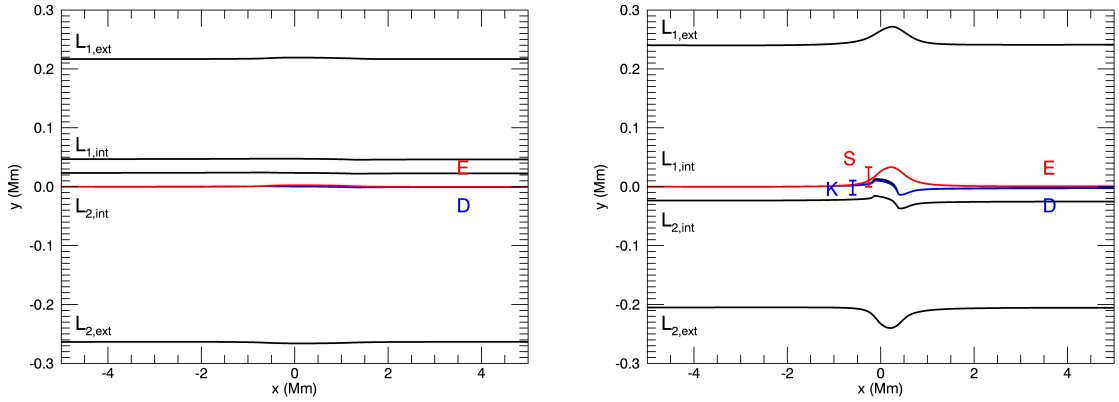

Figure 5.19: Plot of the internal pair $L_{1,int}, L_{2,int}$ and external pair $L_{1,ext}, L_{2,ext}$ of fieldlines at $t = 20$s, together with the expansion E and the displacement D of the external pair and internal pair of fieldlines, respectively, and the kink K (blue) and sausage S (red) amplitudes, for simulation 137 (left panel) and simulation 158 (right panel). In the left panel we have not overplotted the size of K and S, to keep the plot readable.

Kinetic energy and thermal pressure

In this section we investigate in more detail why the blobs in most simulations do not collide. Figure 5.20 shows the initial volume integrated kinetic energy associated with the x-component of the velocity ($\int \frac{\rho v_x^2}{2} dV$) in the domain of the 191 simulations, normalised to the initial kinetic energy of the reference simulation of Chapter 4, which was used to model the oscillations presented in Antolin et al. (2018). We normalise against this simulation as we know that for the parameters in this reference simulation there is a collision beteen the blobs, followed by significant oscillations. The blobs in the reference simulation have a trapezoidal shape and are 3 Mm long and 1 Mm wide. They have a density of 1×10^{-10} kg/m^3 and a speed of 70 km/s, which are both slightly higher than the median values in the current parameter study, Med$(\rho_1) = 8.5 \times 10^{-11}$ kg/m^3 and Med$(v) = 65.6$ km/s. The magnetic field in the reference simulation is initially straight and uniform, with a field strength of $B = 6$ G.

The left panel of Figure 5.20 shows that all of the simulations have a smaller kinetic energy than the reference simulation (shown by the dashed line at 1). The average relative kinetic energy of the simulations is 0.08 (blue dashed line). The kinetic energies are smaller mainly because of the smaller blob dimensions ($\langle L_1 \rangle = 0.73$ Mm, $\langle L_2 \rangle = 3.3$ Mm and $\langle W_1 \rangle = \langle W_2 \rangle = 0.31$ Mm), and the smaller densities. The velocities of the blobs are on average comparable. Generally speaking, the blobs need to have enough kinetic energy in order to collide, to overcome the negative work done by the thermal

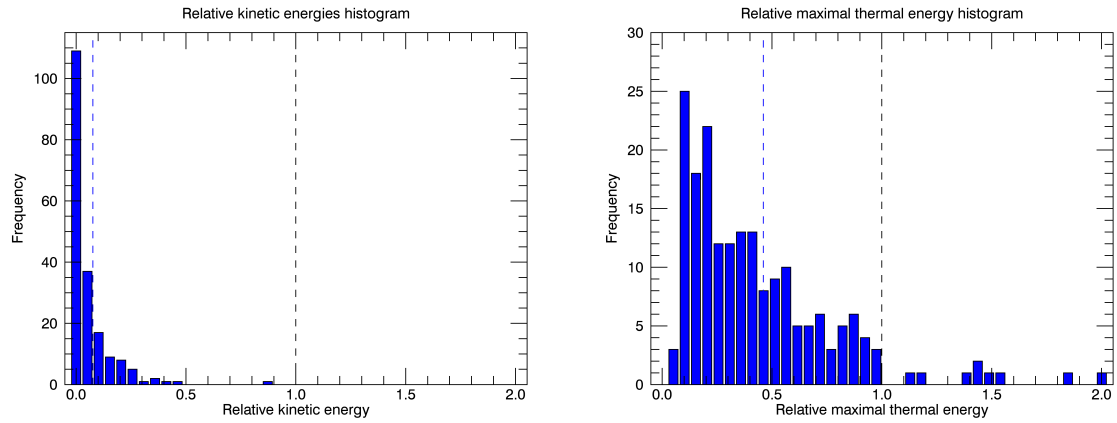

Figure 5.20: Histograms of the relative kinetic energy of the simulations (left panel) and the relative maximal thermal energy in the simulations (right panel), normalised to the reference simulation (black dashed vertical lines). The blue dashed vertical lines mark the average relative kinetic energy, 0.08 and the average relative maximal thermal pressure, 0.46.

pressure gradient force on the blobs. The right panel of Figure 5.20 shows a plot of the maximal thermal energy $\frac{p}{\gamma-1}$ in the domain in all the simulations, compared to the reference simulation (dashed line at 1). The maximal thermal energies are on average smaller than in the reference simulation (black dashed line), with 0.46 the average relative maximal thermal energy. This is because the blobs have on average a smaller kinetic energy (see left panel of Figure 5.20), and hence they compress the plasma less. However, in 11 simulations the maximal thermal energy is larger. The main reason for this is that the background density is 44% larger than in Chapter 4. Because of the smaller kinetic energies and the smaller and comparable thermal energies in the domain, collisions will be less common in most simulations. The kinetic energy of the blobs is in general not sufficient to overcome the thermal pressure which builds up between the blobs as they propagate towards each other.

Figure 5.21 shows a plot of the evolution of the ratio of the volume integrated kinetic energy associated with the x-component of the velocity in the domain, to the average thermal energy in a square between the blobs, for the 3 simulations discussed previously and the reference simulation. The square over which the thermal energy is averaged is 20×20 gridpoints (0.23×0.23 Mm^2), centred on $x = y = 0$. The ratio of the kinetic energy to the average internal energy is significantly larger for the reference simulation (black), than for the three simulations considered here (the blue line is the maximal simulation (158), and the green and red line are the average simulations, 137 and 165, respectively). When the blobs approach each other, the energy ratio decreases

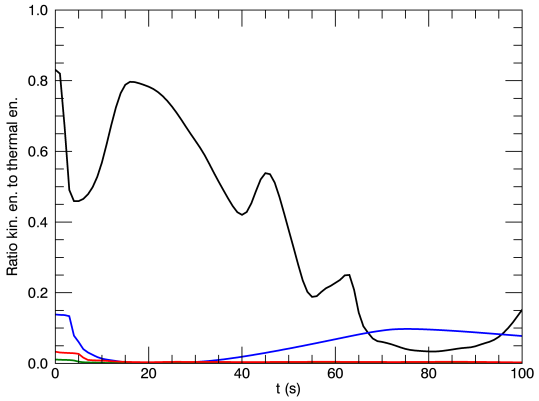

Figure 5.21: Plot of the ratio of the volume integrated kinetic energy associated with the x-component of the velocity in the domain, to the average internal energy in a 0.23×0.23 Mm^2 square centred at $x = y = 0$ Mm, for the reference simulation (black line), the maximal simulation (simulation 158, blue line), and the two average simulations (simulation 137, green line and simulation 165, red line).

as the blobs are slowed down due to the increase in thermal pressure between the blobs. This figure suggests that on average, the blobs in the new simulations do not collide because they do not have enough kinetic energy to overcome the increasing thermal pressure between the blobs. In the reference simulation, there is a collision and the oscillations in the domain are also reflected in this quantity. This behaviour is not present in the blue, green or red lines.

Figure 5.22 shows a log-log plot of the initial kinetic energy to the average thermal energy ratio for all 191 simulations, with the density ratio ρ_1/ρ_2 of the blobs on the x-axis. The horizontal and vertical dashed lines are the median kinetic to thermal energy ratio (0.015) and the median density ratio (4.67). The symbols indicate whether there is a collision (diamond symbol) or no collision (asterisk symbol). Blobs are considered to be colliding if the front of the blobs are closer than a certain distance (0.3 Mm) during the course of the simulation, and if the density between the blobs reaches a certain threshold (40 times the external background density) due to a compression of the external plasma by the blobs. The simulations are coloured according to the offset between the blobs in a simulation: blue if the blobs have an offset O less than half of the median offset ($O \leq 0.048$ Mm), green if the offset is between half the median and the median offset ($0.048 < O \leq 0.097$ Mm), and red if the blobs have an offset larger than the median ($O > 0.097$ Mm). We can see that the blobs collide in only 7 simulations, and that these simulations have, on average, a larger kinetic to thermal energy ratio (energy ratio larger than $\sim 10^{-1.5} \approx 0.03$). However, there are a substantial

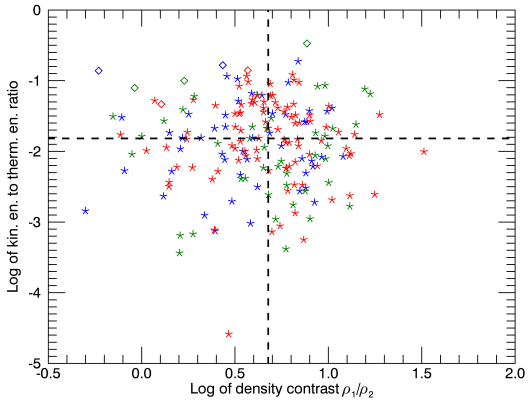

Figure 5.22: Log-log plot of the ratio of the volume integrated kinetic energy associated with the x-component of the velocity in the domain, to the average internal energy in a 0.23×0.23 Mm^2 square centred at $x = y = 0$ Mm at $t = 0$s for each simulation, with the density ratio ρ_1/ρ_2 of the blobs on the x-axis. The horizontal and vertical dashed lines are the median energy ratio (0.015) and the median density ratio (4.67). The diamond symbols represent a collision, and the asterisk symbols no collision. The simulations are coloured according to the offset between the blobs in a simulation: blue if the blobs have an offset O less than half of the median offset ($O \leq 0.048$ Mm), green if the offset is between half the median and the median offset ($0.048 < O \leq 0.097$ Mm), and red if the blobs have an offset larger than the median ($O > 0.097$ Mm).

number of simulations which have an equally large energy ratio but where a collision does not occur. One reason is that in these simulations, the blobs have a relatively large offset (red colour). Five of the seven simulations that do collide have an offset smaller than the median offset. In addition, in six of the seven simulations the density ratio ρ_1/ρ_2 is smaller than the median density ratio (vertical dashed line). In some of the simulations that have a high energy ratio, but there is no collision, the density ratio between the blobs is too large ($\rho_1 \gg \rho_2$, top right corner of Figure 5.22). In this case, when the blobs approach each other, the second (less dense) blob is compressed and pushed 'downwards' (i.e. towards $y < 0$). It was shown in Chapter 4 (parameter study 3) that if the density ratio ρ_1/ρ_2 of the blobs is too large, the collision is less efficient and the second (less dense) blob is compressed and pushed downwards.

It is worth remarking that in all of the simulations where a collision happens, the blobs have an Alfvén Mach number of $0.4 - 0.7$ (first blob) or $0.25 - 0.7$ (second blob), which is significantly larger than the median Alfvén Mach numbers (Med$(M_{A,1}) = 0.27$ and Med$(M_{A,2}) = 0.13$).

5.4.3 Decreasing the magnetic field and the background pressure

We repeat the three simulations discussed in the previous section with a lower magnetic field and a lower background pressure. We first decrease the magnetic field and keep the other background plasma parameters as before. We consider the cases $B = \{5, 10, 15, 20, 25\}$ G, where 25 G is the magnetic field used previously and which we consider representative of active region loops.

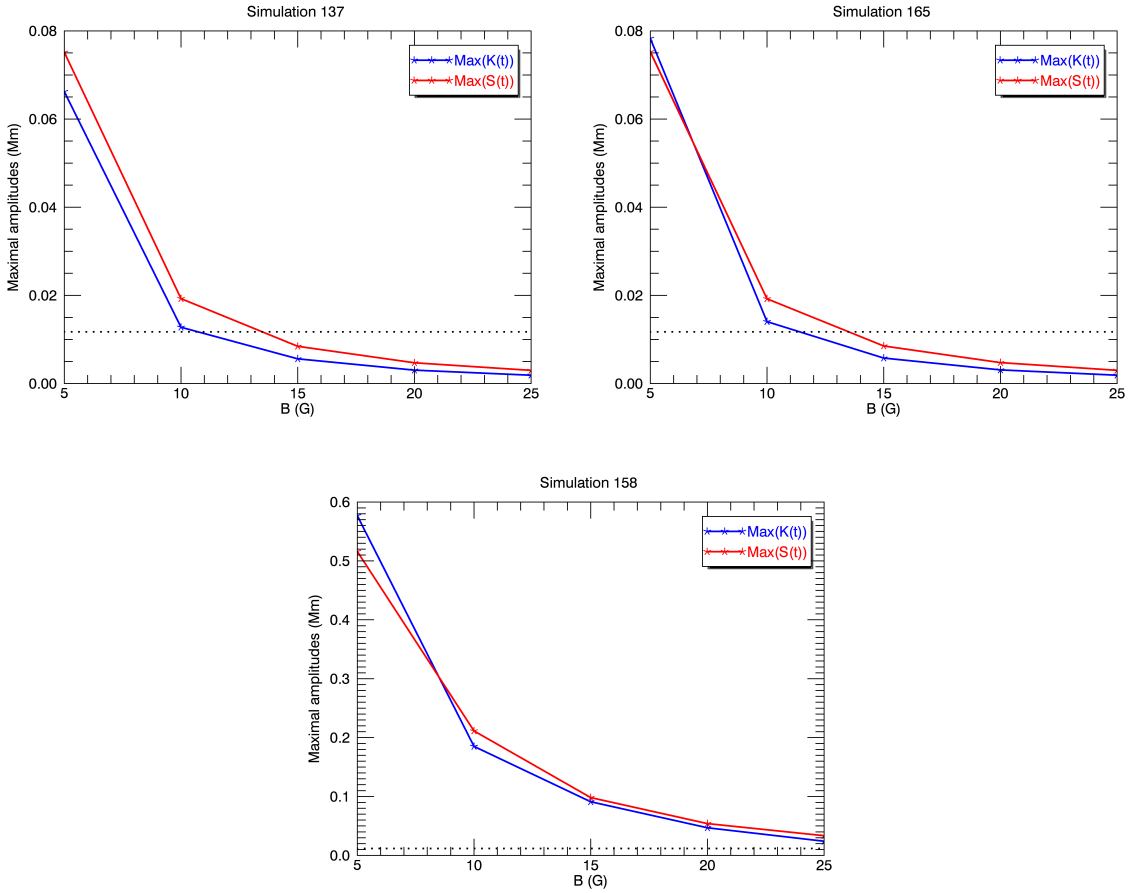

Figure 5.23: Plots of the maximal kink (blue) and maximal sausage (red) amplitudes for simulations 137 (top left panel), 165 (top right panel) and 158 (bottom panel), as a function of the magnetic field strength. The horizontal dotted line marks the gridsize in the simulations (11.7 km).

Figure 5.23 shows a plot of the maximal kink (blue) and sausage (red) amplitudes for simulations 137 (top left panel), 165 (top right panel) and 158 (bottom panel) for the different magnetic field strength cases. The horizontal dotted line marks the gridsize in the simulations (11.7 km). We see that in simulations 137 and 165, the maximal amplitudes are only above the gridsize for $B \leq 10$ G. We remark that the

blobs in these cases still do not collide, because the background pressure is unchanged, but the field distortion is now larger. In all cases, the maximal amplitudes increase with decreasing magnetic field strength and the increase roughly follows a $\sim \frac{1}{B^2}$ scaling, which is not unexpected, as the restoring forces (the magnetic tension force and the magnetic pressure force), also scale with B^2. In simulation 158 in the $B = 5$ G case, the relative increase in the kink and sausage amplitudes appears smaller, which could be because the collision is now quite violent and the fieldlines become very distorted (see left panel of Figure 5.24), such that the method to measure the kink amplitude fails. This is shown by the right panel of Figure 5.24 which shows the internal and external pair of fieldlines used to measure the amplitudes, at $t = 32$s. The interpolated internal fieldlines $L_{1,int}, L_{2,int}$ used for the measurement of the kink amplitude do not capture the complete distortion of the fieldlines in the left panel of Figure 5.24, and the measured kink amplitude is significantly smaller. The increase of the sausage amplitude in this case is also smaller, possibly because of a saturation effect due to the restoring forces of the external magnetic field. A similar saturation effect was also present in Parameter Study 6 of Chapter 4.

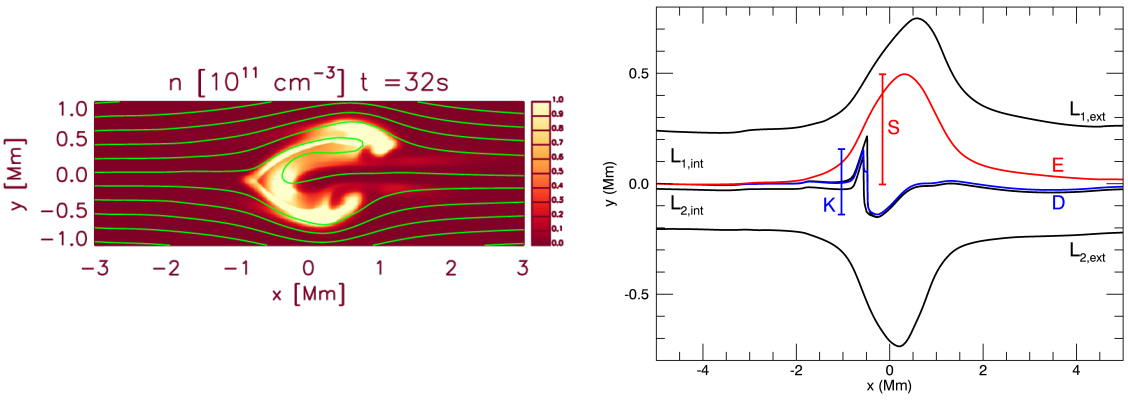

Figure 5.24: (Left) Contour of the number density at $t = 32$s with magnetic fieldlines overplotted in green, for simulation 158 in the $B = 5$ G case. (Right) Plot of the internal pair and external pair of fieldlines at $t = 32$s for the same simulation, together with the expansion E and the displacement D of the external pair and internal pair of fieldlines, respectively, and the kink K (blue) and sausage S (red) amplitudes.

We also rerun the three simulations with a decreased background pressure to see if this allows the blobs to collide. We decrease the background density with a factor of 10 such that $\rho_{ext,new} = 1.44 \times 10^{-13}$ kg/m^3 and we keep the external temperature at $T_{ext} = 1$ MK. The magnetic field is kept at 25 G, and the plasma beta is 0.001. Figure 5.25 again shows contours of the number density for the simulations 137 (top row), 165

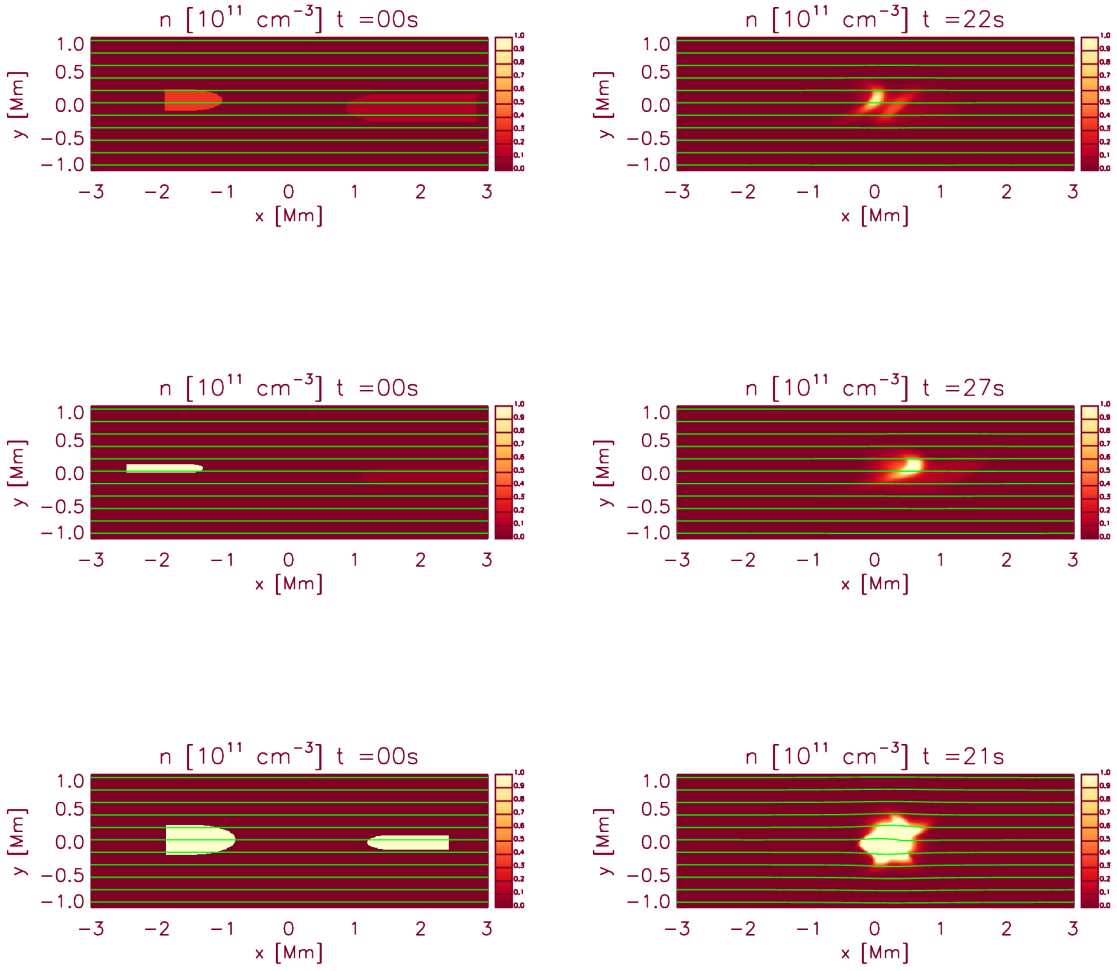

Figure 5.25: Contours of the number density initially (left panels) and at the time of the maximal kink amplitude (right panel) for the three simulations 137 (top row), 165 (middle row) and 158 (bottom row) with the lower background pressure.

(middle row) and 158 (bottom row), at $t = 0$s (left column) and at the time of the maximal kink amplitude (right column). A clear difference with Figure 5.18 is that now the blobs also collide in simulations 137 and 165, because of the lower background pressure.

Figure 5.26 again shows a plot of the evolution of the ratio of the volume integrated kinetic energy associated with the x-component of the velocity to the average thermal energy between the blobs, for the three simulations discussed previously and the reference simulation. We see that the initial values are 10 times higher, compared to Figure 5.21, which facilitates the onset of collisions. The blue curve goes up after $t \sim 30$s because in simulation 158 the blobs still have a lot of kinetic energy after the collision

and the thermal energy in the middle of the domain decreases because of rarefraction.

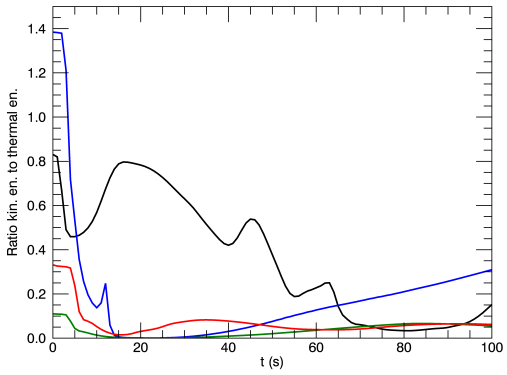

Figure 5.26: Plot of the ratio of the volume integrated kinetic energy associated with the x-component of the velocity in the domain, to the average internal energy in a 0.23×0.23 Mm^2 square between the blobs, for the same simulations as in Figure 5.21, but with the lower background density for simulation 137 (green line), 158 (blue line) and 165 (red line). The black line corresponds to the reference simulation.

5.5 Results: Quiet Sun background

In this section, we rerun the 191 simulations from section 5.4 but with a lower background pressure and in a lower magnetic field configuration, in order to allow more collisions of blobs and oscillations. We decrease the background density by a factor of 10, $\rho_{ext} = 1.44 \times 10^{-13}$ kg/m^3 and keep the external temperature at $T_{ext} = 1$ MK. Because the background pressure is 10 times lower, the temperatures of the blobs will also be 10 times lower compared to Figure 5.14. The magnetic field is taken to be 5 G and the plasma beta is 0.024. Although these background quantities are reasonable for the Quiet Sun (QS) (see e.g. Brooks et al. (2009), Long et al. (2013), Brooks (2019)), coronal rain is not commonly observed in QS regions. Therefore, this modified parameter study should mostly be seen as a theoretical investigation.

The external Alfvén speed is $v_{A,ext} = 1175$ km/s and the external sound speed is $c_{s,ext} = 166$ km/s. As the magnetic field is 5 times lower, the internal Alfvén speed of the blobs is 5 times lower and the internal Alfvén Mach number is 5 times larger. This results in Med$(M_{A,1}) = 1.36$ and Med$(M_{A,2}) = 0.65$, with 72% of the first blobs super-Alfvénic (19% of the second blobs). Because the temperature of the blobs is 10 times lower than before, the internal sound speed is $\sqrt{10}$ times lower and Med$(M_{S,1}) = 9.61$

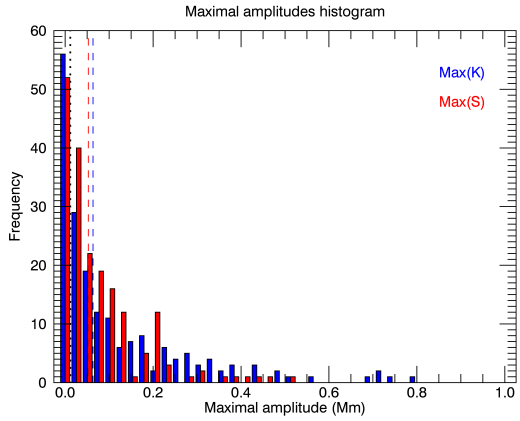

Figure 5.27: Histogram of the maximal kink amplitudes (blue) and the maximal sausage amplitudes (red) in Mm for the 191 simulations. The dashed blue and red lines at 0.064 Mm and 0.053 Mm represent the median of the maximal kink and maximal sausage amplitudes. The dotted vertical line is the gridsize in the simulations (0.0117 Mm). The binsize of the histogram is 0.025 Mm.

and Med($M_{S,2}$) = 4.58, with all blobs supersonic in the simulations. Because a large proportion of the simulations have super-Alfvénic blobs, information will not be able to transmit upstream and the colliding blobs will not immediately be slowed down by the collision, hence we expect more (violent) collisions to happen.

Figure 5.27 shows the histogram of the maximal kink (blue) and sausage (red) amplitudes for all simulations. The median maximal kink amplitude (64 km) and median maximal sausage amplitude (53 km) are represented by the blue and red dashed line, respectively. The dotted vertical line marks the gridsize of the simulations (11.7 km). We can see that the maximal amplitudes are on average $10 - 20$ times larger than in Figure 5.17. We find that in 28 simulations the maximal kink and/or sausage amplitude is smaller than the gridsize, i.e. some of the simulations in the first histogram bin in Figure 5.27.

5.5.1 Collisions

Figure 5.28 shows the equivalent plot of Figure 5.22, but now for the QS simulations. The horizontal and vertical dashed lines are the median kinetic to thermal energy ratio (0.15) and the median density ratio (4.67). Due to the lower background pressure and the lower magnetic field strength, the blobs can collide more easily and produce oscillations. There are 155 simulations where the blobs collide ($\sim$ 81%) which is a

significant increase, compared to the 7 collision cases with the higher magnetic field strength and background density (see Figure 5.22). The simulations for which there is a collision (diamond symbols) have an energy ratio larger than $\sim 10^{-1.5} \approx 0.032$. This is a similar lower bound as in Figure 5.22 for the active region background. The simulations where there is no collision (asterisk symbols) have, on average, an energy ratio of $\sim 10^{-2}$. There are a few simulations for which the energy ratio is larger that do not collide, but they have, on average, a large density ratio (bottom right corner of the plot) such that the second (less dense) blob is compressed when the blobs approach each other (see also parameter study 3 of Chapter 4).

In all of the simulations where a collision happens, the median Alfvén Mach numbers are significantly larger (Med($M_{A,1,collision}$) = 1.5 and Med($M_{A,2,collision}$) = 0.71) than the median Alfvén Mach number of all simulations (Med($M_{A,1}$) = 1.36 and Med($M_{A,2}$) = 0.65). In the simulations where there is no collision the Alfvén Mach numbers are nearly all (94%) lower than the median Alfvén Mach numbers of all simulations (Med($M_{A,1,nocollision}$) = 0.66 and Med($M_{A,2,nocollision}$) = 0.28).

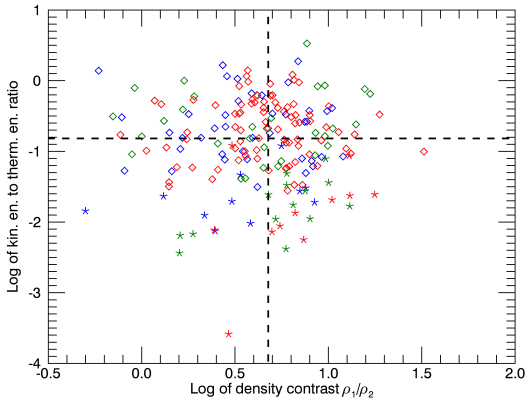

Figure 5.28: Log-log plot of the ratio of the volume integrated kinetic energy associated with the x-component of the velocity in the domain, to the average internal energy in a 0.23×0.23 Mm^2 square centred at $x = y = 0$ Mm at $t = 0$s for each simulation in the Quiet Sun background, according to the density ratio ρ_1/ρ_2 of the blobs. The horizontal and vertical dashed lines are the median energy ratio (0.15) and the median density ratio (4.67). The diamond symbols represent a collision, and the asterisk symbols no collision. The simulations are coloured according to the offset between the blobs in a simulation: blue if the blobs have an offset O less than half of the median offset ($O \leq 0.048$ Mm), green if the offset is between half the median and the median offset ($0.048 < O \leq 0.097$ Mm), and red if the blobs have an offset larger than the median ($O > 0.097$ Mm).

5.5.2 Density oscillations

So far, we have analysed the amplitudes of the collision-induced oscillations by measuring distortions in the magnetic field. However, observationally, such measurements would not be possible and instead, these oscillations would most likely be analysed in intensity images. Therefore, in this section, we look at whether the oscillations are present in the simulation densities, as a proxy for intensities. We will consider 2 simulations from the Quiet Sun study in detail, namely simulation 158 (maximal kink and sausage amplitudes of 745 km and 527 km, respectively) and simulation 137 (maximal kink and sausage amplitudes of 73 km and 50 km, respectively).

Figure 5.29 shows a plot of the evolution of the kink (blue) and sausage (red) amplitude with time, for simulations 137 (left) and 158 (right panel). We can see that there are clear oscillations in the kink and sausage amplitudes for simulation 158, but they are less apparent in simulation 137. From the difference in minima and maxima we estimate the kink period to be $\sim$ 55s and the sausage period $\sim$ 40s in simulation 158. In simulation 137, the kink period is $\sim$ 35s but the sausage period is less clear from the evolution of $S(t)$ after $t = 24$s since there are no significant oscillations in $S(t)$ following the initial peak.

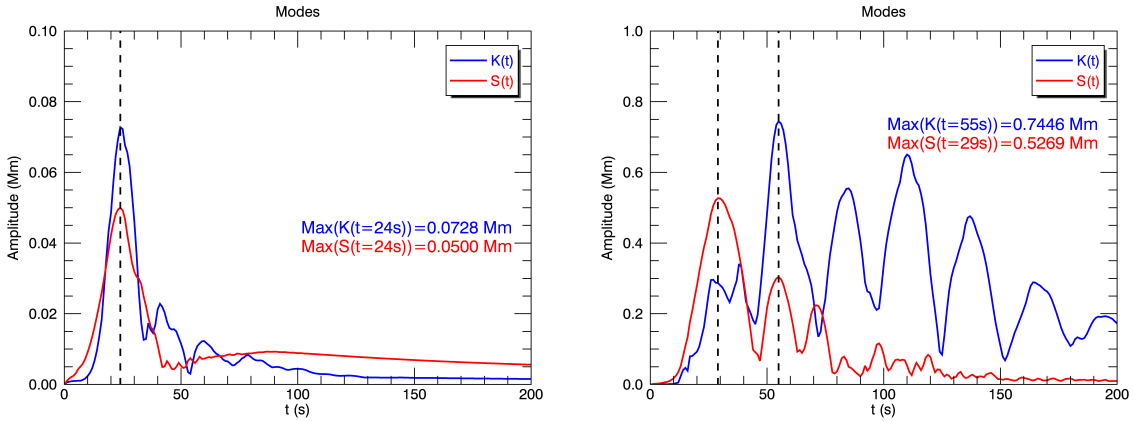

Figure 5.29: Plot of the evolution of the kink (blue) amplitude $K(t)$ and the sausage (red) amplitude $S(t)$ for simulation 137 (left panel) and simulation 158 (right panel). The dashed vertical lines are the times of the maximal $K(t)$ and $S(t)$.

To analyse the oscillations in the density, we create time-distance maps of the density along a slit in the domain. We will consider two different types of slits, namely a fixed slit, placed symmetrically between the initial positions of the two blobs ($x \sim 0$ Mm), and a moving slit following the maximal density along the symmetry line of the

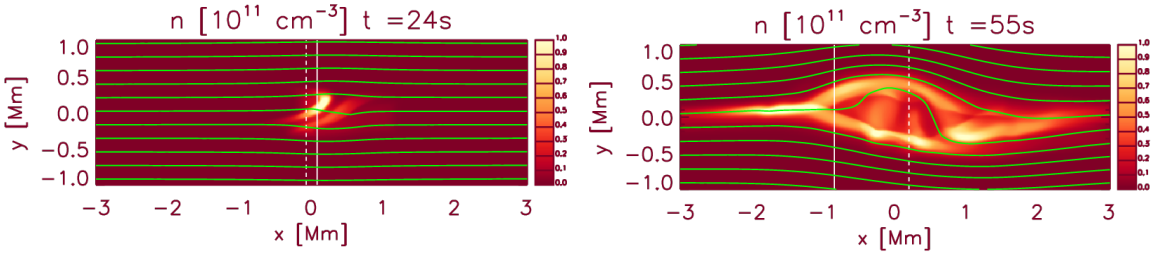

Figure 5.30: Contour of the number densities for simulations 137 (left panel) and 158 (right panel) at the time of the maximal kink amplitude ($t = 24$s and $t = 55$s). The dashed vertical line is the fixed slit, the solid vertical line the moving slit at the relevant time.

collision (i.e. the symmetry line of the overlapping area of the blobs). A contour of the density of the two simulations at the time of their maximal kink amplitude with the two different slits overplotted can be found in Figure 5.30, where the solid vertical line is the moving slit and the dashed vertical line the fixed slit.

Figure 5.31 shows a time-distance map for the fixed (left panel) and moving (right panel) slit for simulation 158. We can see in the contour of the fixed slit that the blobs collide around $t \sim 15$s and that this produces several oscillations in the domain. The amplitude of the oscillations is of the order of 0.5 Mm, which is consistent with the maximal sausage amplitude for simulation 158 measured from the magnetic field (0.53 Mm). From the oscillations we estimate the period to be 40s (the difference between the first and third peak of the oscillations), which agrees with the sausage period in Figure 5.29. The moving slit shows less clear results. Between 15s and 35s the collision and oscillation are visible, however afterwards the oscillations are a lot less clear. This is because the moving slit is positioned at the location of the maximal density along the symmetry line of the collision, and after the collision this location can jump when the plasma compresses and rarefies at different locations in the domain during the oscillations, as can also be seen in the right panel of Figure 5.30.

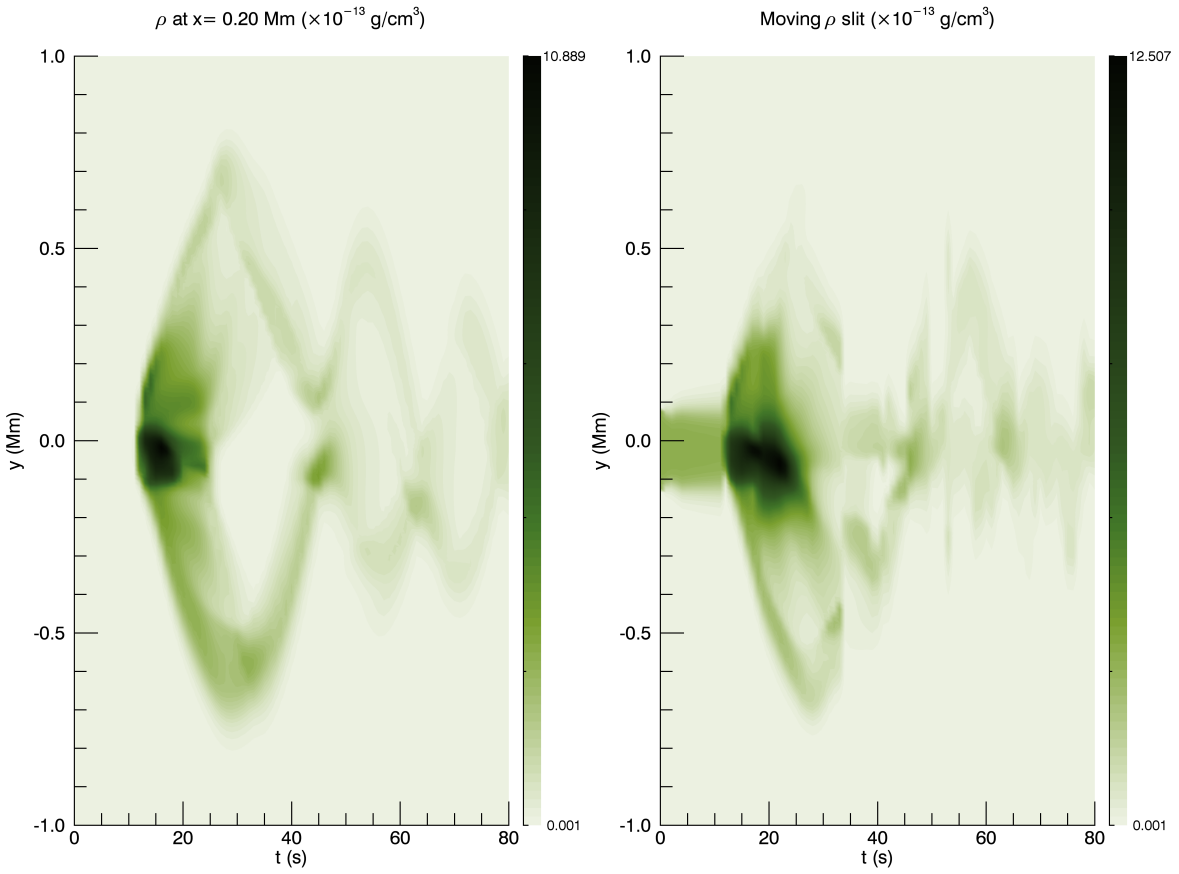

Figure 5.31: Time-distance maps of the fixed slit symmetrically between the blobs (at $x = 0.2$ Mm) (left panel) and the moving slit following the maximal density along the symmetry line of collision (right panel), for simulation 158.

Figure 5.32 shows similar time-distance maps for the fixed (left panel) and moving (right panel) slits for simulation 137. For the fixed slit, we see that the first blob arrives at around 15s but afterwards there is no clear collision or oscillation visible. This is because the denser, left blob compresses the right, less dense blob and the region of the collision is located towards larger x ($x \sim 0.2$ Mm, see left panel of Figure 5.30). The right panel of Figure 5.32 shows the moving slit, following the maximal density along the symmetry line of the overlapping region of the blobs. Initially the moving slit follows the denser left blob, and we can see that the collision starts at around $t \sim 15$s. Because of the offset, the upper part of the first blob and the lower part of the second blob continue to propagate (as can also be seen in the left panel of Figure 5.30), which is represented by the diagonal green bands at $y = \pm 0.2$ Mm around $t \sim 20$s (see e.g. Figure 5.25 for the initial offset of the blobs). The collision is located between $y = 0$ Mm and $y = 0.1$ Mm, but it is difficult to see any oscillations. This is also because the amplitudes are significantly smaller, compared to simulation 158. Moreover, because the blobs have an offset, the vertical oscillation is somewhat tilted, which makes it harder to observe the oscillations in a vertical slit.

Because in our parameter study the blobs have different dimensions, densities and offsets, it is difficult to have one automated method to measure the oscillations in a slit. Although the oscillations can be measured as distortions in the magnetic field, they are harder to measure in the densities and hence they are less likely to be observable.

5.5.3 Frequencies and wavelengths

In this section, we investigate the different frequencies and wavelengths of the oscillations, and how much power there is in the oscillations.

The period/frequency of an oscillation can be obtained via different methods. In Chapter 4, we calculated the kink and sausage period from the difference in minima and maxima in the evolution of the kink and sausage amplitudes. We also verified that this period matched with the wavelength and the internal Alfvén speed resulting from the collision ($P = \lambda / v_A$). In this chapter, we introduce a third method to obtain the frequencies, by performing a Fast Fourier Transform (FFT) on the evolution of the kink and sausage amplitudes in each simulation. We then assign a kink frequency and a sausage frequency to each simulation by taking the frequency at the second maximum (as the first maximum tends to pick up the overall trend in the data rather than the

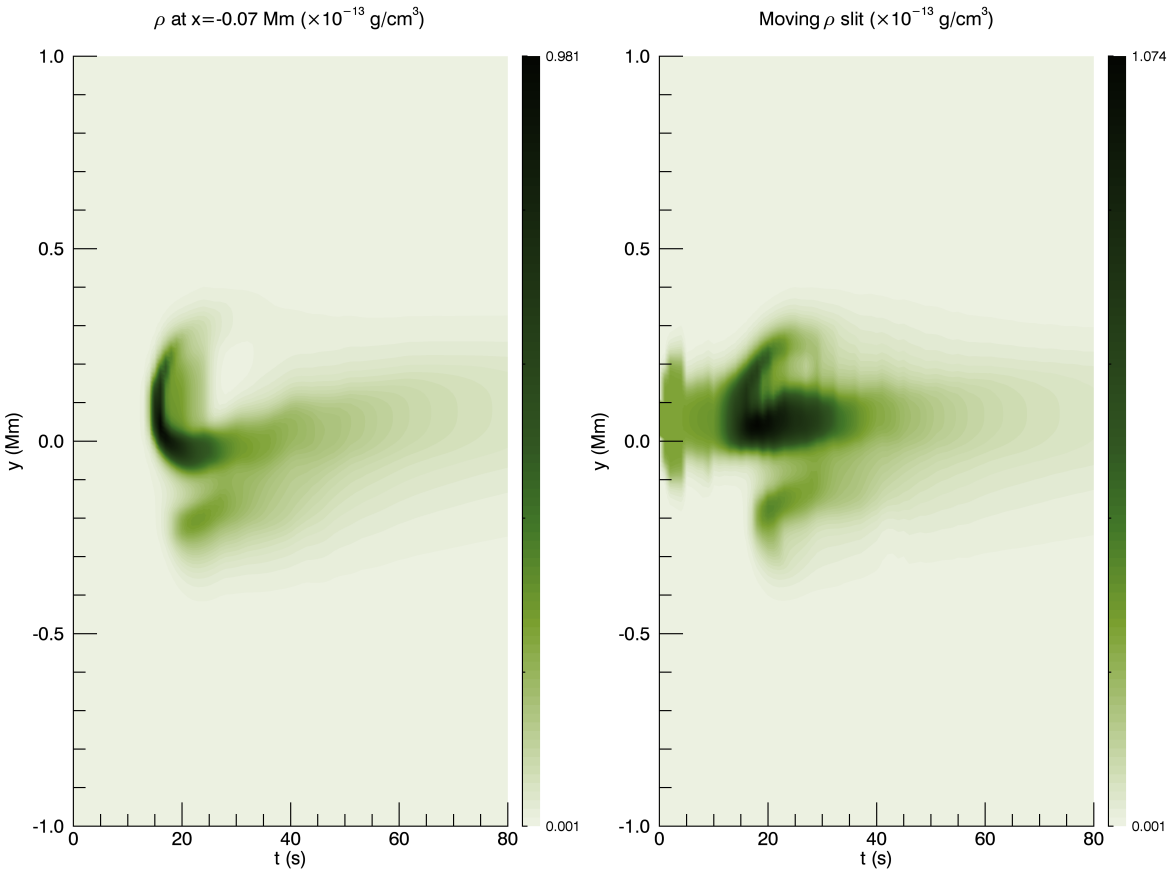

Figure 5.32: Time-distance maps of the fixed slit symmetrically between the blobs (at $x = -0.07$ Mm) (left panel) and the moving slit following the maximal density along the symmetry line of collision (right panel), for simulation 137.

oscillations). This method is essentially the same as the first method, but is easier to automate.

Figure 5.33 shows log-log plots of the kink (left panel) and sausage (right panel) frequency vs the FFT power, for each simulation. We see that the frequencies range between $\sim 10^{-1} - 10^{-2}$ Hz, which corresponds to periods between $\sim 10 - 100$s. The median kink frequency is 0.04 (period of 25s) and the median sausage frequency is 0.055 (period of 18s). Both panels show a downwards trend with more power in the lower frequencies (longer periods). This is expected since longer period oscillations are generally produced by longer blobs (Parameter Study 6 in Chapter 4), and longer blobs have, on average, more kinetic energy than shorter blobs, since they have, on average, more mass and a higher velocity since longer blob lengths correspond to faster blobs in our model.

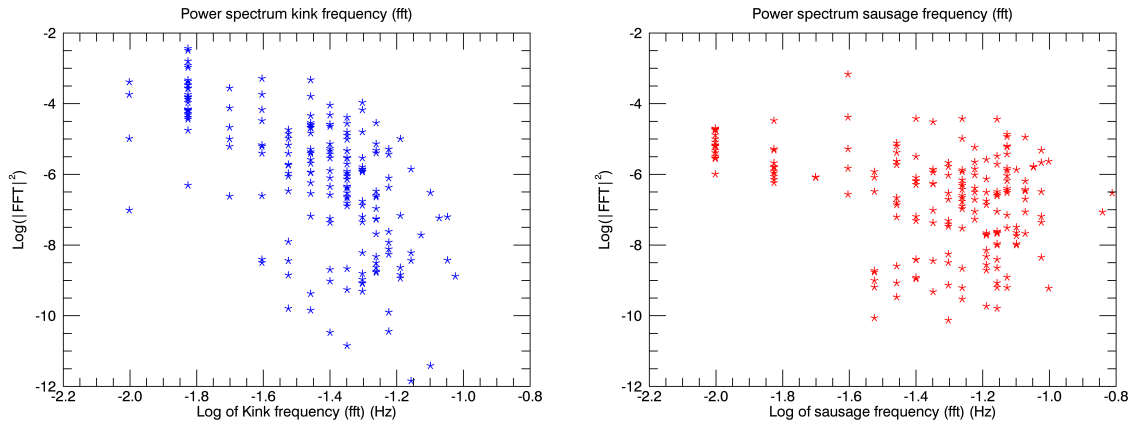

Figure 5.33: Log-log plots of the kink frequency (left panel) and sausage frequency (right panel) vs FFT power for each simulation.

Figure 5.34 shows a plot of the kink (blue) and sausage (red) wavelengths (at the time of the maximal amplitudes) vs the maximal kink (blue) and maximal sausage (red) amplitudes squared, for each simulation. The wavelengths are measured in the same way as in Chapter 4. We can see that the majority of the kink and sausage wavelengths are in the range $1 - 10$ Mm (median kink wavelength is 1.5 Mm), and that the sausage wavelength is on average slightly larger (median of 2.2 Mm). The wavelengths are of a similar order as the length of the blobs, which is a consequence of how these oscillations are generated: first a distortion of the field due to the collision of the blobs, and then the release of the field after the collision. Although observing the distortions of the magnetic field with sufficient accuracy to analyse the oscillations in detail is currently not possible (Section 5.5.2), comparing the 'size' of the oscillation with the size (length) of the blobs would be possible with current instrumentation. In general, we would expect there to be more energy in the longer wavelength oscillations, since these oscillations are again, on average, produced by longer blobs (Parameter Study 6 in Chapter 4) which have, on average, more kinetic energy. However, the trend in Figure 5.34 seems to be less clear, as similar wavelength oscillations can have different maximal amplitudes squared. It was also shown in PS6 of Chapter 4 that there can be a saturation effect in the maximal amplitudes for longer blobs, because of the restoring force of the external magnetic field. This effect could possibly also play a role here.

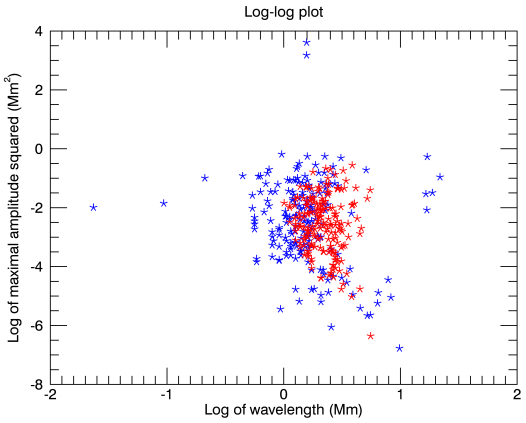

Figure 5.34: Log-log plot of the kink wavelength (blue) and sausage wavelength (red) vs maximal kink and sausage amplitude squared, respectively, for each simulation.

5.6 Discussion and conclusion

In this chapter we have investigated coronal rain collisions and oscillations in coronal loops. We ran a large number of simulations ($\sim$ 200) of colliding coronal rain blobs, using the model of Chapter 4. We based the properties of the blobs on the extensive observational study of coronal rain by Antolin and Rouppe van der Voort (2012).

In a first parameter study, we considered simulations of the blobs in a background representative of active region loops, where coronal rain is mostly observed on the Sun. We found that the blobs collided only in a few simulations and that because of the large magnetic field strength (25 G), the distortion of the field was minimal and no oscillations were present. In most of the simulations, the increase in thermal pressure between the blobs was too large for a collision to happen and the resulting field distortion was extremely small. The internal Alfvén Mach numbers of the blobs were also significantly smaller than 1. Hence, from this first set of simulations we can conclude that coronal rain collisions are rather unlikely in active region loops. Only if the blobs have enough kinetic energy can they collide and produce oscillations. The collision and oscillations presented in Antolin et al. (2018) did possibly only happen because of the large dimensions, and large kinetic energy, of the blobs ($\sim$ 3 Mm long and $\sim$ 1 Mm wide), which are significantly longer than the average length and width of the blobs in our simulations ($\langle L_1 \rangle = 0.73$ Mm, $\langle L_2 \rangle = 3.3$ Mm and $\langle W_1 \rangle = \langle W_2 \rangle = 0.31$ Mm).

In the second parameter study, we considered a Quiet Sun background, by decreasing the background density with a factor of 10, and decreasing the magnetic field

to 5 G. In this setup, the background pressure is 10 times smaller and the restoring magnetic forces are 25 times smaller, which facilitates blob collisions and oscillations. We remark that this setup might be less representative, since coronal rain has mostly been observed in active region loops. We found that in the Quiet Sun simulations, the majority of the blobs collide ($\sim 81\%$; with a large proportion of the blobs super-Alfvénic), and the maximal amplitudes were 10 to 20 times larger than in the first parameter study. However, most of the amplitudes would still be too small to be observable with the resolution of current instruments (the median maximal amplitudes were of the order of 60 km). Analysing the evolution of the densities, we found that the time-distance maps of the density along both a fixed and moving slit only showed measurable oscillations in a very limited number of cases, with the largest amplitudes. We investigated the frequencies and wavelengths of these oscillations and found that the periods range between $10-100$s and the wavelengths are of the order of $1-10$ Mm, which is comparable to the length of the clumps. We found that there was, on average, more power in the longer wavelength and longer period oscillations, as we expected from Parameter Study 6 in Chapter 4.

In summary, the simulations and analysis presented in this chapter suggest that coronal rain collisions are rather unlikely in active region loops, as a typical background pressure and magnetic field strength are on average too large to facilitate collisions and oscillations. If the blobs have large dimensions such that they have enough kinetic energy, collisions and oscillations can be possible in this environment (see e.g. Antolin et al., 2018).

Chapter 6

Conclusions and future work

In this thesis, we have presented the results of numerical simulations of MHD waves in coronal loops. In Chapters 2 and 3 we investigated the effect of chromospheric evaporation on phase mixing of Alfvén waves in coronal loops. In Chapters 4 and 5 we studied the generation of transverse MHD waves by colliding counter-propagating clumps in coronal loops.

In Chapter 2, we introduced the detailed setup of our 2D coronal loop model for the phase mixing simulations presented in Chapter 3. The setup included the effects of gravitational stratification, thermal conduction, and optically thin radiation, with the chromosphere included as a mass reservoir. Sufficient resolution in the field-aligned direction was obtained by artificially broadening the Transition Region, using the technique proposed by Lionello et al. (2009) and Mikić et al. (2013). Imposing a background heating function which is uniform in the field-aligned direction, but which varies in the cross-field direction, generated a density profile representative of a coronal loop which is suitable for our phase mixing simulations.

In Chapter 3, we used an additional force term in the momentum equation to generate Alfvén waves near the top of the chromosphere. The Alfvén waves subsequently propagated in the corona and phase-mixed in the shell regions of the loop. By comparing with the equivalent ideal and non-driven simulations, we showed that the field-aligned flows were a combination of long-period oscillations (~ 650s) resulting from the ongoing relaxation to the imposed background heating profile, the ponderomotive effects associated with the driven Alfvén waves, and the evaporative upflows resulting from the heating of the phase-mixed Alfvén waves. Despite their relatively small amplitude, we were able to distinguish the evaporative upflows from the other field-aligned flows

by comparing with the ideal simulation. The amount of heating through viscous dissipation of the phase-mixed Alfvén waves in the corona was found to be extremely small ($\sim$ 4000 K). Consequently, the evaporative upflows associated with this heating were insignificant ($\sim 5-20$ m/s). Hence, in our study, the heating-evaporation cycle has no noticeable effect on the transverse density profile (or the Alfvén speed profile) in the loop.

One of the reasons why the heating, and hence, evaporation, in our simulations was limited is the choice of a high-frequency driver ($P \sim 12$ s). Although a high-frequency driver allows the rapid development of phase mixing in the shell regions of the loop, the high-frequency waves suffer less reflection in the TRs and, hence, more energy is lost to the lower atmosphere (see e.g. Hollweg 1984b,a; Berghmans and de Bruyne 1995; De Pontieu et al. 2001). We found that about 10-15% of the Poynting flux is not dissipated in the shell regions by the time the waves reach the far TR. However, increasing the amplitude of the driven Alfvén waves in future simulations could have a significant effect as there is still a subtantial amount ($\sim 85-90\%$) of the wave energy dissipated in the shell regions. In the core of the loop, almost all energy ($\sim$ 85%) is transmitted to the far TR and chromosphere.

Future work could also focus on how to contain more wave energy in the coronal volume of the loop. One way of doing this is to decrease the frequency of the driver, as this will lead to longer wavelengths in the corona and more reflection at the boundaries between the coronal part and the lower atmosphere. Moreover, waves and oscillations observed so far in the solar corona mostly have periods on the order of a few minutes (e.g. De Moortel and Nakariakov 2012; Morton et al. 2016). For longer wavelength waves, the phase mixing process would initially be less pronounced, but over time it would lead to large gradients and the subsequent dissipation of the wave energy in the coronal part of the shell regions of the loop. However, longer wavelength waves would take longer to phase mix and therefore, even if more energy is contained in the corona, it is still to be investigated whether this can result in more energy converted into heating and stronger evaporative upflows on relevant timescales. In summary, these considerations do not allow definitive predictions on heating and evaporation in the presence of lower frequency waves and thus more investigation is needed.

Several other aspects could be included to make our model more representative of actual coronal loops. For example, in the current study we have only considered vis-

cosity and neglected the effect of resistivity. As the resistivity is expected to be very low in the solar corona, omitting the effect of resistivity might be acceptable but it would still be instructive to investigate the potentially competing effects of a changing background Alfvén speed profile (because of diffusion of the background magnetic field), and the stronger heating resulting from the additional resistive dissipation. Further possibilities include a more realistic broadband driver (see e.g. Pagano et al., 2019) to establish how this affects the energy input into the corona or a magnetic field configuration with concentrated sources near the footpoints, as stronger divergence of the magnetic field in the TR and the corona could enhance the phase mixing process (see e.g. De Moortel et al., 2000). Finally, the study presented here mostly maintains the background initial conditions (i.e. the actual loop profile) through the presence of an imposed artificial background heating function. Without the presence of the background heating, Cargill et al. (2016) argued that the thermal evolution (the loop cooling) would lead to significant changes in the cross-field density profile (mostly due to draining of the core of the loop) on timescales quicker than the heating provided by the phase mixing of Alfvén waves. This heating occurs moreover in the boundary shells of the loop, and not in the interior, where the strongest radiation is present, and hence, the process of phase mixing alone cannot sustain the required density gradient.

In Chapter 4, we investigated the generation of transverse MHD waves in coronal loops by colliding counter-propagating clumps of plasma, inspired by the observations presented in Antolin et al. (2018). Using a 2D MHD model, we conducted a large parameter study to investigate the relationship between the parameters of the clumps and the properties of the generated transverse MHD waves. By varying the density and the speed of the clumps, we found that the amplitude of the generated modes scales with the kinetic energy of the system. If the density is varied in an asymmetric way, the collisions are less efficient and the less dense clump is compressed. We varied the angle of the colliding interface and the offset between rectangular clumps and found that kink modes are preferentially generated when an asymmetry in the system is present and that sausage modes are unaffected by the symmetry of the setup. On the other hand, too much asymmetry leads to less efficient collisions and smaller maximal amplitudes. We varied the length and the width of the clumps and found that longer clumps lead to longer collision times and an increase in the wavelength of the generated modes. The width of the clumps does not have a significant effect on the wavelength of the generated modes, but affects the damping time of the oscillations.

In Chapter 5, we applied the model of Chapter 4 to coronal rain clumps, by basing the properties of the clumps on an extensive observational study by Antolin and Rouppe van der Voort (2012). We devised a set of representative simulations and investigated the likelihood of collisions and oscillations of coronal rain clumps in coronal loops. We found that in active region loops, coronal rain collisions and oscillations are rather unlikely to happen, because of the large background pressure and magnetic field strength. The increase of thermal pressure between the counter-propagating clumps brought the blobs to a halt before they collided and the distortion of the field was extremely small due to the relatively large magnetic field strength ($\sim$ 25 G). In a second parameter study, we decreased the background pressure and magnetic field strength, to facilitate collisions and oscillations. Although this background could be representative of Quiet Sun regions, coronal rain has been observed mostly in active regions, and therefore this parameter study should be considered mostly as a theoretical investigation. We found a significant increase in the number of collisions of clumps and oscillations, however the majority of the maximal amplitudes and oscillations were still too small to be observable with current instrumentation. We investigated the amplitudes and wavelengths of the oscillations, and found that there is more power in the lower frequency oscillations, which corresponded to longer period oscillations and collisions by longer blobs in our model.

In Chapter 4 and 5, we have demonstrated a potential mechanism for the in-situ generation of MHD waves in the solar corona, by the collision of counter-propagating plasma clumps. Future work could investigate whether the collision of two clumps can lead to the formation of the Kelvin-Helmholtz instability (KHI) due to shearing of the clumps with the environment. This could lead to mixing and smaller length scales, which, when non-ideal MHD effects such as magnetic resistivity or viscosity are included, could lead to dissipation and potentially magnetic reconnection in cases where the collision produces strong distortions of the magnetic field, with further fragmentation and clump formation. Fang et al. (2016) performed similar numerical simulations of colliding and shearing flows which lead to the generation of the KHI and magnetic reconnection. However it should be noted that the timescales of these processes are in general larger than the evolution of the collisions.

Appendix A

Radiation and conduction timescales

In this appendix, we derive the conduction and radiation timescales in our 2D coronal loop model in Chapter 3. The radiation and conductive timescales can be derived by considering the thermal conduction and optically thin radiation in turn on the RHS of the energy equation (Equation (3.3)):

$$\rho \frac{D\epsilon}{Dt} = -\nabla \cdot F_c, \tag{A.1}$$

$$\rho \frac{D\epsilon}{Dt} = -\rho^2 \chi T^{\alpha}. \tag{A.2}$$

By performing a dimensional analysis, we can rewrite equation (A.1) and (A.2) as

$$\tau_{cond} \sim \frac{PL^2}{(\gamma - 1)\kappa_0 T^{7/2}}, \tag{A.3}$$

$$\tau_{rad} \sim \frac{P}{(\gamma - 1)\rho^2 \chi T^{\alpha}}, \tag{A.4}$$

where all the variables have been defined before and L is a relevant length scale. We use $L = 50$ Mm, which is roughly half the length of the coronal part of the loop, as a representative length scale. This is also the maximum length scale over which heat can propagate in the domain. Figure A.1 shows a plot of the radiation τ_{rad} (left panel) and the conduction timescale τ_{cond} (right panel) as a function of y (along $x = 0$ Mm) after the numerical relaxation of our 2D model in Chapter 3. The vertical lines mark the boundaries of the TR. We can see that $\tau_{rad} \sim 3000 - 4000$s in the corona, and that $\tau_{cond} \sim 1000 - 5000$s for most of the corona. From these plots we can conclude

that running the simulations in Chapter 3 for ~ 6000s is sufficient to see the effects of thermal conduction and optically thin radiation.

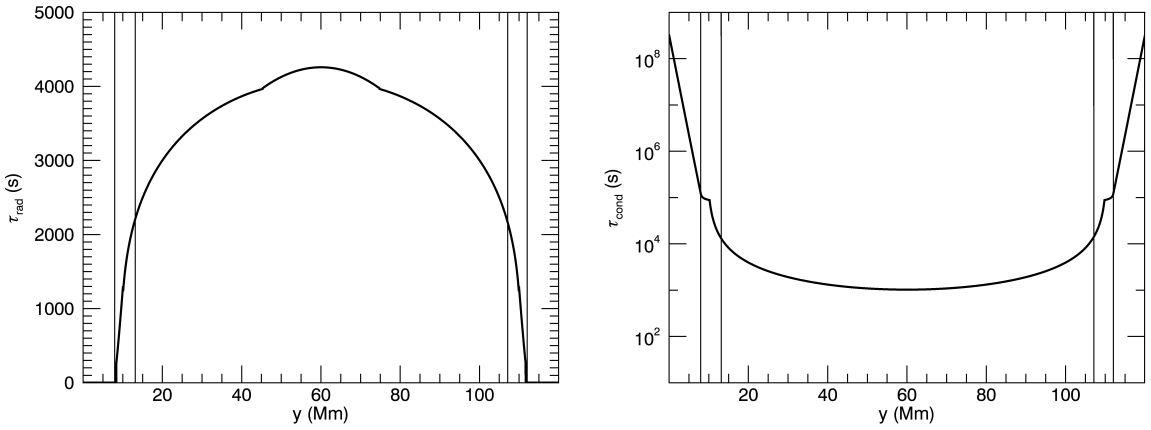

Figure A.1: Plot of the radiation τ_{rad} (left) and conduction τ_{cond} (right) timescales in the domain as a function of y (along $x = 0$ Mm). The vertical lines mark the boundaries of the TR.

Appendix B

Ponderomotive force

The aim of this appendix is to investigate the ponderomotive effects associated with the Alfvén wave driver in our 2D model in Chapter 3.

B.1 Introduction

The ponderomotive force is the non-linear magnetic pressure force associated with an Alfvén wave. Suppose we have a straight initial magnetic field $\mathbf{B_0} = (0, B_0, 0)$ in the y direction and a linear perturbation $\mathbf{b} = (0, 0, b)$ in the invariant z direction. The magnetic field is then given by $\mathbf{B} = \mathbf{B_0} + \mathbf{b}$, and the Lorentz force can be written as

$$\mathbf{j} \times \mathbf{B} = \frac{1}{\mu_0} \left((\nabla \times (\mathbf{B_0} + \mathbf{b})) \times (\mathbf{B_0} + \mathbf{b}) \right), \tag{B.1}$$

$$= \frac{1}{\mu_0} \left((\nabla \times \mathbf{B_0}) \times \mathbf{B_0} + (\nabla \times \mathbf{b}) \times \mathbf{B_0} + (\nabla \times \mathbf{B_0}) \times \mathbf{b} + (\nabla \times \mathbf{b}) \times \mathbf{b} \right). \tag{B.2}$$

The last term is second order and is the non-linear component of the Lorentz force. This can be further reduced to

$$(\nabla \times \mathbf{b}) \times \mathbf{b} = \left(-b\frac{\partial b}{\partial x}, -b\frac{\partial b}{\partial y}, 0 \right), \tag{B.3}$$

$$= -\mathbf{b} \cdot \nabla b, \tag{B.4}$$

$$= -\nabla \left(\frac{b^2}{2} \right), \tag{B.5}$$

where we have also used the fact that z is the invariant direction ($\frac{\partial}{\partial z} = 0$). The ponderomotive force has a transverse (x) and a field aligned (y) component. The former can create fast waves (see e.g. Thurgood and McLaughlin, 2013), while the

latter can create upflows along the field. Verwichte et al. (1999) analyse the evolution of an Alfvén pulse in a cold uniform plasma ($\beta = 0$). This Gaussian pulse splits into a left and right propagating Alfvén pulse along the field (y), such that the expression for b is

$$b \sim f(y + v_A t) + g(y - v_A t),$$

with f and g the left and right propagating wave respectively, propagating at the Alfvén speed v_A. The field aligned ponderomotive force is then given by

$$-\frac{1}{2}\frac{\partial b^2}{\partial y} \sim -\frac{1}{2}\frac{\partial}{\partial y}\left(f^2(y + v_A t) + g^2(y - v_A t) - 2f(y + v_A t)g(y - v_A t)\right).$$

Here f^2 and g^2 are the ponderomotive wings associated with the Alfvén waves and the last term is the cross-ponderomotive force, which is related to the slow wave. Note that in a cold plasma the slow wave does not propagate. The associated upflows and density perturbations can be derived from the second order part of the linearised MHD equations (Verwichte et al., 1999):

$$\frac{\rho(y)}{\rho_0} \sim f^2(y + v_A t) + g^2(y - v_A t) + F_1(t), \tag{B.6}$$

$$v_y \sim -f^2(y + v_A t) + g^2(y - v_A t) + F_2(t). \tag{B.7}$$

The upflows consist of a strictly positive (negative) part associated with the right (left) propagating Alfvén pulses ('ponderomotive wings') and a function $F_2(t)$ related to the cross-ponderomotive force. The expression B.6 for the density perturbations also shows a positive density perturbation for right and left propagating Alfvén waves. This means that the ponderomotive wings carry mass away from the location where they are generated. In both expressions the upflows and density perturbations associated with the ponderomotive wings propagate at the Alfvén speed and have half the wavelength of the Alfvén wave (e.g. $f^2(x + v_A t)$ compared to $f(x + v_A t)$). The terms associated with the cross-ponderomotive force in Equations B.6 and B.7 ($F_1(t)$ and $F_2(t)$) have mixed properties and for more information on these terms we refer to Verwichte et al. (1999).

B.2 Uniform model

We set up an experiment using the numerical code Lare2D Arber et al. (2001). The x dimension extends from $x = -2$ Mm to $x = 2$ Mm, and the y domain runs from $y = 0 - 600$ Mm. The magnetic field is uniform and straight in the y direction, $B_y = 10$ G. The x and z directions are invariant. The plasma has a uniform coronal-like density of $\rho = 6 \times 10^{-13}$ kg/m^3 and a uniform coronal temperature of $T = 1.55$ MK, which results in an Alfvén speed of $v_A = \frac{B}{\sqrt{\mu_0 \rho}} = 1150$ km/s and a sound speed of $c_s = \sqrt{\frac{p\gamma}{\rho}} = 188$ km/s. The plasma beta is $\beta = 0.03$. The boundary conditions are periodic in x and zero-gradient at $y = 0$. At $y = 600$ Mm we add a damping layer of length 900 Mm where the velocities and magnetic field perturbations in x and z are artificially damped to mimic an open boundary. More precisely, the velocity and magnetic field components (except for the guide field B_y) are damped as follows:

$$
\begin{aligned}
v_x &= g(y) v_x, \\
v_y &= g(y) v_y, \\
v_z &= g(y) v_z, \\
B_x &= g(y) B_x, \\
B_z &= g(y) B_z,
\end{aligned}
$$

where $g(y)$ is the dimensionless function

$$
g(y) = \begin{cases} -b(y-d)^p + 1 & \text{for } y > d, \\ 1 & \text{for } y < d, \end{cases}
$$

with y in Mm and $b = 3 \times 10^{-7}$ Mm^{-2}, $d = 600$ Mm, $p = 2$ constants. This means that the velocities and magnetic field perturbations are damped for $y > 600$ Mm and that the damping increases quadratically.

We run two simulations with a driver implemented in different locations. In the first simulation we drive the bottom boundary ($y = 0$ Mm) continuously in the invariant direction (z):

$$
v_z = v_0 \sin(\omega t), \tag{B.8}
$$

$$
B_z = -v_z \sqrt{\rho}, \tag{B.9}
$$

where $v_0 = 10.4$ km/s is 1% of the Alfvén speed and $\omega = 0.54$ Hz. This results in a period P of 11.6s. This driver creates right propagating Alfvén waves along y. Slow waves are also generated as a consequence of the non-linear ponderomotive force which creates a pressure perturbation.

The second simulation has a driver implemented in the domain at $y = 200$ Mm. Instead of driving v_z and B_z directly, we drive the system through a force in the momentum equation in the z direction:

$$\rho \frac{dv_z}{dt} = \rho v_1 \omega \cos(\omega t), \tag{B.10}$$

with ω described as above and v_1 chosen such that the amplitude of v_z is 10.4 km/s. Because the implementation of the force driver is different to the boundary driver, v_1 has been multiplied by a constant ($v_1 = \alpha v_0$) to have the same v_z amplitude as in the boundary driver simulation. This driver generates left and right propagating Alfvén waves along y. The force is applied to a strip of 10 gridpoints, symmetrically distributed about $y = 200$ Mm.

In both simulations we define a region over which we analyse the mass evolution, to investigate the effect of the ponderomotive force on the upflows and the mass flow along the field. In the first simulation the region extends from $y = 30$ Mm to $y = 60$ Mm, and in the second simulation from $y = 230$ Mm to $y = 260$ Mm.

B.2.1 Propagation of the Alfvén waves and associated upflows

Figure B.1 shows a plot of v_z and $B_z/\sqrt{\rho}$ for the boundary driver (top panels) and the force driver (bottom panels) at $x = 0$ Mm at $t = 46$s (4 periods of the driver). The vertical lines at $y = 30$ Mm ($y = 230$ Mm) and $y = 60$ Mm ($y = 260$ Mm) mark the boundaries of the region over which we analyse the mass evolution in the respective simulations. In both panels the maximal amplitude of v_z is $v_0 = 10.4$ km/s and we can see that $v_z = -B_z/\sqrt{\rho}$ holds, a property of right propagating Alfvén waves. Moreover these waves propagate at the Alfvén speed. Remark that the first pulse of the force driver simulation is discontinuous as the applied force is maximal at $t = 0$ (see Equation B.10). However in both simulations the same number of wavelengths ($1.75\lambda_{\text{Alfvén}}$) is located in the region at $t = 46$s. The two panels on the right of Figure B.1 show the simultaneous field aligned upflows v_y (km/s) along $x = 0$ Mm. These upflows are generated by the ponderomotive force $\nabla\left(\frac{B_z^2}{2}\right)$, as discussed in section B.1. They consist of the ponderomotive wings (always positive) for $y > 10$ Mm ($y > 210$ Mm for

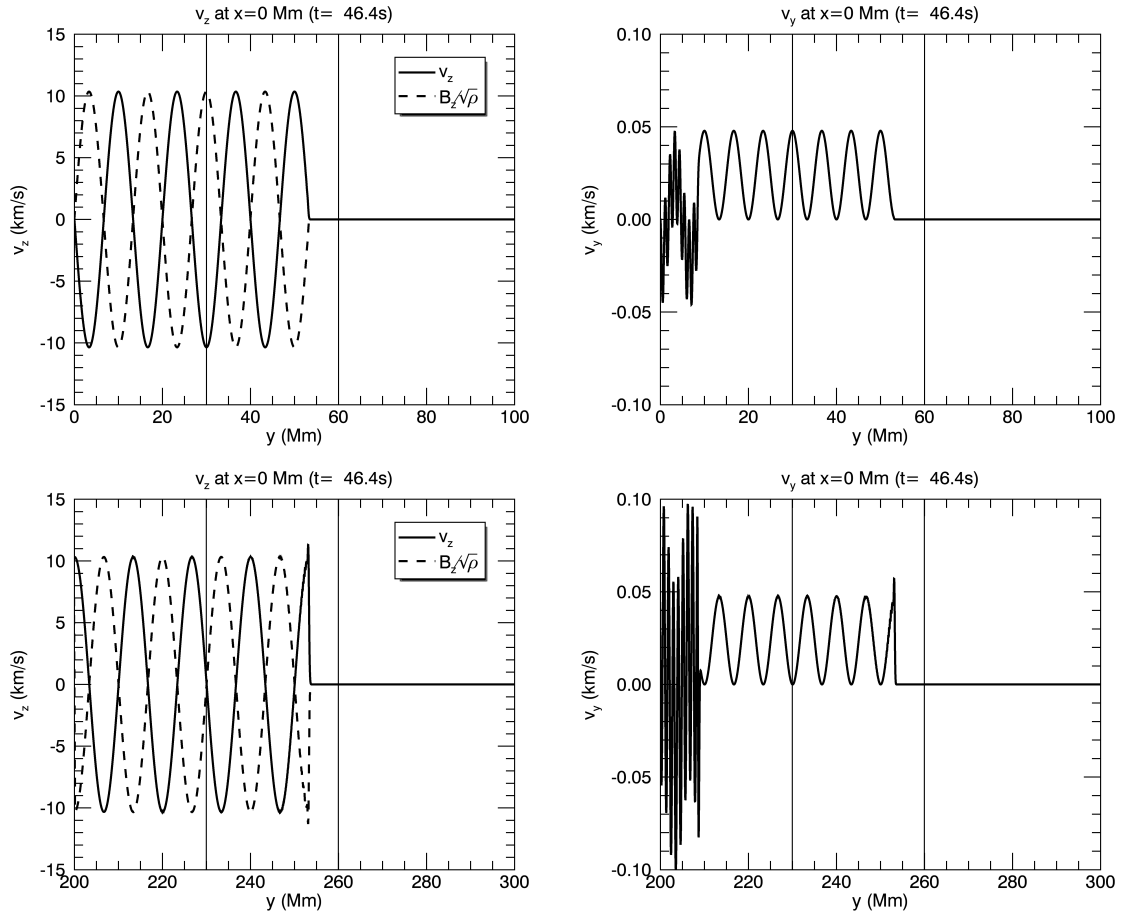

Figure B.1: (Top left) Plot of the Alfvén wave v_z (km/s) (solid line) and $\frac{B_z}{\sqrt{\rho}}$ (dashed line) at $t = 46$s and at $x = 0$ Mm for the boundary driver. (Top right) Plot of the upflows v_y (km/s) caused by the ponderomotive force at $t = 46$s and at $x = 0$ Mm for the boundary driver. (Bottom panels) Similar plots for the force driver.

the force driver) associated with the Alfvén waves and a separate oscillation associated with the slow waves ($y < 10$ Mm for the boundary driver and $y < 210$ Mm for the force driver). The ponderomotive wings propagate at the Alfvén speed and have half the wavelength of v_z and B_z. Because the ponderomotive wings are strictly positive, these upflows move mass upwards along the field. The separate oscillation is the response to the cross-ponderomotive force (associated with the slow wave) and propagates at the sound speed. These upflows are not strictly positive, and they have a very short wavelength ($\lambda_{\text{Alfvén}}/12$) on top of the longer wavelength ($\lambda_{\text{Alfvén}}/2$), because of the smaller slow speed (see the right panels of Figure B.1), which is consistent with the ratio of $\frac{c_s}{v_A} \approx \frac{1}{6}$. The amplitude in v_y of the cross-ponderomotive tail is about twice as large for the force driver simulation compared to the boundary driver simulation. This happens because of the different implementation of the force driver, although it needs

more investigation. The ponderomotive wings associated with the left propagating Alfvén waves have a negative field aligned v_y (see Equation B.7). However the density perturbation ρ/ρ_0 is positive (Equation B.6), which means that the left propagating Alfvén waves in the force driver simulation also move mass away from the location of the driver.

B.2.2 Standing modes

The force driver generates left propagating Alfvén waves and slow waves and these Alfvén waves reflect of the bottom boundary ($y = 0$ Mm) at $t = 174$s. A standing mode is generated at a particular location in $0 < y < 200$ Mm when the reflected Alfvén waves reach that location. At $t = 347$s the standing mode reaches the location of the driver ($y = 200$ Mm) where it becomes a node in v_z from that time onwards, and B_z becomes an antinode. This is shown by the top left panel of Figure B.3. The wavelength of the standing mode is determined by the length of the domain (200 Mm) and the driving frequency of the driver. In general the wavelength of the n-th harmonic of a standing mode is given by

$$\lambda_n = \frac{2L}{n},$$

where $L = 200$ Mm is the length from the bottom boundary to the location of the driver. The wavelength of the Alfvén waves generated by the driver is given by $\lambda_{\text{driver}} = v_A P = 13.3\text{Mm} = \frac{L}{15}$, where v_A is the Alfvén speed and P the period of the driver. This shows that the 30th harmonic has $\lambda_{30} = \lambda_{\text{driver}}$, and that this harmonic will resonate as a standing mode. The location of the nodes and antinodes of v_z are respectively given by

$$\{y = 2i\frac{L}{2n} | i \in \{0, ..., n\}\} = \{y = i\frac{\lambda_n}{2} | i \in \{0, ..., n\}\},$$

$$\{y = (2i+1)\frac{L}{2n} | i \in \{0, ..., n-1\}\} = \{y = (2i+1)\frac{\lambda_n}{4} | i \in \{0, ..., n-1\}\}.$$

Remark that for a standing mode, v_z and B_z are out of phase and that the nodes of B_z are the antinodes of v_z and vice versa. In Figure B.2 we plot v_z and B_z as a function of time at the 10th node ($y = \frac{10L}{30} = 66.6$ Mm) and the 10th antinode ($y = \frac{21L}{60} = 70$ Mm) of v_z. At $t = 240$s the reflected Alfvén waves reach $y = 66.6$ Mm and the regime changes from propagating waves to a standing wave. This can be seen by the fact that $y = 66.6$ Mm becomes a node of v_z and $y = 70$ Mm an antinode of v_z for $t > 240$s. The right panel of Figure B.2 shows a similar plot of B_z and confirms that the nodes of B_z are the antinodes of v_z and vice versa.

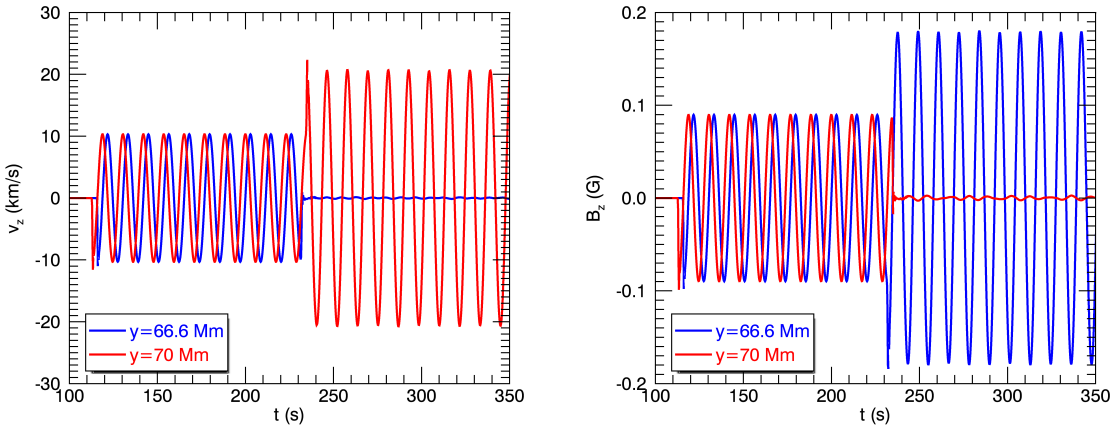

Figure B.2: (Left) Plot of v_z (km/s) as a function of time at $y = 66.6$ Mm (blue) and $y = 70$ Mm (red). (Right) Similar plot but for B_z (G).

In Figure B.3 we plot $v_z/\max(v_z)$ and $B_z/\max(B_z)$ at the location of the driver ($y = 200$ Mm), averaged over the 10 gridpoints of the driver. We can see that at $t = 347$s - the time when the reflected Alfvén waves reach the location of the driver - the propagating wave becomes a standing wave and the location of the driver becomes a node of v_z and an antinode of B_z. The top right panel of Figure B.3 shows the magnetic pressure force $-\nabla_y \left(\frac{B_z^2}{2}\right)$ (black line), the pressure force $-\frac{\partial p}{\partial y}$ (black dotted dashed line) and the sum of these forces (green line) in the y direction as a function of time at the location of the driver. At $t = 347$s the magnetic pressure force increases significantly as a consequence of the antinode of B_z at the location of the driver, which leads to a larger positive upflow v_y at the location of the driver (middle panel of Figure B.3). As mass is moved upwards along the field by this upflow, the pressure increases for $y > 200$ Mm and decreases at the location of the driver ($y = 200$ Mm) (bottom panel in Figure B.3). This increases the pressure force at the location of the driver (top right panel of Figure B.3), soon after the magnetic pressure force increases. This delay in the increase of the pressure force is also shown by the total force in the y direction (green line) which has a large peak at $t = 347$s, but afterwards it oscillates about zero. After $t = 347$s, v_y oscillates about a positive value (0.15km/s). Remark that for $t < 347$s, v_y oscillates about 0 (with the period of the ponderomotive wings (6s)) because of the cross-ponderomotive response which is immediately generated at the location of the driver (similar as in the bottom right panel of Figure B.1). We also remark that a larger period (30s) on top of the period of the ponderomotive wings (6s) is visible in the plots of the pressure and the upflows (v_y) after $t = 347$s, because a slow wave is generated at $t = 347$s when the plasma is compressed by the larger upflows.

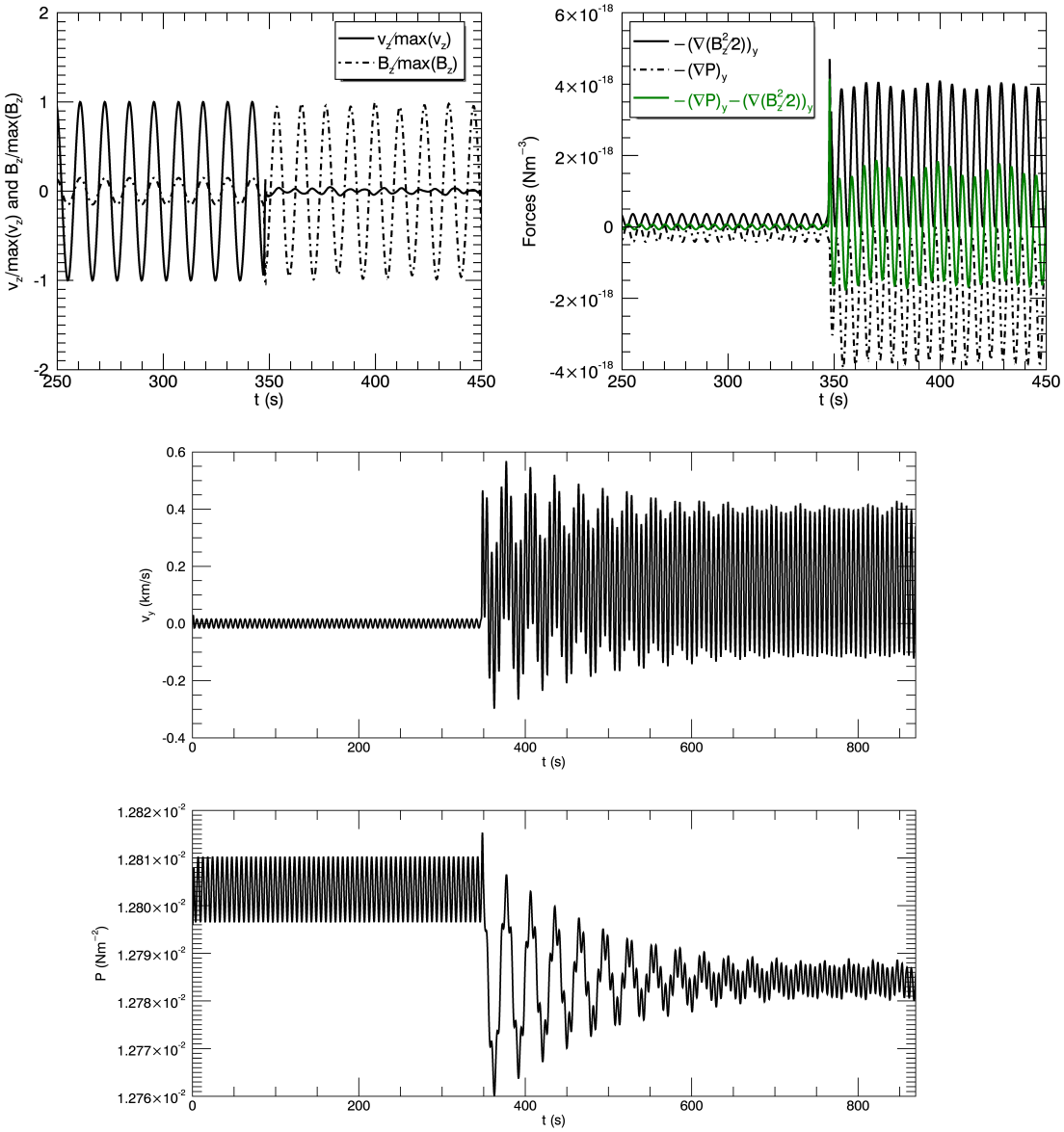

Figure B.3: (Top left) Plot of $v_z/\max(v_z)$ and $B_z/\max(B_z)$ as a function of time at $y = 200$ Mm. (Top right) Plot of the ponderomotive force $-\nabla_y\left(\frac{B_z^2}{2}\right)$ (solid black line), the pressure force $-\frac{\partial p}{\partial y}$ (black dotted dashed line) and the total force $-\nabla_y\left(\frac{B_z^2}{2}\right) - \frac{\partial p}{\partial y}$ in the y direction (green line) at the location of the driver. (Middle) Plot of the upflows v_y at $y = 200$ Mm as a function of time. (Bottom) Plot of the pressure P at $y = 200$ Mm as a function of time.

Standing mode and length of the domain

The location of the nodes and antinodes of v_z and B_z depends on the length L between the bottom boundary and the location of the driver. In some cases L is not necessarily a multiple of λ_{driver}, and the standing regime will be less efficiently generated. Therefore,

the location of the driver does not always have to be a node of v_z and an antinode of B_z. To show this we run a simulation where we increase the length L by moving the bottom boundary a distance of $\lambda_{\rm driver}/4$ to the left, so $L_{\rm new} = L + \lambda_{\rm driver}/4 = L + L/60 = 203.33$ Mm. The driver is still at $y = 200$ Mm, but the lower boundary is now at $y = -3.33$ Mm instead of $y = 0$ Mm. The wavelength of the n-th harmonic of the system is then given by

$$\lambda_n = \frac{2L_{\rm new}}{n} = \frac{2(L + \frac{L}{60})}{n} = \frac{61L}{30n}.$$

If we equate λ_n and $\lambda_{\rm driver}$, we get

$$\frac{61L}{30n} = \frac{L}{15} \Leftrightarrow n = \frac{61}{2} = 30.5.$$

Because n is not an integer, there is no harmonic which has $\lambda_n = \lambda_{\rm driver}$. The standing mode in the system will be less efficiently generated and it will be a superposition of different harmonics. The bottom boundary ($y = -3.33$ Mm) is still a node of v_z and an antinode of B_z, but the location of the driver is now a node of B_z and an antinode of v_z. This is shown in Figure B.4 which plots v_z and B_z at the location of the driver (200 Mm) and at $y = 196.7$ Mm. The location $y = 196.7$ Mm is a node in v_z and an antinode in B_z, but the location of the driver is an antinode in v_z and a node in B_z. This shows that in general the location of the driver does not always have to be an antinode of B_z, and that this is determined by the length L between the location of the driver and the location where the Alfvén waves reflect. The consequence of this is that the magnetic pressure force associated with B_z will not necessarily increase at the location of the driver, and hence it will not lead to higher upflows along the field. Indeed, this is shown in Figure B.5 where we show the forces and the upflows at the location of the driver. The magnetic pressure force decreases at the location of the driver when the standing mode is generated, because of the node in B_z. This leads to an overall decrease in the upflows v_y.

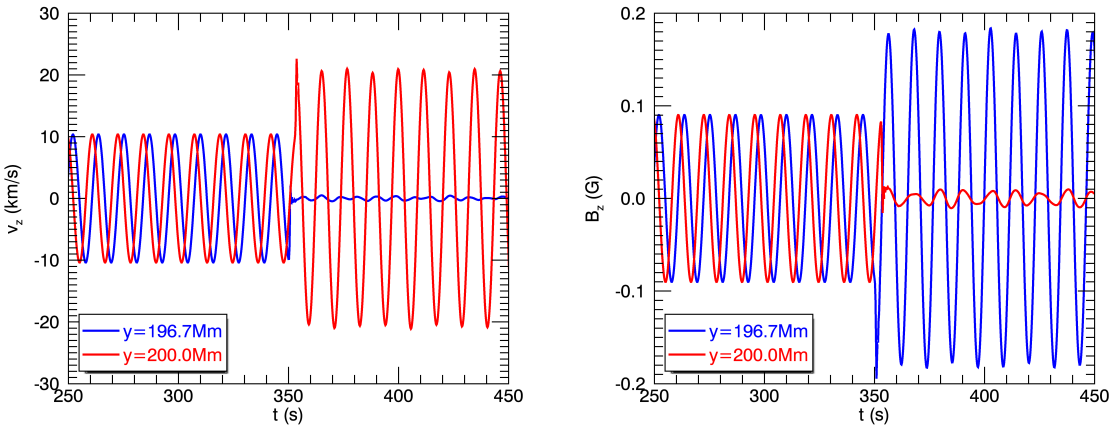

Figure B.4: (Left) Plot of v_z (km/s) as a function of time at $y = 196.7$ Mm (blue) and $y = 200$ Mm (red). (Right) Similar plot for B_z (G).

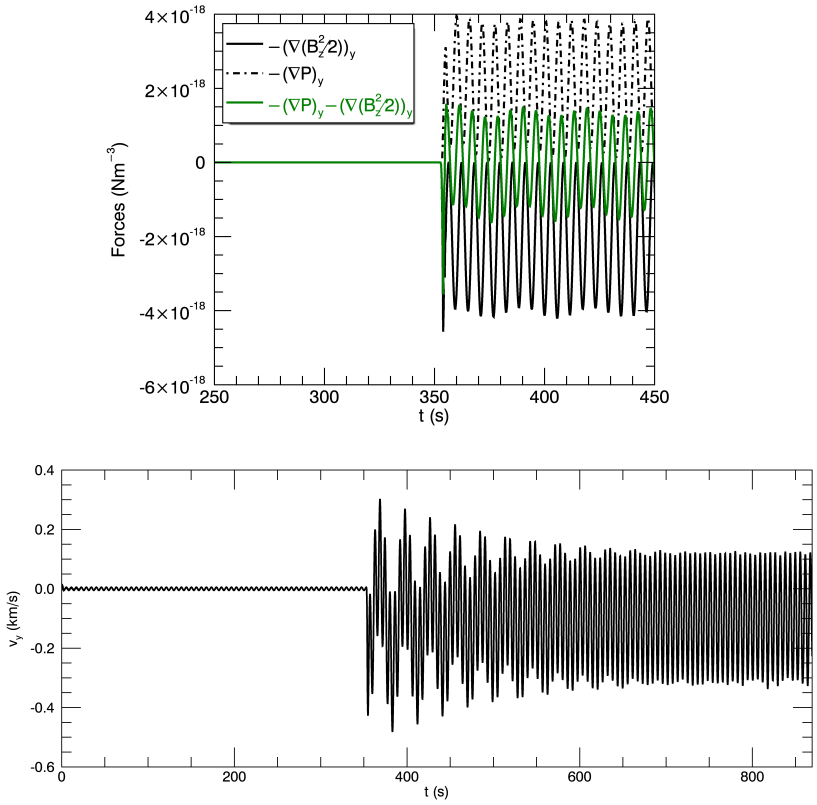

Figure B.5: (Top) Plot of the ponderomotive force $-\nabla_y \left(\frac{B_z^2}{2}\right)$ (solid black line), the pressure force $-\frac{\partial p}{\partial y}$ (black dotted dashed line) and the total force $-\nabla_y \left(\frac{B_z^2}{2}\right) - \frac{\partial p}{\partial y}$ in the y direction (green line) at the location of the driver. (Bottom) Plot of the field aligned flows v_y at $y = 200$ Mm as a function of time.

B.2.3 Density perturbations and mass increase

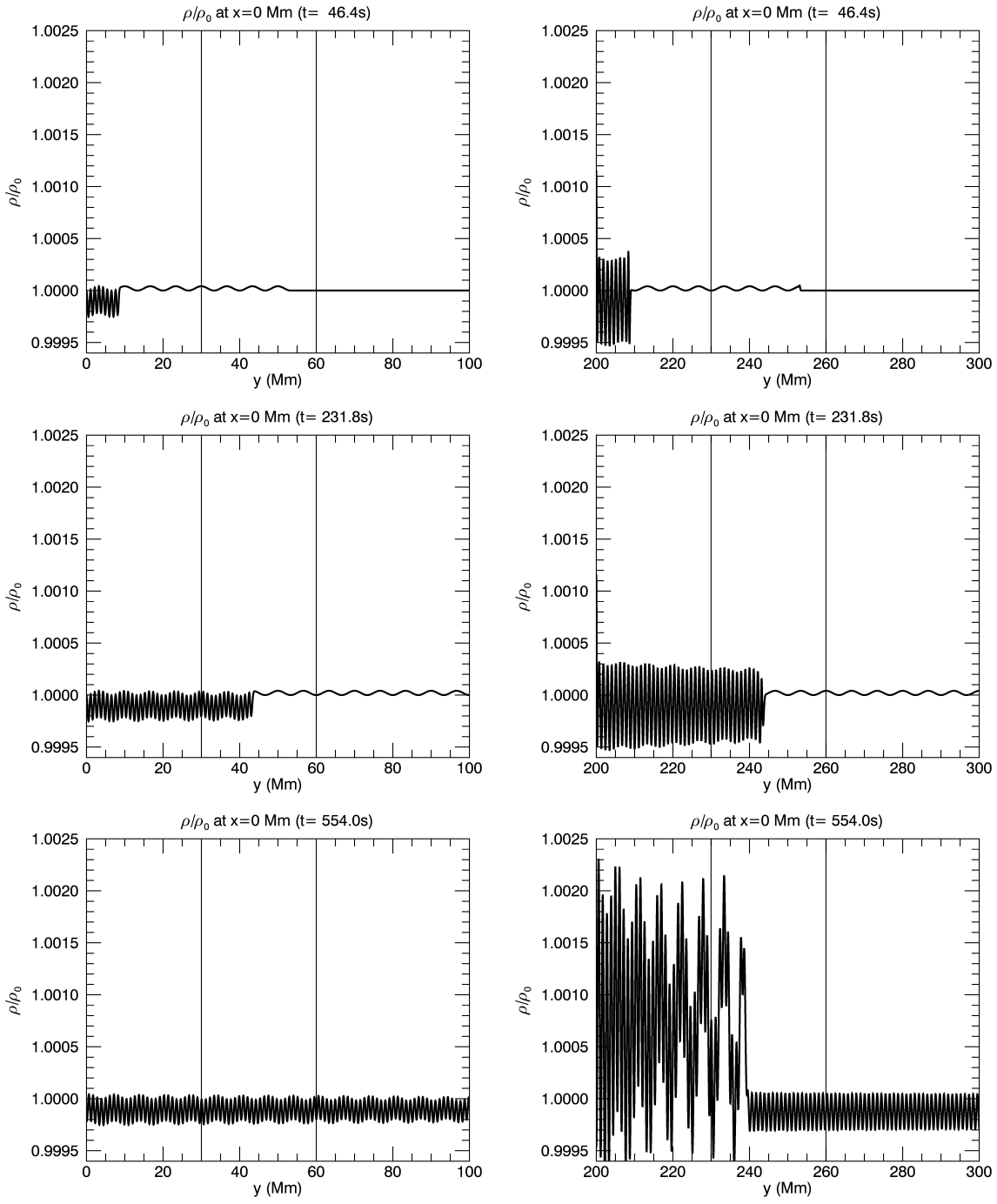

Figure B.6: Plot of the density perturbations $\frac{\rho}{\rho_0}$ at $t = 46, 233, 554$s and at $x = 0$ Mm for the boundary driver (left panels) and the force driver (right panels).

In this section we analyse the mass evolution in the region from $y = 30$ Mm to $y = 60$ Mm for the boundary driver simulation, and in the region from $y = 230$ Mm to $y = 260$ Mm for the force driver simulation. Before we do this, we show the

density perturbations caused by the ponderomotive wings, the cross-ponderomotive force and the standing wave (generated in $0 < y < 200$ Mm). Figure B.6 shows the density perturbations ρ/ρ_0 at $t = 46, 233, 554$s, for the boundary driver ($0 < y < 100$ Mm; left panels) and force driver ($200 < y < 300$ Mm; right panels). These times are chosen such that the ponderomotive wings, the cross-ponderomotive force and the density perturbation associated with the standing wave are approximately located in the middle of the region. At $t = 46$s the front of the Alfvén wave train is located at $y = 53$ Mm ($y = 253$ Mm for the simulation with the force driver). The ponderomotive wings associated with the Alfvén wave cause a positive density perturbation ($\rho/\rho_0 > 1$) and hence these increase the mass when they enter the region until they leave the region again (because then the inflow of mass equals the outflow of mass). This is also shown by Figure B.7 where we show the mass increase $\int(\rho - \rho_0)dV$ and the relative mass increase $\int(\rho - \rho_0)/\rho_0 dV$ for the boundary driver simulations (left panels) and the force driver simulation (right panels) ($\rho_0 = \rho(t = 0)$). Here the vertical coloured lines represent the timescales related to the travel time of an Alfvén wave (blue) and a slow wave (red) to reach and leave the region. The first two vertical blue lines at $t = 25$s and $t = 51$s represent the time when the front of the (right propagating) Alfvén wave train reaches and leaves the region. During this time span the density perturbations caused by the ponderomotive wings increase the mass in the region. After $t = 51$s the mass then remains constant as the ponderomotive wings carry mass into the region at the same rate they are carrying mass out of the region (until $t = 156$s). The cross-ponderomotive force associated with the slow waves causes an overall negative density perturbation, as can be seen in the middle panels of Figure B.6, at $t = 232$s, when the cross-ponderomotive force has propagated into the region and has reached $y \approx 43$ Mm ($y \approx 243$ Mm). The cross-ponderomotive force decreases the mass when these density perturbations propagate through the region. Indeed in Figure B.7, we see that at $t = 156$s (the first vertical red line) the front of the slow wave train reaches the beginning of the region and the mass starts to decrease. The mass then decreases for 155s (the time it takes for the slow waves to propagate through the region) until $t = 311$s when the front of the slow waves leaves the region. In the simulation of the boundary driver the mass in the region then remains constant after $t = 311$s, and has decreased with 0.01% compared to the initial mass.

The bottom right panel of Figure B.6 shows the density perturbations at $t = 554$s for the force driver simulation. We see an increase in the density perturbations for $200\text{Mm} < y < 240\text{Mm}$. This is a consequence of the standing mode generated at $t = 347$s at the location of the driver ($y = 200$ Mm), which creates a larger upflow v_y

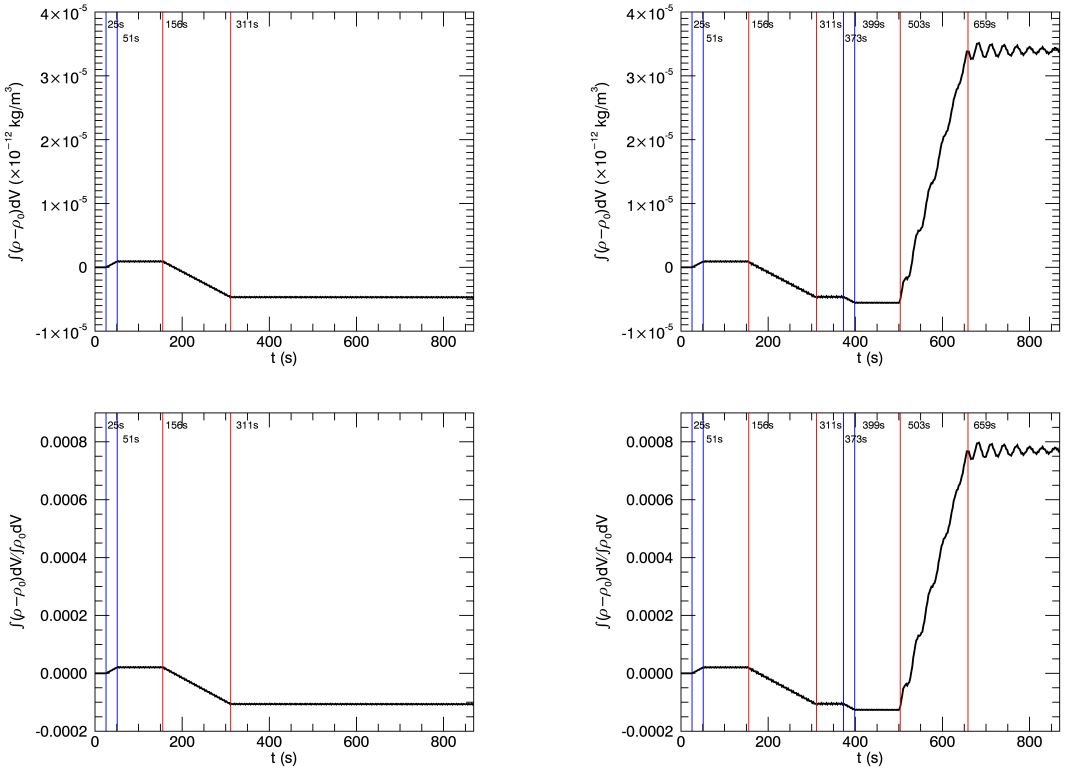

Figure B.7: Plots of the mass increase $\int(\rho - \rho_0)dV$ (top panels) and the relative mass increase $\int(\rho - \rho_0)dV / \int \rho_0 dV$ (bottom panels) in the region. The left panels are for the boundary driver simulation, the right panels for the force driver simulation. The blue (red) vertical lines are timescales when Alfvén waves (slow waves) reach and leave the region $y = 30$ Mm to $y = 60$ Mm for the boundary driver simulation, or $y = 230$ Mm to $y = 260$ Mm for the force driver simulation.

along the field as shown in the previous section. These upflows compress the plasma and increase the density perturbations significantly, which then propagate as slow waves in the domain. At $t = 554$s these slow waves have reached the region ($y = 230$ Mm) where they start to increase the mass. This is shown by the right panels in Figure B.7, where the red vertical lines at $t = 503$s and $t = 659$s represent the time when these slow waves reach and leave the region. The mass increases significantly and at the end of the simulation is 0.08% higher than the initial mass of the region. There is also an earlier, slight decrease in the mass from $t = 373$s to $t = 399$s in the force driver simulation (second pair of vertical blue lines). This is due to (right propagating) Alfvén waves that are generated by the driver at $t = 347$s, the time when the reflected Alfvén waves reach the location of the driver. The generated Alfvén waves (destructively) interfere with the reflected Alfvén waves and have a smaller B_z perturbation. This leads to a smaller ponderomotive wing in the density perturbation, so when these Alfvén waves reach the start of the region ($y = 230$ Mm) the inflow is smaller than the outflow.

B.3 Model with a stratified atmosphere

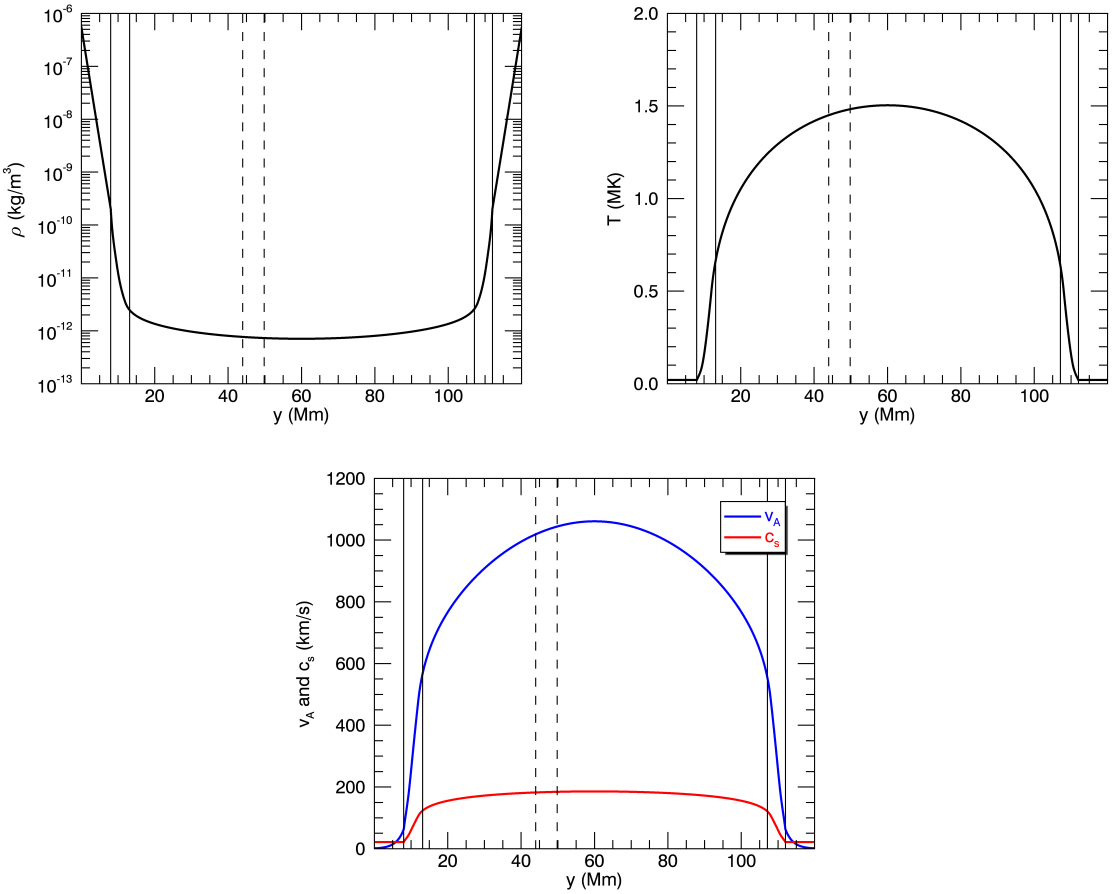

Figure B.8: (Top row) Plot of the initial density (left) and temperature (right) at $x = 0$ Mm. (Bottom) Plot of the initial Alfvén speed v_A (blue) and the sound speed c_s (red) at $x = 0$ Mm. The vertical solid black lines in each figure mark the boundaries of the first and second TR, the dashed vertical lines mark the boundaries of the region in the corona over which the mass evolution is calculated.

In this section we extend the uniform model to a model including gravity, thermal conduction, optically thin radiation and a background heating. The field aligned coordinate is y and extends from 0 to 120 Mm. The x coordinate is the invariant direction and extends from $x = -2$ Mm to $x = 2$ Mm. The model consists of two chromospheres (CHROM) each with a length of 8 Mm, two transition regions (TR) of length ~ 5 Mm and a corona of length ~ 94 Mm. The TR has been broadened using the technique proposed by Lionello et al. (2009) and Mikić et al. (2013), with $T_c = 5 \times 10^5$ K. Figure B.8 shows a plot of the density and the temperature as a function of y at $x = 0$ Mm. The density decreases exponentially from the base of the chromospheres ($\rho \sim 10^{-6}$ kg/m^3) to the base of the TR (at $y = 8$ Mm and $y = 112$ Mm) ($\rho \sim 10^{-10}$ kg/m^3).

In the corona the density is fairly constant ($\rho_{cor} \sim 10^{-12}$ kg/m^3). The temperature is uniform in the chromospheres ($T_{chrom} = 2 \times 10^4$ K) and increases in the corona up to 1.5 MK. The vertical solid lines at $y = 8$ Mm, $y = 13$ Mm, $y = 107$ Mm and $y = 112$ Mm mark the base and top of the TRs. The vertical dashed lines mark the boundaries of the region ($y = 44$ Mm and $y = 50$ Mm) over which we track the mass evolution. Figure B.8 also shows a plot of the Alfvén speed v_A and the sound speed c_s as a function of y at $x = 0$ Mm. The plasma beta in the corona is $\beta = \frac{2}{\gamma}\left(\frac{c_s}{v_A}\right)^2 \sim 0.03$.

The system is numerically relaxed in Lare2D (until the field aligned flows are significantly less than 1% of the local c_s or v_A). After the relaxation, we implement the force driver (Equation B.10) near the top of the first chromosphere ($y = 7.8$ Mm), with $\omega = 0.54$ Hz and $v_0 = 0.7$ km/s (1% of the local v_A) as before.

B.3.1 Standing mode

Because of the stratified atmosphere in our model, waves can reflect at other locations besides the bottom ($y = 0$ Mm) and top boundary ($y = 120$ Mm) of the domain. In general, waves can reflect at locations of high density gradient and regions where the Alfvén speed gradient is high. Several papers have studied the reflection and transmission of Alfvén waves from the corona into the lower atmosphere (see e.g. Hollweg 1984b,a; Berghmans and de Bruyne 1995; De Pontieu et al. 2001; Ofman 2002). In our model we expect the Alfvén waves to significantly leak into the chromosphere because of the short wavelength ($\sim 85\%$), where they undergo damping and reflection.

Because the reflection happens throughout the chromosphere and not exactly in one location, the generation of the standing mode will be less efficient (as was also discussed in section B.2.2).

Figure B.9 shows the envelope of v_z (km/s) and B_z (G) (maximal amplitudes over each period) at the location of the driver ($y = 7.8$ Mm) with time. The vertical blue line at $t = 703$s in Figure B.9 is the time for a left propagating Alfvén wave to reflect in the first chromosphere ($y \sim 3$ Mm) and come back at the location of the driver. The blue line at $t = 1019$s is the time when the front of a right propagating Alfvén wave similarly reflects in the second chromosphere ($y \sim 117$ Mm) and reaches the driver again. Because the reflection happens throughout the chromosphere, these lines only represent an average time for the reflection in the chromosphere, and they are chosen to match the decrease and increase in B_z in Figure B.9. From the previous experiments we expect a standing mode to be generated at the time the reflected left

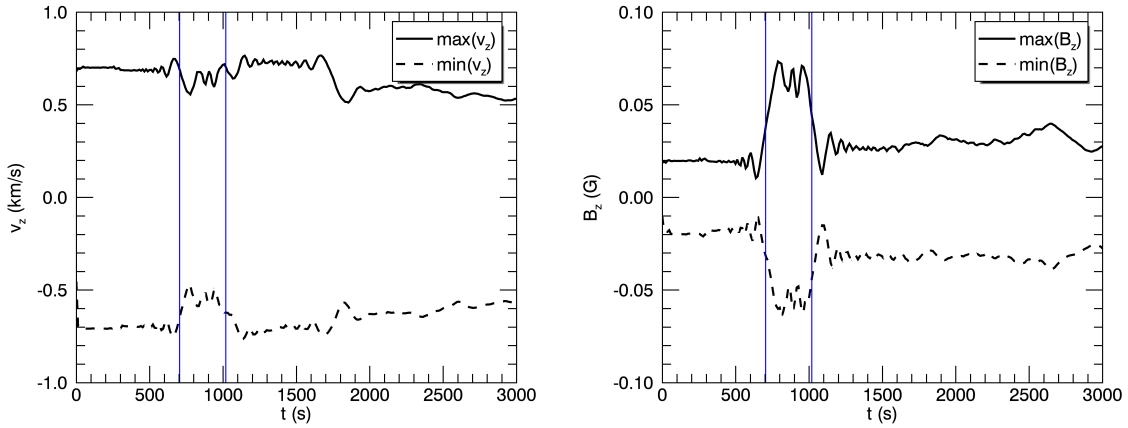

Figure B.9: Plot of the maximal and minimal amplitude of v_z (km/s) and B_z (G) (taken every period 11.6s of the driver) at the location of the driver ($y = 7.8$ Mm).

propagating Alfvén waves reach the driver again (~ 700s). We see that the sudden increase (decrease) in B_z (v_z) can indeed be associated with this timescale. The standing regime seems to last for $\sim 300 - 400$s, which corresponds with the second blue line. Because the reflection happens throughout the chromosphere, the length between the location of the driver and the location of reflection is not exact, and the location of the driver is not a perfect node/antinode. This was also explained in Section B.2.2. In the timespan $\sim 700 - 1100$s the magnetic pressure force increases at the location of the driver, which increases the upflows and the associated mass flows (see Figure B.11).

The reason why the standing mode regime only seems to last for a short time, is because it can be destroyed by the interference with other propagating waves. When the right propagating Alfvén waves reflect in the second chromosphere and propagate back to the location of the driver, the standing regime can be destroyed. To show this we repeat the uniform simulation with the force driver implemented at $y = 200$ Mm from section B.2.2, however the top boundary of the numerical domain ($y = 600$ Mm) is now a reflective boundary rather than the location where a damping layer has been added. Figure B.10 shows a plot of v_z (km/s) at the location of the driver. At $t = 347$s (the first vertical blue line), the reflected left propagating Alfvén waves reach the location of the driver again and create a standing mode with a node in v_z. However at $t = 694$s (the second vertical blue line) the right propagating Alfvén waves that have reflected of the top boundary reach the location of the driver and v_z is no longer a node. This happens because the reflected right propagating Alfvén waves interfere with the standing wave and the regime changes to a propagating wave again.

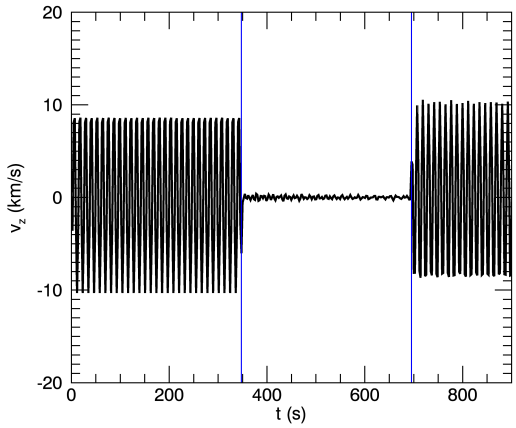

Figure B.10: Plot of v_z (km/s) at the location of the driver ($y = 200$ Mm), for the uniform simulation with reflective boundaries.

B.3.2 Mass evolution

Figure B.11 shows the relative mass evolution in the region ($44 < y < 50$ Mm), for the continued relaxation simulation (dashed line) and the driving simulation (solid line). In the continued relaxation simulation no driver has been implemented, but the system is allowed to relax further for the same amount of time as the driven simulation. We see that for the continued relaxation simulation the mass change oscillates about zero, because of the field aligned flows present from the continued relaxation. The period of the mass change is related to the travel time for a slow wave from one end of the loop to the other (~ 500s). The mass change in the driving simulation increases from the start and it then gradually increases until it reaches a steady state ($t > 1500$s). The largest increase corresponds with the time of the antinode in B_z (Figure B.9). The reason why the mass starts to increase earlier than 700s is because of the gradual reflection of the Alfvén waves in the chromosphere. Near the end of the simulation (3000s) the relative mass has increased by $\sim 0.03\%$.

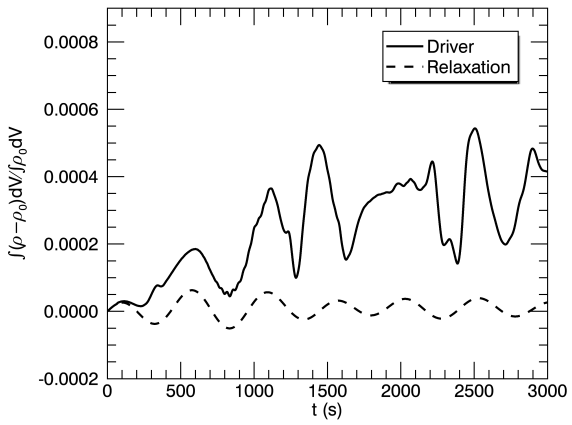

Figure B.11: Plot of the relative mass increase $\int(\rho - \rho_0)dV / \int \rho_0 dV$ for the region $44 < y < 50$ Mm, for the continued relaxation simulation (dashed line) and the driver simulation (solid line).

Bibliography

Toufik E. Abdelatif. Heating of Coronal Loops by Phase-mixed Shear Alfven Waves. *Astrophys. J.*, 322:494, November 1987. doi: 10.1086/165745.

Kwangsu Ahn, Jongchul Chae, Kyung-Suk Cho, Donguk Song, Heesu Yang, Philip R. Goode, Wenda Cao, Hyungmin Park, Jakyung Nah, Bi-Ho Jang, and Young-Deuk Park. Active Region Coronal Rain Event Observed by the Fast Imaging Solar Spectrograph on the NST. *Solar Phys.*, 289(11):4117–4136, Nov 2014. doi: 10.1007/s11207-014-0559-x.

S. K. Antiochos, P. J. MacNeice, D. S. Spicer, and J. A. Klimchuk. The Dynamic Formation of Prominence Condensations. *Astrophys. J.*, 512:985–991, February 1999. doi: 10.1086/306804.

P. Antolin and L. Rouppe van der Voort. Observing the Fine Structure of Loops through High-resolution Spectroscopic Observations of Coronal Rain with the CRISP Instrument at the Swedish Solar Telescope. *Astrophys. J.*, 745:152, February 2012. doi: 10.1088/0004-637X/745/2/152.

P. Antolin and E. Verwichte. Transverse Oscillations of Loops with Coronal Rain Observed by Hinode/Solar Optical Telescope. *Astrophys. J.*, 736(2):121, Aug 2011. doi: 10.1088/0004-637X/736/2/121.

P. Antolin, K. Shibata, T. Kudoh, D. Shiota, and D. Brooks. Signatures of Coronal Heating Mechanisms. *Astrophysics and Space Science Proceedings*, 19:277–280, 2010a. doi: 10.1007/978-3-642-02859-5-21.

P. Antolin, K. Shibata, and G. Vissers. Coronal Rain as a Marker for Coronal Heating Mechanisms. *Astrophys. J.*, 716(1):154–166, Jun 2010b. doi: 10.1088/0004-637X/716/1/154.

P. Antolin, T. J. Okamoto, B. De Pontieu, H. Uitenbroek, T. Van Doorsselaere, and T. Yokoyama. Resonant Absorption of Transverse Oscillations and Associated Heat-

ing in a Solar Prominence. II. Numerical Aspects. *Astrophys. J.*, 809(1):72, August 2015a. doi: 10.1088/0004-637X/809/1/72.

P. Antolin, G. Vissers, T. M. D. Pereira, L. Rouppe van der Voort, and E. Scullion. The Multithermal and Multi-stranded Nature of Coronal Rain. *Astrophys. J.*, 806: 81, June 2015b. doi: 10.1088/0004-637X/806/1/81.

P. Antolin, P. Pagano, I. De Moortel, and V. M. Nakariakov. In Situ Generation of Transverse Magnetohydrodynamic Waves from Colliding Flows in the Solar Corona. *Astrophys. J. Lett.*, 861:L15, July 2018. doi: 10.3847/2041-8213/aacf98.

Patrick Antolin. Thermal instability and non-equilibrium in solar coronal loops: from coronal rain to long-period intensity pulsations. *Plasma Physics and Controlled Fusion*, 62(1):014016, Jan 2020. doi: 10.1088/1361-6587/ab5406.

T. D. Arber, A. W. Longbottom, C. L. Gerrard, and A. M. Milne. A Staggered Grid, Lagrangian-Eulerian Remap Code for 3-D MHD Simulations. *Journal of Computational Physics*, 171:151–181, July 2001. doi: 10.1006/jcph.2001.6780.

I. Arregui. Wave heating of the solar atmosphere. *Philosophical Transactions of the Royal Society of London Series A*, 373:20140261–20140261, April 2015. doi: 10.1098/rsta.2014.0261.

Iñigo Arregui, Ramón Oliver, and José Luis Ballester. Prominence Oscillations. *Living Reviews in Solar Physics*, 9(1):2, April 2012. doi: 10.12942/lrsp-2012-2.

Markus J. Aschwanden, Lyndsay Fletcher, Carolus J. Schrijver, and David Alexander. Coronal Loop Oscillations Observed with the Transition Region and Coronal Explorer. *Astrophys. J.*, 520(2):880–894, August 1999. doi: 10.1086/307502.

Markus J. Aschwanden, Bart de Pontieu, Carolus J. Schrijver, and Alan M. Title. Transverse Oscillations in Coronal Loops Observed with TRACE II. Measurements of Geometric and Physical Parameters. *Solar Phys.*, 206(1):99–132, March 2002. doi: 10.1023/A:1014916701283.

Markus J. Aschwanden, Richard W. Nightingale, Jesse Andries, Marcel Goossens, and Tom Van Doorsselaere. Observational Tests of Damping by Resonant Absorption in Coronal Loop Oscillations. *Astrophys. J.*, 598(2):1375–1386, December 2003. doi: 10.1086/379104.

D. Banerjee, R. Erdélyi, R. Oliver, and E. O'Shea. Present and Future Observing Trends in Atmospheric Magnetoseismology. *Solar Phys.*, 246(1):3–29, November 2007. doi: 10.1007/s11207-007-9029-z.

D. Banerjee, D. Pérez-Suárez, and J. G. Doyle. Signatures of Alfvén waves in the polar coronal holes as seen by EIS/Hinode. *Astron. Astrophys.*, 501(3):L15–L18, July 2009. doi: 10.1051/0004-6361/200912242.

David Berghmans and Peter de Bruyne. Coronal Loop Oscillations Driven by Footpoint Motions: Analytical Results for a Model Problem. *Astrophys. J.*, 453:495, Nov 1995. doi: 10.1086/176410.

G. J. J. Botha, T. D. Arber, V. M. Nakariakov, and F. P. Keenan. A developed stage of Alfvén wave phase mixing. *Astron. Astrophys.*, 363:1186–1194, November 2000.

S. J. Bradshaw and P. J. Cargill. The Influence of Numerical Resolution on Coronal Density in Hydrodynamic Models of Impulsive Heating. *Astrophys. J.*, 770:12, June 2013. doi: 10.1088/0004-637X/770/1/12.

S. J. Bradshaw and H. E. Mason. The radiative response of solar loop plasma subject to transient heating. *Astron. Astrophys.*, 407:1127–1138, September 2003. doi: 10.1051/0004-6361:20030986.

S. I. Braginskii. Transport Processes in a Plasma. *Reviews of Plasma Physics*, 1:205, 1965.

David H. Brooks. Properties of the Diffuse Emission around Warm Loops in Solar Active Regions. *Astrophys. J.*, 873(1):26, March 2019. doi: 10.3847/1538-4357/ab0179.

David H. Brooks, Harry P. Warren, David R. Williams, and Tetsuya Watanabe. Hinode/Extreme-Ultraviolet Imaging Spectrometer Observations of the Temperature Structure of the Quiet Corona. *Astrophys. J.*, 705(2):1522–1532, November 2009. doi: 10.1088/0004-637X/705/2/1522.

David H. Brooks, Harry P. Warren, and Ignacio Ugarte-Urra. Solar Coronal Loops Resolved by Hinode and the Solar Dynamics Observatory. *Astrophys. J. Lett.*, 755 (2):L33, August 2012. doi: 10.1088/2041-8205/755/2/L33.

P. K. Browning and E. R. Priest. Kelvin-Helmholtz instability of a phased-mixed Alfven wave. *Astron. Astrophys.*, 131(2):283–290, February 1984.

Paul S. Cally. Alfvén waves in the structured solar corona. *Mon. Not. Roy. Astron. Soc.*, 466(1):413–424, April 2017. doi: 10.1093/mnras/stw3215.

P. J. Cargill. Some implications of the nanoflare concept. *Astrophys. J.*, 422:381–393, February 1994. doi: 10.1086/173733.

P. J. Cargill, I. De Moortel, and G. Kiddie. Coronal Density Structure and its Role in Wave Damping in Loops. *Astrophys. J.*, 823:31, May 2016. doi: 10.3847/0004-637X/823/1/31.

N. Dadashi, L. Teriaca, and S. K. Solanki. The quiet Sun average Doppler shift of coronal lines up to 2 MK. *Astron. Astrophys.*, 534:A90, October 2011. doi: 10.1051/0004-6361/201117234.

N. Dadashi, L. Teriaca, D. Tripathi, S. K. Solanki, and T. Wiegelmann. Doppler shift of hot coronal lines in a moss area of an active region. *Astron. Astrophys.*, 548: A115, December 2012. doi: 10.1051/0004-6361/201220329.

A. De Groof, C. Bastiaensen, D. A. N. Müller, D. Berghmans, and S. Poedts. Detailed comparison of downflows seen both in EIT 30.4 nm and Big Bear Hα movies. *Astron. Astrophys.*, 443(1):319–328, Nov 2005. doi: 10.1051/0004-6361:20053129.

I. De Moortel and P. Browning. Recent advances in coronal heating. *Philosophical Transactions of the Royal Society of London Series A*, 373:20140269–20140269, April 2015. doi: 10.1098/rsta.2014.0269.

I. De Moortel and A. W. Hood. The damping of slow MHD waves in solar coronal magnetic fields. *Astron. Astrophys.*, 408:755–765, September 2003. doi: 10.1051/0004-6361:20030984.

I. De Moortel and V. M. Nakariakov. Magnetohydrodynamic waves and coronal seismology: an overview of recent results. *Philosophical Transactions of the Royal Society of London Series A*, 370:3193–3216, July 2012. doi: 10.1098/rsta.2011.0640.

I. De Moortel, A. W. Hood, J. Ireland, and T. D. Arber. Phase mixing of Alfvén waves in a stratified and open atmosphere. *Astron. Astrophys.*, 346:641–651, June 1999.

I. De Moortel, A. W. Hood, and T. D. Arber. Phase mixing of Alfvén waves in a stratified and radially diverging, open atmosphere. *Astron. Astrophys.*, 354:334–348, February 2000.

B. De Pontieu, P. C. H. Martens, and H. S. Hudson. Chromospheric Damping of Alfvén Waves. *Astrophys. J.*, 558(2):859–871, Sep 2001. doi: 10.1086/322408.

B. De Pontieu, S. W. McIntosh, M. Carlsson, V. H. Hansteen, T. D. Tarbell, C. J. Schrijver, A. M. Title, R. A. Shine, S. Tsuneta, Y. Katsukawa, K. Ichimoto, Y. Suematsu, T. Shimizu, and S. Nagata. Chromospheric Alfvénic Waves Strong Enough to Power the Solar Wind. *Science*, 318(5856):1574, December 2007. doi: 10.1126/science.1151747.

G. Del Zanna. Flows in active region loops observed by Hinode EIS. *Astron. Astrophys.*, 481(1):L49–L52, April 2008. doi: 10.1051/0004-6361:20079087.

P. M. Edwin and B. Roberts. Wave propagation in a magnetic cylinder. *Solar Phys.*, 88:179–191, October 1983. doi: 10.1007/BF00196186.

R. Erdélyi and V. Fedun. Are There Alfvén Waves in the Solar Atmosphere? *Science*, 318(5856):1572, December 2007. doi: 10.1126/science.1153006.

X. Fang, C. Xia, and R. Keppens. Multidimensional Modeling of Coronal Rain Dynamics. *Astrophys. J. Lett.*, 771(2):L29, July 2013. doi: 10.1088/2041-8205/771/2/L29.

X. Fang, C. Xia, R. Keppens, and T. Van Doorsselaere. Coronal Rain in Magnetic Arcades: Rebound Shocks, Limit Cycles, and Shear Flows. *Astrophys. J.*, 807(2): 142, July 2015. doi: 10.1088/0004-637X/807/2/142.

Xia Fang, Ding Yuan, Chun Xia, Tom Van Doorsselaere, and Rony Keppens. The Role of Kelvin-Helmholtz Instability for Producing Loop-top Hard X-Ray Sources in Solar Flares. *Astrophys. J.*, 833(1):36, Dec 2016. doi: 10.3847/1538-4357/833/1/36.

U. Feldman, I. E. Dammasch, and G. A. Doschek. Redshifts, Widths, and Radiances of Spectral Lines Emitted by the Solar Transition Region. *Astrophys. J.*, 743(2): 165, December 2011. doi: 10.1088/0004-637X/743/2/165.

C. Froment, F. Auchère, G. Aulanier, Z. Mikić, K. Bocchialini, E. Buchlin, and J. Solomon. Long-period Intensity Pulsations in Coronal Loops Explained by Thermal Non-equilibrium Cycles. *Astrophys. J.*, 835(2):272, February 2017. doi: 10.3847/1538-4357/835/2/272.

C. Froment, P. Antolin, V. M. J. Henriques, P. Kohutova, and L. H. M. Rouppe van der Voort. Multi-scale observations of thermal non-equilibrium cycles in coronal loops. *Astron. Astrophys.*, 633:A11, Jan 2020. doi: 10.1051/0004-6361/201936717.

Marcel Goossens, Robert Erdélyi, and Michael S. Ruderman. Resonant MHD Waves in the Solar Atmosphere. *Space Sci. Rev.*, 158(2-4):289–338, July 2011. doi: 10.1007/s11214-010-9702-7.

N. Guerreiro, Viggo Hansteen, and B. De Pontieu. The Cycling of Material between the Solar Corona and Chromosphere. *Astrophys. J.*, 769(1):47, May 2013. doi: 10.1088/0004-637X/769/1/47.

V. H. Hansteen, H. Hara, B. De Pontieu, and M. Carlsson. On Redshifts and Blueshifts in the Transition Region and Corona. *Astrophys. J.*, 718(2):1070–1078, August 2010. doi: 10.1088/0004-637X/718/2/1070.

J. Heyvaerts and E. R. Priest. Coronal heating by phase-mixed shear Alfven waves. *Astron. Astrophys.*, 117:220–234, January 1983.

J. V. Hollweg. Resonances of coronal loops. *Astrophys. J.*, 277:392–403, Feb 1984a. doi: 10.1086/161706.

J. V. Hollweg. Alfvénic resonant cavities in the solar atmosphere: Simple aspects. *Solar Phys.*, 91(2):269–288, Apr 1984b. doi: 10.1007/BF00146299.

J. V. Hollweg. Transition region, corona, and solar wind in coronal holes. *J. Geophys. Res.*, 91(A4):4111–4125, April 1986. doi: 10.1029/JA091iA04p04111.

A. W. Hood. Instabilities in the solar corona. *Plasma Physics and Controlled Fusion*, 34(4):411–442, April 1992. doi: 10.1088/0741-3335/34/4/002.

A. W. Hood and E. R. Priest. The equilibrium of solar coronal magnetic loops. *Astron. Astrophys.*, 77(1-2):233–251, August 1979.

A. W. Hood, J. Ireland, and E. R. Priest. Heating of coronal holes by phase mixing. *Astron. Astrophys.*, 318:957–962, February 1997.

A. W. Hood, S. J. Brooks, and A. N. Wright. Coronal heating by the phase mixing of individual pulses propagating in coronal holes. *Proceedings of the Royal Society of London Series A*, 458(2026):2307, October 2002. doi: 10.1098/rspa.2002.0959.

A. W. Hood, S. J. Brooks, and A. N. Wright. Phase mixing of Alfvén pulses and wavetrains propagating in coronal holes. *Proceedings of the Royal Society of London Series A*, 461(2053):237–252, January 2005. doi: 10.1098/rspa.2004.1384.

T. A. Howson, I. De Moortel, and P. Antolin. Energetics of the Kelvin-Helmholtz instability induced by transverse waves in twisted coronal loops. *Astron. Astrophys.*, 607:A77, November 2017. doi: 10.1051/0004-6361/201731178.

T. A. Howson, I. De Moortel, J. Reid, and A. W. Hood. Magnetohydrodynamic waves in braided magnetic fields. *Astron. Astrophys.*, 629:A60, September 2019. doi: 10.1051/0004-6361/201935876.

T. A. Howson, I. De Moortel, and J. Reid. Phase mixing and wave heating in a complex coronal plasma. *Astron. Astrophys.*, 636:A40, April 2020. doi: 10.1051/0004-6361/201937332.

J. A. Ionson. Resonant absorption of Alfvénic surface waves and the heating of solar coronal loops. *Astrophys. J.*, 226:650–673, December 1978. doi: 10.1086/156648.

D. B. Jess, R. J. Morton, G. Verth, V. Fedun, S. D. T. Grant, and I. Giagkiozis. Multiwavelength Studies of MHD Waves in the Solar Chromosphere. An Overview of Recent Results. *Space Sci. Rev.*, 190(1-4):103–161, July 2015. doi: 10.1007/s11214-015-0141-3.

David B. Jess, Mihalis Mathioudakis, Robert Erdélyi, Philip J. Crockett, Francis P. Keenan, and Damian J. Christian. Alfvén Waves in the Lower Solar Atmosphere. *Science*, 323(5921):1582, March 2009. doi: 10.1126/science.1168680.

C. D. Johnston, A. W. Hood, P. J. Cargill, and I. De Moortel. A new approach for modelling chromospheric evaporation in response to enhanced coronal heating. I. The method. *Astron. Astrophys.*, 597:A81, January 2017a. doi: 10.1051/0004-6361/201629153.

C. D. Johnston, A. W. Hood, P. J. Cargill, and I. De Moortel. A new approach for modelling chromospheric evaporation in response to enhanced coronal heating. II. Non-uniform heating. *Astron. Astrophys.*, 605:A8, August 2017b. doi: 10.1051/0004-6361/201730486.

C. D. Johnston, P. J. Cargill, A. W. Hood, I. De Moortel, S. J. Bradshaw, and A. C. Vaseekar. Modelling the solar transition region using an adaptive conduction method. *Astron. Astrophys.*, 635:A168, March 2020. doi: 10.1051/0004-6361/201936979.

K. Karampelas, T. Van Doorsselaere, and P. Antolin. Heating by transverse waves in simulated coronal loops. *Astron. Astrophys.*, 604:A130, August 2017. doi: 10.1051/0004-6361/201730598.

J. T. Karpen, S. E. M. Tanner, S. K. Antiochos, and C. R. DeVore. Prominence Formation by Thermal Nonequilibrium in the Sheared-Arcade Model. *Astrophys. J.*, 635(2):1319–1328, Dec 2005. doi: 10.1086/497531.

J. A. Klimchuk. On Solving the Coronal Heating Problem. *Solar Phys.*, 234:41–77, March 2006. doi: 10.1007/s11207-006-0055-z.

J. A. Klimchuk, S. Patsourakos, and P. J. Cargill. Highly Efficient Modeling of Dynamic Coronal Loops. *Astrophys. J.*, 682:1351-1362, August 2008. doi: 10.1086/589426.

P. Kohutova and E. Verwichte. Analysis of coronal rain observed by IRIS, Hinode/SOT, and SDO/AIA: Transverse oscillations, kinematics, and thermal evolution. *The Astrophysical Journal*, 827(1):39, aug 2016. doi: 10.3847/0004-637x/827/1/39.

P. Kohutova and E. Verwichte. Excitation of vertical coronal loop oscillations by plasma condensations. *Astron. Astrophys.*, 606:A120, October 2017. doi: 10.1051/0004-6361/201731417.

P. Kohutova and E. Verwichte. Excitation of vertical coronal loop oscillations by impulsively driven flows. *Astron. Astrophys.*, 613:L3, May 2018a. doi: 10.1051/0004-6361/201832656.

Petra Kohutova and Erwin Verwichte. Simulating the Dynamics of Coronal Plasma Condensations. In Claire Foullon and Olga E. Malandraki, editors, *Space Weather of the Heliosphere: Processes and Forecasts*, volume 335 of *IAU Symposium*, pages 23–25, Aug 2018b. doi: 10.1017/S1743921317010997.

S. Krishna Prasad, D. B. Jess, and Elena Khomenko. On the Source of Propagating Slow Magnetoacoustic Waves in Sunspots. *Astrophys. J. Lett.*, 812(1):L15, October 2015. doi: 10.1088/2041-8205/812/1/L15.

N. P. M. Kuin and P. C. H. Martens. On the thermal stability of hot coronal loops - The coupling between chromosphere and corona. *Astron. Astrophys.*, 108(2):L1–L4, Apr 1982.

J. Martin Laming. The First Ionization Potential Effect from the Ponderomotive Force: On the Polarization and Coronal Origin of Alfvén Waves. *Astrophys. J.*, 844(2): 153, Aug 2017. doi: 10.3847/1538-4357/aa7cf1.

Y. Lin, R. Soler, O. Engvold, J. L. Ballester, Ø. Langangen, R. Oliver, and L. H. M. Rouppe van der Voort. Swaying Threads of a Solar Filament. *Astrophys. J.*, 704 (1):870–876, October 2009. doi: 10.1088/0004-637X/704/1/870.

R. Lionello, J. A. Linker, and Z. Mikić. Multispectral Emission of the Sun During the First Whole Sun Month: Magnetohydrodynamic Simulations. *Astrophys. J.*, 690: 902–912, January 2009. doi: 10.1088/0004-637X/690/1/902.

D. M. Long, D. R. Williams, S. Régnier, and L. K. Harra. Measuring the Magnetic-Field Strength of the Quiet Solar Corona Using "EIT Waves". *Solar Phys.*, 288(2): 567–583, December 2013. doi: 10.1007/s11207-013-0331-7.

D. Martínez-Gómez, R. Oliver, E. Khomenko, and M. Collados. Two-dimensional simulations of coronal rain dynamics. I. Model consisting of a vertical magnetic field and an unbounded atmosphere. *Astron. Astrophys.*, 634:A36, February 2020. doi: 10.1051/0004-6361/201937078.

M. Mathioudakis, D. B. Jess, and R. Erdélyi. Alfvén Waves in the Solar Atmosphere. From Theory to Observations. *Space Sci. Rev.*, 175(1-4):1–27, June 2013. doi: 10.1007/s11214-012-9944-7.

T. Matsumoto and R. Kitai. Temporal Power Spectra of the Horizontal Velocity of the Solar Photosphere. *Astrophys. J. Lett.*, 716:L19–L22, June 2010. doi: 10.1088/2041-8205/716/1/L19.

Scott W. McIntosh, B. De Pontieu, and S. Tomczyk. Reconciling Chromospheric and Coronal Observations of Alfvenic Waves. In *AAS/Solar Physics Division Meeting #40*, AAS/Solar Physics Division Meeting, page 13.03, May 2009.

Scott W. McIntosh, Bart de Pontieu, Mats Carlsson, Viggo Hansteen, Paul Boerner, and Marcel Goossens. Alfvénic waves with sufficient energy to power the quiet solar corona and fast solar wind. *Nature*, 475(7357):477–480, July 2011. doi: 10.1038/nature10235.

Scott W. McIntosh, Hui Tian, Marybeth Sechler, and Bart De Pontieu. On the Doppler Velocity of Emission Line Profiles Formed in the "Coronal Contraflow" that Is the Chromosphere-Corona Mass Cycle. *Astrophys. J.*, 749(1):60, April 2012. doi: 10.1088/0004-637X/749/1/60.

Z. Mikić, R. Lionello, Y. Mok, J. A. Linker, and A. R. Winebarger. The Importance of Geometric Effects in Coronal Loop Models. *Astrophys. J.*, 773:94, August 2013. doi: 10.1088/0004-637X/773/2/94.

R. J. Morton, S. Tomczyk, and R. F. Pinto. A Global View of Velocity Fluctuations in the Corona below 1.3 R with CoMP. *Astrophys. J.*, 828(2):89, September 2016. doi: 10.3847/0004-637X/828/2/89.

Richard J. Morton, Gary Verth, David B. Jess, David Kuridze, Michael S. Ruderman, Mihalis Mathioudakis, and Robertus Erdélyi. Observations of ubiquitous compressive waves in the Sun's chromosphere. *Nature Communications*, 3:1315, December 2012. doi: 10.1038/ncomms2324.

S. P. Moschou, R. Keppens, C. Xia, and X. Fang. Simulating coronal condensation dynamics in 3D. *Advances in Space Research*, 56(12):2738–2759, December 2015. doi: 10.1016/j.asr.2015.05.008.

V. M. Nakariakov, B. Roberts, and K. Murawski. Alfven Wave Phase Mixing as a Source of Fast Magnetosonic Waves. *Solar Phys.*, 175(1):93–105, September 1997. doi: 10.1023/A:1004965725929.

V. M. Nakariakov, B. Roberts, and K. Murawski. Nonlinear coupling of MHD waves in inhomogeneous steady flows. *Astron. Astrophys.*, 332:795–804, April 1998.

V. M. Nakariakov, L. Ofman, E. E. Deluca, B. Roberts, and J. M. Davila. TRACE observation of damped coronal loop oscillations: Implications for coronal heating. *Science*, 285:862–864, August 1999. doi: 10.1126/science.285.5429.862.

Valery M. Nakariakov and Erwin Verwichte. Coronal Waves and Oscillations. *Living Reviews in Solar Physics*, 2(1):3, May 2005. doi: 10.12942/lrsp-2005-3.

L. Ofman. Chromospheric Leakage of Alfvén Waves in Coronal Loops. *Astrophys. J. Lett.*, 568(2):L135–L138, Apr 2002. doi: 10.1086/340329.

L. Ofman and J. M. Davila. Nonlinear resonant absorption of Alfvén waves in three dimensions, scaling laws, and coronal heating. *J. Geophys. Res.*, 100(A12):23427–23442, December 1995. doi: 10.1029/95JA01907.

L. Ofman, J. A. Klimchuk, and J. M. Davila. A Self-consistent Model for the Resonant Heating of Coronal Loops: The Effects of Coupling with the Chromosphere. *Astrophys. J.*, 493(1):474–479, January 1998. doi: 10.1086/305109.

T. J. Okamoto, S. Tsuneta, T. E. Berger, K. Ichimoto, Y. Katsukawa, B. W. Lites, S. Nagata, K. Shibata, T. Shimizu, R. A. Shine, Y. Suematsu, T. D. Tarbell, and A. M. Title. Coronal Transverse Magnetohydrodynamic Waves in a Solar Prominence. *Science*, 318(5856):1577, December 2007. doi: 10.1126/science.1145447.

Takenori J. Okamoto, Patrick Antolin, Bart De Pontieu, Han Uitenbroek, Tom Van Doorsselaere, and Takaaki Yokoyama. Resonant Absorption of Transverse Oscillations and Associated Heating in a Solar Prominence. I. Observational Aspects. *Astrophys. J.*, 809(1):71, August 2015. doi: 10.1088/0004-637X/809/1/71.

R. Oliver, R. Soler, J. Terradas, and T. V. Zaqarashvili. Dynamics of Coronal Rain and Descending Plasma Blobs in Solar Prominences. II. Partially Ionized Case. *Astrophys. J.*, 818:128, February 2016. doi: 10.3847/0004-637X/818/2/128.

P. Pagano and I. De Moortel. Contribution of mode-coupling and phase-mixing of Alfvén waves to coronal heating. *Astron. Astrophys.*, 601:A107, May 2017. doi: 10.1051/0004-6361/201630059.

P. Pagano, D. J. Pascoe, and I. De Moortel. Contribution of phase-mixing of Alfvén waves to coronal heating in multi-harmonic loop oscillations. *Astron. Astrophys.*, 616:A125, August 2018. doi: 10.1051/0004-6361/201732251.

P. Pagano, H. J. Van Damme, P. Antolin, and I. De Moortel. MHD simulations of the in situ generation of kink and sausage waves in the solar corona by collision of dense plasma clumps. *Astron. Astrophys.*, 626:A53, June 2019. doi: 10.1051/0004-6361/201935539.

Susanna Parenti. Solar Prominences: Observations. *Living Reviews in Solar Physics*, 11(1):1, March 2014. doi: 10.12942/lrsp-2014-1.

E. N. Parker. Heating Solar Coronal Holes. *Astrophys. J.*, 372:719, May 1991. doi: 10.1086/170015.

C. E. Parnell and I. De Moortel. A contemporary view of coronal heating. *Philosophical Transactions of the Royal Society of London Series A*, 370:3217–3240, July 2012. doi: 10.1098/rsta.2012.0113.

D. J. Pascoe, A. N. Wright, and I. De Moortel. Coupled Alfvén and Kink Oscillations in Coronal Loops. *Astrophys. J.*, 711(2):990–996, March 2010. doi: 10.1088/0004-637X/711/2/990.

D. J. Pascoe, A. N. Wright, and I. De Moortel. Propagating Coupled Alfvén and Kink Oscillations in an Arbitrary Inhomogeneous Corona. *Astrophys. J.*, 731:73, April 2011. doi: 10.1088/0004-637X/731/1/73.

D. J. Pascoe, C. R. Goddard, G. Nisticò, S. Anfinogentov, and V. M. Nakariakov. Damping profile of standing kink oscillations observed by SDO/AIA. *Astron. Astrophys.*, 585:L6, January 2016. doi: 10.1051/0004-6361/201527835.

N. S. Petrukhin, M. S. Ruderman, and E. G. Shurgalina. Phase mixing of Alfvén waves in axisymmetric non-reflective magnetic plasma configurations. *Mon. Not. Roy. Astron. Soc.*, 474(2):2289–2301, February 2018. doi: 10.1093/mnras/stx2914.

S. Poedts and J. P. Goedbloed. Nonlinear wave heating of solar coronal loops. *Astron. Astrophys.*, 321:935–944, May 1997.

O. Porth, C. Xia, T. Hendrix, S. P. Moschou, and R. Keppens. MPI-AMRVAC for Solar and Astrophysics. *Astrophys. J. Suppl.*, 214:4, September 2014. doi: 10.1088/0067-0049/214/1/4.

W. H. Press, B. P. Flannery, S. A. Teukolsky, and W. T. Vetterling. *Numerical Recipes 3rd Edition: The Art of Scientific Computing*. 2007.

Eric Priest. *Magnetohydrodynamics of the Sun*. 2014. doi: 10.1017/CBO9781139020732.

A. P. K. Prokopyszyn, A. W. Hood, and I. De Moortel. Phase mixing of nonlinear Alfvén waves. *Astron. Astrophys.*, 624:A90, Apr 2019. doi: 10.1051/0004-6361/201834939.

F. Reale. Coronal Loops: Observations and Modeling of Confined Plasma. *Living Reviews in Solar Physics*, 7:5, November 2010. doi: 10.12942/lrsp-2010-5.

R. Rosner, W. H. Tucker, and G. S. Vaiana. Dynamics of the quiescent solar corona. *Astrophys. J.*, 220:643–645, March 1978. doi: 10.1086/155949.

M. S. Ruderman and B. Roberts. The Damping of Coronal Loop Oscillations. *Astrophys. J.*, 577(1):475–486, September 2002. doi: 10.1086/342130.

M. S. Ruderman, M. L. Goldstein, D. A. Roberts, A. Deane, and L. Ofman. Alfvén wave phase mixing driven by velocity shear in two-dimensional open magnetic configurations. *J. Geophys. Res.*, 104(A8):17057–17068, August 1999. doi: 10.1029/1999JA900144.

Michael S. Ruderman and Robert Erdélyi. Transverse Oscillations of Coronal Loops. *Space Sci. Rev.*, 149(1-4):199–228, December 2009. doi: 10.1007/s11214-009-9535-4.

Michael S. Ruderman and Nikolai S. Petrukhin. Phase mixing of Alfvén waves in two-dimensional magnetic plasma configurations with exponentially decreasing density. *Astron. Astrophys.*, 620:A44, November 2018. doi: 10.1051/0004-6361/201833639.

Michael S. Ruderman, Valery M. Nakariakov, and Bernard Roberts. Alfven wave phase mixing in two-dimensional open magnetic configurations. *Astron. Astrophys.*, 338: 1118–1124, October 1998.

Carolus J. Schrijver. Catastrophic cooling and high-speed downflow in quiescent solar coronal loops observed with TRACE. *Solar Phys.*, 198(2):325–345, Feb 2001. doi: 10.1023/A:1005211925515.

Carolus J. Schrijver, Markus J. Aschwanden, and Alan M. Title. Transverse oscillations in coronal loops observed with TRACE I. An Overview of Events, Movies, and a Discussion of Common Properties and Required Conditions. *Solar Phys.*, 206(1): 69–98, March 2002. doi: 10.1023/A:1014957715396.

E. Scullion, L. Rouppe van der Voort, S. Wedemeyer, and P. Antolin. Unresolved Fine-scale Structure in Solar Coronal Loop-tops. *Astrophys. J.*, 797(1):36, Dec 2014. doi: 10.1088/0004-637X/797/1/36.

P. D. Smith, D. Tsiklauri, and M. S. Ruderman. Enhanced phase mixing of Alfvén waves propagating in stratified and divergent coronal structures. *Astron. Astrophys.*, 475(3):1111–1123, December 2007. doi: 10.1051/0004-6361:20078218.

R. Soler, J. Terradas, R. Oliver, and J. L. Ballester. Propagation of Torsional Alfvén Waves from the Photosphere to the Corona: Reflection, Transmission, and Heating in Expanding Flux Tubes. *Astrophys. J.*, 840:20, May 2017. doi: 10.3847/1538-4357/aa6d7f.

Abhishek Kumar Srivastava, Juie Shetye, Krzysztof Murawski, John Gerard Doyle, Marco Stangalini, Eamon Scullion, Tom Ray, Dariusz Patryk Wójcik, and Bhola N. Dwivedi. High-frequency torsional Alfvén waves as an energy source for coronal heating. *Scientific Reports*, 7:43147, March 2017. doi: 10.1038/srep43147.

T. K. Suzuki and S.-i. Inutsuka. Making the Corona and the Fast Solar Wind: A Self-consistent Simulation for the Low-Frequency Alfvén Waves from the Photosphere to 0.3 AU. *Astrophys. J. Lett.*, 632:L49–L52, October 2005. doi: 10.1086/497536.

J. Terradas, I. Arregui, R. Oliver, J. L. Ballester, J. Andries, and M. Goossens. Resonant Absorption in Complicated Plasma Configurations: Applications to Multi-stranded Coronal Loop Oscillations. *Astrophys. J.*, 679(2):1611–1620, June 2008. doi: 10.1086/586733.

J. O. Thurgood and J. A. McLaughlin. On Ponderomotive Effects Induced by Alfvén Waves in Inhomogeneous 2.5D MHD Plasmas. *Solar Phys.*, 288(1):205–222, Nov 2013. doi: 10.1007/s11207-013-0298-4.

J. O. Thurgood, R. J. Morton, and J. A. McLaughlin. First Direct Measurements of Transverse Waves in Solar Polar Plumes Using SDO/AIA. *Astrophys. J. Lett.*, 790 (1):L2, July 2014. doi: 10.1088/2041-8205/790/1/L2.

S. Tomczyk, S. W. McIntosh, S. L. Keil, P. G. Judge, T. Schad, D. H. Seeley, and J. Edmondson. Alfvén Waves in the Solar Corona. *Science*, 317:1192, August 2007. doi: 10.1126/science.1143304.

Steven Tomczyk and Scott W. McIntosh. Time-Distance Seismology of the Solar Corona with CoMP. *Astrophys. J.*, 697(2):1384–1391, June 2009. doi: 10.1088/0004-637X/697/2/1384.

Durgesh Tripathi, Helen E. Mason, Giulio Del Zanna, and Steven Bradshaw. Observations of Plasma Upflow in a Warm Loop with Hinode/EIS. *Astrophys. J. Lett.*, 754(1):L4, July 2012a. doi: 10.1088/2041-8205/754/1/L4.

Durgesh Tripathi, Helen E. Mason, and James A. Klimchuk. Active Region Moss: Doppler Shifts from Hinode/Extreme-ultraviolet Imaging Spectrometer Observations. *Astrophys. J.*, 753(1):37, July 2012b. doi: 10.1088/0004-637X/753/1/37.

A. Tritschler, T. R. Rimmele, S. Berukoff, R. Casini, J. R. Kuhn, H. Lin, M. P. Rast, J. P. McMullin, W. Schmidt, F. Wöger, and DKIST Team. Daniel K. Inouye Solar Telescope: High-resolution observing of the dynamic Sun. *Astronomische Nachrichten*, 337(10):1064, November 2016. doi: 10.1002/asna.201612434.

H. J. Van Damme, I. De Moortel, P. Pagano, and C. D. Johnston. Chromospheric evaporation and phase mixing of Alfvén waves in coronal loops. *Astron. Astrophys.*, 635:A174, March 2020. doi: 10.1051/0004-6361/201937266.

T. Van Doorsselaere, C. S. Brady, E. Verwichte, and V. M. Nakariakov. Seismological demonstration of perpendicular density structuring in the solar corona. *Astron. Astrophys.*, 491(2):L9–L12, November 2008a. doi: 10.1051/0004-6361:200810659.

T. Van Doorsselaere, V. M. Nakariakov, and E. Verwichte. Detection of Waves in the Solar Corona: Kink or Alfvén? *Astrophys. J. Lett.*, 676(1):L73, March 2008b. doi: 10.1086/587029.

S. Vasheghani Farahani, T. Van Doorsselaere, E. Verwichte, and V. M. Nakariakov. Propagating transverse waves in soft X-ray coronal jets. *Astron. Astrophys.*, 498(2): L29–L32, May 2009. doi: 10.1051/0004-6361/200911840.

G. Verth, J. Terradas, and M. Goossens. Observational Evidence of Resonantly Damped Propagating Kink Waves in the Solar Corona. *Astrophys. J. Lett.*, 718 (2):L102–L105, August 2010. doi: 10.1088/2041-8205/718/2/L102.

E. Verwichte and P. Kohutova. Excitation and evolution of vertically polarised transverse loop oscillations by coronal rain. *Astron. Astrophys.*, 601:L2, May 2017. doi: 10.1051/0004-6361/201730675.

E. Verwichte, V. M. Nakariakov, and A. W. Longbottom. On the evolution of a nonlinear Alfvén pulse. *Journal of Plasma Physics*, 62:219–232, August 1999. doi: 10.1017/S0022377899007771.

E. Verwichte, V. M. Nakariakov, and F. C. Cooper. Transverse waves in a post-flare supra-arcade. *Astron. Astrophys.*, 430:L65–L68, January 2005. doi: 10.1051/0004-6361:200400133.

E. Verwichte, P. Antolin, G. Rowlands, P. Kohutova, and T. Neukirch. Kinematics of coronal rain in a transversely oscillating loop: Ponderomotive force and rain-excited oscillations. *Astron. Astrophys.*, 598:A57, Feb 2017. doi: 10.1051/0004-6361/201629634.

E. Verwichte, P. Kohutova, P. Antolin, G. Rowlands, and T. Neukirch. Excitation and Evolution of Transverse Loop Oscillations by Coronal Rain. In C. Foullon and O. E. Malandraki, editors, *Space Weather of the Heliosphere: Processes and Forecasts*, volume 335 of *IAU Symposium*, pages 36–38, August 2018. doi: 10.1017/S1743921317011024.

Amy Winebarger, Durgesh Tripathi, Helen E. Mason, and Giulio Del Zanna. Doppler Shifts in Active Region Moss Using SOHO/SUMER. *Astrophys. J.*, 767(2):107, April 2013. doi: 10.1088/0004-637X/767/2/107.

G. L. Withbroe and R. W. Noyes. Mass and energy flow in the solar chromosphere and corona. *Annual. Rev. Astron. Astrophys.*, 15:363–387, Jan 1977. doi: 10.1146/annurev.aa.15.090177.002051.

C. Xia, P. F. Chen, R. Keppens, and A. J. van Marle. Formation of Solar Filaments by Steady and Nonsteady Chromospheric Heating. *Astrophys. J.*, 737(1):27, Aug 2011. doi: 10.1088/0004-637X/737/1/27.

C. Xia, R. Keppens, and X. Fang. Coronal rain in magnetic bipolar weak fields. *Astron. Astrophys.*, 603:A42, July 2017. doi: 10.1051/0004-6361/201730660.

P. Zacharias, H. Peter, and S. Bingert. Ejection of cool plasma into the hot corona. *Astron. Astrophys.*, 532:A112, August 2011. doi: 10.1051/0004-6361/201116708.

T. V. Zaqarashvili and R. Erdélyi. Oscillations and Waves in Solar Spicules. *Space Sci. Rev.*, 149(1-4):355–388, December 2009. doi: 10.1007/s11214-009-9549-y.